INVESTIGATING THE EARLY STAGES OF MASSIVE STAR FORMATION IN
PROTOCLUSTER ENVIRONMENTS: MULTIWAVELENGTH STUDIES OF
EXTENDED GREEN OBJECTS

Allison Patricia Miksa Towner
Tucson, Arizona

B.S. Astronomy, University of Arizona, 2013

B.S. Physics, University of Arizona, 2013

M.S. Astronomy, University of Virginia, 2016

A Dissertation Presented to the Graduate
Faculty of the University of Virginia
in Candidacy for the Degree of
Doctor of Philosophy

Department of Astronomy

University of Virginia
August 2020

Committee Members:

Dr. Crystal L. Brogan
Dr. Remy Indebetouw
Dr. Zhi-Yun Li
Dr. Karen Kafadar

Abstract

Massive stars have a predilection for forming in clustered environments with other proto-stars. Therefore, the study of Massive Young Stellar Objects (MYSOs) necessarily requires the study of clusters of forming stars (protoclusters). Distinguishing between competing theories of massive star formation requires observing massive protoclusters at various stages in their evolutionary process. Extended Green Objects (EGOs) are signposts of massive young protoclusters believed to be in an evolutionary state just prior to the emergence of Ultracompact (UC) H II regions. This phase of protocluster evolution - in which the presence of massive stars can be confirmed but the natal clump has not yet been destroyed by the radiative feedback from MYSOs - is a critical one for distinguishing between competing star-formation theories. We have been conducting a multiwavelength study of a sample of 20 nearby EGOs with the goal of determining source bolometric luminosity, source multiplicity, and the evolutionary state of the most massive protocluster members. We have examined this sample using proprietary and archival infrared data (3.6 to 870 μm) and modeled their Spectral Energy Distributions (SEDs). We have further examined this sample at 1.3 and 5 cm with the VLA, and determined continuum-source flux densities, spectral indices, and spatial distributions within these regions, as well as associations with H_2O, CH_3OH, and NH_3 masers.

The average massive-source multiplicities (number of massive sources) are 1$\sim$2 per EGO, regardless of whether infrared or radio selection criteria are used. This is consistent with the model of EGOs as observational signposts of massive protoclusters that will form one to a few massive stars only, rather than extreme star-forming regions (e.g. 30 Doradus). Their luminosity-to-mass ratios (L/M) are broadly consistent with other massive protoclusters, but specifically seem to straddle the "IR-quiet" and "IR-bright" categories of MYSO classification identified by, e.g., the ATLASGAL Top100 and *Herschel* HOBYS

project teams. Generally, the difference between "IR-quiet" and "IR-bright" sources is the presence of a protostar which has started to produce significant radiative feedback, i.e. $M > 8M_\odot$ in the central star. This suggests that EGOs may be in a particularly consequential stage of evolution compared to other samples with different selection criteria. We also find ubiquitous weak, compact 1.3 and 5 cm continuum emission, as well as a plethora of H_2O masers, a mild association with NH_3 (3,3) masers, and a 100% association with 6.7 GHz CH_3OH masers (which are exclusively associated with massive protostars). Even at our high angular resolutions ($\sim$1000 au), most of our continuum sources remain unresolved. Their spectral indices span a broad range ($-0.5 \lesssim \alpha \lesssim 2$) and are consistent with multiple possible emission mechanisms, from synchrotron to thermal free-free to thermal dust emission. In order to distinguish between these possibilities, high-resolution millimeter data are needed in order to perform detailed modeling of the radio SEDs across multiple decades in frequency.

Acknowledgements

"Per aspera ad astra."

First and foremost among the people I want to thank in this document are my parents, Dr. Ronald Towner and Dr. Elizabeth Miksa. I'm not sure if me ending up in academia was inevitable - I still remember my four-year-old self declaring my intention to become a veterinarian once I learned vets didn't "have to go to grad school" - but I know I would never have made it here without you. From my decision to transfer as an undergrad to my decision to move clear across the country for grad school, and the entirely unexpected challenges I've had on top of grad school itself, your wisdom, advice, and love have meant the world to me. This thesis is dedicated to you both.

Professionally, I owe many, many thanks to my adviser, Dr. Crystal Brogan. Crystal, you are a true expert in your field, and I could not have gotten luckier than to get to work with you during grad school. I have learned so much over these last six years, and yet I am certain there is even more that you could still teach. In working with you I have learned how to write, how to read, and how to evaluate my own work and others'. Through both instruction and your own demonstrated practices, you have taught me the skills I need to be my own independent scientist. Lastly, on a more personal note: I knew academia would not be easy, but I think I can safely say I did not expect quite the set of challenges I was given. I am especially grateful that, when my path through grad school deviated rather sharply from what I had planned, you worked with me, supported me, asked me what I needed, and then did those things. You have been a true mentor to me when I needed one most. Thank you.

I would also like to thank Dr. Brett McGuire, Dr. Ryan Loomis, and Dr. Laura Fissel for putting up with my many questions over the years. Thanks especially to Ryan and Brett for all of your advice, edits, and reminders to breathe while I applied to jobs this year.

Many thanks also go to Dr. Todd Hunter, for his expertise in CASA, aU, and python in general, and for letting me pick his brain on these topics at length.

Next, I'd be entirely remiss if I did not thank Mandy Walker-LaFollette, who despite being three thousand miles away has always been up for whatever random thoughts I have in my head at 3 am. I miss being able to have these conversations in person, but I have enjoyed all of them immensely, and I promise to come visit you in Seattle as soon as we can all travel again. Props also go to Allison Matthews, Walter Freeman, and Brianna Mills for putting up with similar "random thoughts at 3 am" behavior from me for the last several months as I finish my thesis. Thanks to Lucas Mix for his invaluable advice and commiseration at the end of my grad school experience - and for putting up with some very out-of-the-blue philosophical questions from me over the years - and to Carter-Thaxton Smith, who has always shown me that time and distance are small things when it comes to friendship.

To Brian, Andrew, Dylan, Chris S., and the rest of the D&D gang, thank you so much for your imagination and companionship and for introducing me to the game in such a fun way. Even if I did die, it was worth it to see Jet speeding by at 240 miles an hour. Special thanks go to Brian, for also putting up with me as an officemate for two years, and to Chris H., for doing the same. Thanks to the rest of my class (Poon, Thankful, Pallavi, Sean, and Dylan again) as well. You all have always been there whenever I've had a question or coding challenge or just needed to vent.Thanks to Lauren, Sandy, Kim, Kristen, and all the other astrowomen, for being, well, the astrowomen.

Many, many thanks must also go to Whitney, Barbara, JJ, Danielle, Connie, and Jackie for all of the administrative work you do to keep the Astronomy Department and NRAO running, for putting up with my (very many) questions about funding and reimbursement, and generally being an unfailing source of support and knowledge of the intricacies of

academia. I think I can safely say that none of us at UVa/NRAO would be here without you.

On a more serious note, thanks especially to the following members of the Charlottesville medical community: Dr. S., Dr. T., Dr. X., Dr. D., Dr. M., Dr. S., and Dr. S., and Dr. S. When I developed chronic pain during my second semester of grad school, I didn't know what was wrong or how to fix it. I was scared. This list of medical professionals are the people who are responsible for taking my pain seriously, working with me to find effective treatments, and helping me put my life back together again. Without your help, your willingness to see my problem as real and myself as a rational human being deserving of empathy, and your hard-won expertise in your own unique fields, I would never have finished grad school. You are the reason the phrase at the top of this section reads, "Per aspera ad astra" and not just "aspera." From the bottom of my heart, thank you.

Finally, I must thank my officemate of the last four months, who has been an invaluable companion during the SARS-CoV-2 (coronavirus) pandemic of 2020. He generously acted as a sounding-board for my analysis in Chapter 4 of this thesis, and was a stalwart companion while I tried to write Chapter 1 without devolving into writing a review article. He has put up with my constant presence in his space while also, even, reminding me of mealtimes and bedtimes, sometimes very loudly. All this, despite keeping to his own rigorous schedule of sleeping 20 hours a day . . . because he is, of course, my cat Sibelius.

Table of contents

Chapter 1

Introduction

Massive stars drive some of the most significant radiative, kinematic, and chemical processes in galaxies. Though they are rare compared to low and intermediate mass stars, their extreme luminosities ionize their immediate neighborhoods (i.e. H II regions), they drive strong, hot stellar winds which push away nearby gas and create shocks and pressure differentials, and their spectacular deaths as supernovae seed in the interstellar medium with heavy elements and additional turbulence. The cumulative nature of these effects is such that understanding massive stars is important not only for understanding stellar populations on a local level, but also for understanding the structure and evolution of galaxies as a whole.

Unlike low-mass stars, for which the basic process of protostellar evolution is fairly well-understood, significant questions remain about the formation process of high-mass stars ($M_\star \geq 8M_\odot$, spectral type B3 and earlier; see Motte et al. 2018b; Tan et al. 2014). Understanding how massive stars form is necessary in order to explain their comparative rarity, why they are usually found in stellar systems which are high-order multiples, and to understand the timeline on which they begin to affect their surroundings. Because most stars form in groups (protoclusters, Lada & Lada 2003; Kennicutt & Evans 2012), a robust

understanding of massive star formation and the means and timeline on which massive stars begin to dominate their surroundings is also important for understanding how the stellar Initial Mass Function (IMF) gets its shape (Lada & Lada 2003; McKee & Ostriker 2007). The study of massive star formation seeks to answer these questions by investigating what, if anything, is unique to the formation of high-mass stars and their protocluster environments that effects these outcomes.

1.1 Structures of Interest

Before we explicate the current understanding of and open questions in massive star formation, it will be useful to define several terms, structures, and size scales relevant to this work. The smallest physical scale of interest to us is ~0.01-0.02 pc. This is the minimum separation one should expect between two forming stars (protostars) that are not gravitationally bound to each other (McKee & Ostriker 2007). Individual protostars exist within larger, dense structures called cores ($n_{H_2} \sim 10^4$ - 10^6 cm^{-3}), which are self-gravitating and are observed to exhibit a range of masses (order 0.1 to several tens of $M_\odot$, Sadavoy et al. 2010; Di Francesco et al. 2007). If a core is known to have a protostar or has observational signposts associated with protostars (such as bipolar outflows) it is called a protostellar core; if no such signposts exist but a core can be shown to be self-gravitating or even collapsing, it might be called a "pre-stellar" core, i.e., it has not formed a protostar yet but could in the (relatively) near future. Pre-stellar cores are typically cold (5~20 K), while protostellar cores can be cold (5~20 K), warm (20~100 K), or hot ($\gtrsim$100 K). Protostellar cores are usually presumed to be internally heated, so the temperature of an individual core is often assumed to be dependent on the state of evolution of the protostar the core hosts. Pre- or protostellar cores may also be externally heated by, e.g., cosmic rays, shock-heating, or ambient radiation (Shirley et al. 2005). Classically, a core is thought of as a ~0.1 pc struc-

ture that will collapse to form a single protostar or proto-binary system, though not all of the gas in the core will necessarily end up in the protostar due to feedback effects such as outflows (Lada & Lada 2003). Because the gas in these objects is also mixed with dust, the term "dust core" is also sometimes used.

Cores generally exist within "clumps": larger clouds of gas that are $\sim$1-10 pc in size and typically host multiple cores. On a global scale, clumps can be treated as relatively cold (10$\sim$30 K) and dense, although they are less dense than cores ($n_{H_2} \lesssim 10^4$ cm^{-3}) and it is not clear that all clumps are necessarily self-gravitating (Kennicutt & Evans 2012). Clumps themselves usually exist within even larger structures called Giant Molecular Clouds, or GMCs (10 to >100 pc in size), which are more diffuse ($n_{H_2} > 10^2$ cm^{-3}) and often contain filaments (long, thin, roughly cylindrical overdensities in the gas and dust) in addition to clumps (Kennicutt & Evans 2012; Motte et al. 2018b). A schematic representation of the classical understanding of clumps, cores, and protostars, including relevant size scales, is shown in Figure 1.1. Panel c of this figure also shows the different components which are typically present in a protostar (central star, accretion disk, envelope, and bipolar outflows). In this work we use the term "protostar" to refer to this entire ensemble of components, but sometimes the term "circumprotostellar environment" or "protostellar core" is also used.

Overall, star-forming regions contain many different physical structures (from hot central protostars to cold ambient gas, and protostellar disks to outflows and jets) which span many decades in size, density, and temperature. Some structures may emit predominantly one only one or a few wavelength regimes, while some may produce radiation at a broad range of wavelengths. This presents a challenge for observers wishing to fully constrain the star-formation activity in any one particular region. We will discuss these challenges, and the methods observers use to address them, in § 1.4.

A note on terminology: In this work, we use the term "massive protostar" to refer to a protostar that will likely form a massive star. Designating a source as a "massive protostar" does not necessarily mean that the *central star* in the protostellar system has accreted more than 8 $M_\odot$ as yet. Protostars are by definition still accreting matter, so the mass of the central star in a protostellar system is not a constant. Instead, identifying a source as a massive protostar means that the aggregate properties of the entire protostellar system are such that a star with $M_\star > 8M_\odot$ can reasonably be expected to form by the end of the evolutionary process. We discuss our criteria for determining what is or is not likely a "massive protostar" later in this Chapter.

1.2 Current Understanding of and Open Questions in Massive Star Formation

It is generally accepted that the majority of stars form in groups of a few tens to several hundred (Lada & Lada 2003). It is easy to see how this might be a natural consequence of the physical situation shown in Figure 1.1a: if a clump contains multiple cores, each of which will form one star or binary pair, then it naturally follows that multiple stars may be found forming at the same time in the same clump. While the resulting main-sequence stars may not be gravitationally bound to each other, these groups of star-forming cores are usually treated as a single star-forming region. These star-forming regions can vary widely in their star formation rates (Lada & Lada 2003), the number, number density, and masses of the stars they are forming (Sadavoy et al. 2010), and overall qualities such as clump density and size (Kennicutt & Evans 2012).

A massive protostar will produce significant amounts of radiative feedback as it reaches the main sequence and forms an H II region. Regardless of other feedback mechanisms

within the star-forming clump, H II regions are generally assumed to quench additional star formation in their immediate environs once they are sufficiently evolved. Massive stars are also likely to have significant gravitational effects on their nearest neighbors, although the exact degree of these effects are still being debated (see § 1.3 below). Regions forming massive stars, then, may exhibit properties very different from their lower-mass counterparts, especially as regards protostellar feedback and the destruction of the host clump (Zinnecker & Yorke 2007, and references therein).

A general schematic diagram of massive star formation is shown in Figure 1.2. In this diagram, multiple cold cores are found in the same region of a clump, and some of those cores may go on to form massive stars. As these massive protostars evolve towards the main sequence and begin to radiatively ionize their surroundings (thus forming very young, dense Hypercompact (HC) H II regions, then Ultracompact (UC) H II regions, and then "normal" H II regions in equilibrium with their surroundings), they drive ambient gas out of their local neighborhoods, and star formation halts within the clump. Note especially the size scales relevant for HC versus UC H II regions in Figure 1.2.

When investigating the formation of high-mass stars, one quality in particular quickly becomes apparent: massive stars are rarely found forming in isolation. Early studies of massive star formation focused on massive clumps and cores - usually those that are bright in the infrared, which was taken as an indication of internal heating by a massive protostar. These studies often treated the massive cores as hosting individual protostars, just as one would do for a low-mass protostellar system (e.g. Wood & Churchwell 1989; Kraemer et al. 1999; Plume et al. 1997). As UC H II regions (Wood & Churchwell 1989), a signpost of young OB stars, were often associated with massive sources which were bright in the infrared, the assumption was not unreasonable. However, follow-up observations of these regions have shown that what were initially thought to be single protostars of very high
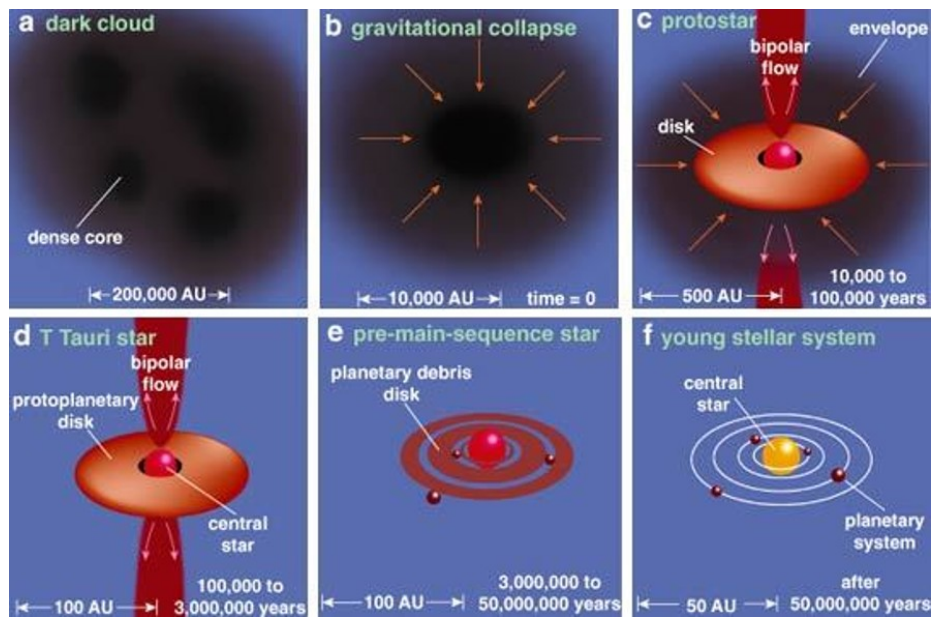
Fig. 1.1.— Schematic representation of the formation of a young stellar system (Greene 2001).
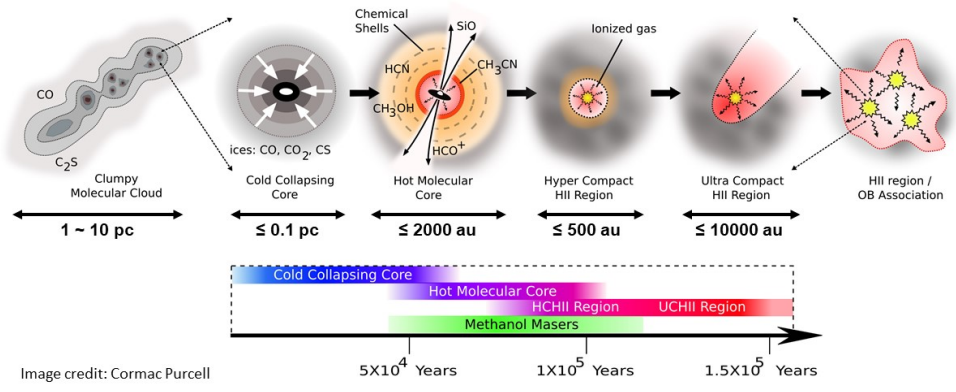
Fig. 1.2.— A general view of star formation in protocluster environments, in which some of the cores in a clump go on to form massive stars and H II regions. Original graphics from the personal website of Dr. Cormac Purcell, Macquarie University.

mass nearly always resolved into multiple sources when observed with higher spatial resolutions (Cyganowski et al. 2007; Brogan et al. 2009; Stephens et al. 2017; Beuther et al. 2018). Rather than *individual protostars*, these massive clumps and cores hosted *collections* of protostars of which at least one was massive. We now call these objects "massive proto*clusters*": clusters of protostars in which at least one protostar is massive. While low-mass stars can often be found forming in relative isolation within a clump, massive protostars are most often found surrounded by or in near proximity to multiple additional protostars of varying masses (Motte et al. 2018b).

Additionally, high-resolution observations of massive star-forming regions over the past decade have particularly challenged the framework of size scales and star-formation "components" we outlined in § 1.1. Beuther et al. (2018) routinely find multiple dust cores - each presumed to host a single star or binary system - within 20,000 au ($\sim$0.1 pc) of each other in their sample of 20 high-mass star-forming regions ($L > 10^4 L_\odot$). A selection of these sources is shown in Figure 1.3. The authors note that, while there is diversity of morphology within their sample, the smallest projected linear separations between cores is approximately equal to the angular resolution limit of their data ($0''.4$). From this, they conclude that additional fragmentation of the cores may occur at even smaller scales than they can observe. This finding of high fragmentation of cores at sub-0.1 pc scales is not unique to Beuther et al. (2018); it is also observed in massive star-forming regions such as NGC6334I (Brogan et al. 2016; Hunter et al. 2017), G358.93-0.03 (Brogan et al. 2019), G11.92–0.61 (Cyganowski et al. 2017), and others. The projected separation of dust cores observed in these regions is variable, but typically of order a few thousand au. This severely challenges the notion of individual, well-separated cores within a clump evolving in relative isolation over time, at least in massive star-forming regions.

These new observations raise several important questions:

- Why do we so frequently find closely-spaced cores in massive protoclusters? In particular, do massive protoclusters naturally form cores this close together, or are the cores formed further apart and become close to each other only as the protocluster evolves?

- Given the apparently close separation between protostars in protoclusters (for whatever reason), how do the most massive protostars affect their nearest neighbors? Do they drive (or suppress) star formation in their immediate environments even before they form H II regions?

- Given the assumption that the formation of an H II region halts local star formation, on what timeline and by what mechanism do massive protostars form H II regions? How do the formation timeline and mechanism affect the distribution of masses of stars formed in massive protoclusters, if at all?

Any theoretical framework of massive star formation must be able to explain these open questions.

1.3 Theoretical Frameworks

The theoretical and observational investigations of massive star formation over the last several decades have led researchers to believe that massive proto*cluster* formation is key to addressing a number of open questions in both the star formation and stellar populations communities. In particular, massive protocluster formation may explain why massive stars are found in high-order multiples at a much higher rate than stars of other masses (Chini et al. 2013), and how the overall stellar Initial Mass Function (IMF) - the number of stars formed at each mass - gets its shape. This last point is key not only for understanding

the history and evolution of our own Milky Way galaxy, but also for understanding the evolution of galaxies in general.

In the last two decades, two main theoretical paradigms have emerged to explain massive star formation in protocluster environments: Monolithic Collapse models and Hierarchical Collapse models. In Monolithic models, such as Turbulent Core Accretion (McKee & Tan 2002) or the numerical simulations described in Banerjee & Kroupa (2017), the initial condition for protostellar formation is a single core of order ∼0.1 pc. More massive stars are thus formed from more massive cores. These models are sometimes called "a scaled-up version of low-mass star formation" because the mass that forms the eventual stars still comes only from the ∼0.1 pc core. In Monolithic collapse models, a parent clump contains many such single cores with a mass distribution which mirrors the stellar IMF, offset by some efficiency factor ϵ. These models tend to produce protoclusters in which the protostars are more centrally-concentrated than are the stars in main-sequence (unembedded) star clusters. They make no prediction as to stellar birth order (i.e. low-mass stars vs. high-mass stars form first/last). They require the presence of stable, massive starless cores, possibly up to of order 10^2 Jeans masses (Tan et al. 2014). These stable, massive cores are sustained against gravitational collapse by higher-than-average levels of kinetic turbulence within the cores themselves. Because Monolithic models predict that the stellar IMF is inherited from the the distribution of masses of the cores within a clump (Core Mass Function; CMF), several teams are now seeking to identify and characterize massive, starless cores in pre-stellar clumps or young massive protoclusters (Tan et al. 2013), and in fact several candidates have been identified (Lin et al. 2019; Cyganowski et al. 2014). At present, however, the observational evidence regarding the CMF compared to the IMF is conflicting at best; some teams find evidence that the CMF is significantly flatter at high masses than the IMF (Motte et al. 2018a), while others find that the CMF and IMF shapes

at the high mass end are quite similar (Massi et al. 2019). The in-progress ALMA-IMF project (a Large Program; PI: F. Motte) seeks to sample the full range of core masses in 15 massive star-forming regions in order to compare the CMF and IMF, and examine the possibility of CMF evolution with time.

In contrast, Hierarchical collapse models suggest that evolution of individual protostars is not separable from the protocluster environment as a whole. The Competitive Accretion Model (Bonnell et al. 2001, 2004; Bonnell & Bate 2006) suggests that all protostars within a protocluster "compete" for the same reservoir of gas (i.e. gas in the parent clump); it is those stars at the bottom of the gravitational potential that will accrete the most material and thus become the most massive members of the protocluster. Competitive Accretion dictates that high- and low-mass stars should be found forming *simultaneously*, rather than, e.g., low-mass stars forming first. It also predicts that some low-mass stars should be found forming within the much-larger accretion reservoir of a central, high-mass star. The Global Hierarchical Collapse (GHC; Vázquez-Semadeni et al. 2017) model, in contrast, suggests that the star formation rate in a protocluster increases with time. Mass is funneled by filaments onto protostellar cores in gravitational potential minima; these cores will become the high-mass stars in the protocluster. As the filaments increase in density, lower-mass stars will begin to form within the filaments themselves, and thus the filaments begin to direct both gas *and stars* toward the higher-mass cores. As these higher-mass cores become massive protostars and begin to produce powerful radiative and outflow feedback, star formation within the cluster is quenched. GHC predicts some low- and high-mass stars forming simultaneously, but also a small ($\sim 1/3$ of the total) population of older low-mass stars within the cluster, formed during the earliest stages of star formation in the cluster. The GHC model therefore predicts a stellar birth order in which the high-mass stars form last. As a group, Hierarchical formation models tend to produce "subclusters" of a few

to a few tens of stars, which then eventually merge to form the final, complete cluster (Bonnell et al. 2003). Consequently, Hierarchical models predict protoclusters that are less centrally-concentrated than their main-sequence counterparts. In Hierarchical models, it is the protostars at the bottom of the gravitational potential that become the most massive cluster members. Because core mass is determined by location within the cloud and can vary with time, Hierarchical Collapse models do not require that the CMF mirror the IMF.

1.4   Observational Strategies for Constraining Massive Star Formation

Conducting observational tests of these theoretical paradigms is challenging for a number of reasons. First, massive stars are comparatively rare. This rarity means that most massive star-forming regions are located > 1 kpc away, and consequently, probing the *physical* scales of interest in any particular region requires much higher *angular* resolution than would be needed to observe nearby objects. Second, massive stars reach the main sequence more rapidly than their lower-mass counterparts. This means that the window of time for observing massive star formation is shorter than for low-mass stars. Third, because massive stars are typically still deeply embedded in their natal clouds of dust and gas when they reach the main sequence, the wavelength regimes in which they can be directly observed at sub-0.1 pc scales are limited. Fourth, and perhaps most obviously, massive star formation is a dynamic process which takes place on timescales much longer than a single human life; observing a protostar with $M_\star < 8M_\odot$ now does not guarantee that that protostar will not become a massive star in the future. Finally, as stated in § 1.1, star-forming regions contain many different physical structures which may emit at different preferred wavelengths, or may produce emission that spans broad, often overlapping wavelength ranges. This can

be especially true of objects which may contain multiple emission mechanisms, such as an ionized jet producing both thermal and synchrotron emission (e.g. Purser et al. 2016).

To probe the physical scales of interest ($\lesssim$5000 au, 0.02 pc), observational teams have increasingly turned to radio and submillimeter interferometry, using facilities like the Jansky Very Large Array (JVLA), Atacama Large Millimeter/submillimeter Array (ALMA), the Australia Telescope Compact Array (ATCA), and others. This provides exquisite angular resolution for these regions, but it does limit these sub-0.02 pc observations to those processes which emit in the radio through submillimeter regimes. In order to constrain the many different sources of emission in star-forming regions, observations must be made at multiple wavelengths. For instance, a protostar with an accretion disk, envelope, and ionized jet/outflow system may produce emission in the infrared (warm dust from the envelope, ionized atomic lines at the interface of the outflow and ambient medium, and perhaps stellar radiation escaping through the outflow cavity). However, these same components will likely also produce emission in the radio through submillimeter regimes: the warm dust in the envelope will emit at submillimeter, millimeter, and perhaps even centimeter wavelengths, the ionized jet will produce thermal free-free emission at centimeter wavelengths, and the shocks produced by the jet/outflow system may produce non-thermal (synchrotron) emission in addition to collisionally-excited masers. This strategy - of observing protoclusters with both high angular-resolution radio interferometers and at other (primarily infrared) wavelengths - is becoming more and more common in the star-formation community, although typically observations in the different wavelength regimes are carried out by different teams.

To overcome the temporal limitations of observing massive star formation (i.e. it is both rapid compared to low-mass star formation and takes place on long timescales relative to human lifetimes), observational teams have typically employed one of two strategies. Both

of these strategies have to do with characterizing the evolutionary states of massive star-forming regions, and each has its own particular strengths. The first approach is to observe a statistically-significant sample of massive star-forming regions, in which the regions are selected to span a broad range in those physical properties assumed to be indicative of evolutionary state (primarily: outflow activity, core temperature, bolometric luminosity, infrared flux density, and the presence or absence of molecular, atomic, or ionized emission lines). An reasonable evolutionary sequence for massive protoclusters can then be constructed based on that sample, usually assuming steady increases in infrared and radio continuum emission, temperature, and bolometric luminosity (L_{bol}) as the protocluster evolves with time. This observation-based sequence can then be compared with theoretical predictions.

Multiple teams have constructed samples meant to accomplish this goal. Tigé et al. (2017) observe the star-forming region NGC 6334 in the far-infrared and characterize the 32 observed massive cores as starless, IR-quiet protostellar, and IR-bright protostellar, proposing an evolutionary sequence from the first to the last (although they do note that it is not certain all starless dense cores in their sample will eventually form stars). Rosero et al. (2016) and Rosero et al. (2019b) conducted a 6 and 1.3 cm survey of 58 massive star-forming regions in the Milky Way, and constructed their sample specifically to include statistically-significant numbers of what they identify as: cold massive cores without infrared counterparts, cold massive cores with infrared counterparts, and hot massive cores. They find different rates of radio-frequency emission in these different subsamples, and suggest that these selection criteria describe an evolutionary sequence of massive star-forming regions from pre-stellar/largely quiescent to HC H II regions. The in-progress ALMAGAL project (an ALMA Large Program; PI: S. Molinari) seeks to characterize massive star-forming regions in the Milky Way at all stages of evolution at 1 mm in order to

evaluate the characteristics of protocluster formation.

The second strategy is to observe a sample of sources in what is believed to be a very specific evolutionary state, and describe how the properties of the sources in that state fit - or don't fit - within a given evolutionary framework for protocluster evolution. Svoboda et al. (2019), for instance, focus on massive clumps which should be capable of forming massive protoclusters but which only have observational signposts of the very earliest stages of star formation (e.g. self-gravitation and evidence of infall). In their sample, they find widespread evidence of weak outflow activity from low-luminosity sources, which challenges the notion of a truly "pre-stellar" stage of clump evolution.

One particularly beneficial evolutionary state to examine is one in which the protocluster is evolved enough that the presence of massive protostars can be confirmed, but is still young enough that those massive protostars have not had time to dissipate the surrounding natal environment. This allows the observer to examine the protostellar population for mass segregation, diversity of protostellar evolutionary states, and overall structure in the clump gas reservoir without having to make assumptions as to the likelihood of the clump forming a massive protostar in the future. This last strategy is what we employ in this work.

1.5   Questions Addressed in This Thesis

For this work, we selected a sample of 20 of the nearest and youngest-appearing Extended Green Objects (EGOs) from the published catalogs of Cyganowski et al. (2008) and Chen et al. (2013) for targeted multi-wavelength follow-up observations. We observed these sources in the infrared through radio regimes (3.6 μm through 5 cm) using multiple facilities and archival data in order to constrain the full Spectral Energy Distributions (SEDs) of each source with high angular resolution at each wavelength. Our goal was to answer, for this sample, the following questions:

1. What are the luminosity-to-mass ratios of these clumps, and what relationship, if any, does L/M have to clump mass (M_{clump}) and evolutionary state?

2. What is the nature and effect of ionized emission when it first appears in these sources?

3. What are the properties of the massive protostars in particular? What constraints can we place on the emergence of ionizing radiation from these massive protostars?

4. What are the demographics of the protostars in these regions? In particular, what are the multiplicities of massive sources; do we see any evidence of clustering/subclustering within the overall protostellar population; and is there any indication of a preference for stellar birth order within the clumps?

The first question helps us place EGOs in context in the broader evolutionary process of massive protoclusters; this is critical for understanding how to compare their properties to those of other samples or numerical simulations. The second and third questions address the issue of protostellar feedback - specifically feedback from massive protostars. There are many competing theories at present regarding how massive protostars form H II regions; some suggest that massive protostars ionize their accreting material first, thus creating ionized accreting flows (Keto 2007), some suggest that a bipolar cavity (such as that created by a jet/outflow) must exist prior to the onset of ionizing radiation in order for the H II region to grow and avoid quenching by the presumably-high accretion rate (Tanaka et al. 2016), and still others suggest that H II regions can produce anywhere from spherical to bipolar to variable morphologies depending on their specific formation mechanism and the instantaneous accretion rate (Keto 2003; Klessen et al. 2011; Rosen et al. 2016). Some of these theories of H II region formation are closely linked to specific models of protocluster formation (e.g. Tanaka et al. 2016), so constraining the onset of strong radiative feedback in protoclusters

can address questions about both individual massive protostars and protocluster evolution as a whole. The fourth question above addresses many of the key discriminating features of the various massive protocluster formation theories discussed in § 1.3 - namely, the differing predictions for the masses, evolutionary states, and locations within the clump of the individual protostars.

In Chapter 2, we discuss our mid-infrared observations of 12 of these 20 EGOs using the Stratospheric Observatory for Infrared Astronomy (SOFIA) in combination with archival data in order to construct well-constrained SEDs from 3.6 to 870 μm, and our subsequent results for the L/M values for these sources. Chapter 2 has been previously published as Towner et al. (2019). In Chapter 3, we discuss $\sim$3$''$-resolution observations of 1.3 cm continuum and 25 GHz CH$_3$OH emission at $\sim$mJy sensitivities in all 20 regions. We find that the CH$_3$OH emission - both thermal and maser - is ubiquitous in these regions, and that the continuum emission is, if present, both weak and compact. One of the primary conclusions of this chapter is that follow-up centimeter observations with both higher angular resolution and greater sensitivity were needed. Chapter 3 has been previously published as Towner et al. (2017). In Chapter 4, we present these high-resolution, high-sensitivity follow-up observations at 5 and 1.3 cm for nine of the 20 EGOs. We describe the nature of the continuum emission given the morphologies and derived spectral indices of the continuum sources, and discuss these results in context with the H$_2$O, CH$_3$OH, and NH$_3$ maser emission we also observe in these regions. In general, we find that the individual centimeter continuum detections in this sample are consistent not with one single emission mechanism, but with a range of emission mechanisms. Chapter 4 will shortly be submitted to the Astrophysical Journal for publication as Towner et al. (2020). In Chapter 5, we present our overall conclusions from these observations and discuss future directions for the work. Below, we briefly discuss the observational history of EGOs to provide greater context for our use of

them as a target sample.

1.6   Observational History of EGOs

EGOs were initially discovered and described by Cyganowski et al. (2008) using infrared data from the Galactic Legacy Infrared Mid-Plane Survey Extraordinaire (GLIMPSE) project (Benjamin et al. 2003; Churchwell et al. 2009). GLIMPSE was carried out using the *Spitzer* IRAC instrument at 3.6, 4.5, 5.8, and 8.0 μm. In the GLIMPSE data, EGOs are identifiable by the fact that their emission is extended - rather than point-like - in the IRAC 4.5 μm band. This extended morphology is only present in the 4.5 μm data, not the other IRAC bands. The extended emission typically spans a diameter of order 0.1 pc, and is generally attributed to line emission from shocked H_2 in the 4.5 μm band (Marston et al. 2004). EGOs are called "green" because the IRAC 4.5 μm band is commonly shown as green in 3-color images made from IRAC data. The sample of EGOs originally identified by Cyganowski et al. (2008) is >300 sources and covers $10° < l < 65°$ and $295° < l < 350°$, $b = \pm 1°$. Additional EGO samples have been reported by Chen et al. (2011, 2012). EGOs have typical masses of 10^2 - 10^3 $M_\odot$, and typical luminosities of 10^3 - 10^5 $L_\odot$. They are therefore consistent with other known massive star-forming regions, though they are on the lower end in both mass and luminosity.

Targeted follow-up observations of EGO subsamples revealed a preferential association with Infrared Dark Clouds (IRDCs) as well as strong associations with 44 and 95 GHz Class I CH_3OH masers, 22 GHz H_2O masers, and 6.7 GHz Class II CH_3OH masers (Cyganowski et al. 2009; Cyganowski et al. 2014). Class I masers are collisionally pumped, and thus often associated with shock-inducing processes such as protostellar outflows, jets, and disks. Class II masers are radiatively pumped and thus trace radiative conditions; 6.7 GHz CH_3OH masers in particular are exclusively associated with massive protostars, due to the physical

conditions and radiation levels required to induce population inversion (Minier et al. 2003).

The evidence that the extended 4.5 μm emission is due to protostellar outflows is strong (shocked H_2, Class I masers), and given the causal link between accretion and ejection (Frank et al. 2014), we assume that these objects are thus actively-accreting protostars. The presence of 6.7 GHz CH_3OH masers suggests that at least one protostar in each region must be also massive. However, most EGOs are not associated with known H II or UCH II regions, which are a hallmark of massive stars. In fact, deep (at the time) 3.6 cm continuum observations conducted with the VLA revealed weak (<1 mJy beam^{-1}) or no continuum emission in a sample of 14 EGOs (Cyganowski et al. 2011b). Therefore, although EGOs appear to host massive protostars, these massive protostars have clearly not yet reached a state in which they can produce the significant radiative and stellar-wind feedback that will eventually destroy the host clump. In other words, EGOs appear to be in a particular stage of evolution which is very useful for discriminating between current theories of massive star formation.
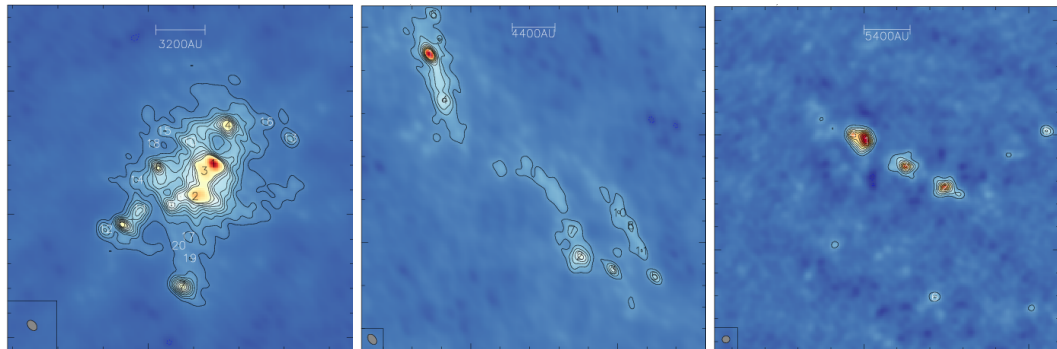
Fig. 1.3.— 1.37 mm continuum images of (left to right) IRAS21078, S87IRS1, and NGC7538S from Beuther et al. (2018). Linear scales are shown at the top of each panel. Each source shows clear multiplicity at scales <20000 au, i.e., <0.1 pc. Panels shown are taken from Figure 5 of Beuther et al. (2018).

Chapter 2

SOFIA *FORCAST* Photometry of 12 Extended Green Objects in the Milky Way

2.1 Chapter Summary

Massive young stellar objects are known to undergo an evolutionary phase in which high mass accretion rates drive strong outflows. A class of objects believed to trace this phase accurately is the GLIMPSE Extended Green Object (EGO) sample, so named for the presence of extended 4.5 μm emission on sizescales of $\sim$0.1 pc in *Spitzer* images. We have been conducting a multi-wavelength examination of a sample of 12 EGOs with distances of 1 to 5 kpc. In this paper, we present mid-infrared images and photometry of these EGOs obtained with the SOFIA telescope, and subsequently construct SEDs for these sources from the near-IR to sub-millimeter regimes using additional archival data. We compare the results from greybody models and several publicly-available software packages which produce model SEDs in the context of a single massive protostar. The models yield typical

$R_\star \sim 10\ R_\odot$, $T_\star \sim 10^3$ to 10^4 K, and $L_\star \sim 1 - 40 \times 10^3\ L_\odot$; the median L/M for our sample is 24.7 $L_\odot/M_\odot$. Model results rarely converge for $R_\star$ and $T_\star$, but do for $L_\star$, which we take to be an indication of the multiplicity and inherently clustered nature of these sources even though, typically, only a single source dominates in the mid-infrared. The median L/M value for the sample suggests that these objects may be in a transitional stage between the commonly described "IR-quiet" and "IR-bright" stages of MYSO evolution. The median T_{dust} for the sample is less conclusive, but suggests that these objects are either in this transitional stage or occupy the cooler (and presumably younger) part of the IR-bright stage.

2.2   Introduction

Massive young stellar objects (MYSOs) are challenging to observe due to their comparative rarity and short-lived natal phase, large distances from Earth, and highly-obscured formation environments. Early observations of suspected MYSOs were performed mostly with large beams, and probed size scales ranging from cores to clumps and clouds ($\sim$0.1 pc, $\sim$1 pc, and $\sim$10 pc, respectively; see Kennicutt & Evans 2012). Detailed descriptions of early surveys for MYSOs and their results can be found in, e.g., Molinari et al. (1996), Sridharan et al. (2002), and Fontani et al. (2005). Follow-up observations with improved sensitivity and spatial resolution, such as interferometric radio and millimeter observations, revealed that many of the objects originally identified as "MYSOs" were actually sites in which multiple protostars were forming simultaneously (e.g. Hunter et al. 2006; Cyganowski et al. 2007; Vig et al. 2007; Zhang et al. 2007, to name just a few). This predilection for forming in clustered environments means that the study of high-mass protostars is necessarily the study of proto*clusters*: clusters of protostars with a range of masses and in a variety of evolutionary stages. Current theories of high mass star formation differ in their predictions of the aggregate properties of these protoclusters, such as mass

segregation (if any), sub-clustering of the protostars, and stellar birth order (e.g. Vázquez-Semadeni et al. 2017; Banerjee & Kroupa 2017; Bonnell & Bate 2006; McKee & Tan 2003). It is therefore necessary to consider each high-mass protostar in combination with its environment.

Extended Green Objects (EGOs) were first identified by Cyganowski et al. (2008) using data from the Galactic Legacy Infrared Midplane Survey Extraordinaire (GLIMPSE, Benjamin et al. 2003; Churchwell et al. 2009) project. EGOs are named for their extended emission in the 4.5 μm *Spitzer* IRAC band (commonly coded as "green" in three-color RGB images), which is due to shocked H_2 from powerful protostellar outflows (e.g., Marston et al. 2004). Follow-up observations of $\sim$20 EGOs with the Karl G. Jansky Very Large Array (VLA) by Cyganowski et al. (2009) established both the presence of massive protostars (traced by 6.7 GHz Class II CH_3OH masers) and shocked molecular gas indicative of outflows (traced by 44 GHz Class I CH_3OH masers). The causal link between accretion and ejection (Frank et al. 2014) thus implies that these objects contain protostars undergoing active accretion, and the maser data indicate that these protostars are massive. The youth of the massive protostars within these EGOs was confirmed by deep (at that time) VLA continuum observations (Cyganowski et al. 2011b), which yielded only a few 3.6 cm detections, and by later VLA 1.3 cm continuum observations (Towner et al. 2017), which revealed primarily weak ($<$1 mJy beam^{-1}), compact emission. The low detection rates and integrated flux densities of the centimeter continuum emission in these sources demonstrate that any free-free emission is weak, consistent with a stage prior to the development of ultracompact HII regions.

Given that high-mass stars form in clusters, it is likely that EGOs are signposts for protoclusters rather than isolated high-mass protostars, though the level of multiplicity of massive sources ($>8M_\odot$) and overall cluster demographics remain open questions. Mil-

limeter dust continuum observations of EGOs with $\sim 3''$ resolution, suggest that the number of massive protostars per EGO is typically one to a few (e.g. Cyganowski et al. 2012, 2011a; Brogan et al. 2011). However, the precise physical properties of protoclusters traced by EGO emission - such as total mass, luminosity, and massive protostellar multiplicity - remain largely unexplored in EGOs as a class.

The infrared emission from EGOs, and indeed MYSOs in general, is often challenging to characterize due to the presence of high extinction from their surrounding natal clumps (as they are still deeply embedded), and confusion from more evolved sources nearby. The latter issue has been particularly affected by the relatively poor angular resolution ($> 1'$) that has heretofore been available at mid- and far-infrared wavelengths, where the high extinction can be overcome. Yet these wavelengths contain crucial information as hot dust, shocked gas, and polycyclic aromatic hydrocarbons (PAHs) all emit in this regime. Scattered light originating from the protostar itself may also sometimes escape through outflow cavities and would likewise be visible in the infrared. Thus mid-infrared wavelengths are a crucial component of the Spectral Energy Distribution (SED) which is a useful tool for constraining important source properties such as mass, bolometric luminosity, and temperature.

These properties are of particular interest for MYSOs, as recent analysis of the Herschel InfraRed Galactic Plane Survey (Elia et al. 2017) and a full census of the properties of ATLASGAL Compact Source Catalog (CSC) objects Urquhart et al. (2018) shows how the luminosity to mass ratio L/M of protostellar clumps can be used to both qualitatively and quantitatively discriminate between the different evolutionary stages of pre- and protostellar objects. In theoretical terms, L/M is tied to evolutionary state primarily due to abrupt changes in luminosity during different stages of MYSO/clump evolution (see, e.g., the stages described in Hosokawa & Omukai 2009; Molinari et al. 2008).

In this paper, we present new data that directly address the questions of the multiplicity and physical properties (temperature, mass, and luminosity) of the massive protoclusters traced by EGOs. We have utilized the unique capabilities of the Stratospheric Observatory for Infrared Astronomy (SOFIA, Temi et al. 2014) to image a well-studied sample of 12 EGOs at two mid-IR wavelengths: 19.7 and 37.1 μm with the necessary sensitivity ($\sim$0.05 to $\sim$0.25 Jy beam^{-1}) and angular resolution ($\sim 3''$) to detect and resolve the mid-infrared emission from the massive protocluster members. By combining these results with ancillary multi-wavelength archival data, we create well-constrained SEDs from the near-infrared through submillimeter regimes. We then use three SED modelling packages published by Robitaille et al. (2006), Robitaille (2017), and Zhang & Tan (2018), to constrain physical parameters (see, e.g., Gaczkowski et al. 2013; De Buizer et al. 2017). In § 2.3, we describe our targeted SOFIA observations and the observational details of the archival data at each wavelength. In § 2.4, we describe our aperture-photometry procedures for each data set and discuss our detection rates and trends. We also present sets of multi-scale, multiwavelength images for each object in order to better demonstrate their small- and large-scale properties and overall environments. In § 2.5, we compare the physical parameters obtained from the various SED modeling methods, including L/M, which help to place EGOs into a broader evolutionary context. In § 2.6 we discuss the implications of our results, and outline future investigations.

2.3   The Sample & Observations

In this paper, we conduct a multiwavelength aperture-photometry study of 12 EGOs using the SOFIA Faint Object infraRed CAmera for the SOFIA Telescope (FORCAST Herter et al. 2012). We use new SOFIA FORCAST 19 μm and 37 μm observations in conjunction with publicly-available archival datasets from *Spitzer*, *Herschel*, and the Atacama

Pathfinder EXperiment[1] (APEX) telescope, to model the SED of the dominant protostar in each of our target EGOs. Details of source properties for our sample are listed in Table 2.1.

2.3.1 SOFIA FORCAST Observations: 19.7 & 37.1 μm

We used SOFIA FORCAST to observe our 12 targets simultaneously at 19.7 μm and 37.1 μm. Observations were performed in the asymmetric chop-and-nod imaging observing mode C2NC2. The measured[2] FWHM are 2$''$5 at 19.7 μm and 3$''$4 at 37.1 μm. At the nearest (1.13 kpc) and farthest (4.8 kpc) source distances, these FWHM correspond to physical size scales of 2,830 to 12,000 au at 19.7 μm and 3,840 to 16,300 au at 37.1 μm. The instantaneous field of view (FOV) of FORCAST is 3$'$4 $\times$ 3$'$2, with pixel size $\theta = 0''768$ after distortion correction. This FOV corresponds to 1.1 $\times$ 1.1 pc at a distance of 1.13 kpc, and 4.8 $\times$ 4.5 pc at a distance of 4.8 kpc. Table 2.2 summarizes observation information for each EGO. The project's Plan ID is 04_0159.

Data calibration and reduction are performed by the SOFIA team using the SOFIA data-reduction pipeline[3]. After receipt of the Level 3 data products (artifact-corrected, flux-calibrated images), we converted our images from Jy pixel^{-1} to Jy beam^{-1} in order to more easily perform photometric measurements in CASA (McMullin et al. 2007). Conversion was accomplished by using the CASA task `immath` to multiply each image by the beam-to-pixel conversion factor $X_\lambda = (beam\ area)/(pixel\ area)$. This factor depends on beam size and pixel size, and therefore is different for each wavelength. The beam-to-pixel conversion

---

[1]This publication is based on data acquired with the Atacama Pathfinder Experiment (APEX). APEX is a collaboration between the Max-Planck-Institut fur Radioastronomie, the European Southern Observatory, and the Onsala Space Observatory.

[2]These FWHM are the average values in dual-channel mode for each wavelength as measured by the SOFIA team since Cycle 3. More information can be found in the Cycle 5 Observer's Handbook on the SOFIA website at https://www.sofia.usra.edu/science/proposing-and-observing/sofia-observers-handbook-cycle-5

[3]The FORCAST Data Handbook can be found on the SOFIA website at https://www.sofia.usra.edu/science/proposing-and-observing/data-products

Table 2.1.   EGO Source Properties

Source	V_{LSR}^a (km s^{-1})	Distance^b (kpc)	EGO^c Cat	IRDC^d	H_2O^e Maser	CH$_3$OH Masers (GHz)^f 6.7^g	44^h	95^i
G10.29–0.13	14	1.9	2	Y	Y	Y	Y	Y
G10.34–0.14	12	1.6	2	Y	Y	Y	Y	Y
G11.92–0.61	36	$3.38^{+0.33}_{-0.27}$ (3.5)	1	Y	Y	Y	Y	Y
G12.91–0.03	57	4.5	1	Y	Y	Y	?	Y
G14.33–0.64	23	$1.13^{+0.14}_{-0.11}$ (2.3)	1	Y	Y	?	Y	Y
G14.63–0.58	19	$1.83^{+0.08}_{-0.07}$ (1.9)	1	Y	Y	Y	?	Y
G16.59–0.05	60	$3.58^{+0.32}_{-0.27}$ (4.2)	2	N	Y	Y	?	Y
G18.89–0.47	66	4.2	1	Y	Y	Y	Y	Y
G19.36–0.03	27	2.2	2	Y	N	Y	Y	Y
G22.04+0.22	51	3.4	1	Y	Y	Y	Y	Y
G28.83–0.25	87	4.8	1	Y	Y	Y	Y	?
G35.03+0.35	53	$2.32^{+0.24}_{-0.20}$ (3.2)	1	Y	Y	Y	Y	Y

^{a}LSRK velocities are the single dish NH$_3$ (1,1) values from Cyganowski et al. (2013).

^{b}Distances without errors are estimated from the LSRK velocity and the Galactic rotation curve parameters from Reid et al. (2014). Parallax distances (with their uncertainties) are given where available from Reid et al. (2014) and references therein, with the kinematic distance in parentheses for comparison. All kinematic distances are the near distance. The uncertainty on each kinematic distance is assumed to be 15%, based on the median percent difference between the parallax-derived and kinematic distances from the five sources which have both.

^{c}This is the Table number of the EGO in Cyganowski et al. (2008). In that paper, Tables 1 & 2 list "likely" EGOs for which 5-band (3.6 to 24 μm) or only 4.5 μm *Spitzer* photometry can be measured, respectively.

^{d}Coincidence of EGO with IRDC as indicated by Cyganowski et al. (2008).

^{e}Water maser data from the Cyganowski et al. (2013) Nobeyama 45-m survey of EGOs.

^{f}Sources for which we could find no information in the literature are indicated by "?".

^{g}The 6.7 GHz maser detection information comes from Cyganowski et al. (2009) using the VLA, except for G12.91–0.03, G14.63–0.58, and G16.59–0.05, which come from Green et al. (2010, and references therein) observations using the Australia Telescope Compact Array (ATCA).

^{h}Information for 44 GHz masers come from the VLA and were taken from Cyganowski et al. (2009), except for G14.33–0.64, which comes from Slysh et al. (1999).

^{i}Most information for 95 GHz masers was taken from Chen et al. (2011) using the Mopra 22 m telescope. The exceptions are G14.33–0.64 from Val'tts et al. (2000) using Mopra, G16.59–0.05 from Chen et al. (2012) using the Purple Mountain Observatory 13.7 m telescope, and G35.03+0.35 from Kang et al. (2015) using the Korean VLBA Network.

Table 2.2.   SOFIA FORCAST Observing Parameters

| Source | Pointing Center (J2000) | | Obs. Date[a] | TOS[b] | σ (MAD)[c] | |
	RA	Dec		(s)	37 μm	19 μm
G10.29−0.13	18:08:49.2	-20:05:59.3	2016 July 13	502	0.26	0.08
G10.34−0.14	18:08:59.9	-20:03:37.3	2016 Sept 27	626	0.30	0.07
G11.92−0.61	18:13:58.0	-18:54:19.3	2016 July 12	604	0.22	0.07
G12.91−0.03	18:13:48.1	-17:45:41.3	2016 July 19	1000	0.18	0.04
G14.33−0.64	18:18:54.3	-16:47:48.3	2016 July 12	593	0.24	0.07
G14.63−0.58	18:19:15.3	-16:29:57.3	2016 July 13	641	0.22	0.07
G16.59−0.05	18:21:09.0	-14:31:50.3	2016 July 20	810	0.19	0.04
G18.89−0.47	18:27:07.8	-12:41:38.3	2016 Sept 27	626	0.25	0.06
G19.36−0.03	18:26:25.7	-12:03:56.3	2016 Sept 20	285	0.46	0.09
G22.04+0.22	18:30:34.6	-09:34:49.3	2016 Sept 20	642	0.21	0.05
G28.83−0.25	18:44:51.2	-03:45:50.3	2016 Sept 27	470	0.26	0.07
G35.03+0.35	18:54:00.4	+02:01:15.7	2016 Sept 22	500	0.29	0.08

[a]All July observations were performed on flights from Christchurch, New Zealand; all September observations were performed on flights from Palmdale, CA, USA.

[b]This column lists the total time on source (TOS) for each target. The original proposal called for 600 s of integration on each source. For four sources, 600 s could not be achieved due to either high clouds (G19.36) or telescope issues (G10.29, G28.83, G35.03). G12.91 was a shared observation with another group whose observations required additional integration time.

[c]The background noise of the SOFIA images is non-Gaussian in the majority of sources. This column gives the scaled $MAD = 1.482 \times MAD$ values for all sources, where MAD is the median absolute deviation from the median background pixel value; MAD must be multiplied by 1.482 to become rms-like. Aperture photometry was performed using cutoffs based on MAD for all sources. MAD values listed here are in Jy beam^{-1}.

factors are $X_{19.7\mu m}$ = 12.0067 pixels/beam and $X_{37.1\mu m}$ = 22.2076 pixels/beam.

2.3.2 Archival Data

Spitzer IRAC (GLIMPSE) Observations: 3.6, 5.8, & 8.0 μm

All of our EGO targets were originally selected due to their extended emission at 4.5 μm as seen in *Spitzer* GLIMPSE images. In order to constrain the SEDs of the driving sources themselves, we used the archival *Spitzer* observations at 3.6 μm, 5.8 μm, and 8.0 μm (bands I1, I3, and I4, respectively) from the GLIMPSE project (Benjamin et al. 2003; Churchwell et al. 2009). The point response function (PRF) of the IRAC instrument varies by band and position on the detector. The mean FWHM in bands I1, I3, and I4 are 1.″66, 1.″72, and 1.″88, respectively, as detailed in Fazio et al. (2004). All archival GLIMPSE data were downloaded from the NASA/IPAC Infrared Science Archive (IRSA) Gator Catalog List. The images returned by the archive are all in units of MJy sr^{-1}.

Spitzer MIPS (MIPSGAL) Observations: 24 μm

We utilized archival 24 μm data from the MIPSGAL survey to provide additional mid-IR constraints on our SEDs for 9 of our 12 targets. For the remaining 3 targets (G14.33, G16.59, G35.03), MIPSGAL 24 μm data could not be used for the second task due to saturated pixels in the regions of interest. MIPSGAL images have a native brightness unit of MJy sr^{-1}, and were converted to Jy beam^{-1} by first multiplying each image by 1×10^6 (to convert from MJy to Jy) and then multiplying by the solid angle subtended by the 6.″0 $\times$ 6.″0 MIPS beam at 24 μm. Technical details of the MIPS instrument can be found in Rieke et al. (2004). For details of the MIPSGAL observing program, see Carey et al. (2009) and Gutermuth & Heyer (2015). All MIPSGAL data were downloaded from the IRSA Gator Catalog List.

Herschel PACS (Hi-GAL) Observations: 70 & 160 μm

We used archival 70 μm and 160 μm data from the Herschel Infrared Galactic Plane Survey (Hi-GAL, Molinari et al. 2016), observed with the *Herschel* Photoconductor Array Camera and Spectrometer (PACS; Poglitsch et al. 2010) instrument, to probe the far-IR portion of the spectrum. These data were originally observed as part of the Herschel Hi-GAL project (Molinari et al. 2010, 2016) between 2010 October 25 and 2011 November 05. The observations were performed in parallel mode with a scan speed of 60$''$/s. Beam sizes, which are dependent on observing mode, were $\theta_{70\mu m} = 5.8'' \times 12.1''$ and $\theta_{160\mu m} = 11.4'' \times 13.4''$ as reported in Molinari et al. (2016). The native brightness unit of the Hi-GAL data is MJy sr^{-1}. Therefore, these images were converted to Jy beam^{-1} using the same method as in §2.3.2.

We chose to use the Hi-GAL data over the archival PACS data available on the European Space Agency (ESA) Heritage Archive due to the additional astrometric and absolute flux calibration performed by the Hi-GAL team, as detailed in Molinari et al. (2016). All Hi-GAL data were obtained from the Hi-GAL Catalog and Image Server on the Via Lactea web portal[4].

APEX LABOCA (ATLASGAL) Observations: 870 μm

We used archival 870 μm observations from the APEX Telescope Large Area Survey of the Galaxy (ATLASGAL, Schuller et al. 2009) to populate the submillimeter portion of the SED. The data were retrieved from the ATLASGAL Database Server[5]. The ATLASGAL beam size is 19$\rlap{.}''$2 $\times$ 19$\rlap{.}''$2; additional observational details can be found in Schuller et al. (2009). These images were already in units of Jy beam^{-1}, and thus required no unit conversion.

---

[4]http://vialactea.iaps.inaf.it/vialactea/eng/index.php
[5]http://atlasgal.mpifr-bonn.mpg.de/cgi-bin/ATLASGAL_DATABASE.cgi

2.4   Results

Figures 2.1 through 2.4 show pairs of three-color (RGB) images for each source. The left-hand panels show a 5$\farcm$3 field of view with 160, 70, and 24 μm data mapped to R, G, and B, respectively, and with 870 μm contours overlaid. These panels show the large-scale structure of the cloud and overall environment in which each EGO is located. The right-hand panels all have a 1$\farcm$0 FOV with the *Spitzer* IRAC 8.0, 4.5, and 3.6 μm data mapped to R, G, and B, respectively; the extended green emission in these images shows the extent of each EGO. SOFIA FORCAST 19.7 and 37.1 μm contours and ATLASGAL 870 μm contours are overlaid, and 6.7 GHz CH$_3$OH masers (Cyganowski et al. 2009) are marked with diamonds. These panels show the small-scale structure and detailed NIR and MIR emission of each EGO, how this emission relates to the larger-scale 870 μm emission, and the locations of any associated markers of MYSOs, such as 6.7 GHz CH$_3$OH masers.

Below we discuss in detail the photometric methodology used for each band for the SED analysis. Because the angular resolution and sensitivity - and hence level of confusion - vary significantly among the different observations, we have elected to use a photometry method best suited for each particular wavelength in order to minimize (as much as feasible) contamination from unrelated sources. In the following sections we describe in some detail how the photometry was done for each wavelength.

2.4.1   SOFIA FORCAST Photometry

Table 2.3 shows the photometry for the 19.7 and 37.1 μm SOFIA images. In this section, we describe the SOFIA astrometry, source selection, and photometry in more detail.

Astrometry   The SOFIA images required additional astrometric corrections. While the relative astrometry between the 19.7 and 37.1 μm data was accurate to less than one pixel,

the absolute astrometry of the SOFIA data varied considerably. Relative to the *Spitzer* MIPS 24 μm data, the positions of the SOFIA images varied by up to $\sim 3''$. In order to properly register the SOFIA images, we selected field point sources that were present in both the 24 μm images and either the 37.1 and 19.7 μm images, fit a 2-dimensional gaussian to that point source in both the 24 μm and SOFIA frame and applied the calculated position difference to both SOFIA images. In most cases, we were able to find a position match with the 24 μm data in only one of the two SOFIA frames, and relied on the sub-pixel relative astrometry between the two SOFIA images in order to correct the non-matched frame. Post-astrometric correction, we consider the absolute astrometric accuracy of the SOFIA images to be dominated by the absolute position uncertainty of the MIPS 24 μm images: $\sim 1''\!.4$.

Mid-IR Source Selection and Nomenclature We limit our analysis to those mid-IR sources we consider to be plausibly associated with the protocluster in which the EGO resides (with some exceptions described below). For short, we call these sources "EGO-associated." In this context, "EGO-associated" means one of two things: a) the mid-IR source is coincident with the extended 4.5 μm emission of the EGO and is therefore likely tracing some aspect of the EGO driving source in the mid-IR, or b) the mid-IR source lies outside the 5σ level of the 4.5 μm emission but is still near to the EGO, and it is unclear whether the source is related or is a field source. In order to create a self-consistent system for selecting sources in the latter category, we establish two criteria: i) the source must lie above the 25% peak intensity level of the ATLASGAL emission and ii) it must be detected at both 19.7 and 37.1 μm. If a mid-IR detection is not within the bounds of the 4.5 μm emission and does not meet both criteria i) and ii), then it is considered to be a field source.

One source, G14.33−0.64_b meets neither criteria and is likely a field source. It is coincident with the known H II region IRAS 18159−1648. However, it was necessary to

explicitly fit this source in order to get accurate flux density results for the EGO-associated sources.

For a given EGO field, source "a" is always the brightest EGO-associated source at 37 μm, source "b" is the second-brightest at 37 μm (of all analyzed sources for that FOV), and so on in order of decreasing brightness. The 37 μm source name designations are used for all the wavelengths analyzed in this paper.

Photometry   After source selection, we fit each source with 2-dimensional gaussian functions using the CASA task `imfit` in order to determine the total flux density, peak intensity, and major and minor axes. We then applied a multiplicative correction factor (an "aperture correction") to each fitted flux in order to account for the deviation of the SOFIA PSF from a true gaussian. Our detailed procedure was as described below.

We first selected emission-free regions in each image in order to determine the background noise levels. These emission-free regions are identical for all three mid-IR data sets (SOFIA 37.1 μm and 19.7 μm, and MIPS 24 μm) for a given source. However, the SOFIA images in particular have background levels that typically do not show noise variations about zero. Therefore, we chose to use the scaled MAD as an estimate of the noise (1.482$\times$MAD, where MAD is the median absolute deviation from the median), rather than the rms or standard deviation. With the exception of the ATLASGAL data, all data sets analyzed in this work have noise variations that are not centered about zero. Therefore, we have used the scaled MAD for all data sets for the sake of consistency. From this point forward, the "σ" symbol refers to the scaled MAD whenever we are estimating or discussing background noise levels of the images.

We then performed the fitting for each source using `imfit`. We iteratively refined each fit (e.g. by holding certain parameters, such as source position, fixed during the fit) until we determined the fit to be satisfactory. We declared a fit to be satisfactory once the absolute

value of the residual intensities of all pixels in the central Airy disk were below $4\times$MAD of the residual image, with the majority below $2\times$MAD. In cases where source parameters are held fixed, `imfit` does not return an uncertainty for those specific parameters, so the uncertainty is due entirely due to user choice of source position, size, etc. For these fits, our position uncertainties are 0.01 pixels, and uncertainties in the major and minor axes or position angles are $0.1°$. All the uncertainties for parameters held fixed during the fit are listed in italics in Table 2.3.

Finally, we determined a wavelength-dependent multiplicative correction factor to the `imfit` flux results. The SOFIA PSF is an obscured Airy diffraction pattern - its central bright disk has a slightly narrower width than a standard Airy diffraction pattern due to the effect of a central obscuration in the light path (the secondary mirror). However, `imfit` only fits 2-dimensional Gaussians. In effect, it fits a Gaussian to the central Airy disk and ignores the surrounding Airy rings. These correction factors are effectively serving as "aperture corrections" for our data; the only difference is that they are corrections to the fitted flux values returned by `imfit`, rather than corrections to direct measurements. As Airy diffraction patterns are wavelength-dependent, we calculated separate aperture corrections for our 19.7 μm and 37.1 μm data. While the best practice in aperture photometry would be to measure the PSF of an unrelated, isolated point source in each field and then apply that PSF correction to the data, we found that almost none of our fields contained an unrelated point source, much less one bright enough to measure the PSF with any confidence. Instead, we employed the procedure described below.

We first created four 100×100-pixel Airy diffraction patterns using the optical properties of the SOFIA telescope (primary and secondary mirror size and separation, etc.) at each of our two wavelengths. The PSFs are sampled with $0.''768$ pixels, the same as the FOR-CAST instrument. At this pixel size, the total grid is $76.''8$ in diameter; this is $\sim$23 times the

FWHM at 37.1 μm (3$\farcs$4) as quoted in the Handbook, and $\sim$31 times the FWHM at 19.7 μm (2$\farcs$5). Although Airy-disk diffraction patterns mathematically extend to infinity, on a practical level, our synthetic PSFs had to be truncated to a particular size; we considered >20 times the quoted FWHM to be sufficient. The four PSFs for a given wavelength are mathematically identical, but each center position is given either zero- or half-pixel offsets in both the x and y directions. This effectively gives us four different sampling scenarios for the PSF. This was done to account for the fact that the peak of a given point source might not always fall neatly onto a single pixel, but instead might be sampled relatively equally between two or even four pixels. We then used `imfit` to fit the central disk of each of these four PSFs, and compared the flux returned by `imfit` for the central disk alone to the flux measured within an aperture of radius 50 pixels (38$\farcs$4 at 0$\farcs$768 per pixel; 50 pixels was the largest aperture radius available to us for a 100$\times$100-pixel grid). We calculated the ratio of measured to fitted fluxes for each of the four PSF grids for one wavelength, and took the mean of these ratios as our aperture correction factor for that wavelength. The aperture correction at 37 μm is 1.17 $\pm$ 0.02, and the aperture correction at 19 μm is 1.11 $\pm$ 0.04, where the uncertainties are the standard deviation of the four measured-to-fitted flux ratios at each wavelength.

Table 2.3 shows the aperture-corrected `imfit` results for our 37 μm and 19 μm data. Non-detections are noted as upper limits. Our detection rate at 37 μm is 92%; the only target for which we did not detect any 37 μm emission is G10.29-0.13. Overall, we detect 24 separate 37 μm sources in our 12 targets. Our detection rate at 19 μm is slightly lower - we detect 19 μm emission in only 9 of our 12 targets, for a detection rate of 75%. Overall, we detect 18 separate 19 μm sources in our 12 targets.

The uncertainties on the integrated flux density values are the quadrature sum of three values: the fitted-flux uncertainties returned by the imfit task, the uncertainty of our mea-

Table 2.3.   SOFIA FORCAST 19.7 μm and 37.1 μm Fitted Flux Densities

EGO	Source[a]	Coordinates (J2000)[b] RA (h m s)	Dec (° ′ ″)	Fitted Size[b] Major × Minor (″ × ″)	PA (°)	19 μm Flux[c] Density (Jy)	37 μm Flux[c] Density (Jy)
G10.29–0.13	a	⋯	⋯	⋯	⋯	<0.40	<1.3
G10.34–0.14	a	18:09:00.001 (0.003)	–20:03:34.53 (0.04)	1.41 × 1.01 (0.31 × 0.45)	97 (31)	<0.36	14 (3)
	b	18:09:00.02 (0.02)	–20:03:28.8 (0.2)	4.55 × 2.97 (0.71 × 0.61)	97 (15)	0.7 (0.2)	9 (2)
G11.92–0.61	a	18:13:58.078 (0.002)	–18:54:20.16 (0.04)	2.63 × 2.39 (*0.1* × 0.05)	32 (9)	1.1 (0.4)	57 (12)
	b	18:13:58.113 (0.008)	–18:54:16.25 (0.09)	3.41 × 2.59 (0.14 × 0.13)	100 (6)	0.7 (0.3)	25 (5)
G12.91–0.03	a	18:13:48.227 (0.004)	–17:45:38.46 (0.06)	2.17 × 1.58 (0.26 × 0.30)	148 (17)	0.2 (0.1)	9 (2)
	b	18:13:48.276 (0.005)	–17:45:45.91 (0.09)	2.01 × 1.49 (0.40 × 0.48)	160 (29)	0.7 (0.2)	6 (1)
	c	18:13:48.44 (0.01)	–17:45:32.5 (0.2)	1.43 × 1.11 (0.84 × 0.91)	35 (140)	<0.20	2.2 (0.6)
G14.33–0.64	a	18:18:54.232 (0.003)	–16:47:48.40 (0.06)	5.40 × 3.41 (0.08 × 0.06)	4.2 (1.3)	0.7 (0.3)	85 (17)
	b	18:18:53.36 (0.01)	–16:47:42.3 (0.1)	11.42 × 10.23 (0.15 × 0.13)	107 (5)	22 (5)	200 (41)
	c	18:18:54.64 (0.01)	–16:47:49.6 (0.1)	point source	pt. src.	<0.33	7 (1)
G14.63–0.58	a	18:19:15.225 (0.009)	–16:30:03.3 (0.1)	3.60 × 2.91 (0.41 × 0.39)	59 (22)	<0.34	10 (2)
G16.59–0.05	a	18:21:09.124 (0.002)	–14:31:48.79 (0.03)	2.47 × 2.41 (0.04 × 0.04)	89 (29)	0.7 (0.2)	67 (14)
	b	18:21:09.509 (*0.001*)	–14:31:55.88 (*0.01*)	6.14 × 5.18 (*0.1* × 0.09)	141 (4)	5 (1)	68 (14)
	c	18:21:08.511 (*0.001*)	–14:31:57.92 (*0.01*)	1.91 × 1.91 (*0.1* × *0.1*)	167 (360)	0.8 (0.3)	6 (1)
G18.89–0.47	a	18:27:07.835 (0.008)	–12:41:35.1 (0.1)	1.93 × 1.85 (0.70 × 0.72)	167 (307)	<0.31	5 (1)
	b	18:27:08.46 (0.03)	–12:41:29.8 (0.5)	5.0 × 3.3 (1.7 × 1.5)	23 (31)	<0.31	4 (1)
G19.36–0.03	a	18:26:25.750 (0.005)	–12:03:52.57 (0.07)	2.69 × 2.48 (0.28 × 0.28)	70 (52)	0.3 (0.1)	24 (5)
	b	18:26:25.591 (0.009)	–12:03:47.9 (0.1)	3.78 × 2.56 (0.41 × 0.39)	84 (12)	1.7 (0.5)	20 (4)
G22.04+0.22	a	18:30:34.635 (0.003)	–09:34:45.74 (0.04)	2.13 × 1.57 (0.13 × 0.15)	135 (9)	0.4 (0.2)	21 (4)
	b	18:30:33.43 (0.01)	–09:34:47.9 (0.2)	4.81 × 4.34 (0.40 × 0.38)	95 (32)	1.8 (0.4)	14 (3)
G28.83–0.25	a	18:44:51.138 (*0.001*)	–03:45:48.05 (*0.01*)	4.41 × 2.53 (0.16 × 0.14)	87.5 (*0.1*)	0.3 (0.2)	32 (7)
	b	18:44:50.938 (0.008)	–03:45:56.5 (0.2)	2.61 × 1.34 (0.42 × 0.63)	159 (12)	1.1 (0.3)	8 (2)
G35.03+0.35	a	18:54:00.524 (0.003)	+02:01:19.16 (0.04)	3.64 × 3.10 (0.03 × 0.03)	115 (2)	1.5 (0.4)	160 (31)
	b	18:54:00.700 (0.007)	+02:01:23.2 (0.1)	5.47 × 3.91 (0.09 × 0.07)	131 (2)	0.8 (0.3)	100 (20)

[a]The listed source positions and fitted sizes are from the 37.1 μm fit results only.

[b]G10.29–0.13 has " … " in place of coordinates and fitted size because it was a non-detection at both wavelengths.

[c]Upper limits are given for sources that have no emission above 5σ. In these cases, the listed upper limit is the 5σ value for the FOV.

sured aperture corrections, and the absolute flux calibration uncertainty for the SOFIA FORCAST data. Herter et al. (2012) quote an absolute flux calibration accuracy to within 20% of the total integrated flux for a given object, and that is the value we adopt here. The uncertainties on the integrated flux densities returned by `imfit` are set by the background noise level, which we set to the scaled MAD for each source and wavelength during the fitting procedure. The uncertainties of our aperture correction factors are discussed above.

2.4.2 Photometry of Archival Data

Spitzer IRAC Photometry

In order to constrain the near-infrared portion of the SEDs, we chose to perform aperture photometry for our targets at 3.6 μm, 5.8 μm, and 8.0 μm (the IRAC I1, I3, and I4 bands, respectively) using CASAViewer. However, because the flux in these bands likely includes emission from some sources or processes unrelated to our sources of interest, and because the SED models we employ in § 2.5.2 do not include emission from PAHs, we chose to include these data as upper limits.

We obtained the necessary IRAC images from the NASA/IPAC Gator Catalog List, and aperture corrections were applied to each measurement according to the table on page 27 of the IRAC Instrument Handbook[6]. We did not include measurements in the 4.5 μm (I2) band because the emission in this band is extended in all cases (this was the original classification criterion for this object type).

The background noise level for the IRAC bands, as for all other wavelengths, is the scaled MAD within an emission-free region in each image. The emission-free regions were identical for all three IRAC bands used. For each source with significant ($>5\sigma$) emission at 37.1 μm, we measured the integrated IRAC band flux within a circular aperture centered

---

[6]https://irsa.ipac.caltech.edu/data/SPITZER/docs/irac/iracinstrumenthandbook/

on the 37.1 μm coordinates. We also measured the flux within an annulus of corresponding size. Aperture and annulus sizes were chosen based on the aperture corrections listed in the IRAC Instrument Handbook and the FWHM of each source in each band. For a given source, we used the same aperture for all three IRAC bands (i.e. we did not modify the size of the aperture with wavelength); we chose the smallest aperture that would successfully fit a source in all three bands. Each integrated flux measurement was corrected for background emission by subtracting the product of the median intensity value within the annulus and the size of the aperture from the direct aperture-flux measurement. After this subtraction, we applied the appropriate aperture corrections as listed in the IRAC Instrument Handbook. All aperture and annulus radii, aperture corrections, and corrected fluxes for our sources are listed in Table 2.4.

Due to the very crowded nature of these fields in the IRAC bands and the generally clustered nature of our sources, it was sometimes necessary to use annuli for local background subraction that were not centered on our sources. When this was necessary, we chose isolated stars within the same field of view and centered our annuli on those sources. We were careful to choose annulus stars of similar or lower brightness than the source in question. Choosing a star of equal or lower brightness for background subtraction would only have the effect of *increasing* the measured flux density. While it does sacrifice some precision, allowing the measured flux density to perhaps be artificially increased maintains the self-consistency of the photometry, as the data from these bands will only be used as upper limits.

The uncertainties on the integrated flux densities are the quadrature sum of three values: the background noise levels, the absolute flux calibration uncertainty for the IRAC bands, and the uncertainty in the aperture-correction values. The background noise levels are discussed above. The IRAC Instrument Handbook quotes an absolute flux calibration

Table 2.4.   IRAC Integrated Flux Densities

EGO	Source	Aperture[a] Radius ('')	Annulus[a] Radii ('')	Aperture Correction[b]			Aperture-Corrected Flux Density (mJy)		
				3.6 μm	5.8 μm	8.0 μm	3.6 μm	5.8 μm	8.0 μm
G10.29−0.13	a	3.6	3.6 to 8.4	1.125	1.135	1.221	0.4 (0.3)	15 (3)	22 (8)
G10.34−0.14	a	3.6	3.6 to 8.4	1.125	1.135	1.221	16.0 (0.8)	94 (6)	99 (14)
	b	3.6	3.6 to 8.4	1.125	1.135	1.221	11.2 (0.6)	137 (7)	350 (21)
G11.92−0.61	a	2.4	2.4 to 7.2	1.215	1.366	1.568	10.0 (0.4)	66 (3)	40 (2)
	b	2.4	2.4 to 7.2	1.215	1.366	1.568	22.9 (0.9)	193 (7)	152 (6)
G12.91−0.03	a	3.6	3.6 to 8.4	1.125	1.135	1.221	8.7 (0.4)	52 (3)	20 (5)
	b	4.8	14.4 to 24.0	1.070	1.076	1.087	1.3 (0.2)	55 (4)	130 (13)
	c	3.6	3.6 to 8.4	1.125	1.135	1.221	0.5 (0.2)	15 (2)	34 (5)
G14.33−0.64	a	4.8	14.4 to 24.0	1.070	1.076	1.087	6.6 (0.4)	86 (4)	136 (9)
	b	12.0	14.4 to 24.0	1.000	1.000	1.000	141 (6)	1600 (70)	4300 (180)
	c	3.6	3.6 to 8.4	1.125	1.135	1.221	2.1 (0.2)	26 (1)	31 (3)
G14.63−0.58	a	2.4	2.4 to 7.2	1.215	1.366	1.568	0.9 (0.1)	10.5 (0.1)	13 (2)
G16.59−0.05	a	3.6	3.6 to 8.4	1.125	1.135	1.221	3.3 (0.3)	108 (5)	107 (7)
	b	6.0	6.0 to 12.0	1.060	1.063	1.084	60 (3)	740 (30)	1840 (80)
	c	6.0	6.0 to 12.0	1.060	1.063	1.084	43 (2)	330 (15)	820 (40)
G18.89−0.47	a	4.8	14.4 to 24.0	1.070	1.076	1.087	4.6 (0.6)	46.2 (0.4)	20 (11)
	b	4.8	14.4 to 24.0	1.070	1.076	1.087	22 (1)	104 (6)	200 (15)
G19.36−0.03	a	4.8	14.4 to 24.0	1.070	1.076	1.087	24 (1)	151 (7)	190 (12)
	b	3.6	3.6 to 8.4	1.125	1.135	1.221	11.0 (0.5)	101 (4)	220 (10)
G22.04+0.22	a	4.8	14.4 to 24.0	1.070	1.076	1.087	1.4 (0.3)	30 (2)	26 (6)
	b	9.6	14.4 to 24.0	1.011	1.011	1.017	79 (4)	791 (32)	1980 (83)
G28.83−0.25	a	4.8	14.4 to 24.0	1.070	1.076	1.087	23 (1)	77 (5)	17 (8)
	b	4.8	14.4 to 24.0	1.070	1.076	1.087	8.0 (0.6)	91 (5)	220 (13)
G35.03+0.35	a	3.6	3.6 to 8.4	1.125	1.135	1.221	17.0 (0.8)	140 (6)	58 (6)
	b	3.6	3.6 to 8.4	1.125	1.135	1.221	30 (1)	121 (6)	34 (6)

[a]These columns list the radii of the aperture and annuli used for aperture photometry for each source. Radii are listed in arcseconds. Pixel scale is 1.''2/pixel for all IRAC bands.

[b]Aperture correction factors are from the IRAC Instrument Handbook.

accuracy to within 3% of the total integrated flux for a given object, and that is the value we adopt here. Additionally, the Handbook quotes an absolute aperture-correction accuracy to within 2% of the total aperture-correction factor.

Spitzer MIPS Photometry

We used CASA's `imfit` task to determine the integrated flux densities of our targets at 24 μm using the same fitting procedure described in § 2.4.1. Due to the MIPS 24 μm images' significant Airy rings for point sources (up to 22% of the total integrated flux according to the MIPS Instrument Handbook[7]), the MIPS fit results require an aperture correction similar to that discussed in § 2.4.1. Fortunately, the MIPS images, unlike our SOFIA images, contain a plethora of isolated point sources with which to measure the PSF directly.

In order to determine the value of the necessary aperture correction, we performed the `imfit` fitting procedure described in § 2.4.1 on five isolated, relatively bright point sources with fluxes listed in the MIPSGAL Point Source Catalog (Gutermuth & Heyer 2015). We selected the sources to span a range of colors and 24 μm flux densities. As with the SOFIA sources, we considered fits to be "satisfactory" when the absolute value of the residuals within the Airy disk were all under $4\times$MAD of the residual image, with the majority under $2\times$MAD. We compared the integrated fluxes returned by the `imfit` task to those listed in the MIPSGAL Point Source Catalog. We found a consistent aperture correction value of 1.59 ± 0.00893. Table 2.5 shows the positions, catalog fluxes, fitted flux results, and calculated flux ratios for these five standard stars.

We then applied the fitting procedure and measured aperture correction to our science targets. As for the SOFIA *FORCAST* data, sometimes certain parameters (source position, size, etc.) were held fixed during the fitting procedure; these cases are noted in Table 2.6.

---

[7]http://irsa.ipac.caltech.edu/data/SPITZER/docs/mips/mipsinstrumenthandbook/

Our results are listed in Table 2.6, which presents the final, aperture-corrected fitted flux results (to be used in the SED fitting) as well as the initial, un-corrected `imfit` flux results.

As with the SOFIA data, the uncertainties on the integrated flux density values are the quadrature sum of the uncertainties returned by the `imfit` task, the uncertainty of our calculated aperture-correction value, and the absolute flux calibration uncertainty for the MIPS data. The MIPS Instrument Handbook quotes an absolute flux calibration accuracy to within 5% of the total integrated flux of a given object. The uncertainties on both the peak intensity and the integrated flux density returned by `imfit` are set by the background noise level, which we set to the scaled MAD during the fitting procedure. The uncertainty of the calculated aperture correction value we take to be the standard deviation of the five measured values: 8.93×10^{-3}.

Hi-GAL and ATLASGAL Photometry

Unlike with the near- and mid-infrared data sets, our far-IR data could rarely be considered point-like. Therefore, instead of fitting gaussians to the emission using `imfit`, we measured the integrated flux of each source within a given intensity level using CASAViewer. The intensity levels were chosen uniquely for each source depending on local background emission and the overall image noise level (σ). Generally, apertures for the ATLASGAL data followed the 5σ level. Apertures for the Hi-GAL data varied between 60σ and 200σ at 70 μm and between 40σ and 150σ at 160 μm. These apertures follow comparatively high contours due to the combination of low scaled *MAD* values (typically of order 10^{-1}) and, in most cases, relatively bright large-scale ambient emission. Each integrated flux measurement was corrected for this background emission by subtracting the product of the median intensity value within a local annulus and the size of the aperture from the direct aperture-flux measurement. The mean and median aperture radii at 70 μm are $19\rlap{.}''6$ and

18.ʺ8, respectively, as compared to the HiGAL 70 μm beam size of 5.ʺ8 × 12.ʺ1. The mean and median aperture radii at 160 μm are 26.ʺ3 and 26.ʺ7, respectively, as compared to the HiGAL 160 μm beam size of 11.ʺ4 × 13.ʺ4. Positions and integrated flux values for the Hi-GAL and ATLASGAL data are listed in Table 2.7.

Our far-IR flux uncertainties are the quadrature sum of two values. First, there is the statistical uncertainty of the measurement itself, which we take to be the product of the background noise level σ in Jy beam^{-1} and the square root of the aperture size in beams. Second, there is the inherent uncertainty of the image due to flux calibration accuracy. Molinari et al. (2016) quote an absolute flux uncertainty of 5% for the Hi-GAL data, and Schuller et al. (2009) quote an absolute flux uncertainty of 15% for the ATLASGAL survey. We adopt these values for our uncertainty calculations for the Hi-GAL and ATLASGAL data, respectively.

Far-IR source selection   Beginning at 70 μm, the fluxes of sources that are not dominant at 37.1 μm (sources "b" and "c" for each FOV) begin to decrease, in some cases rapidly. This decrease in flux is usually such that, by either 160 μm or 870 μm, there is only one dominant source at that wavelength. In all cases, that dominant source is spatially coincident with the location of the brightest source at 37.1 μm. However, the angular resolution of the FIR data worsens as wavelength increases, so even if there are multiple sources present in the FIR images, the angular resolution may be insufficient to separate them. Because of the comparatively low resolution of these images, it is not uncommon to see FIR flux that is spatially coincident with one of the "b" or "c" sources for a given EGO, but neither is it clear that the spatial coincidence is not merely a result of resolution limitations. In cases where the morphology of the 70 μm or 160 μm emission was consistent with a single source, we assigned all the emission in that band to source "a." In cases where it was clear that there were multiple sources present in the Hi-GAL data, we took one of two

approaches. First, we attempted to fit the emission using multiple gaussian components using `imfit`. If we achieved satisfactory fits with this approach, the fitted fluxes of both sources are listed in Table 2.7. Second, if we could not achieve satisfactory fits with multiple gaussian components, we attempted to estimate the maximum possible amount of flux that could be ascribed to the weaker source. We then performed the photometric procedure described above on the emission as a whole (dominant and weaker source combined) and assigned all of the resulting flux to the dominant 37.1 μm source, and added the estimated flux from the weaker source to our uncertainty value for the dominant source. For these cases, the measured fluxes are marked in bold in Table 2.7. While imperfect, this method does allow us to at least account for the effects of multiple blended sources even when we cannot satisfactorily deblend the emission itself.

Source confusion was not an issue in any of the ATLASGAL images, since the ATLAS-GAL data a) have an angular resolution that is significantly poorer than any of the other data sets, thus potentially blending any individual sources past the point where one could recognize separate sources, and b) necessarily probe cooler gas. This effectively means that the emission in the ATLASGAL images originates primarily in the outer regions of the parent clump, which is an identifiably larger physical size scale than those probed by the Hi-GAL and our mid- or near-IR data sets. Due to source morphology in the ATLASGAL data and the aforementioned drop in flux in the FIR for sources that are not the dominant source at 37.1 μm, we attribute all 870 μm flux to the single, dominant 37.1 μm source in all cases.

The effect of these source-selection criteria is that full SEDs are constructed for the brightest 37.1 μm sources (the "a" sources) only, and these SEDS are based on the explicit assumption that these sources are by far the most dominant in the far-IR.

2.4.3 Images and Trends

Figures 2.1 through 2.4 show the detected SOFIA 19.7 and 37.1 μm emission in the vicinity of each EGO. We detected 37.1 μm emission in all twelve fields; in eleven cases, this emission was associated with the EGO. This is in itself a high detection rate. However, we detect an average of only two sources per target, of which only one, on average, is actually associated with the EGO. This suggests that, rather than detecting multiple protostars within each protocluster, we are typically detecting only the dominant source in each EGO. Likewise, we detect 19.7 μm emission in nine of our twelve fields, but it is only associated with the target EGO in eight cases. We detect more 19.7 μm emission toward sources that are not associated with the target EGOs than emission toward sources that are (10/18 not associated versus 8/18 that are). At 19.7 μm, we still detect an average of two sources per target. Taken together, these trends suggest that our target protoclusters are still quite young and/or deeply-embedded; this would explain the trend of overall dominance by a single source, as well as the poorer detection rate of even these dominant sources at 19.7 μm.

Of our 37.1 μm sources, all but one are located entirely within the 25% ATLASGAL contours of the clump associated with the target EGO, for a total of 23 37.1 μm sources within eleven ATLASGAL clumps (G10.29−0.13 has no 37.1 μm emission toward the EGO itself, so its ATLASGAL clump is not counted). This is an average of slightly more than two mid-infrared sources per clump. The one 37.1 μm source not located within an ATLASGAL clump is G14.33−0.64_b, which has some extended emission within the 870 μm contours but is centered outside of it; our source G14.33−0.64_b is the known H II region IRAS 18159−1648 (Jaffe et al. 1982).

Eleven of our sources are located in IRDCs; the only exception is G16.59−0.05. Eleven sources are known to be coincident with 6.7 GHz CH$_3$OH masers (references for maser de-

tections are in the tablenotes of Table 2.1); the remaining source, G14.33–0.64, has no published 6.7 GHz data at the time of writing. Three sources - G10.29–0.13 and G10.34–0.14 (near the W31 H II region G10.32–00.15, see Westerhout 1958), and G28.83–0.25 (near N49, see Wink et al. 1982) - are adjacent to are known H II or UCH II regions.

2.4.4 Mid-infrared Multiplicity

There is some evidence of multiplicity at mid-infrared wavelengths for nearly all of our targets, with G10.29–0.13 (lacking any mid-IR detection) and G14.63–0.58 being the only exceptions. The evidence for mid-IR multiplicity for the other sources falls generally into two categories: individual EGO-related sources (i.e. within the boundaries of extended 4.5 μm emission) that have unresolved substructure at the angular resolution of our SOFIA data, and sources that have nearby ($\lesssim 10''$) 37.1 μm detections which are not within the extended 4.5um emission of the EGO, and whose association with the EGO is unclear. We discuss each category in greater detail in the following sections. The naming convention of the new detections is described in § 2.4.1.

EGO Sources with Unresolved Substructure at 37.1 μm

The dominant EGO-related sources in G11.92–0.61, G14.33–0.58, G28.83–0.25, G35.03+0.35 exhibit elongated, unresolved 37.1 μm emission suggestive of multiplicity at scales $\lesssim 5''$ (the SOFIA angular resolution is $3\rlap{.}''4$). Below we explore how the mid-IR emission compares to existing high resolution centimeter to millimeter data. This comparison helps inform the nature of the emission at each wavelength. Mid-IR emission may trace both hot cores and outflow cavities, while centimeter emission can trace both free-free emission (e.g. H II region, ionized jet) and the long-wavelength end of the Rayleigh-Jeans tail of dust emission. Millimeter observations (in this context) primarily serve to identify individ-

ual cores from dust continuum emission. By comparing the emission from these different wavelength regimes, we can attempt to disentangle the possible sources of mid-IR emission in these objects.

G11.92−0.61   G11.92−0.61 is elongated roughly N-S at 37.1 μm, and shows two distinct sources at 19.7 μm which lie along the axis of the 37.1 μm elongation (Fig. 2.1). The southern and northern mid-IR sources (G11.92−0.61_a and G11.92−0.61_b) are coincident with the (sub)millimeter protostellar sources MM1 and MM3, respectively (Cyganowski et al. 2011a, 2017). Both MM1 and MM3 are associated with 6.7 GHz CH$_3$OH masers (a signpost of massive star formation Cyganowski et al. 2009, 2011a), and both have also been detected at centimeter wavelengths (the centimeter sources are designated CM1 and CM2 Cyganowski et al. 2011b; Cyganowski et al. 2014; Moscadelli et al. 2016; Ilee et al. 2016; Towner et al. 2017).

To further explore how sensitive the SOFIA data are to the presence of multiple protostellar sources, we turn to high-angular resolution, high-sensitivity millimeter data. Atacama Large Millimeter/submillimeter Array (ALMA) observations of G11.92−0.61 (1.05 mm, $0\rlap{.}''49 \times 0\rlap{.}''34$ synthesized beam) by Cyganowski et al. (2017) reveal at least eight 1.05 mm sources within a 5$''$ radius of the peak of the 37.1 μm emission, two of which correspond to MM1 and MM3). Of these eight, the authors estimate that six are low-mass objects, one is intermediate- or high-mass (MM3), and one is high-mass (MM1). Indeed, follow-up observations of MM1 at 1.3 mm using ALMA, with a synthesized beam of $0\rlap{.}''106 \times 0\rlap{.}''079$, find that this source is likely a proto-O star whose circumstellar disk dynamics yield an enclosed mass of M$_{enc} \sim 40 \pm 5 M_\odot$ (Ilee et al. 2018). These radio data suggest that the mid-IR morphology of G11.92−0.61 is dominated by the two intermediate to massive protostellar sources (MM1 and MM3), rather than, e.g., a poorly-resolved outflow cavity. This result also indicates that our SOFIA data are sensitive to massive protostellar multiplic-

ity, though as expected the mid-IR data are not sensitive to lower mass (and luminosity) protocluster members (also see § 2.5.3).

G14.33−0.64 The dominant EGO-related source G14.33−0.64_a (Fig. 2.2) is slightly elongated N-S at 37.1 μm, and there is a 19.7 μm detection associated with the northern portion of the elongation. The brightest component, G14.33−0.64_b, is coincident with the known evolved H II region IRAS 18159−1648. In order to achieve satisfactory fits to the 37.1 μm emission toward G14.33−0.64_a, it is necessary to fit a third component. G14.33−0.64_c is located $\sim 4''$ east-southeast of G14.33−0.64_a, is faint at both 37.1 μm and 24 μm, and is undetected at 19.7 μm.

Towner et al. (2017) report significant JVLA 1.3 cm ($4\rlap{.}''6 \times 2\rlap{.}''5$ beam) emission coincident with G14.33−0.64_a and the H II region G14.33−0.64_b, as well as a marginal detection at the location of G14.33−0.64_c (to within stated position uncertainties), though they were unable to get a satisfactory fit for its (weak) 1.3 cm flux density. Unfortunately, there are no published high-angular resolution millimeter continuum data for this source, though the mid-IR and centimeter data hint that there may be at least two massive protostars coincident with the EGO.

G28.83−0.25 G28.83−0.25_a is elongated E-W, consistent with unresolved substructure; this source is not detected at 19.7 μm (Fig. 2.4). Based on the 37.1 μm emission alone, it is unclear whether this elongation is indicative of multiple unresolved sources or is due to a different cause, such as an unresolved outflow cavity. Interestingly, the elongation follows the same axis as the extended 4.5 μm emission, which is thought to be due to outflow activity. Towner et al. (2017) detect two 1.3 cm continuum sources toward this EGO: one is coincident with the peak of the 37.1 μm emission (called CM2), and one that is coincident with the extended "spur" on the western edge of G28.83−0.25_a (called CM1).

Both 1.3 cm sources are unresolved at the angular resolution of the 1.3 cm data ($\sim 3''$). Both sources are also reported by Cyganowski et al. (2011b) at 3.6 cm with $\sim 1''$ resolution. Comparing the two centimeter wavelengths, Towner et al. (2017) suggest that either CM2 has a steeper free-free SED than CM1 or has a higher contribution from dust. If free-free emission is present, then the E-W elongation at both 1.3 cm and 37.1 μm suggests that this emission could be due to an ionized jet. In the absence of higher-resolution MIR images, and comparable millimeter wavelength data we cannot definitively attribute the elongation in this source to either outflow activity or multiple unresolved protostellar sources.

G35.03+0.35 The 37.1 μm emission for G35.03+0.35 is elongated NE-SW and is indicative of at least two unresolved sources (Fig. 2.4); at 19.7 μm, the emission is resolved into two distinct sources, which lie along the major axis of the 37.1 μm elongation. When observed at 1.3 cm with similar angular resolution ($\sim 3''$) to the 37.1 μm data, the brighter 37.1 μm source, G35.03+0.35_a, is coincident with compact, unresolved 1.3 cm continuum emission as reported by Brogan et al. (2011); Towner et al. (2017). However, higher angular resolution 3.6 cm VLA observations (~ 1) resolve the continuum emission for G35.03+0.35 into at least five distinct, compact centimeter sources (Cyganowski et al. 2011b). Four of these 3.6 cm sources are coincident with the brighter 37.1 μm source, G35.03+0.35_a, and the unresolved 1.3 cm source. The two strongest of these 3.6 cm sources (CM1 and CM2), trace a known ultra-compact H II region (Kurtz et al. 1994), and likely a hyper-compact H II region (Cyganowski et al. 2011b), respectively. Therefore, G35.03+0.35_a, harbors at least two massive protostars. With ALMA at 0.87 mm, Beltrán et al. (2014) also detect CM1 and CM2, but not CM3, suggesting the latter is not a protostar. More recent high angular resolution JVLA observations of G35.03+0.35 ($0.''34$ resolution) and analysis of the SEDs by Sanna et al. (2019), suggest that the hyper-compact H II region CM2 is driving a powerful outflow and that CM3 corresponds to jet emission launched from CM2. The fifth

3.6 cm source (denoted CM3) lies in the direction of the weaker 19.7 and 37.1 μm detections, G35.03+0.35_b, but the 19.7 μm source appears to extend further to the NE than the 3.6 cm emission. Thus, G35.03+0.35_b may be tracing an outflow cavity that extends to the NE of G35.03+0.35_a (and the likely powering source CM2).

37.1 μm Detections For Which the Association with EGOs is Unclear

Many of the non-dominant 37.1 μm sources in our sample (the "b" and "c" sources) lie close to ($\lesssim 10''$) the dominant 37.1 μm source but outside the bounds of the 4.5 μm extended emission. They also typically are redder in color than the "a" sources. The association of these non-dominant MIR sources with the EGOs is unclear, but understanding this association is an important component of understanding the mid-IR multiplicities in this sample.

One example of such a case is EGO G19.36−0.03, which has two sources identified in Table 2.3. They are fully separable at 19.7 μm but only marginally separable at 37.1 μm (Fig. 2.3). The fainter source at 37.1 μm, G19.36−0.03_b, lies outside the extended 4.5 μm emission of the EGO. Both sources have unresolved 1.3 cm continuum counterparts, reported by Towner et al. (2017). G19.36−0.03_b is the stronger source at 1.3 cm, and also has compact emission at 3.6 cm (Cyganowski et al. 2011b) with $\sim 1''$ resolution. It is also coincident with MIPS 24 μm and IRAC emission, and is associated with a line of 44 GHz Class I CH$_3$OH masers; Cyganowski et al. (2011b) suggest that it is therefore a candidate for an expanding H II region. If G19.36−0.03_b is indeed associated with the EGO, then the multiplicity of massive protostars in this EGO is 2. Furthermore, this would make G19.36−0.03 an example of a massive protocluster in which multiple stages of high-mass star formation are occurring simultaneously, as noted by Cyganowski et al. (2011b). In this case, the classification of the EGO protocluster is significantly impacted by the association

(or lack thereof) between the two 37.1 μm detections.

Other such cases in our sample include G10.34−0.14_b, G18.89−0.47_b, and G12.91−0.03_c. If every one of our "b" and "c" sources is truly associated with an EGO (except the H II region IRAS 18159-1648), then our average multiplicity of massive sources in this sample − at 37.1 μm with ∼3″ resolution − is 1.9. If only half are truly associated, the average multiplicity is 1.4. These values are roughly in line with the results of **?**), who find no strong evidence of high mulitplicity (>2 massive sources) in a subset of similar massive protostellar sources from the SOFIA Massive Star Formation Survey (SOMA) sample (see De Buizer et al. 2017, and Section 4.3.4 of this work, for a discussion of the SOMA sample and subsamples).

In order to properly address this multiplicity question, additional observations are needed along the lines of those described above for G11.92−0.61 and G35.03+0.35. Such observations must be able to distinguish individual dust cores ($\lesssim 0.02$ pc spatial resolution) and establish the nature (ionized jet, H II region, synchrotron, etc.) of the centimeter-wavelength emission. The former allow the identification of individual sources, and the latter allow the differentiation between ionized jets and HC H II regions. Indeed, we have observations underway for the majority of the EGOs in this sample with sub-arcsecond resolution in the JVLA C- and K-bands, and with ALMA Band 3 and Band 6. The results of these observations will be published in future work.

2.5   Analysis

In order to estimate temperature and mass of the parent clumps, we performed greybody fits to the SEDs in order to derive representative temperatures for each EGO. Our greybody fits use only the far-IR (Hi-GAL and ATLASGAL) data for each source, and are used to derive dust temperatures that were then used to calculate clump masses based on the ATLASGAL

870 μm integrated flux densities. In order to independently assess gas temperature in these clumps, we also examine the gas kinetic temperatures determined by Cyganowski et al. (2013), as described below. Table 2.8 shows the NH_3 and greybody temperature results for each source, along with corresponding estimated masses. The last column also lists the FIR luminosity of each EGO, as returned by the greybody fits.

In order to determine $L_\star$ for each target, we fit the SEDs with several different publicly-available SED models including those published in Robitaille et al. (2006), Robitaille (2017), and Zhang & Tan (2018). The different underlying assumptions and components for each model are described below, in order of model publication date. Figure 2.5 and Figures A.1 through A.12 show the SEDs and model fits in the following order for each source: six panels showing Robitaille (2017) models, one panel showing Robitaille et al. (2006) models, and one panel showing Zhang & Tan (2018) models. Figures A.1 through A.12 are located in Appendix A.

2.5.1   Temperature and Mass From Dust and NH_3 Emission

In order to determine the mass of the ATLASGAL clumps (the mass reservoirs) in which our sources are located, we need to know the temperature of the emitting material. This is typically accomplished either by fitting models to molecular line emission (e.g. NH_3, CH_3CN) or by fitting greybody functions to far-IR dust emission. For this work, we chose to employ each method separately and compare results.

For the gas temperature, we adopt the single-component NH_3 fit results of Cyganowski et al. (2013), who performed a H_2O maser and NH_3(1,1) through (3,3) inversion-line survey of 94 GLIMPSE-identified EGOs using the Nobeyama Radio Observatory 45-meter telescope. The kinetic temperature (T_{kin}) results from Cyganowski et al. (2013) are shown

in Table 2.8. The Cyganowski et al. (2013) NH$_3$ temperatures for our sample[8] have minimum, maximum, and median values of 20.5, 29.5, and 25.8 $\pm$ 2.5 K, respectively, where the uncertainty on the median is the MAD.

In order to estimate dust temperature and derive clump mass, we used the Python package `lmfit` to fit a series of greybody curves to our far-IR (70 μm, 160 μm, and 870 μm) flux densities and thereby derive a temperature T$_{dust}$ for each source. During this procedure, the grain opacity spectral index (β) was fixed at 1.7 (Brogan et al. 2016; Sadavoy et al. 2016). We defined a grid of T$_{dust}$ ranging from 18.0 K to 40.0 K in steps of 1.0 K. For each value of T$_{dust}$, we fit for the opacity at a reference wavelength and computed the corresponding luminosity (L$_{FIR}$). The best-fit temperature was defined as the temperature for which χ^2 was closest to 1, and the best-fit luminosity was the luminosity corresponding to this best-fit temperature. Then, we calculated the total gas mass of each source as

$$M_{gas} = R \left(\frac{F_\nu D^2}{B_\nu(T_{dust})\kappa_\nu} \right) \left(\frac{\tau}{1 - e^{-\tau}} \right) \tag{2.1}$$

where $R = 100$ is the gas-to-dust mass ratio, F_ν is the measured 870 μm flux density of the source, D is the distance to the source, $B_\nu(T_{dust})$ is the blackbody function, κ_ν is the dust opacity, and τ is the optical depth at 870 μm. The dust opacity was fixed at $\kappa_{870\mu m} = 1.85$ cm^2 g^{-1}, which is the value Schuller et al. (2009) interpolate from Table 1 of Ossenkopf & Henning (1994) and which is employed by Cyganowski et al. (2017) for their calculation of the mass reservoir of G11.92−0.61. In all cases, the fitted opacity is sufficiently small at 870 μm that $\frac{\tau}{1-e^{-\tau}} \approx 1$. We calculate mean and median T_{dust} =25.8 K and 26.0 K, respectively, with a standard deviation of 2.9 K and a MAD of 1.5 K.

While the mean and median values of the two temperature estimates are in statistical

---

[8]While Cyganowski et al. (2013) note that the NH$_3$ (3,3) masers detected by Brogan et al. (2011) in G35.03+0.35 (Brogan et al. 2011) are not readily distinguishable as a non-thermal contribution in the Nobeyama data, contamination by (3,3) masers is unlikely to significantly impact the fitted temperatures.

agreement, there is a general trend that the temperatures calculated using NH_3 inversion transitions are slightly lower than those calculated from FIR dust emission. The median difference between the dust- and gas-derived temperatures is only 0.92 K, so the trend is weak and further, more precise investigation is needed in order to make a definitive statement about the implications of such a trend. However, it should be noted that this *is* in broad agreement with the trends noted by König et al. (2017) and Giannetti et al. (2017) for the ATLASGAL Top100 sample[9]. Both authors find that dust and NH_3 temperatures are well-correlated for massive star-forming clumps overall, but that NH_3 emission tends to trace gas that is warmer than dust in very cold clumps ($\lesssim$15 K), and gas that is cooler than dust in warmer clumps ($>$15 K).

The median EGO greybody-derived T_{dust} (26.0 K) is similar to that of the the median dust temperature of the Top100 sample (24.7 K, see Table 2 in König et al. 2017). However, König et al. (2017) sort the Top100 sources into four subcategories, of which the "IR-weak" ($F_{24\mu m}$ < 2.6 Jy, median T_{dust} = 21.4 K) and "IR-bright" ($F_{24\mu m}$ > 2.6 Jy, median T_{dust} = 28.2 K) samples are the most similar to the EGO sample. Indeed, when scaled appropriately for distance[10], half of our sources have $F_{24\ \mu m}$ < 2.6 Jy, and half have $F_{24\ \mu m}$ > 2.6 Jy. Interestingly, we find that the EGO median dust temperature also falls in between the median T_{dust} of the IR-weak and IR-bright populations, though it is closer to the IR-bright T_{dust}. However, it is notable that the temperature ranges of the two categories are broad: 11.7 to 26.2 K for IR-weak and 21.9 to 35.4 K for IR-bright, with overlap in the 21.9 to 26.2 K range. Indeed, approximately 50% of the IR-weak and 40% of the IR-bright sources fall in this overlapping range of T_{dust}, so these two subcategories are not

---

[9]König et al. (2017) and Giannetti et al. (2017) are the third and fifth papers, respectively, in a series on the ATLASGAL Top100 sample, which consists of 110 of the brightest submillimeter sources in the ATLASGAL compact source catalog selected to span a full range of evolutionary stages. For a description of the sample properties and selection criteria, see Giannetti et al. (2014).

[10]König et al. (2017) and Giannetti et al. (2017) both adopt 2.6 Jy as the 24 μm IR-weak/bright cutoff as that is the flux density of a B3 star at 4 kpc; for the flux comparison above, we scale the 24 μm fluxes listed in Table 2.6 for a distance of 4 kpc.

distinct with regard to the dust temperature. Interestingly, all of the EGO T_{dust} fall within the Top100 IR-bright range, with the majority (75%) also falling in the overlap region. Two of the EGO-12 sources, G14.63−0.58 and G18.89−0.47, are included in the Top100 sample, and both are classified as IR-weak. This is consistent with our distance-scaled $F_{24\mu m}$ discussed above.

The strong overlap of the EGO and IR-bright T_{dust} suggests that the two samples may be drawn from the same parent population, but the clustering of the EGO T_{dust} in the IR-weak/IR-bright overlap region is nontrivial and cannot be discounted. Based on these competing factors, it seems likely that either a) EGOs preferentially lie somewhere between the IR-weak and IR-bright samples in temperature space, or b) EGOs represent the colder end of the IR-bright sample, but are still only a subset of the IR-bright population and do not constitute a separate population. Unfortunately, König et al. (2017) do not correlate the Top100 sources with sources in the EGO catalogs of Cyganowski et al. (2008) and Chen et al. (2013), so we cannot say definitively whether or not EGOs are well-represented in the current Top100 sample. If they are, this could explain the apparent overlap in population, and if not, a comparison of the properties of EGOs with the Top100 sample would be warranted.

The Cyganowski et al. (2013) NH_3 temperatures for our sample are slightly warmer than the NH_3 temperatures for both the "IR-weak" and "IR-bright" subcategories of the Top100 sample ($\sim$18 K and $\sim$22 K, respectively; Giannetti et al. 2017). The masses calculated from the two temperatures have mean and median differences of 1.8% and 4.3%, respectively, with a maximum difference of 40.6% and a standard deviation of 17.2%. The mean and median of the ratio of greybody-derived to ammonia-derived mass are 98.2% and 95.7%, respectively, again with a standard deviation of 17.2%. This difference might indicate that the greybody temperatures systematically produce slightly lower masses than

the NH_3-derived masses, in agreement with the trend noted above that NH_3 generally traces cooler material than dust except in the very coldest environments. However, we do not find that those sources where greybody fits produce lower masses than the NH_3 fits are systematically the warmest or coldest clumps (using either the greybody or NH_3 temperatures). Furthermore, the high standard deviations on both of these numbers suggest that the two sets of masses are effectively identical; there is no statistically-significant trend biasing one mass estimate higher than the other. Given that a sample size of 12 is still well within the regime of small-number statistics, we would strongly caution against over-extrapolating from these particular results - either for or against a particular mass-ratio trend.

Overall, the luminosities we calculate from the greybody fits to our sources are in good agreement with results published by other teams for these or similar sources. Moscadelli et al. (2016) constructed SEDs for 40 high-mass YSOs, including four of our targets (G11.92−0.61, G14.63−0.58, G16.59−0.05, and G35.03+0.35), using integrated fluxes from the online image archives for the MSX (Egan et al. 2003) and WISE (Wright et al. 2010) surveys and the point-source catalogs of IRAS (Neugebauer et al. 1984) and SCUBA (Di Francesco et al. 2008). They calculated bolometric luminosity for each source by directly integrating the area under the SED curve. The L from our greybody fits for these four EGOs agree with the Moscadelli et al. (2016) luminosities within $\pm20\%$, with no trend toward over- or under-estimation. Urquhart et al. (2018) conducted a systematic analysis of the properties of $\sim$8,000 dense clumps in the ATLASGAL Compact Source Catalog (CSC), including deriving L, M, and temperature. They performed automated aperture photometry for each clump using the ATLASGAL 870 μm maps in conjunction with Hi-GAL 70 to 500 μm images, MSX emission maps at 8, 12, 14, and 21 μm, and WISE 12 and 24 μm images, and fit the resulting SEDs to derive T_{dust} and L. Each SED was fit with either one (greybody-only) or two (greybody+blackbody) components, depending one whether the

source was best represented by a single cold component or a combination of cold and hot components. Clumps were fit with two components if they had at least two flux measurements at $\lambda < 70$ μm. All twelve of our sources are represented in the Urquhart et al. (2018) sample, and the median ratio of their luminosities to ours is +1.5. The Urquhart et al. (2018) L are higher than our greybody-derived L in all cases; this likely reflects the fact that our greybody fits are exclusively single-component fits, while the fitting procedure of Urquhart et al. (2018) requires that at least eleven of our sources were fit with two components in their analysis. The explicit inclusion of a hot component in the fit would be expected to increase the overall luminosity derived for a clump.

2.5.2   SED Modeling

In § 2.5.2, 2.5.2, and 2.5.2, we provide brief summaries of the model assumptions and underlying physics for each of the three SED model types we used (Robitaille et al. 2006; Robitaille 2017; Zhang & Tan 2018). While we present the Robitaille (2017) results first in our figures for easy visual comparison (Figure 2.5, and all figures in Appendix A), we have chosen to present the models in chronological order by publication date in these summary sections, as the improvements in the Robitaille (2017) models were directly influenced by the Robitaille et al. (2006) models.

In Figure 2.5 and Appendix A, the χ^2 value shown on the plots is χ^2 per data point, where a "data point" is defined as any flux density used for the fit that is not an upper or lower limit. (For G11.92, for example, n_{data} is 6.) From this point forward, any discussion of "χ^2" values refers to χ^2 per data point unless explicitly stated otherwise.

Robitaille et al. (2006) Model Grid

The Robitaille et al. (2006) models are a single grid of 200,000 model SEDs for YSOs. All Robitaille et al. (2006) models include a central star, rotationally-flattened infalling (Ulrich-type) envelope, bipolar cavities, and a flared accretion disk. The models use the dust optical constants of Laor & Draine (1993), and neither include emission from PAHs nor account for the possibility of ice-coated grains. The models were interpolated along evolutionary tracks in order to derive stellar radius ($R_\star$) and stellar temperature ($T_\star$) from a given combination of stellar mass ($M_\star$) and age ($t_\star$). They use two sets of evolutionary tracks: Bernasconi & Maeder (1996) for stars with $M_\star > 9M_\odot$, Siess et al. (2000) for stars with $M_\star < 7M_\odot$, and a combination of the two for stars with $7M_\odot < M_\star < 9M_\odot$. The grid values of $M_\star$ and $t_\star$ were sampled from probability density distributions: $M_\star$ was sampled between $M_{min} = 0.1\ M_\odot$ and $M_{max} = 50\ M_\odot$ such that there was a constant density of models in $\log_{10}M_\star$ space, and $t_\star$ was sampled between $t_{min} = 10^3$ yr and $t_{max} = 10^7$ yr such that there was a nearly-constant density of models in $\log_{10}t_\star$ space, with a slight bias toward higher values of $t_\star$.

The ranges of the envelope accretion rate $\dot{M}_{env}/M_\star$, envelope outer radius, cavity opening angle θ_{cavity}, and cavity density are dependent on the age of the central source. Overall in the grid, $\dot{M}_{env}/M_\star$ varies from $\sim 5 \times 10^{-4}$ to $\sim 10^{-9}$, and spans two orders of magnitude for any given source age. $\dot{M}_{env}/M_\star$ is sampled uniformly in logarithmic space. It is held constant for $t_\star < 10^4$ yr, then decreases, and finally goes to zero around 10^6 yr. For models with $M_\star > 20\ M_\odot$, $\dot{M}_{env}/M_\star$ was sampled with the same range as a 20 $M_\odot$ model. That is, $\dot{M}_{env}/M_\star$ for sources with $M_\star > 20\ M_\odot$ is no longer specific to each stellar mass, but a general rate used for all stars with $M_\star > 20\ M_\odot$.

The envelope outer radius ranges from 10^3 to 10^5 AU, sampled uniformly in $log(R)$ space. Bipolar cavities follow a conical shape described in cylindrical coordinates by

$z = c\omega^d$, ω is the radial coordinate, $d = 1.5$ is a fixed value, and c is a constant of proportionality defined as $c = (R_{env}^{max})/(R_{env}^{max}\tan(\theta_{cavity}))$. θ_{cavity} is sampled from a range of values that increases with $t_\star$; values range from $0°$ to $60°$ in the grid overall, but are limited to $\sim 0° - 10°$ for the youngest sources and gradually shift to $\sim 20° - 60°$ for the oldest sources. Envelope cavity density is sampled from a range one order of magnitude wide that decreases with evolutionary age; it ranges from 8×10^{-20} g cm^{-3} to 1×10^{-22} g cm^{-3}, except in cases where the ambient density is greater than the cavity density. In such cases, the cavity density is reset to the density of the ambient medium, which is constant in both space and time and ranges from $\sim 1.67 \times 10^{-22}$ $(M_\star/M_\odot)$ g cm^{-3} to $\sim 6.68 \times 10^{-22}$ $(M_\star/M_\odot)$ g cm^{-3} (for precise ranges and sampling conditions, see § 2.2.2.5 of Robitaille et al. 2006).

The flared accretion disk is described by five parameters: disk mass, disk outer radius, disk inner radius, disk structure, and disk accretion rate. Disk mass is originally sampled from $\sim 0.001 - 0.1 M_\odot$ for sources with $t_\star < 1$ Myr, and then sampled over a wider range of masses for later evolutionary stages. Disk outer radius is usually associated with the centrifugal radius R_C, so R_C is sampled from 1 to 10,000 AU, but is time-dependent such that earlier evolutionary stages may have smaller radii than later stages. Disk inner radius was set to the dust sublimation radius R_{sub} for one third of the models, and sampled between R_{sub} and 100 AU or the disk outer radius, whichever was smaller, in the remaining two thirds of the models. Additionally, the envelope inner radius was set to the disk inner radius for all models. The disk structure is described by the disk flaring parameter β and scale height factor z_{factor}, both of which were sampled from ranges dependent on the disk outer radius. The disk accretion rate is calculated using the disk α_{disk} parameter (a unitless measure of the efficiency of angular momentum transport, which is dependent on disk radius and always less than 1) and accretion-to-α relations published in prior works (for details, see Robitaille et al. 2006, and references therein). α_{disk} is sampled from 10^{-3} to

10^{-1} in log space.

Robitaille (2017) Model Sets

The Robitaille (2017) models are a set of eighteen different YSO model grids, each with 10,000 to 80,000 models. The models were created using a similar computational method to Robitaille et al. (2006), but with different physical components and parameter ranges. Each grid (referred to as a "model set" in Robitaille (2017), nomenclature that we henceforth adopt here) contains a different combination of physical components. Each model set includes a central stellar/protosteller source, and then may or may not include 1) an ambient medium, 2) a power-law envelope or an Ulrich-type envelope, 3) bipolar cavities, 4) a passive disk, and 5) an "inner hole" (gap between the stellar surface and the inner radius of the disk/envelope). The Robitaille (2017) models do not assume a particular evolutionary track; it is left to the user to determine additional protostellar properties (other than those returned by the model) using the evolutionary track of their choice. Users are encouraged to test multiple model sets against their data and identify trends in model results in order to determine which physical components do or do not make a significant difference to the goodness-of-fit.

Given that we already have evidence that our targets have outflow activity (e.g. Cyganowski et al. 2008, 2009) and most are embedded in IRDCs, we chose to run all models with bipolar cavities, except for two controls (one with a disk, envelope, and no cavities and one with an envelope and neither a disk nor cavities). However, while the outflow activity of our target sources is suggestive of the presence of disks, they have been confirmed in few of our targets (e.g. G11.92–0.61). Therefore, we have chosen to run all models with bipolar cavities - including those without disks - in order to avoid biasing our analysis towards only models with disks.

In all eighteen Robitaille (2017) model sets, T$_{star}$ varies from 2000 K to 30000 K. In models with a disk, the disk shape varies from from hydrostatic (flared) to flat. All disks in all models are passive (accretion is not explicitly included in the model). A detailed explanation of the reasoning for using only passive disks can be found in Robitaille (2017), § 3.2.2. The disk density distribution goes as $r^{(\beta-p)}e^{(z/h)^2}$, where disk flaring power ($1 < \beta < 1.3$), disk surface density power ($-2 < p < 0$), and disk scale height (1 AU $< h <$ 20 AU) are free parameters. The envelope can be either Ulrich-type, in which case the centrifugal radius (R$_C$) varies from 50 to 5000 AU, or power-law, in which case the envelope power (γ) ranges from -2 to -1. The shape of the bipolar cavities follows a power-law, where the cavity power (c) varies from 1 to 2. The bipolar cavities are assumed to be filled with dust of a constant density, where the density ranges from 10^{-23} to 10^{-20} g cm^{-3}. The ambient medium is defined as a lower limit to the density and temperature of the envelope (T$_{amb}$ = 10 K, $\rho_{amb} = 10^{-23}$ g cm^{-3}). The dust in the Robitaille (2017) models is taken from Draine (2003a,b) and Weingartner & Draine (2001), and does not include emission from PAHs. Each SED is computed for nine viewing angles between 0° and 90°, where the viewing angles are selected using stratified sampling: viewing angle is randomly chosen within a specific range, so that each SED is sampled at one random angle between 0° and 10°, one random angle between 10° and 20°, and so on up to 90°.

The model sets we used are as follows:

s-pbhmi: model contains a central star, no passive disk, a power-law envelope, a bipolar cavity, an ambient medium, and a variable inner envelope radius (rather than the inner radius being set to the dust sublimation radius). This variability has the effect of creating an "inner hole" between the inner radius of the envelope and the stellar surface.

s-ubhmi: model contains a central star, no passive disk, an Ulrich envelope, a bipolar cavity, an ambient medium, and an inner hole.

s-pbsmi: model contains a central star, no passive disk, a power-law envelope (no rotational flattening), a bipolar cavity, an ambient medium, and no inner hole (i.e. the inner radius is the dust sublimation radius).

s-ubsmi: model contains a central star, no passive disk, an Ulrich (rotationally-flattened) envelope, a bipolar cavity, an ambient medium, and no inner hole.

spubsmi: model contains a central star, a passive disk, an Ulrich envelope, a bipolar cavity, an ambient medium, and no inner hole.

spubhmi: model contains a central star, a passive disk, an Ulrich envelope, a bipolar cavity, an ambient medium, and an inner hole.

spu-smi: model contains a central star, a passive disk, an Ulrich envelope, no bipolar cavities, an ambient medium, and no inner hole.

s-u-smi: model contains a central star, no passive disk, an Ulrich envelope, no bipolar cavities, an ambient medium, and no inner hole.

A complete key, including diagrams, for all eight of these model sets can be found in Robitaille (2017), Table 2.

Zhang & Tan (2018) Model Grid

The Zhang & Tan (2018) models are a grid of $\sim$9000 YSO model SEDs. These models are based on the Turbulent Core theory of high-mass star formation (McKee & Tan 2003). The

Zhang & Tan models all assume a central source, disk, envelope, and bipolar outflow; they neither assume nor fit an ambient medium or emission from the parent clump. The model grid is composed of five variables (three physical, two observational): core mass, mass surface density, stellar mass, A_V along the line of sight, and inclination/viewing angle. Core mass is sampled from 10 to 480 $M_\odot$, mass surface density ranges from 0.1 g cm^{-3} to 3.16 g cm^{-3}, and stellar mass ranges from 0.5 to 160 $M_\odot$. Each model SED is sampled at 20 viewing inclinations, from $\cos(\theta_{view}) = 0.975$ to $\cos(\theta_{view}) = 0.025$. The range of A_V is set by the user; we chose to use $40 < A_V < 1000$, as we did for both types of Robitaille models.

In the Zhang & Tan (2018) models, the initial core is assumed to have an r$^{-3/2}$ power-law density distribution, and is assumed to exhibit inside-out collapse and rotational-flattening (i.e. is assumed to be an Ulrich-type envelope). Zhang & Tan (2018) assume that the ratio of disk mass to protostellar mass is constant, at $M_{disk}/M_\star = 1/3$. They assume that all disks are hydrostatic (modified alpha disks). In order to return protostellar radius, temperature, and luminosity, the models assume the evolutionary tracks of Hosokawa & Omukai (2009). Zhang & Tan (2018) use the same dust models as Robitaille et al. (2006).

2.5.3 Model Results: Robitaille et al. (2006), Robitaille (2017), and Zhang & Tan (2018)

Due to the different physical assumptions and parameters fit by each model, the number of physical parameters that could be compared directly is small. Table 2.9 shows the stellar radii ($R_\star$) and stellar temperatures ($T_\star$) returned by each of the three model grids, as well as the Stefan-Boltzmann luminosities ($4\pi R_\star^2 \sigma T_\star^4$) calculated from those radii and temperatures. The χ^2 values shown are χ^2 per data point, as described in § 2.5.2. The individual $R_\star$ and $T_\star$ values returned by the three different sets of SED models for a particular source

frequently span up to two orders of magnitude. However, the Stefan-Boltzmann luminosities calculated from the different combinations of $R_\star$ and $T_\star$ (hereafter $L_\star$) tend to agree to within a factor of 3.

Robitaille (2017) stress that the model sets therein are best used to compare how much the presence or absence of a particular physical component (e.g. bipolar cavities) affects the accuracy of each model. In order to accomplish this, the author suggests that a Bayesian analysis (rather than χ^2 scores alone) are needed. Unfortunately, we cannot compare Bayesian scores from the Robitaille (2017) models to Bayesian scores from the Robitaille et al. (2006) and Zhang & Tan (2018) set, as this approach of comparing probabilities assumes the models in question have similar underlying parameters and parameter ranges. The Robitaille et al. (2006) and Zhang & Tan (2018) models sample different parameter ranges and, in the case of Zhang & Tan (2018), different parameters altogether, so the comparison of probabilities cannot be performed. For the purposes of comparing the results from the different sets of published models, we use χ^2. A detailed discussion of the Bayesian scores for the Robitaille (2017) models – and how this approach affects the overall trends as compared to the χ^2 analysis – can be found in Appendix B.

Expected Luminosity Sensitivity

The only source which had no 37.1 μm emission detected toward the EGO is G10.29–0.13 (see Table 2.3, Fig. A.1). This source is also a non-detection at 19.7 and 24 μm, and has fairly isolated Hi-GAL and ATLASGAL emission compared to the rest of the sample. Therefore, based on the non-detection of this source and its comparative isolation and morphological simplicity, we use G10.29–0.13 as a test case in order to estimate the minimum luminosity sensitivity of the SOFIA observations. The 37.1 μm observations of 10.29–0.13 have an integration time of 502 s and $\sigma = 0.26$ Jy beam^{-1}, and the assumed

distance is 1.9 kpc.

We construct a synthetic SED for this source by inserting the 3σ upper limits at 37.1 and 24 μm as actual photometric measurements with uncertainties of 1σ. The 19.7 μm data remain as upper limits, while the values and treatment of flux densities from the other six wavelengths are likewise unchanged. We modeled this SED using the eight Robitaille (2017) model sets described in § 2.5.2, and the best-fit model returned a Stefan-Boltzmann luminosity of $L_{min} = 1.1 \times 10^3 L_\odot$.

This approximate lower limit is consistent with 92% of the luminosities shown in Table 2.9. There are four models which produced $L_\star < 1.1 \times 10^3$, and interestingly all of these come from the Zhang & Tan (2018) models. These four low luminosity Zhang & Tan (2018) model results also correspond to the largest discrepancies between the three types of models assessed. See additional discussion of the trends, limitations, and overall quality of the three model packages below.

Stefan-Boltzmann Luminosities

The $L_\star$ (calculated from $R_\star$ and $T_\star$) are almost always larger than the L returned by the greybody fits, typically by a factor of $\sim$2. This trend is consistent with the fact that our greybody fits are single-component and largely account for emission from cold dust, whereas the fits to the full SEDs can also account for emission from hotter components (e.g., hot cores) that emit predominantly in the NIR and MIR. This is also consistent with our previous comparison to the luminosities reported in Urquhart et al. (2018). We find that the ratio between the Urquhart et al. (2018) luminosities and ours has decreased; the median ratio between the Urquhart et al. (2018) L and those listed in Table 2.9 is now +1.27. The median ratios between the Urquhart et al. (2018) L and ours for the individual model packages are +1.22 for Robitaille et al. (2006), +1.31 for Robitaille (2017), and −0.21 for

Zhang & Tan (2018).

There are a few cases in which the $L_\star$ calculated from our SED model results was lower than L returned by our greybody fits (hereafter L_{grey}, to distinguish from $L_\star$). We believe that these cases can be explained by flux or confusion limitations during the aperture photometry procedure, which then lead to the SED models returning low $L_\star$ results. We identify three categories of SEDs which exhibit the $L_{grey} > L_\star$ discrepancy:

Confusion problems at 160 μm: The majority of $L_\star$−L_{grey} discrepancies occur in sources which suffer from angular confusion in the 160 μm Hi-GAL data (G12.91−0.03, G18.89−0.47, G22.04+0.22; see Figs. A.4, A.8, and A.10). In all cases, the measured 160 μm flux was unexpectedly high, not low. For these three sources, at least one and as many as all three SED modeling packages produced $L_\star < L_{grey}$. While we tried to account for the 160 μm confusion issue by significantly increasing the errors on the flux measurements for these sources, it is still possible that either a) the high 160 μm values or the large uncertainties on those values are leading to poor fits from the SED modeling packages, or b) the high 160 μm points lead to greybody fits that overestimate L_{grey}. Either cause (or possibly both) would result in $L_{grey} > L_\star$.

Poorly-constrained SEDs: All sources use flux measurements at eight or nine separate wavelengths in order to construct the SEDs. In most sources, three of these data points (IRAC bands) are always upper limits. However, in one source (G10.29−0.13), six of the nine flux measurements (67%) are upper limits, and the Zhang & Tan (2018) SED-derived $L_\star$ value is extremely low. We believe that this discrepancy can be explained by the very poor constraints on the MIR and NIR flux measurements, which makes it possible to fit a wide variety of models to the data (see Fig. A.1); it is therefore unsurprising that at least one of these models produces a very low $L_\star$.

Upper limits at 19 μm: There are four sources in our sample which are non-detections at 19 μm, and so use upper limits for the 19 μm flux instead of direct measurements. Of these four sources, two have additional issues (overall poor constrains on the SED, confusion problems at 160 μm) that have already been discussed. However, the remaining two sources have no additional issues with flux measurements, but do still have $L_\star < L_{grey}$ for at least one SED-derived $L_\star$. It is possible that, in these cases, the use of an upper limit at 19 μm is allowing the SED modeling packages to underestimate the true 19 μm fluxes, which then leads to spuriously low $L_\star$ values. See Figs. A.2 and A.6 for SEDs for these two sources.

Spread in Physical Parameters Returned by the Radiative-Transfer Models

Within our sample, the values of $R_\star$, $T_\star$, and $L_\star$ produced by a given model package typically span one order of magnitude. Exceptions are the $R_\star$ values produced by the Robitaille et al. (2006) models, which span two orders of magnitude across our 12 sources, and the $L_\star$ values from the Zhang & Tan (2018) models, which span four orders of magnitude. Conversely, when comparing the results of all three model packages for a given source, the $R_\star$ results typically span one order of magnitude, but can span two; the $T_\star$ results typically also span one order of magnitude. The $L_\star$ results are more consistent with each other: 75% of the $L_\star$ results from all three models agree to within a factor of 3. This result should not be overlooked − the models rarely converge for physical parameters that assume specific geometries (i.e. $R_\star$), but do converge to properties that can be extracted from SED shape alone (i.e. $L_\star$).

The different model packages will have difficulty converging to a single combination of $R_\star$ and $T_\star$ if the geometry of a single source is not one of those assumed by the models (e.g. multiple protostellar sources, accretion disk much more or less massive than the

range in the model grid, etc.). All three of these sets of models do fit only one protostar at a time − they assume only one source is contributing to the emission. However, recent research suggests that less-massive protostars may form in the accretion reservoirs of more massive companions (<0.2 pc separation), and in fact there is compelling evidence that this is the case for at least one of our sources (G11.92−0.61; see Cyganowski et al. 2017, and references therein). Furthermore, the nine different wavelengths used to create these SEDs probe different spatial scales due to the angular resolution of individual telescopes (e.g. $1.''66$ for *Spitzer* IRAC band I1 versus $19.''2$ for the ATLASGAL survey). This may also contribute to the scatter in $R_\star$ and $T_\star$ for individual sources if, for instance, the NIR and MIR fluxes are correctly attributed to only one protostellar source but the FIR fluxes are instead the blended fluxes of multiple adjacent sources in a clustered environment.

Finally, it is possible that the SED fits themselves are good but the fits to individual parameters poor because the assumption by the models of hierarchical structure (i.e. central source(s), disk, envelope, cavities) is true, but the assumption that all structures are present in a single source (i.e. the same individual protostar) is false. Possible scenarios in which this could occur are the case in which multiple cores are present within a single envelope, such as for a protobinary system, or IR-bright outflows due to multiple cores, even if only one core is visible in the MIR.

Trends by Model

The trends in $R_\star$, $T_\star$, and $L_\star$ suggest that the Robitaille et al. (2006) models favor cooler, larger - and hence younger - protostars to describe our data, while the Zhang & Tan (2018) models favor smaller, hotter protostars. The Robitaille (2017) $R_\star$ and $T_\star$ results typically fall between the two other model packages, but the resulting Stefan-Boltzmann luminosities agree fairly well with those of Robitaille et al. (2006). The Robitaille et al. (2006) models

tend to produce similar χ^2 values as the χ^2 of the best-fit Robitaille (2017) models, and produce χ^2 values that are lower than those of the Zhang & Tan (2018) models in all but two cases. The only notable trend in the Robitaille et al. (2006) models is a slight tendency to overestimate the 37.1 μm flux (see Figs. A.1 through A.12, Appendix A). This effect is sometimes also present in the Robitaille (2017) models, though to a lesser degree.

We found that the Robitaille (2017) models without bipolar cavities routinely gave very poor results, as expected (χ^2 values that are factors of $\sim$10 to 40 higher than the models with bipolar cavities).

Models s-pbsmi through spubhmi are shown Figures A.1 through A.12 in Appendix A; models spu-smi and s-u-smi are not shown, as in all cases they produced significantly poorer fits than any of the other six Robitaille (2017) model sets. Overall, the best-fit models (as determined by minimum χ^2 value) were always of the sets s-pbhmi, s-pbsmi, or spubhmi, in order of decreasing frequency. That is, the models overall favored no disk and a power-law envelope. For some sources, some model sets are clearly inappropriate, as they consistently underestimate long-wavelength emission or overestimate short-wavelength emission (e.g. model sets s-ubsmi and s-ubhmi for G14.33–0.64, Figure A.5; model sets s-ubsmi, s-ubhmi, spubsmi, spubhmi for G14.63–0.58, Figure A.6). However, in very few cases were there no Robitaille (2017) model sets that could reasonably fit our data.

In general, we find that the Zhang & Tan (2018) models fit some of the mid-IR fluxes fairly well, but consistently overestimate the 37 μm and 70 μm fluxes and underestimate the emission at 160 μm and 870 μm. The sources for which this is not the case are either very poorly constrained (G10.29) or contain known UC H II regions (G35.03). The Zhang & Tan (2018) models also have the highest χ^2 value in all but these two sources and, in these two sources, $\chi^2 < 1$, which indicates that those models may be overfit. In general,

the Zhang & Tan (2018) χ^2 values are an order of magnitude higher than at least one of the other two models; in nine of twelve sources, it is higher than both. Since the Zhang & Tan (2018) models do not include an ambient medium/emission from the parent clump, it is likely that this omission is leading the model to underestimate our measured emission at long wavelengths, and to produce higher χ^2 values. The cause of the overestimation in the MIR is currently unclear, though this trend is also present to some degree in the other two model packages as well. Combined with the underestimation of the FIR emission, this MIR overestimation creates a trend wherein the Zhang & Tan (2018) models in general seem to be pushed toward SEDs with peaks at slightly shorter wavelengths than our data exhibit; this may indicate that the Zhang & Tan (2018) models tend to produce better results for slightly older or less deeply-embedded sources.

De Buizer et al. (2017) tested the Zhang & Tan (2018) models against data from their SOFIA Massive Star Formation Survey (SOMA), and compared their results to results from the Robitaille et al. (2006) models. In general, the Zhang & Tan (2018) models produced good results for their sample, and they do not note a systematic underestimation of long-wavelength emission from these models. However, the SOMA survey identifies four source types, and De Buizer et al. (2017) examines only their Type II ("Hypercompact") sources. De Buizer et al. (2017) state that these sources often have jet-like radio emission, and MIR emission that extends beyond the radio emission. While the second criterion applies to our sample, the first does not. The characteristics of our sources are a better match to their Type I ("MIR Sources in IRDCs," which is a quality nearly all of our sources share) or their Type IV ("Clustered Sources," which recent work (e.g. Cyganowski et al. 2017) shows is the case for at least one source in our sample, and likely more). De Buizer et al. (2017) note that there is a rough evolutionary sequence from Type I to Type III sources. If this sequence is accurate, and our sources are more similar to their Type I sources, then our sample would

be slightly younger than that evaluated in De Buizer et al. (2017). In this case, the MIR-emitting sources are indeed likely to be cooler and/or more deeply embedded than those in the SOMA Type II sample, and this would at least partially explain the discrepancy between the model results for our sample (i.e. consistent underestimation of FIR emission) and theirs.

2.5.4 Do the Robitaille (2017) Model Sets Tell Us Something About Source Structure?

The Robitaille (2017) model sets are the only models evaluated in this work which explicitly allow the user to test multiple different source geometries. We briefly evaluate the overall trends in the geometries of the best-fit model sets for our sources in order assess what, if anything, the Robitaille (2017) models are telling us about the structure of the protostellar sources in our sample. Model results for each individual source can be found in Appendix B, along with a discussion of how the method of evaluating which is the "best" fit affects these trends.

G10.29–0.13 is excluded from this discussion of general trends, as its SED is very poorly constrained. For the remaining 11 sources, the Robitaille (2017) model package frequently returns best-fit models which have power-law envelopes and no disks, and do not favor either the presence or absence of an inner hole. However, among model sets specifically with no disk and with a power-law envelope, there is a clear preference (64% to 36%, or 7 to 4) for models with an inner hole. That is, a power-law envelope favors a larger distance between the inner edge of the envelope and the stellar surface. Among models with no disk and an Ulrich envelope, this trend is exactly reversed, with 64% of models (7 out of 11) preferring no inner hole and only 36% (4 out of 11) having one; in this case, the addition of rotation seems to favor a smaller distance between the envelope

inner radius and the stellar surface. It should also be noted that only three of our eight model sets contain a disk (spubhmi, spubsmi, spu-smi), and one of these (spu-smi) was expected to generally give poor fits to our data anyway due to its lack of bipolar cavities. It is possible that the bias against disks may be due, at least in part, to the relative dearth of individual model sets with disks compared to those without. Of the eighteen model sets available to us, we chose to run the six models with bipolar cavities and to "control" models. Two of the six model sets with bipolar cavities have disks, while four do not − this 2-to-1 ratio is simply a feature of the model sets available to us. However, this ratio may give an unphysical "advantage" to the disk-lacking models in the evaluation of model-set statistics.

The lack of disks in the favored models is inconsistent with our more detailed knowledge of particular sources, such as G11.92−0.61 (Ilee et al. 2016, 2018) and G16.59−0.05 (Moscadelli et al. 2016; Rosero et al. 2016), as well as our more general knowledge of these sources based on their additional attributes (e.g. shocked H_2 emission (Cyganowski et al. 2008), both Class I and Class II CH_3OH masers (Cyganowski et al. 2009), etc.). For most sources, the Robitaille (2017) models with disks do not appear (visually) to be significantly different in the mid-infrared ($\sim$10 to 40 μm; see Figures A.1 through A.12) from models without them. This region of the SED is frequently dominated by hot dust emission from the outflow cavity and heated portions of the envelope. A disk that is small relative to the mass of the protostar, or highly extincted by embedding material, might manifest its presence less strongly in the mid-infrared portion of the SED, in which case SED modeling would not need to invoke a disk in order to reproduce the given data.

2.5.5 L/M and Evolutionary State

Figure 2.6 shows the luminosity-to-mass ratio L/M versus mass M for each source using each of the four derived luminosities. For both L/M and M, M is the average of the NH_3-derived and greybody-derived masses for each source. The errors on L/M are determined from the error propagation equation and the errors on L and M, respectively. The uncertainty on each L value, σ_L, is the median absolute deviation from the median (MAD) of the luminosities of all fits with χ^2 within a factor of 3 of the best-fit χ^2 value. The uncertainty on each M value, σ_M, is calculated from the uncertainties on both the greybody-derived and NH_3-derived temperatures, the 870 μm flux $F_{870\mu m}$, and distance, D, using the error propagation equation. Uncertainties in temperature are reported in Table 2.8, and uncertainties in $F_{870\mu m}$ are reported in Table 2.7. Distance uncertainties for parallax-derived distances are from Reid et al. (2014). To estimate a distance uncertainty for the EGOs that only have kinematic distances, we assessed the percent difference between the predicted kinematic distance and the parallax distance for the five sources for which both are available, and found a median percent difference of 15%.

The median L/M for our sources is 24.7 $\pm$ 8.4 $L_\odot/M_\odot$, where the uncertainty is the MAD and the L/M for each source is the median of the four values shown in Figure 2.6. Most L/M values fall in the range $5 - 60$ $L_\odot/M_\odot$, regardless of the method of deriving the luminosity. This result is in line with the results of Carpenter et al. (1990), who studied a set of 21 molecular clouds in the Outer Milky Way whose masses, luminosities, and suspected evolutionary state are comparable to our sample. They report an L/M range of $1.1 - 39.2$ $L_\odot/M_\odot$ (mean 6.8 $L_\odot/M_\odot$). Typical L/M values for low- and intermediate-mass protostars, in contrast, usually span $\sim 0.1 - 10$ $L_\odot/M_\odot$ (see, e.g., L and M values in Enoch et al. 2009).

For most of our sources, the four L/M values we derive span a range of a factor of ~ 2.5, likely due to differences in the four different methods of deriving luminosity. The excep-

tions are G10.29−0.13 and G35.03+0.35, which span ranges of a factor of ∼100 and ∼3, respectively. The spread in L/M for G10.29−0.13 is likely due to poorly-constrained SEDs, as has been previously discussed. G35.03+0.35 is discussed in the context of evolutionary stage in greater detail below.

The only notable trend in our L/M values is the tendency of the Zhang & Tan (2018) models to give L/M values that are either higher than all three other methods, or lower than all three, but never in between. In particular, the Zhang & Tan (2018) results tend to produce lower L/M only when the value is very low ($< 20\ L_\odot/M_\odot$); otherwise, the Zhang & Tan (2018) L/M is higher than both the two Robitaille- and the greybody-derived L/M values. This dichotomy is entirely consistent with the trend in Stefan-Boltzmann luminosities for the Zhang & Tan (2018) results noted in § 2.5.3. We do not note any particular trend in L/M with mass, though it should be noted that the mass range of our sample is small compared to that of other teams (Urquhart et al. 2018; Elia et al. 2017).

A comparison of our results with the results of other teams shows that our L/M are well in line with established values for MYSOs. Both Urquhart et al. (2018) and Elia et al. (2017) compare L and M values for pre- and protostellar clumps. In both samples, massive star-forming regions are distinguished from prestellar sources by the space they occupy in $L-M$ parameter space. Urquhart et al. (2018) note that the L/M values of massive star-forming clumps (as distinct from less massive or prestellar objects) are well-described by lower and upper limits of 1 and 100, respectively. Most L/M in our sample fall in the range 5−60 $L_\odot/M_\odot$ (see Figure 2.6), which is well in line with the star-forming samples of both Urquhart et al. (2018) and Elia et al. (2017). Urquhart et al. (2018) further note that compact H II regions become common in their sample at $L/M > 40$. The median L/M for our sample is ∼25, with a few $L > 40$ from SED fit results. We have only one source which has $L > 40$ for all four luminosities, G35.03+0.35, and this source does have a known UC

H II region within the extended 4.5 μm emission of the EGO.

Similarly, Tigé et al. (2017) examine 46 high-mass pre- and protostellar cores in NGC 6334 as part of the *Hershel*-HOBYS program. They separate their massive dense cores (MDCs) into three categories: IR-bright MDCs, IR-quiet MDCs, and Starless MDC Candidates. To distinguish IR-bright and IR-quiet sources, they use flux limits of 10, 12, and 15 Jy at 21, 22, and 24 μm, respectively. Sources with fluxes above these limits are considered IR-bright, and sources with fluxes below these limits are IR-quiet. The F values are based on the predicted mid-IR emission of a B3-type protostar and calculated for a distance of 1.75 kpc, which is the distance to NGC6334 assumed by Tigé et al. (2017). These values are consistent with the weak-to-bright cutoff used by König et al. (2017) when scaled to 4 kpc (see § 2.8). Tigé et al. (2017) determine their source masses by fitting source SEDs from 70 to 1200 μm using data from *Herschel*, JCMT, APEX, and SEST. In cases of no significant mid-IR emission, Tigé et al. (2017) determine bolometric luminosity by performing greybody fits to the far-IR data, similar to the process we use for our own data (see § 4.1). In cases of significant mid-IR emission, they determine bolometric luminosity by integrating directly under the observed flux values. In this case, they use the data sets described above as well as data from 3.6 to 24 μm from *Spitzer*, MSX, and WISE. Tigé et al. (2017) at all times assume optically thin emission at $\lambda > 100$ μm and use $\beta = 2$.

When we compare our sources with the Tigé et al. (2017) subsamples, an interesting feature emerges. Our median L/M when L is the greybody luminosity is 19.4 ± 7.3 $L_\odot/M_\odot$, and the median L/M when L is the median of all four luminosities is 24.7 ± 8.4 $L_\odot/M_\odot$. Compare this to the median L/M of the IR-quiet and IR-bright cores in the Tigé et al. (2017) sample (3.1 ± 2.8 $L_\odot/M_\odot$ and 70 ± 28 $L_\odot/M_\odot$, respectively, where these medians are calculated from the $L_\star$ and $M_\star$ listed in Tigé et al. (2017), Table 3). The median L/M of our sample falls neatly between the median L/M of the IR-quiet and IR-bright populations

in Tigé et al. (2017), whether we use L from only the greybody fit or the median of all four L-values. Even with uncertainties, our sources are still well-separated from either category. While there are some differences between our methods of deriving L/M and those of Tigé et al. (2017), these are unlikely to significantly change this result. Recalculating our L and M values using $\beta = 2$ (the value used by Tigé et al. (2017)) instead of $\beta = 1.7$ only increases our median L/M by 7.3%. This finding is consistent with Tigé et al. (2017), who calculate that using $\beta = 1.5$ instead of $\beta = 2$ would only alter their calculated masses by 5−10%.

Tigé et al. (2017) suggest that IR-quiet MDCs are precursors to IR-bright MDCs; once IR-quiet cores have accreted enough mass to produce a stellar embryo with M > 8 $M_\odot$, their luminosity sharply increases and they become IR-bright. (See Motte et al. (2018a) for a review of the theory and current observational support for this scenario.) This transition corresponds to the swelling phase of Hosokawa & Omukai (2009), in which a massive protostar rapidly expands after reaching $M \sim 6\ M_\odot$. The rapid expansion is driven by the sudden escape of significant entropy from the interior of the star, which can only occur after the opacity is sufficiently decreased by increasing temperature. The swelling phase is comparatively brief and lasts only until $M \sim 10\ M_\odot$, and is immediately followed by a Kelvin-Helmholtz contraction phase in which the protostellar radius decreases again. Given that our median L/M fall between the values for the well-established "IR-quiet" and "IR-bright" categories of massive protostellar objects, it is possible that our EGO-12 sample represents a transitional stage between the IR-quiet and IR-bright phases of evolution, i.e., a phase in which an accreting protostar reaches some critical (large) mass, undergoes a concrete physical change, and consequently increases sharply in luminosity. Given the lack of predicted observable properties for this swelling/growth phase other than an increase in luminosity, we are hesitant to suggest that this is definitively the state in which our sources exist. However, the possibility is intriguing and suggests an interesting avenue for further

investigation.

If L/M is indeed a reliable indicator of evolutionary state, as asserted by other teams, then it should be unsurprising both that a) the majority of our sample, which were specifically selected due to their *uniformity* of evolutionary state, all exhibit very similar L/M values, and b) that G35.03+0.35, which compared to the majority of the sample is in a very late stage of evolution, has a significantly higher L/M. Such a possibility − that EGOs in particular represent the stage of MYSO evolution immediately prior to the emergence of strong mid-infrared emission and subsequent H II regions − warrants further investigation in future work.

2.6   Conclusions & Future Work

We have conducted a multiwavelength study of twelve typical massive protoclusters in the Milky Way using SOFIA FORCAST imaging and archival infrared data. We performed aperture photometry at each wavelength in order to construct SEDs from the near-IR (3.6 μm) to sub-mm (870 μm), which we then fit with one greybody and three radiative transfer models. The radiative transfer models (Robitaille et al. 2006; Robitaille 2017; Zhang & Tan 2018) all model near-IR to sub-millimeter emission in the context of a single protostar.

The SOFIA images, in conjunction with archival data, suggest that the number of massive sources per EGO is between 0.9 and 1.9. This moderate MYSO multiplicity is in line with published values for similar samples (Rosero et al. 2019) and for G11.92−0.61 (Cyganowski et al. 2017; Ilee et al. 2018). The multiplicity of these sources cannot be further constrained without sub-arcsecond resolution images, in either the mid-infrared or radio regimes. Cyganowski et al. (2017) do detect a plethora of lower-mass sources in G11.92−0.61, none of which are indicated in the SOFIA images; this is consistent with

both our angular resolution limitations and with the luminosity sensitivity limit of 1.1×10^3 that we calculate in § 2.5.3, which indicates these SOFIA observations will not be sensitive to lower-mass, lower-luminosity YSOs.

We find that, for this sample, the temperatures derived from greybody fits to dust emission are quite similar to the temperatures derived from single-component fits to NH_3 (1,1) to (3,3) emission (Cyganowski et al. 2013), with the dust temperatures trending slightly higher than the NH_3 temperatures. While these differences fall below a level of statistical significance, this trend is in line with the published results of other teams (Giannetti et al. 2017; König et al. 2017) which find that, at temperatures above $\sim$15 K, NH_3 emission tends to probe gas that is slightly cooler than the local dust. We find that the median T_{dust} of the EGO-12 sample is consistent with the median T_{dust} of the Top100 sample (König et al. 2017), and most closely aligned with either the "IR-weak" or "IR-bright" subcategories. The overlap between the EGO T_{dust} range and both the IR-weak and IR-bright T_{dust} ranges suggests that EGO-12 sample may represent the cooler end of the IR-bright population, or possibly a separate, intermediate population between the IR-weak and IR-bright subcategories. High-precision temperature measurements over a much larger EGO sample are needed in order to address both possibilities.

The L we derive from the greybody fits agree within 20−50% of other published L for these sources (Moscadelli et al. 2016; Urquhart et al. 2018). We find that the greybody-derived L of Urquhart et al. (2018) are greater than our greybody-derived luminosities in all cases. This is consistent with the fact that our greybody fits assume a single (cold) component, while Urquhart et al. (2018) use both a cold (greybody) and hot (blackbody) component for at least eleven of our sources. The Stefan-Boltzmann luminosities ($L_\star$), which we calculate from the $R_\star$ and $T_\star$ returned by the radiative transfer models and which do account for hot-component emission, are typically of order 2$\times$ higher that the luminosi-

ties returned by our greybody fits. They are also more in line (within $\sim$30% rather than 50%) with the luminosities of (Urquhart et al. 2018).

We find that the individual $R_\star$ and $T_\star$ returned by the three radiative transfer packages vary widely both within and between packages (one order of magnitude in $T_\star$ and up to two in $R_\star$ for both cases). This suggests that the models are having trouble converging to a single set of protostellar parameters, and that perhaps none of the model packages are fitting the sources uniquely well. This result is consistent with the fact that, although we assumed a single dominant source for modeling purposes, these sources are actually protoclusters rather than isolated protostars. Objects of different evolutionary states may be contributing to the total emission even if they are too embedded or too clustered to be detected individually in our SOFIA images. This possibility is further supported by the detection of multiple mid-infrared SOFIA sources within the ATLASGAL emission for most of our targets.

The specific cases of G11.92−0.61, G16.59−0.05, and G35.03+0.35 − for which high-resolution, high-sensitivity (sub)millimeter and/or radio-wavelength data are available − highlights the limitations of such (comparatively) low-resolution photometry when applied to clustered sources. In particular, it strongly suggests that SED model results should not be used to identify or describe the properties of disk candidates in high-mass protostars as is commonly done for isolated low-mass protostars (e.g. Spezzi et al. 2013), or should only be used with extreme caution or in cases where the isolation of the high-mass protostar can be positively confirmed. For clustered sources, lower-resolution infrared data can be a powerful tool for describing global properties of each protocluster and testing the multiplicity of massive sources, but results from models assuming individual protostellar sources should be used with caution.

The L/M values of our sample are well in line with L/M values measured by other

teams (Carpenter et al. 1990), but fall between the two distinct IR-quiet and IR-bright categories suggested in Tigé et al. (2017). Given that the evolutionary stage in which our objects exist - MYSO outflows being powered by active protostellar accretion - is thought to be short-lived, it is possible that our sample represents the transitional stage between the IR-quiet and IR-bright phases of evolution. While intriguing, this possibility requires further investigation before any definitive statements can be made.

If L/M is indeed indicative of evolutionary stage, then it likely correlates with other source properties such as outflow momentum, millimeter luminosity (e.g. as observed by ALMA, SMA, etc.), or the presence and nature of radio continuum emission. In order to assess the existence and strength of such correlations, additional centimeter-millimeter wavelength observations are needed. We have recently obtained or are in the process of obtaining ALMA 1.3 and 3.2 mm and JVLA 1.3 and 5 cm line and continuum observations for this purpose. These observations, and their correlation (or lack thereof) with the infrared and sub-mm results of this paper, will be presented in future publications.

2.7   Acknowledgements

Software `sedfitter`, (Robitaille et al. 2006); `sedfitter`, (Robitaille 2017); `sedfit`, (Zhang & Tan 2018); APLpy, (Robitaille & Bressert 2012), http://aplpy.github.com.
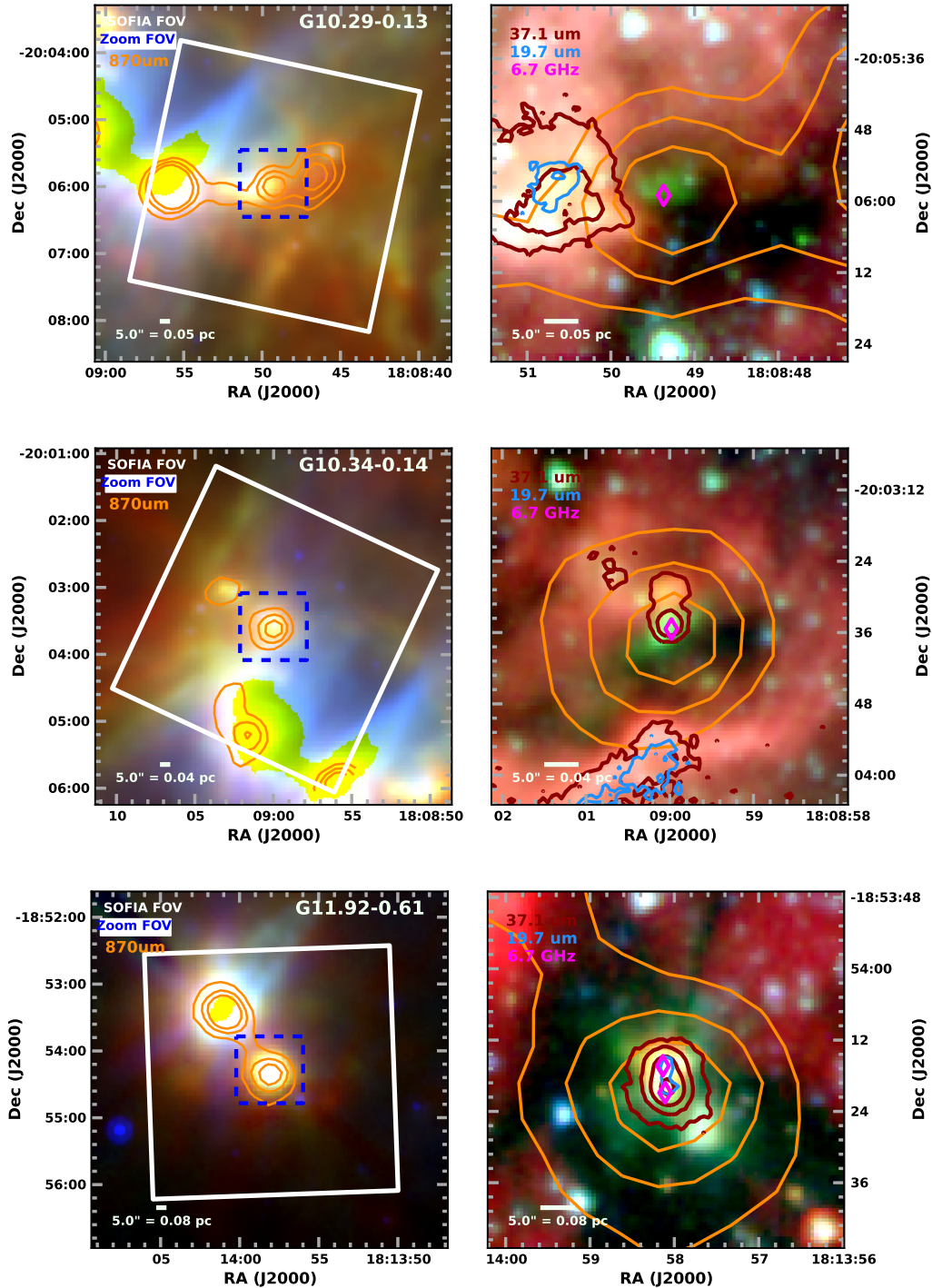
Fig. 2.1.— RGB images for EGO sources. The left panel for each source shows the 160 μm, 70 μm, and 24 μm wavelengths mapped to R, G, and B, respectively, with 870 μm contours overlaid in magenta. The ATLASGAL contour levels are [0.25, 0.5, 0.75]$\times$I$_{max}$, where I_{max} is the peak intensity value of the ATLASGAL data in each FOV. The solid white boxes show the size and approximate orientation of the SOFIA FOV, and the dashed blue boxes show the size and position of the FOV of the zoomed images, shown in the right-hand panels. The right-hand panels show the 8.0 μm, 4.5 μm, and 3.6 μm wavelengths mapped to R, G, and B, respectively; the extended green emission shows the extent of each EGO. SOFIA FORCAST 19.7 μm and 37.1 μm contours are overlaid in blue and red, respectively, and the positions of known 6.7 GHz Class II CH$_3$OH masers are denoted by magenta diamonds. SOFIA contour levels are [5,15,45,125,250]$\times\sigma$ for 37.1 μm, and [4,8,16,28]$\times\sigma$ for 19.7 μm, where σ is the scaled MAD. The I_{max} values for G10.29−0.13, G10.34−0.14, and G11.92−0.61 are 3.31 Jy beam^{-1}, 4.39 Jy beam^{-1}, and 4.01 Jy beam^{-1}, respectively.
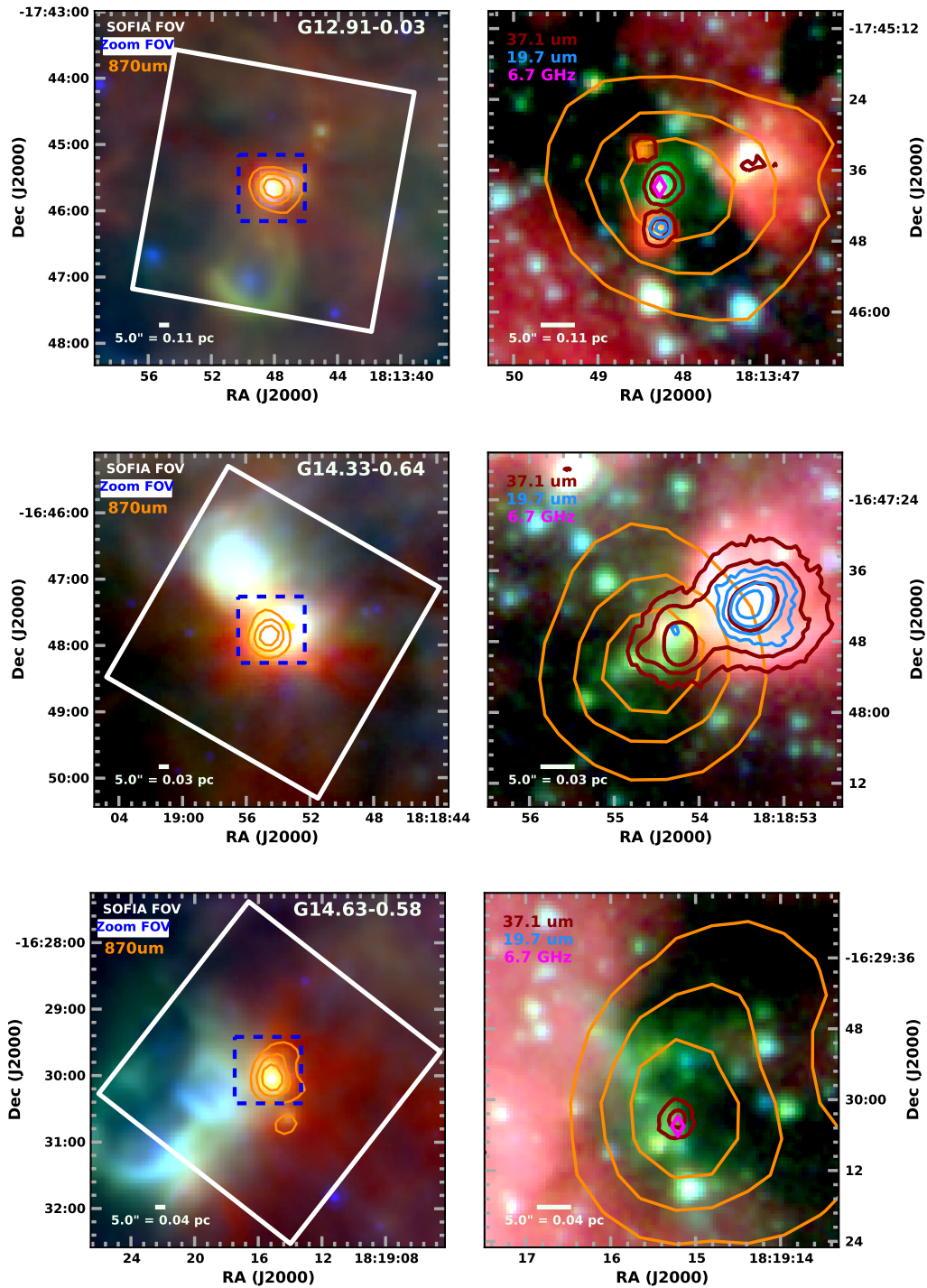
Fig. 2.2.— RGB images for EGO sources. See Figure 2.1 for key. The I_{max} values for G12.91−0.03, G14.33−0.64, and G14.63−0.58 are 2.78 Jy beam^{-1}, 12.98 Jy beam^{-1}, and 4.35 Jy beam^{-1}, respectively.
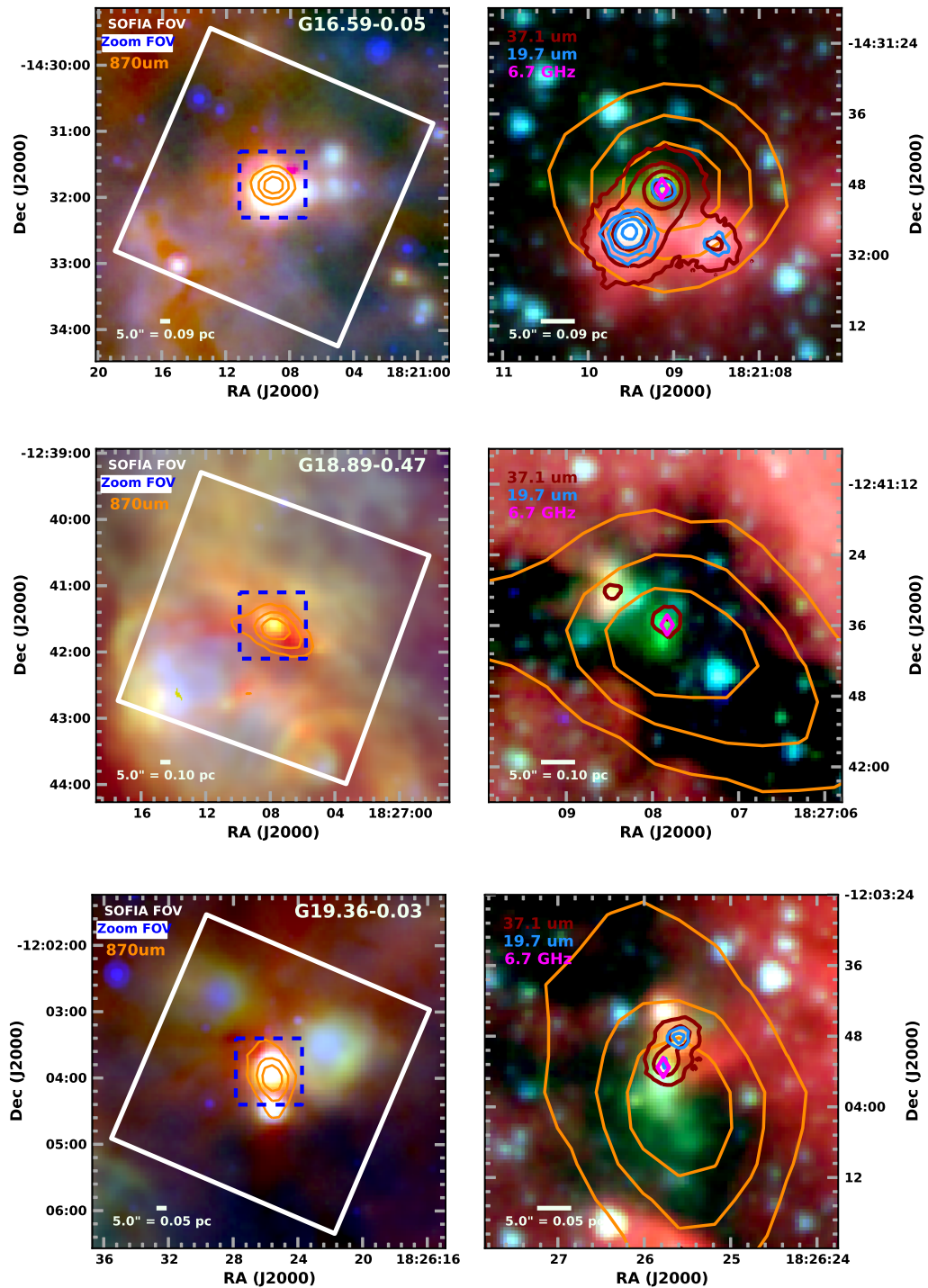
Fig. 2.3.— RGB images for EGO sources. See Figure 2.1 for key. The I_{max} values for G16.59–0.05, G18.89–0.47, and G19.36–0.03 are 5.13 Jy beam^{-1}, 3.30 Jy beam^{-1}, and 2.90 Jy beam^{-1}, respectively.
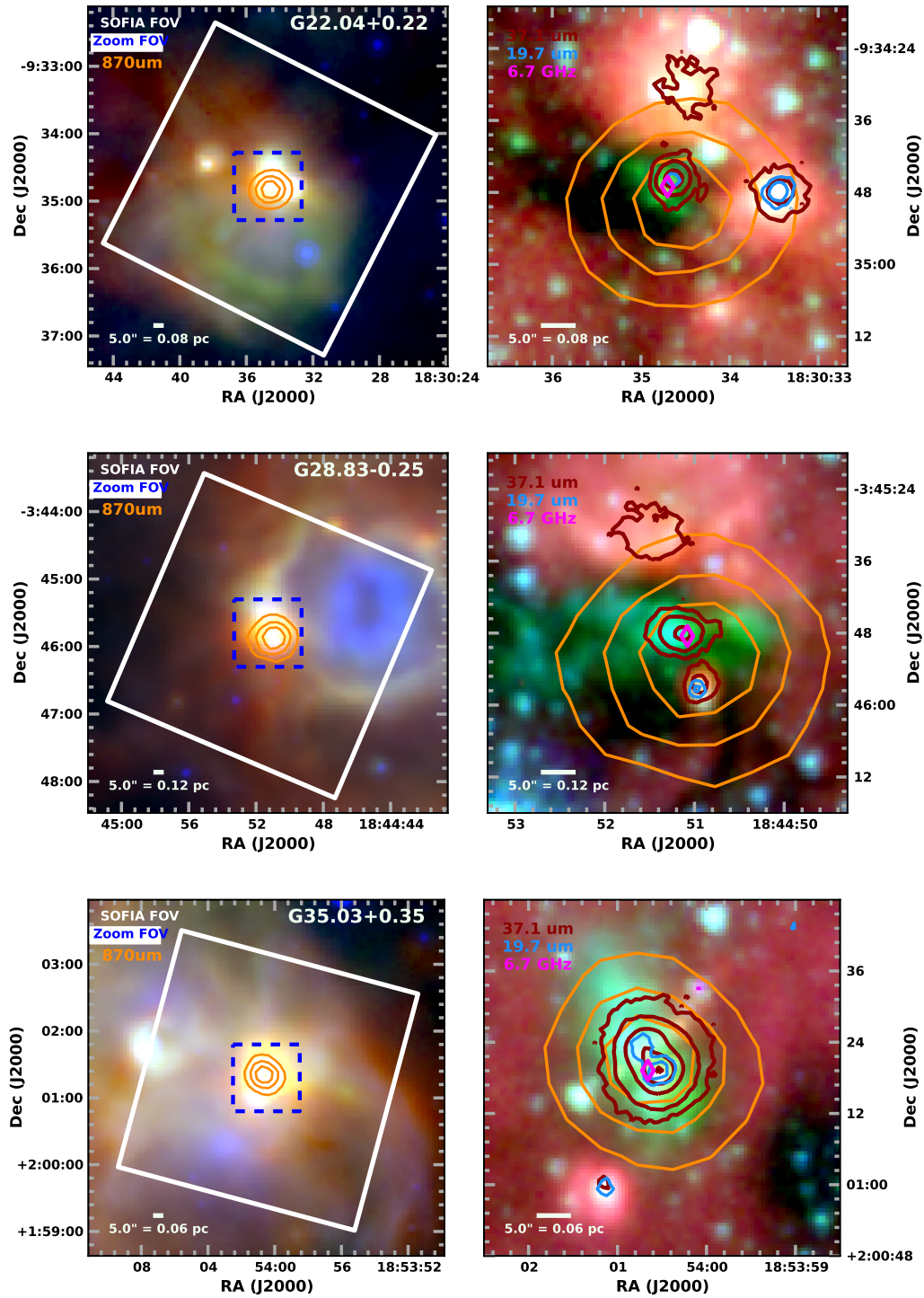
Fig. 2.4.— RGB images for EGO sources. See Figure 2.1 for key. The I_{max} values for G22.04+0.22, G28.83−0.25, and G35.03+0.35 are 3.33 Jy beam^{-1}, 4.08 Jy beam^{-1}, and 4.91 Jy beam^{-1}, respectively.

Table 2.5. MIPS 24 μm Standard Star Fitted and Catalog Fluxes, & Flux Ratios

Star[a]	Coordinates (J2000)[b]		Catalog Flux	Fitted Flux	Flux Ratio
	RA (h m s)	Dec (° ′ ″)	(mJy)	(mJy)	
1	18:30:32.40	-09:35:47.25	1950 (39)	1220 (40)	1.60
2	18:30:12.78	-09:36:47.99	1980 (36)	1250 (38)	1.58
3	18:30:53.95	-09:39:51.27	2960 (55)	1870 (71)	1.58
4	18:30:46.32	-09:32:28.89	1230 (23)	770 (23)	1.60
5	18:30:48.45	-09:36:00.11	780 (14)	490 (17)	1.59

[a]Coordinates and both fitted (this work) and catalog (Gutermuth & Heyer 2015) flux densities for five bright, isolated point sources in the MIPSGAL Point Source Catalog.

[b]Listed coordinates are from the MIPS Point Source Catalog (Gutermuth & Heyer 2015).

Table 2.6.   MIPS 24 μm Aperture-Corrected Fitted Flux Densities

| EGO | Source | Coordinates (J2000)[a] | | Fitted Flux[b] | Aperture-Corrected[c] |
		RA (h m s)	Dec (° ′ ″)	Density (Jy)	Fitted Flux (Jy)
G10.29–0.13	a	$\cdots$	$\cdots$	$\cdots$	<0.28
G10.34–0.14	a	18:08:59.989 (0.004)	-20:03:34.97 (0.06)	0.77 (0.03)	1.23 (0.08)
	b	18:09:00.017 (0.003)	-20:03:28.75 (0.05)	1.51 (0.04)	2.4 (0.1)
G11.92–0.61	a	18:13:58.065 *(0.001)*	-18:54:21.26 *(0.01)*	2.484 (0.003)	4.0 (0.2)
	b	18:13:58.122 *(0.001)*	-18:54:14.97 *(0.01)*	2.262 (0.003)	3.6 (0.2)
G12.91–0.03	a	18:13:48.233 (0.002)	-17:45:38.19 (0.03)	1.11 (0.02)	1.77 (0.09)
	b	18:13:48.283 (0.001)	-17:45:46.21 (0.01)	1.50 (0.01)	2.4 (0.1)
	c	18:13:48.469 (0.004)	-17:45:31.77 (0.04)	0.28 (0.01)	0.45 (0.03)
G14.33–0.64	a	$\cdots$	$\cdots$	confused	$\cdots$
	b	$\cdots$	$\cdots$	saturated	$\cdots$
	c	$\cdots$	$\cdots$	confused	$\cdots$
G14.63–0.58	a	18:19:15.221 (0.001)	-16:30:03.26 (0.02)	0.683 (0.009)	1.09 (0.06)
G16.59–0.05	a	$\cdots$	$\cdots$	saturated	$\cdots$
	b	$\cdots$	$\cdots$	saturated	$\cdots$
	c	$\cdots$	$\cdots$	confused	$\cdots$
G18.89–0.47	a	18:27:07.82 (0.01)	-12:41:35.1 (0.2)	0.34 (0.04)	0.54 (0.07)
	b	18:27:08.45 (0.01)	-12:41:29.5 (0.2)	0.64 (0.07)	1.0 (0.1)
G19.36–0.03	a	18:26:25.782 *(0.001)*	-12:03:53.73 *(0.01)*	2.356 (0.005)	3.8 (0.2)
	b	18:26:25.569 *(0.001)*	-12:03:48.13 *(0.01)*	3.371 (0.006)	5.4 (0.3)
G22.04+0.22	a	18:30:34.627 (0.001)	-09:34:46.24 (0.02)	2.23 (0.02)	3.6 (0.2)
	b	18:30:33.432 *(0.001)*	-09:34:48.39 *(0.01)*	2.79 (0.02)	4.4 (0.2)
G28.83–0.25	a	18:44:51.136 (0.001)	-03:45:47.845 (0.009)	2.230 (0.008)	3.6 (0.2)
	b	18:44:50.931 (0.001)	-03:45:56.506 (0.009)	2.362 (0.008)	3.8 (0.2)
G35.03+0.35	a	$\cdots$	$\cdots$	saturated	$\cdots$
	b	$\cdots$	$\cdots$	saturated	$\cdots$

[a]Source coordinates are the fitted coordinates returned by `imfit`. Sources that have $\cdots$ values in place of coordinate values are either undetected at 24 μm (G10.29–0.13) or suffer from saturation and/or confusion (G14.33–0.64, G16.59–0.05, G35.03+0.35). Sources with position uncertainties in italics (G11.92–0.61, G19.36–0.03, G22.04+0.22_b) had their coordinates held fixed during the fitting procedure, so the position uncertainties come not from the `imfit` results but from the uncertainty in the choice of source position (usually of order 0.01 pixels, or, 0.″0125).

[b]These are the fitted fluxes directly returned by `imfit`; they have not been corrected for aperture effects. Sources with " $\cdots$ " are nondetections at 24 μm. Sources listed as "saturated" are saturated at 24 μm. Sources listed as "confused" are not saturated at 24 μm but suffer from an angular confusion problem, usually with a nearby saturated source.

[c]These are the aperture-corrected fitted flux densities, where the applied aperture correction is 1.59 ± 0.00893, as calculated in Table 2.5. We use the data in this column for constructing our SEDs. Sources listed as " $\cdots$ " could not be fit at 24 μm due to saturation and/or confusion issues and thus have no fitted flux value to which to apply an aperture correction.

Table 2.7.   Hi-GAL 70 μm & 160 μm and ATLASGAL 870 μm Flux Densities

EGO	Source	Hi-GAL[a] 70 μm Notes	70 μm Flux[b] (Jy)	160 μm Flux[b] (Jy)	870 μm Flux (Jy)
G10.29–0.13	a	$\cdots$	75 (6)	298 (30)	5.0 (0.8)
G10.34–0.14	a	$\cdots$	280 (20)	590 (49)	6 (1)
	b	assuming all emission from a	$\cdots$	$\cdots$	$\cdots$
G11.92–0.61	a	$\cdots$	640 (33)	980 (58)	11 (2)
	b	assuming all emission from a	$\cdots$	$\cdots$	$\cdots$
G12.91–0.03	a	$\cdots$	96 (6)	**270 (52)**	7 (1)
	b	assuming all emission from a	$\cdots$	$\cdots$	$\cdots$
	c	assuming all emission from a	$\cdots$	$\cdots$	$\cdots$
G14.33–0.64	a	$\cdots$	**1130 (190)**	1940 (120)	32 (4)
	b	assuming all emission from a	$\cdots$	$\cdots$	$\cdots$
	c	assuming all emission from a	$\cdots$	$\cdots$	$\cdots$
G14.63–0.58	a	$\cdots$	130 (8)	390 (30)	15 (2)
G16.59–0.05	a	$\cdots$	490 (26)	740 (48)	9 (1)
	b	assuming all emission from a	$\cdots$	$\cdots$	$\cdots$
	c	assuming all emission from a	$\cdots$	$\cdots$	$\cdots$
G18.89–0.47	a	sources a and b fit with `imfit`	48 (2)	**180 (27)**	10 (2)
	b	sources a and b fit with `imfit`	19.6 (0.2)	$\cdots$	$\cdots$
G19.36–0.03	a	$\cdots$	250 (14)	470 (41)	8 (1)
	b	assuming all emission from a	$\cdots$	$\cdots$	$\cdots$
G22.04+0.22	a	sources a and b fit with `imfit`	204 (10)	**400 (94)**	5.9 (0.8)
	b	sources a and b fit with `imfit`	59 (3)	$\cdots$	$\cdots$
G28.83–0.25	a	$\cdots$	**510 (65)**	870 (60)	10 (1)
	b	assuming all emission from a	$\cdots$	$\cdots$	$\cdots$
G35.03+0.35	a	$\cdots$	1350 (71)	1230 (84)	8 (1)
	b	assuming all emission from a	$\cdots$	$\cdots$	$\cdots$

[a]This column addresses the confusion of our sources at the 70 μm wavelength and angular resolution. Sources with the note "assuming all emission from a" do have 70 μm emission coincident with the position of source b and/or c, but we assume the emission to be entirely from or significantly dominated by source a. Sources with the note "sources a and b fit with `imfit`" have emission coincident with both source a and source b, and there were two emission regions sufficiently distinguishable at 70 μm to be fit with the `imfit` tool. These notes only apply to the 70 μm data.

[b]The sources in **bold** in these two columns suffer from confusion at either 70 or 160 μm, and were not sufficiently well-separated to be successfully fit with two components `imfit`. In these cases, the uncertainties of the flux densities are increased to reflect this effect. The precise method by which the uncertainties account for the confusion issue is discussed in detail in-text in § 2.4.2.

Table 2.8.   Temperature & Mass From Greybody Fits and Single-dish NH_3 Observations

| EGO | Distance[a] (kpc) | Temperatures (K) | | Masses ($M_\odot$) | | L_{FIR}^b ($10^3\ L_\odot$) |
		T_{dust}^c	T_{NH_3}	Greybody	NH_3-derived[d]	
G10.29–0.13	1.9	24 (1)	21.19 (0.17)	76	91	0.90
G10.34–0.14	1.6	26 (1)	28.23 (0.38)	62	56	1.42
G11.92–0.61	$3.38^{+0.33}_{-0.27}$ (3.5)	27 (1)	26.27 (0.19)	450	466	12.76
G12.91–0.03	4.5	23 (1)	23.56 (0.31)	649	627	5.49
G14.33–0.64	$1.13^{+0.14}_{-0.11}$ (2.3)	29 (2)	25.26 (0.17)	132	159	2.84
G14.63–0.58	$1.83^{+0.08}_{-0.07}$ (1.9)	22 (1)	20.76 (0.32)	234	254	1.31
G16.59–0.05	$3.58^{+0.32}_{-0.27}$ (4.2)	26 (1)	20.51 (0.38)	456	636	10.57
G18.89–0.47	4.2	22 (1)	28.24 (0.19)	879	625	3.04
G19.36–0.03	2.2	26 (1)	24.90 (0.31)	147	155	2.61
G22.04+0.22	3.4	26 (1)	26.71 (0.49)	257	248	4.90
G28.83–0.25	4.8	26 (1)	28.27 (0.50)	851	761	20.62
G35.03+0.35	$2.32^{+0.24}_{-0.20}$ (3.2)	33 (1)	29.54 (0.92)	119	138	9.98

[a]Distances shown without uncertainties are estimated from the LSRK velocity and the Galactic rotation curve parameters from Reid et al. (2014). Parallax distances (with their uncertainties) are given where available from Reid et al. (2014), and references therein, with the kinematic distance in parentheses for comparison. All kinematic distances are the near distance.

[b]Returned by the greybody fits to Hi-GAL 70 μm & 160 μm and ATLASGAL 870μm integrated flux densities.

[c]The T_{dust} was derived from greybody fits using a grid of parameters, in which temperature goes in steps of 1 K. Therefore, the uncertainties for all greybody-derived temperatures are 1 K, except for G14.33–0.64, which had three adjacent temperatures with the same χ^2 value. Here we present the median of those three temperatures, and increase the uncertainty for this source to 2 K.

[d]These are the masses calculated from the ATLASGAL 870 μm fluxes assuming $T_{dust} = T_{kin}(NH_3)$.
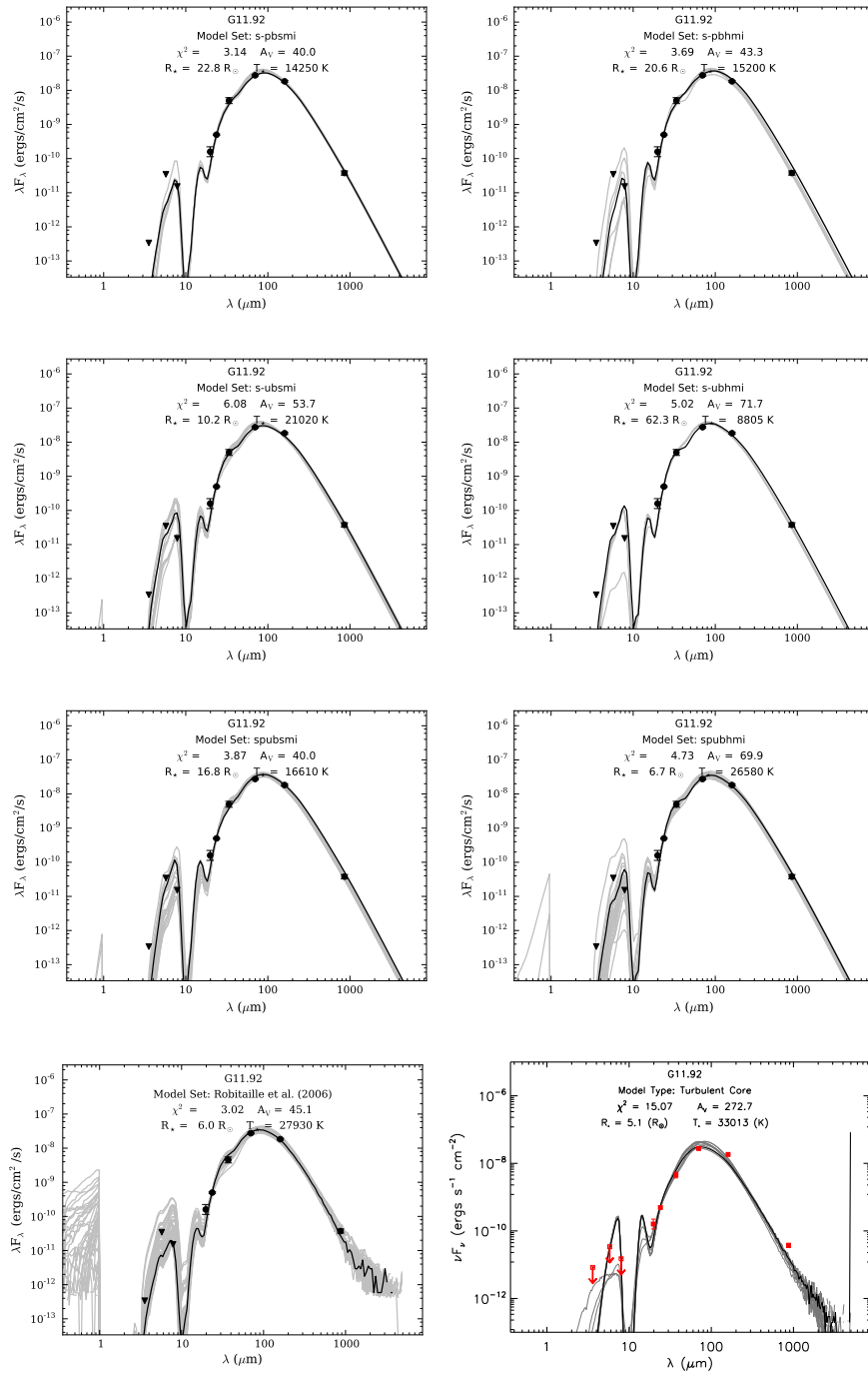
Fig. 2.5.— Robitaille (2017), Robitaille et al. (2006), and Zhang & Tan (2018) SED modeling results for G11.92–0.61. The top three rows are the best six model sets from the Robitaille (2017) model package, the bottom left panel shows the results from Robitaille et al. (2006), and the bottom right panel shows the results from Zhang & Tan (2018). All χ^2 values shown are χ^2/n_{data}, where n_{data} is the number of data points used for the fitting that are not upper or lower limits. For this source, $n_{data} = 6$. The best-fit model for each model set is denoted by a black line. The gray lines are SED models whose χ^2 per data point values were within a factor of 5 of the best-fit χ^2 per data point. The spike in the last wavelength bin in the Zhang & Tan (2018) model is due to a binning error at the first and last wavelength bins: all flux above or below the longest or shortest wavelength is binned into the last or first wavelength bin. The error is present for all Zhang & Tan (2018) models, but only produces a significant spike in a few.

Table 2.9. Stellar Radius, Temperature, and Luminosity Results for SED Model Grids

Source Name	Robitaille (2017)[a,b]					Robitaille et al. (2006)[a]				Zhang & Tan (2018)[a]			
	Model	$R_\star$ ($R_\odot$)	$T_\star$ (K)	$L_\star$ ($10^3\,L_\odot$)	χ^2	$R_\star$ ($R_\odot$)	$T_\star$ (K)	$L_\star$ ($10^3\,L_\odot$)	χ^2	$R_\star$ ($R_\odot$)	$T_\star$ (K)	$L_\star$ ($10^3\,L_\odot$)	χ^2
G10.29−0.13	spubhmi	49.1	6640	4.15	0.0003	71.0	7405	13.41	0.002	7.3	4994	0.03	0.001
G10.34−0.14	s-pbhmi	27.5	7980	2.71	1.51	79.3	4492	2.27	1.45	21.7	6835	0.91	3.98
G11.92−0.61	s-pbsmi	22.8	14250	18.97	3.14	6.0	27930	19.39	3.02	5.1	33013	27.34	15.07
G12.91−0.03	s-pbhmi	6.4	19940	5.73	1.51	118.8	4355	4.49	2.48	11.2	16298	7.83	20.43
G14.33−0.64	s-pbsmi	31.4	7976	3.53	0.45	110.7	4428	4.17	0.81	11.2	16298	7.83	1.89
G14.63−0.58	s-pbhmi	11.8	11330	2.03	3.68	68.6	4172	1.26	1.94	18.5	6780	0.64	20.54
G16.59−0.05	s-pbhmi	31.8	11020	13.20	1.12	65.0	7510	11.89	0.53	5.1	33013	27.34	11.84
G18.89−0.47	s-pbhmi	14.6	10610	2.39	1.00	96.7	4234	2.66	4.2	7.3	4994	0.03	37.73
G19.36−0.03	s-pbsmi	8.4	14420	2.70	1.73	98.3	4493	3.48	1.41	13.6	14585	7.41	10.93
G22.04+0.22	s-pbhmi	14.3	12570	4.52	1.81	27.3	9345	5.03	1.92	11.2	16298	7.83	7.66
G28.83−0.25	s-pbhmi	74.3	8766	28.85	0.81	293.4	4355	27.40	1.62	42.9	12552	40.43	12.96
G35.03+0.35	spubhmi	69.9	8552	23.13	1.08	4.8	31560	20.23	1.31	5.1	33013	27.34	0.66
Median[c]:	⋯	25	10800	4.3	1.31	75	5950	4.8	1.54	11	15440	7.8	12.40

[a] Parameters shown are the $R_\star$ and $T_\star$ returned by the best-fit model in each model package, where "best-fit model" is defined as the model with the lowest χ^2 per data point. $L_\star$ is the Stefan-Boltzmann luminosity ($4\pi R_\star^2 \sigma T_\star^4$) calculated from each combination of $R_\star$ and $T_\star$.

[b] Since the Robitaille (2017) model package contains multiple model grids, we include an extra column stating the name of the model set to which the best-fit model belongs.

[c] Median values are computed for our twelve sources for a given parameter within a given model package. The median $L_\star$ of all 36 best-fit models is $5.83 \times 10^3\,L_\odot$.
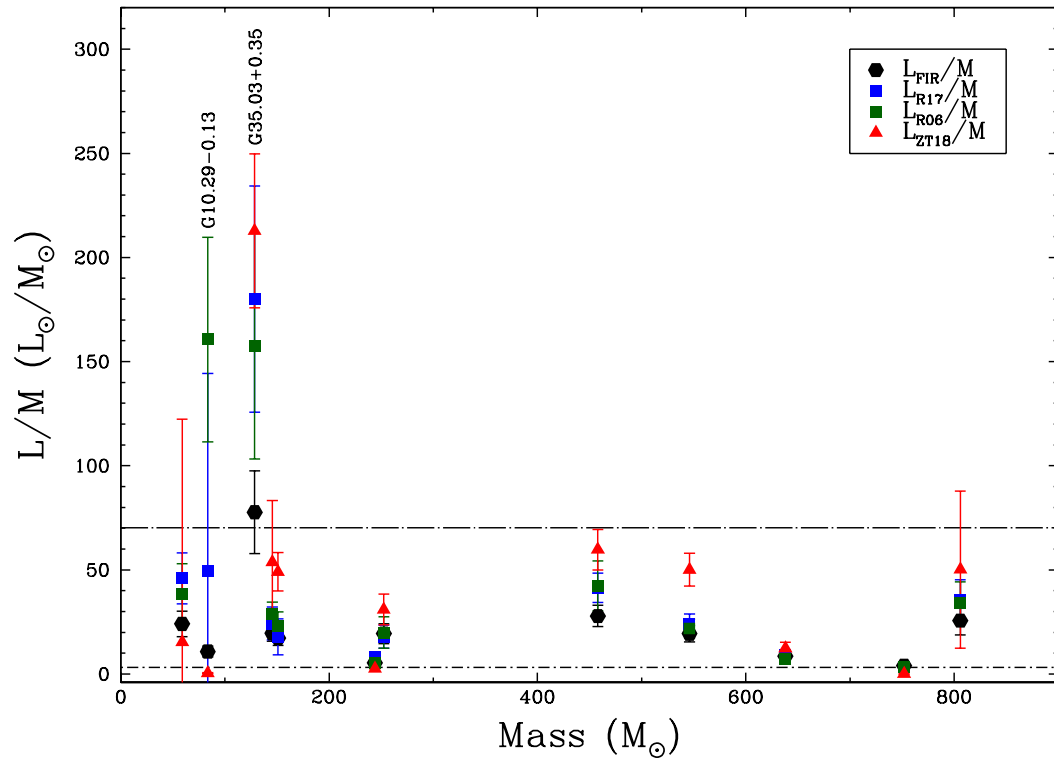
Fig. 2.6.— *L/M* versus *M* for all sources using all four luminosity values. Mass is the average of the NH_3-derived and greybody-derived masses for each source. Symbols denote which luminosity value was used for L/M: black hexagons are the greybody-derived L_{FIR}, blue squares are the luminosity returned by the Robitaille (2017) models, green squares are the luminosity returned by the Robitaille et al. (2006) models, and red triangles are the luminosity returned by the Zhang & Tan (2018) models. The upper and lower dash-dotted lines are the median *L/M* values for the Tigé et al. (2017) "IR-bright" and "IR-quiet" categories, respectively. Sources G10.29–0.13 and G35.03+0.35 are labeled specifically, as they both have some *L/M* values approximately an order of magnitude higher than the rest of our sample.

Chapter 3

VLA Survey of Dense Gas in Extended Green Objects: Prevalence of 25 GHz Methanol Masers

3.1   Chapter Summary

We present $\sim 1-4''$ resolution Very Large Array (VLA) observations of four CH_3OH $J_2 - J_1$-E 25 GHz transitions (J=3, 5, 8, 10) along with 1.3 cm continuum toward 20 regions of active massive star formation containing Extended Green Objects (EGOs), 14 of which we have previously studied with the VLA in the Class I 44 GHz and Class II 6.7 GHz maser lines (Cyganowski et al. 2009). Sixteen regions are detected in at least one 25 GHz line (J=5), with 13 of 16 exhibiting maser emission. In total, we report 34 new sites of CH_3OH maser emission and ten new sites of thermal CH_3OH emission, significantly increasing the number of 25 GHz Class I CH_3OH masers observed at high angular resolution. We identify probable or likely maser counterparts at 44 GHz for all 15 of the 25 GHz masers for which we have complementary data, providing further evidence that these masers trace similar

physical conditions despite uncorrelated flux densities. The sites of thermal and maser emission of CH$_3$OH are both predominantly associated with the 4.5 μm emission from the EGO, and the presence of thermal CH$_3$OH emission is accompanied by 1.3 cm continuum emission in 9 out of 10 cases. Of the 19 regions that exhibit 1.3 cm continuum emission, it is associated with the EGO in 16 cases (out of a total of 20 sites), 13 of which are new detections at 1.3 cm. Twelve of the 1.3 cm continuum sources are associated with 6.7 GHz maser emission and likely trace deeply-embedded massive protostars.

3.2 Introduction

Massive young stellar objects (MYSOs) remain embedded in their parent clouds during the early stages of their evolution, making them difficult to observe directly. MYSOs also evolve more quickly than lower-mass young stellar objects (YSOs), making MYSOs rare and especially difficult to observe during their early stages of evolution. Furthermore, MYSOs frequently form in clustered environments, leading to a confusion problem, and tend to be at large distances (>1 kpc), leading to resolution limitations. One particularly crucial stage of MYSO evolution is the phase in which the object is actively accreting matter and driving outflows. While the process of mass accretion for low-mass stars is fairly well understood (Yorke et al. 1993), it is thought that MYSOs continue to accrete even after hydrogen burning has commenced in the core (Stahler et al. 2000), and it is this continued mass transfer onto the protostar that leads to the formation of massive stars (Zinnecker & Yorke 2007). However, this process of mass transfer, being as it is both heavily obscured and comparatively short-lived, is not observationally well-constrained.

Recent observations have aimed to investigate the observational markers of MYSOs in this critical phase of their evolution. Cyganowski et al. (2008) identified >300 sources with extended 4.5 μm emission in the GLIMPSE-I survey images (Benjamin et al. 2003;

Table 3.1. EGO Source Properties

Source	V_{LSR}^{a} (km s^{-1})	Distance[b] (kpc)	EGO[c] Cat	IRDC[d]	H2O[e] Maser	CH$_3$OH Masers (GHz)[f] 6.7[g]	44[h]	95[i]
G08.67−0.35	35	4.1	C13	N	Y	Y	Y	Y
G10.29−0.13	14	1.9	2	Y	Y	Y	Y	Y
G10.34−0.14	12	1.6	2	Y	Y	Y	Y	Y
G11.92−0.61	36	$3.38^{+0.33}_{-0.27}$ (3.5)	1	Y	Y	Y	Y	Y
G12.68−0.18	55	$2.40^{+0.17}_{-0.15}$ (4.4)	4	Y	Y	Y	?	Y
G12.91−0.03	57	4.5	1	Y	Y	Y	?	Y
G14.33−0.64	23	$1.13^{+0.14}_{-0.11}$ (2.3)	1	Y	Y	?	Y	Y
G14.63−0.58	19	$1.83^{+0.08}_{-0.07}$ (1.9)	1	Y	Y	Y	?	Y
G16.59−0.05	60	$3.58^{+0.32}_{-0.27}$ (4.2)	2	N	Y	Y	?	Y
G18.67+0.03	80	4.8	1	N	Y	Y	Y	Y
G18.89−0.47	66	4.2	1	Y	Y	Y	Y	Y
G19.36−0.03	27	2.2	2	Y	N	Y	Y	Y
G22.04+0.22	51	3.4	1	Y	Y	Y	Y	Y
G24.94+0.07	42	2.8	1	N	Y	Y	Y	Y
G25.27−0.43	60	3.6	1	Y	Y	Y	Y	Y
G28.28−0.36	49	3.0	2	Y	N	Y	N	N
G28.83−0.25	87	4.8	1	Y	Y	Y	Y	?
G35.03+0.35	53	$2.32^{+0.24}_{-0.20}$ (3.2)	1	Y	Y	Y	Y	Y
G45.47+0.05	61	$8.40^{+1.4}_{-1.1}$ (7.1)	1	Y	Y	N	N	N
G49.27−0.34	68	5.4	1	Y	Y	N	Y	Y

[a]LSRK velocities are the single dish NH$_3$ (1,1) values from Cyganowski et al. (2013), except G08.67−0.35 which is the CH$_3$CN value from (Purcell et al. 2006).

[b]Distances without errors are estimated from the LSRK velocity and the Galactic rotation curve parameters from Reid et al. (2014). Parallax distances (with their uncertainties) are given where available from Reid et al. (2014, and references therein), with the kinematic distance in parentheses for comparison. All kinematic distances are the near distance, except for G45.47+0.05 and G49.27−0.34 (which are in the direction of tangent points); for the former source we use the parallax distance for G45.45+0.05 which is an H II region 1′ west of the EGO.

[c]Except for G08.67−0.35, this is the Table number of the EGO in Cyganowski et al. (2008). In that paper, Tables 1 & 2 list "likely" EGOs for which 5-band (3.6 to 24 μm) or only 4.5 μm *Spitzer* photometry can be measured, respectively. Table 4 lists "possible" EGO outflow candidates for which only 4.5 μm photometry is possible. G08.67−0.35 is from Chen et al. (2013).

[d]Coincidence of EGO with IRDC as indicated by Cyganowski et al. (2008), except G08.67-0.35 (Chen et al. 2013).

[e]Water maser data from the Cyganowski et al. (2013) Nobeyama 45-m survey of EGOs, except G08.67-0.35, which comes from Hofner & Churchwell (1996) (VLA) and Breen & Ellingsen (2011) (ATCA).

[f]Sources for which we could find no information in the literature are indicted by "?".

[g]The 6.7 GHz maser detection information comes from Cyganowski et al. (2009) using the VLA, except for G08.67−0.35, G12.68−0.18, G12.91−0.03, G14.63−0.58, G16.59−0.05, and G45.47+0.05 which come from Green et al. (2010, and references therein) and used the ATCA.

[h]Information for 44 GHz masers come from the VLA and were taken from Cyganowski et al. (2009), except for G08.67-0.35 (Gómez et al. 2010) and G45.47+0.05 (Kang et al. 2015).

[i]Most information for 95 GHz masers was taken from Chen et al. (2011) using the Mopra 22 m telescope. The exceptions are G08.67−0.35 and G14.33−0.64 from Val'tts et al. (2000) using Mopra, G35.03+0.35 from Kang et al. (2015) using the Korean VLBA Network, and G16.59−0.05 and G49.27−0.34 from Chen et al. (2012) using the Purple Mountain Observatory 13.7 m telescope.

Churchwell et al. 2009); these extended 4.5 μm soures are strongly correlated with infrared dark clouds (IRDCs) and 6.7 GHz Class II CH$_3$OH masers. The 4.5 μm sources were classified as Extended Green Objects (EGOs) by Cyganowski et al. (2008), for the common coding of the 4.5 μm band as green in three-color composite *Spitzer* InfraRed Array Camera (IRAC) images. EGOs lie in a region of mid-infrared (MIR) color-color space consistent with protostars that are still in infalling envelopes; the extended "green" emission is thought to arise from shocked H$_2$ emission in the 4.5 μm band. Furthermore, because IRDCs mark the earliest stages of high-mass star formation (Rathborne et al. 2007, 2006), and 6.7 GHz Class II CH$_3$OH masers are radiatively pumped and associated exclusively with massive YSOs (Cragg et al. 1992; Szymczak et al. 2005; Ellingsen 2006), Cyganowski et al. (2008) concluded that EGOs must trace massive protostars that are actively accreting and driving outflows. From the identified >300 EGO sources, a sample of $\sim$20 objects was selected for follow-up observations in the Class I 44 GHz and Class II 6.7 GHz CH$_3$OH maser lines and in the outflow tracers HCO$^+$ and SiO (Cyganowski et al. 2009). Class I 44 GHz CH$_3$OH masers were detected towards 90% of the sample. Both the HCO$^+$ line profiles and SiO detections indicated the presence of active outflows in much of the sample, supporting the idea that Class I masers, which are primarily collisionally pumped, trace the impact of outflows on dense gas in star-forming regions (e.g. Plambeck & Menten 1990; Johnston et al. 1992; Kurtz et al. 2004; Voronkov et al. 2006).

Originally discovered in Orion-KL (Barrett et al. 1971, 1975), the Class I CH$_3$OH J_2-J_1-E transitions at 25 GHz form a ladder with energy levels from $\sim$20-140 K for J=2-10 (for a rotational level diagram, see Leurini et al. 2016). Higher resolution observations soon confirmed the suspicion that the emission in these lines arises from maser action (Hills et al. 1975). The first interferometric studies (J=6 and 7) noted a correspondence in the maser positions with 2 μm H$_2$ emission, thus associating them with shocked gas (Matsakis et al.

1980). Further studies of these transitions in other objects find that their intensity usually peaks around J=6, and that they are not always inverted but do consistently trace regions of high density and temperature (Menten et al. 1986, 1988). Statistical equilibrium calculations using the large velocity gradient approach confirm that in gas at $\sim$200 K the J=6 maser can occur at densities of $5 \times 10^{(5-8)}$ cm^{-3} (Leurini et al. 2016). The 25 GHz transitions are thought to probe a similar, but narrower, range of physical conditions compared to the other two families of Class I CH$_3$OH masers (44/95 and 36/84 GHz, Sobolev et al. 2007). Thus, interferometric observations of the 25 GHz lines combined with interferometric observations of other Class I transitions (e.g. Voronkov et al. 2007, 2012) are important to further refine the physical conditions that the 25 GHz lines typically trace.

In this paper, we present a 1.3 cm Karl G. Jansky Very Large Array (VLA) survey of 20 GLIMPSE Extended Green Objects (EGOs) in continuum and several CH$_3$OH transitions. The majority of our targets are selected from the GLIMPSE-I EGO catalog of Cyganowski et al. (2008); only one, G08.67−0.35, is in the GLIMPSE-II survey area (this source is G08.67−0.36 in the GLIMPSE-II EGO catalog of Chen et al. 2013). Table 3.1 summarizes salient information about our target EGOs. We describe the observations in Section § 3.3, present our results in Section § 3.4, discuss the results in Section § 3.5, and summarize our conclusions in Section § 3.6.

3.3   1.3 cm (25 GHz) VLA Observations

We used the VLA (Perley et al. 2011) to observe 20 EGOs at 1.3 cm (25 GHz). Table 3.2 summarizes the project AB1346 phasecenters, observing dates, configuration(s), and phase calibrator for each target EGO. The observations were taken under the Resident Shared Risk Observing (RSRO) program (Chandler & Butler 2014) using 16×8 MHz spectral windows (each with 256 channels and single polarization) to observe four transitions of

Table 3.2.   Observing Parameters

Source	Pointing Center (J2000) RA	Dec	Config.	Date	Phase Cal.	Synth. Beam[a] "×" [P.A.(°)]	Line rms[b] (mJy beam^{-1})	Cont. rms (mJy beam^{-1})
G08.67−0.35	18 06 18.3	−21 37 31	CnB	2011 Jan 22 & Feb 05	J1820−2528	0.81 × 0.59 [65.4]	1.26	0.12
G10.29−0.13	18 08 49.3	−20 05 57	D	2010 Sep 13	J1820−2528	4.52 × 2.38 [14.0]	5.82	0.31
G10.34−0.14	18 09 00.0	−20 03 35	D	2010 Sep 09	J1820−2528	5.15 × 2.51 [21.4]	6.50	0.29
G11.92−0.61	18 13 58.1	−18 54 17	D & CnB	2010 Aug 25 & 2011 Jan 30	J1820−2528	1.30 × 0.87 [−7.3]	2.88	0.08
G12.68−0.18	18 13 54.7	−18 01 47	CnB	2011 Jan 29	J1832−2039	0.87 × 0.54 [71.0]	1.54	0.06
G12.91−0.03	18 13 48.2	−17 45 39	C	2010 Dec 11	J1832−2039	1.47 × 0.86 [−176.0]	2.80	0.05
G14.33−0.64	18 18 54.4	−16 47 46	D	2010 Sep 10	J1832−2039	4.63 × 2.45 [20.0]	5.20	0.10
G14.63−0.58	18 19 15.4	−16 30 07	D	2010 Sep 12	J1832−2039	4.42 × 2.50 [11.4]	3.73	0.06
G16.59−0.05	18 21 09.1	−14 31 48	C	2011 Jan 17	J1832−1035	1.37 × 0.89 [−0.9]	3.54	0.07
G18.67+0.03	18 24 53.7	−12 39 20	C	2011 Jan 07	J1832−1035	1.31 × 0.81 [−2.4]	2.03	0.04
G18.89−0.47	18 27 07.9	−12 41 36	C	2010 Dec 31	J1832−1035	1.36 × 0.82 [−4.0]	2.89	0.06
G19.36−0.03	18 26 25.8	−12 03 57	D	2010 Aug 22	J1832−1035	4.62 × 2.67 [22.6]	6.43	0.11
G22.04+0.22	18 30 34.7	−09 34 47	D	2010 Aug 30	J1832−1035	4.02 × 2.64 [19.0]	6.60	0.11
G24.94+0.07	18 36 31.5	−07 04 16	D	2010 Sep 03	J1832−1035	4.05 × 2.78 [26.7]	3.90	0.09
G25.27−0.43	18 38 56.9	−07 00 48	C	2011 Jan 06	J1832−1035	1.27 × 1.05 [19.5]	3.73	0.05
G28.28−0.36	18 44 13.2	−04 18 04	D	2010 Sep 05	J1832−1035	3.18 × 2.33 [−4.8]	5.31	0.17
G28.83−0.25	18 44 51.3	−03 45 48	C	2011 Jan 08	J1851+0035	1.16 × 0.83 [−8.8]	2.29	0.05
G35.03+0.35	18 54 00.5	+02 01 18	D	2010 Sep 07	J1851+0035	3.75 × 2.81 [−51.9]	4.51	0.10
G45.47+0.05	19 14 25.6	+11 09 28	C	2010 Dec 12 & 24	J1922+1530	0.99 × 0.82 [−19.7]	1.62	0.09
G49.27−0.34	19 23 06.7	+14 20 13	C	2010 Dec 19	J1922+1530	0.95 × 0.83 [−34.4]	2.90	0.07

[a]Synthesized beam of the CH$_3$OH-E 5(2,3)−5(1,4) transition.

[b]Median rms noise per channel in the CH$_3$OH-E 5(2,3)−5(1,4) image cubes. The rms noise in a channel with bright maser emission will be significantly higher due to dynamic range limitations.

CH_3OH, as well as the NH_3 (1,1) through (6,6) metastable transitions and the H63α and H64α radio recombination lines (RRLs). The four remaining spectral windows were placed to cover additional possible, but unlikely to be detected, species of interest. The primary purpose of these "extra" spectral windows is for continuum, and indeed, none of these transitions were detected. In this paper we focus on the 1.3 cm continuum and CH_3OH data; the details of the observed CH_3OH transitions are given in Table 3.3. Hereafter, the CH_3OH transitions will be denoted by the first two values of their upper state quantum number, for example J$'$(K$_a$,K$_c$) - J$''$(K$_a$,K$_c$) = 3(2,1) - 3(1,2) will be 3_2, etc.

The data were calibrated and imaged using the CASA software package. For all sources, the bandpass calibrator was J1924−2914. For all but two sources, 3C286 (J1331+3030), combined with a model for its flux distribution, was used for absolute flux calibration. The two exceptions (where the 3C286 observations failed to provide viable data) were G16.59−0.05 and G35.03+0.35. For these two sources, the derived flux density for the nearest other observation of the same phase calibrator (in time) was used to set the absolute flux scale. Opacities as a function of frequency were derived from the VLA seasonal model[1]. We expect the absolute flux calibration to be good to $\sim$ 10%. Where necessary, antenna position corrections were also applied.

After the standard calibration was applied, "line" datasets were created by removing the continuum in the uv-plane using line-free channels in each spectral window. A few of the EGOs have bright, compact continuum sources in the VLA field of view (FOV) that are not at the phase center: G08.67−0.35, G11.92−0.61, and G28.28−0.36. In these cases, it was necessary to first shift the phase center to the brightest continuum source in the field of view, and then shift back after continuum subtraction to avoid aliasing effects. After continuum subtraction, the 31.25 kHz channel width ($\sim$ 0.38 km s^{-1}) line data were Hanning smoothed

---

[1]See EVLA Memo 143, VLA Test Memo 232, and VLA Scientific Memo 176. All three memos are archived at http://library.nrao.edu/vla.shtml.

and imaged with a velocity channel width of 0.4 km s^{-1}. The D-configuration sources were imaged with a robust parameter of 0.75, while the CnB and C configuration data (see Table 3.2) were imaged with robust=1.0.

The continuum for each EGO comprises 30 MHz of bandwidth from the four "extra" transition spectral windows, plus an additional 15 MHz from the line-free regions of the spectral windows covering the four CH$_3$OH transitions. Fields without RRL detections in the FOV have an additional 7.5 MHz of continuum bandwidth. The continuum images were made with multi-frequency synthesis and robust=1.0 for targets with only weak continuum emission in the FOV, and more uniform weighting and/or a restricted short-spacing uv-range when diffuse/confusing sources are present. The median geometric means of the synthesized beam in the D, C, and CnB configurations are 3.''32, 1.''03, and 0.''69, respectively (the source with D & CnB configuration data is included in the CnB median). The imaged fields of view for both the line and continuum images are similar to the 2$'$ full width to half power (FWHP) of the 25m VLA dishes at 1.3 cm; primary beam correction was applied to all images.

3.4 Results

Figures 3.1 through 3.4 show three-color mid-infrared *Spitzer* GLIMPSE (Benjamin et al. 2003; Churchwell et al. 2009) images of our EGO targets. In all figures, contours of the new VLA 1.3 cm continuum data are overlaid in red. We also overlay 24 μm contours from the MIPS/*Spitzer* Survey of the Galactic Plane (MIPSGAL) (Carey et al. 2009) in yellow. Figs. **??**-3.3 show the 16 targets for which we detected 25 GHz CH$_3$OH emission. Fig. 3.4 shows the two targets for which we detected 1.3 cm continuum emission in the vicinity of the EGO but no 25 GHz CH$_3$OH emission. Note that the two sources (G18.89−0.47 and G25.27−0.43) for which neither 1.3 cm continuum nor 25 GHz CH$_3$OH emission was
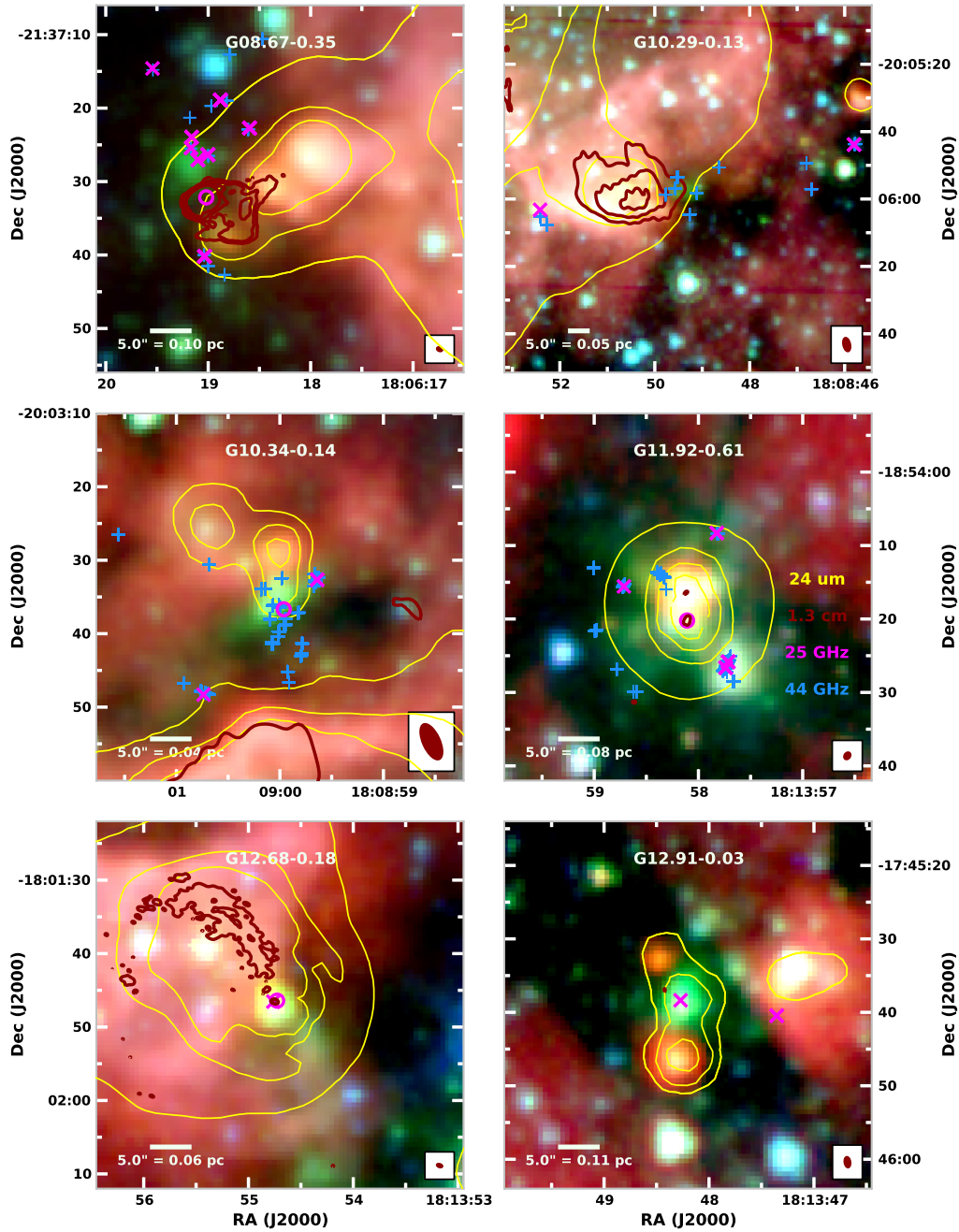
Fig. 3.1.— *Spitzer* GLIMPSE 3-color images (RGB: 8.0, 4.5, and 3.6 μm) for sources with detected 25 GHz CH$_3$OH emission. For each EGO, the displayed FOV is centered on the coordinates given in Table 3.2. *Spitzer* MIPSGAL 24 μm contours are overlaid in yellow (contour levels, in MJy sr^{-1}: G08.67: (300, 800, 1600); G10.29: (1200, 1800); G10.34: (900, 1300, 1700); G11.92: (600, 1200, 1800); G12.68: (900, 1300); G12.91: (300, 600, 1200); G14.33 (1000, 1500, 2000); G14.63: (300, 600); G16.59: (300, 600, 1200); G18.67: (300, 900); G19.36: (300, 600, 1400); G22.04: (300, 900); G24.94: (300, 600, 900); G28.28: (800, 1600); G35.03: (900, 1300, 1700); G45.47: (800, 1600)). VLA 1.3 cm continuum contours are overlaid in dark red (levels: 4, 12, 28, 60×σ, where σ for each field is given in Table 3.2). Sites of 25 GHz CH$_3$OH maser emission are marked by magenta × symbols, while sites of thermal 25 GHz CH$_3$OH emission are marked by magenta ○ symbols. Class I 44 GHz CH$_3$OH masers from the literature (where available) are marked with blue + symbols (see Table 3.1).
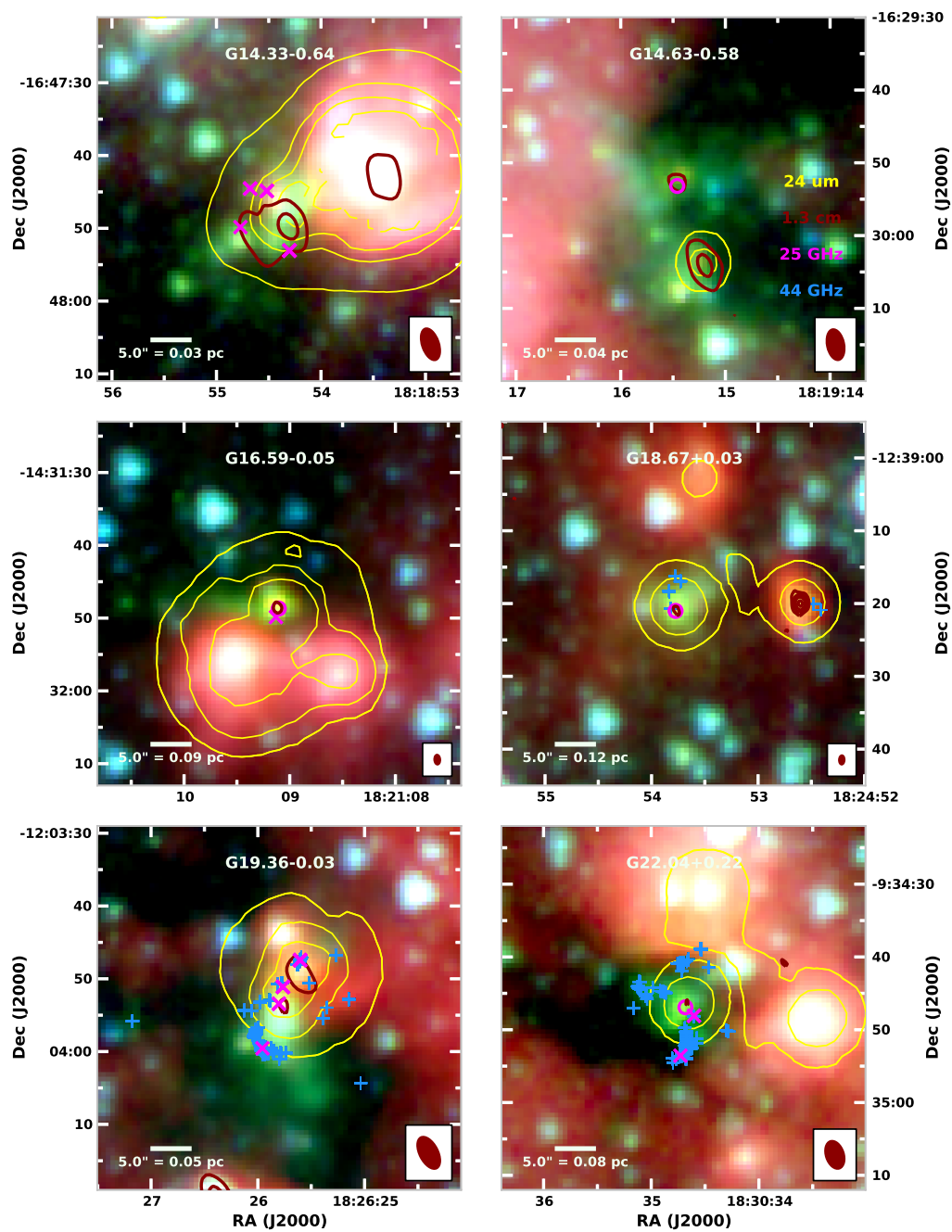
Fig. 3.2.— *Spitzer* GLIMPSE 3-color images (RGB: 8.0, 4.5, and 3.6 μm) for sources with detected 25 GHz CH$_3$OH emission, continued.

Table 3.3.   Observed CH$_3$OH Transitions[a]

Species	Resolved QNs	Frequency[b] (GHz)	E_{upper} (K)	$S_{ij}\,\mu^2$ (D^2)
CH$_3$OH-E	3(2,1)-3(1,2)	24.928707(7)	36.17	2.8073
CH$_3$OH-E	5(2,3)-5(1,4)	24.9590789(4)	57.07	5.0264
CH$_3$OH-E	8(2,6)-8(1,7)	25.2944165(2)	105.84	8.3910
CH$_3$OH-E	10(2,8)-10(1,9)	25.8782661(4)	149.97	10.7398

[a]Transition properties taken from Müller et al. (2004).

[b]Numbers in parentheses denote the measurement uncertainties in units of the least significant figure.
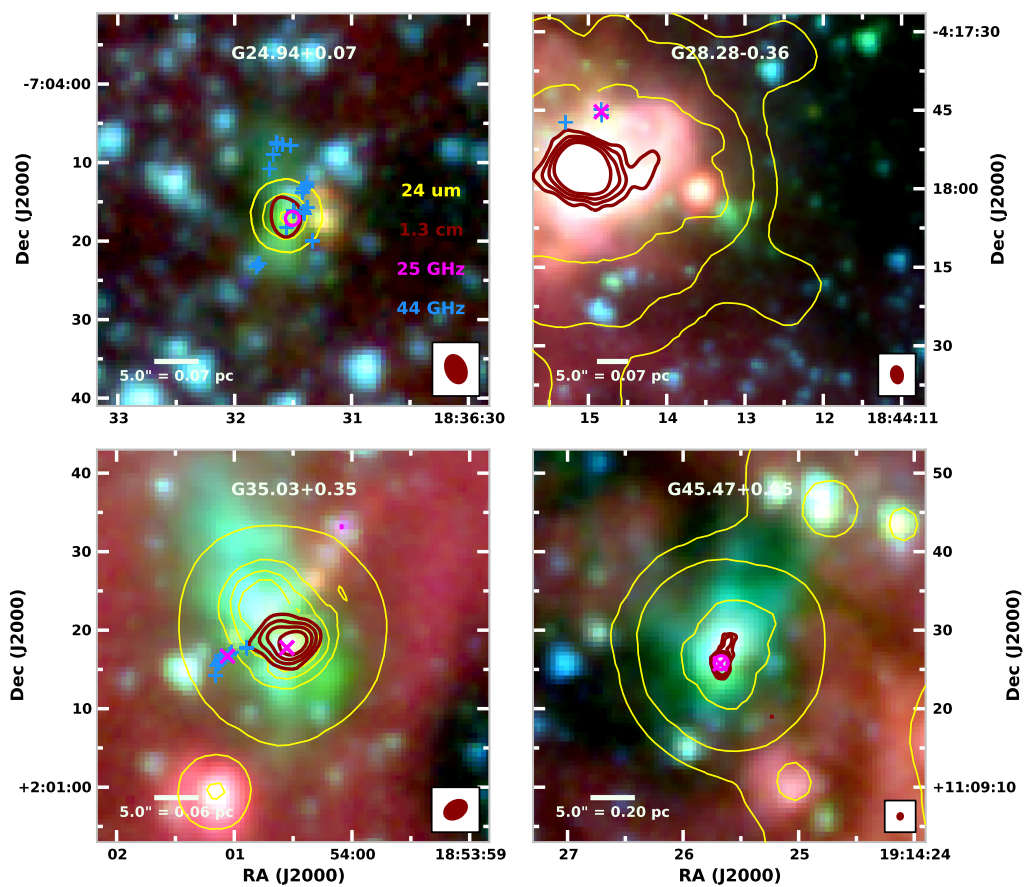
Fig. 3.3.— *Spitzer* GLIMPSE 3-color images (RGB: 8.0, 4.5, and 3.6 μm) for sources with detected 25 GHz CH$_3$OH emission, continued.

detected in the vicinity of the EGO are not shown.

3.4.1   1.3 cm Continuum Emission

We detect 1.3 cm continuum emission within the $2'$ field of view for 19 of the 20 observed fields (only G18.89−0.47 lacks any detectable emission). However, detectable 1.3 cm emission in the vicinities of the EGOs themselves (i.e. within or touching the boundary of the extended 4.5 μm emission) is only detected toward 16 of the 20 fields for a detection rate of 80% (Figs. 3.1 through 3.4). A few of these have more than one distinct region of emission, bringing the total number of individual EGO-associated 1.3 cm detections to 20. The positions and properties of the EGO-associated 1.3 cm continuum detections are detailed in Table 3.4.

Despite the modest aggregate continuum bandwidth obtainable from the relatively narrow spectral windows (see § 3.3), in many cases these data represent the most sensitive cm wavelength (cm-λ) observations of these sources to date. For example, twelve EGOs in our sample were also included in the 1.3 and 3.6 cm VLA EGO continuum survey of Cyganowski et al. (2011b, resolution $\sim 1''$). With the exception of G10.29−0.13 (which is severely dynamic-range-limited by emission from a bright H II region in the field), our new 1.3 cm images are a factor of 2-4 more sensitive than those of Cyganowski et al. (2011b).

Of our 20 EGO-associated continuum detections, 13 are new detections at 1.3 cm and have a median peak intensity of 0.50 mJy beam^{-1}. Of these, 7 are new detections at any cm-λ. Columns 6-9 of Table 3.4 list previous detections of each source at 1.3 cm and other cm-λ. References for previously-detected sources, as well as alternate names where applicable, are listed in columns 7 and 9 and associated table notes. It is notable that if it had been previously observed at 1.3 cm, it is very likely that G08.67−0.35_CM1 would have been detected at past sensitivity levels. The other 12 new 1.3 cm detections, with a median peak

Table 3.4.   1.3 cm Continuum Flux Densities For Emission Associated with EGO Targets

Source Name	J2000 Coordinates $\alpha^{(h\,m\,s)}$	$\delta(°\,′\,″)$	Peak intensity (mJy beam^{-1})	Integrated[a] (mJy)	Prior 1.3 cm Detections?	Ref.[b]	Prior cm-λ Detections?	Ref.
G08.67−0.35_CM1	18:06:19.01	−21:37:32.2	183.0 (0.1)	1141 (1)	N	–	Y	W89
G10.29−0.14_CM1	18:08:50.47	−20:06:01.5	10.7 (0.3)	201 (2)	Y	C11b[c]	Y	C11b[c]
G11.92−0.64_CM1	18:13:58.108 (0.003)	−18:54:20.212 (0.09)	0.62 (0.08)	umr	Y	C11b	Y	M16
_CM2	18:13:58.121 (0.009)	−18:54:16.46 (0.13)	0.32 (0.07)	umr	N	–	Y	C17
G12.68−0.18_CM1	18:13:54.750 (0.002)	−18:01:46.52 (0.01)	0.73 (0.06)	umr	Y	M16	Y	M16
G12.91−0.03_CM1	18:13:48.41 (0.01)	−17:45:36.92 (0.2)	0.23 (0.05)	umr	N	–	N	–
G14.33−0.64_CM1	18:18:54.30	−16:47:50.0	1.78 (0.1)	4.1 (0.3)	N	–	N	–
G14.63−0.58_CM1	18:19:15.19	−16:30:04.0	0.99 (0.06)	1.2 (0.1)	N	–	N	–
_CM2	18:19:15.469 (0.03)	−16:29:52.4 (0.4)	0.29 (0.07)	umr	N	–	N	–
G16.59−0.05_CM1	18:21:09.116 (0.004)	−14:31:48.58 (0.08)	0.56 (0.07)	umr	Y	R16, H11[d], Z06	Y	M16, R16, Z06
G18.67+0.03_CM1	18:24:53.755 (0.007)	−12:39:20.9 (0.2)	0.18 (0.04)	umr	N	–	N	–
G19.36−0.03_CM1	18:26:25.60 (0.02)	−12:03:49.6 (0.4)	0.7 (0.1)	1.3 (0.3)	N	–	Y	C11b[e]
_CM2	18:26:25.77 (0.01)	−12:03:53.7 (0.5)	0.5 (0.1)	umr	N	–	N	–
G22.04+0.22_CM1	18:30:34.70 (0.03)	−09:34:46.2 (0.5)	0.6 (0.1)	umr	N	–	N	–
G24.94+0.07_CM1	18:36:31.563 (0.008)	−07:04:16.8 (0.2)	0.85 (0.09)	umr	N	–	Y	C11b
G28.83−0.25_CM1	18:44:50.74 (0.01)	−03:45:49.19 (0.08)	0.24 (0.04)	umr	N	–	Y	C11b
_CM2	18:44:51.086 (0.005)	−03:45:48.22 (0.08)	0.35 (0.05)	umr	N	–	Y	C11b
G35.03−0.03_CM1	18:54:00.50	+02:01:18.5	13.9 (0.1)	18.5 (0.3)	Y	B11, C11b[f]	Y	C11b
G45.47+0.05_CM1	19:14:25.68	+11:09:25.8	110.09 (0.09)	180.9 (0.4)	Y	H99	Y	W89
G49.27−0.34_CM1	19:23:06.87	+14:20:18.2	1.62 (0.07)	57.8 (0.6)	Y	C11b	Y	C11b

[a]Flux densities with reported values were measured within the 3σ contour; see Table 3.2 for σ values. In this case, the position is that of the peak pixel within the 3σ contour. Flux densities designated by 'umr' indicate that the emission is unresolved. For these cases, the Gaussian fitted position and peak intensity along with the statistical uncertainties are reported.

[b]Reference abbreviations correspond to: B11: Brogan et al. (2011). C11b: Cyganowski et al. (2011b). C17: Cyganowski et al. (2017). H99: Hofner et al. (1999). H11: Hofner et al. (2011). M16: Moscadelli et al. (2016). R16: Rosero et al. (2016). W89: **?**. Z06: Zapata et al. (2006).

[c]Cyganowski et al. (2011b) list this as a field source, designation F-CM1.

[d]Hofner et al. (2011) list this source as IRAS 18182-1433, Component B.

[e]Cyganowski et al. (2011b) list this is a field source, designation F-CM1.

[f]G35.03−0.03_CM1 from the current work is a blend of CM1, CM2, CM4, and CM5 from Cyganowski et al. (2011b).

103

intensity of 0.42 mJy beam^{-1}, are sufficiently weak that these are the first (published) data with the sensitivity to detect them. Sub-mJy emission at 1.3 cm (at kiloparsec distances) can be due to either free-free emission from protostellar winds/jets or hypercompact H II regions, or alternatively the Rayleigh-Jeans tail of dust emission (see for example Brogan et al. 2016). In §3.4.3, we discuss the morphology of the 1.3 cm continuum emission and its relationship to the target EGO for individual sources, and compare with other cm-λ data where possible. Unfortunately, the absence (for the most part) of data at a second cm-λ with resolution and sensitivity comparable to our 1.3 cm images precludes systematic analysis of the underlying emission mechanism(s).

3.4.2   25 GHz CH$_3$OH Emission

Of the four observed CH$_3$OH transitions, the 5_2 transition (see Table 3.3) is by far the most prevalent. Indeed, we detected this transition toward 16 of the 20 EGOs in the sample. In order to quantify the properties of the CH$_3$OH emission, which is mostly very compact, we used the `imfit` task in CASA to fit 2-dimensional Gaussians to each distinct emission component channel-by-channel. We limited the fitting to regions with emission $> 4\sigma$, where σ was measured locally to accurately assess the variable rms noise due to dynamic range limitations. The resulting fitted parameters for the position, velocity of peak emission, velocity range of emission, size, and flux density are given in Table 3.5. The position, peak velocity, fitted flux density, and fitted size for each distinct spatial component are taken from the channel with the highest flux density for the 5_2 transition; only the fitted flux density in the peak channel is given for the other three transitions. The distinct emission regions are named by their galactic EGO name followed by a letter of the alphabet in order of increasing RA.

Table 3.5.   25 GHz CH$_3$OH Emission: Fitted and Derived Properties

Emission Region	Fitted Position (J2000) RA (h m s)	Dec (° ′ ″)	V_{peak}[c] (km s⁻¹)	V_{range}[d] (km s⁻¹)	Fitted Size[a] Major × Minor [PA] (″) × (″) [°]	Fitted Flux Densities[b] 3$_2$ Flux (mJy)	5$_2$ Flux (mJy)	8$_2$ Flux (mJy)	10$_2$ Flux (mJy)	5$_2$ T_B (K)	Emission Type[e]
G08.67-0.35_a	18:06:18.596 (0.005)	-21:37:22.72 (0.09)	38.2	37.0 - 39.0	0.72×<0.69 (0.27)	–	10 (3)	–	–	40	Maser
G08.67-0.35_b	18:06:18.881 (0.002)	-21:37:18.90 (0.02)	38.2	37.4 - 39.0	<0.69	–	13 (2)	5 (1)	–	52	Maser
G08.67-0.35_c	18:06:19.003 (0.001)	-21:37:26.34 (0.01)	35.0	34.2 - 35.8	0.39×<0.69 (0.09)	18 (3)	44 (2)	6 (1)	–	320	Maser
G08.67-0.35_d	18:06:19.019 (0.004)	-21:37:32.15 (0.05)	36.2	35.4 - 39.0	1.63×1.41 [80] (0.18×0.16 [77])	120 (10)	130 (10)	63 (6)	40 (7)	110	Thermal+Abs
G08.67-0.35_e	18:06:19.036 (0.001)	-21:37:40.18 (0.01)	33.4	32.6 - 34.6	0.27×<0.34* (0.06)	23 (5)	99 (3)	31 (2)	–	2110	Maser
G08.67-0.35_f	18:06:19.101 (0.002)	-21:37:27.05 (0.02)	36.2	35.8 - 37.0	0.40×<0.69 (0.15)	–	23 (3)	15 (2)	–	165	Maser
G08.67-0.35_g	18:06:19.162 (0.001)	-21:37:23.95 (0.10)	35.4	35.0 - 36.6	<0.69	–	28 (2)	–	–	116	Maser
G08.67-0.35_h	18:06:19.168 (0.0001)	-21:37:25.427 (0.002)	35.8	34.2 - 37.4	0.15×0.10 (0.05×0.04) [35 (45)]	106 (4)	791 (9)	91 (3)	14 (4)	104000	Maser
G08.67-0.35_i	18:06:19.544 (0.001)	-21:37:14.60 (0.01)	36.6	35.8 - 37.4	<0.69	–	27 (2)	–	–	113	Maser
G10.29-0.13_a	18:08:45.802 (0.001)	-20:05:43.85 (0.04)	14.6	13.8 - 15.0	1.31×<1.64* (0.37)	41 (9)	288 (7)	97 (5)	–	263	Maser
G10.29-0.13_b	18:08:52.416 (0.003)	-20:06:03.20 (0.10)	15.4	15.0 - 16.6	<3.28	–	97 (7)	60 (10)	–	18	Maser
G10.34-0.14_a	18:08:59.640 (0.0002)	-20:03:32.661 (0.01)	14.8	14.0 - 15.6	1.32×0.50 [34.8] (0.08×0.05 [3.3])	1058 (9)	2760 (10)	766 (6)	–	8200	Maser
G10.34-0.14_b	18:08:59.963 (0.022)	-20:03:36.68 (0.39)	12.8	9.2 - 13.6	5.29×<2.51 (1.78)	30 (6)	41 (7)	37 (7)	–	6	Thermal
G10.34-0.14_c	18:09:00.738 (0.014)	-20:03:48.30 (0.42)	11.6	11.2 - 12.4	<3.60	14 (3)	36 (5)	–	–	5.4	Maser
G11.92-0.61_a	18:13:57.715 (0.0001)	-18:54:25.836 (0.01)	34.0	32.8 - 34.4	0.50×0.16 [154] (0.04×0.07 [5])	150 (3)	511 (6)	19 (5)	–	12500	Maser
G11.92-0.61_b	18:13:57.739 (0.001)	-18:54:26.64 (0.02)	35.2	34.8 - 35.6	0.55×1.06 (0.14)	18 (3)	35 (2)	–	–	116	Maser
G11.92-0.61_c	18:13:57.824 (0.002)	-18:54:08.30 (0.11)	36.4	35.6 - 37.2	1.53×1.06 (0.38)	–	18 (3)	–	–	22	Maser
G11.92-0.61_d	18:13:58.109 (0.007)	-18:54:20.21 (0.19)	36.8	33.6 - 40.0	3.71×2.01 [9] (0.50×0.27 [9])	80 (10)	54 (7)	41 (6)	42 (7)	14	Thermal
G11.92-0.61_e	18:13:58.715 (0.002)	-18:54:15.57 (0.06)	36.8	36.4 - 37.2	1.13×0.59 [153] (0.25×0.22 [22])	22 (2)	18 (2)	–	–	53	Maser
G12.68-0.18_a	18:13:54.726 (0.003)	-18:01:46.41 (0.02)	56.0	53.2 - 59.2	1.06×0.69 [90] (0.14×0.10 [17])	24 (4)	33 (3)	39 (3)	43 (4)	90	Thermal
G12.68-0.18_b	18:13:54.763 (0.002)	-18:01:46.54 (0.05)	52.4	52.0 - 52.8	0.91×0.28 [174] (0.18×0.29 [18])	–	18 (2)	13 (2)	19 (3)	140	Maser*
G12.91-0.03_a	18:13:47.355 (0.001)	-17:45:40.46 (0.05)	55.0	54.2 - 56.2	<1.12	–	23 (3)	–	–	36	Maser
G12.91-0.03_b	18:13:48.271 (0.001)	-17:45:38.36 (0.04)	57.8	56.6 - 60.2	1.25×<1.12 (0.15)	50 (20)	59 (3)	27 (3)	–	82	Maser
G14.33-0.64_a	18:18:54.302 (0.006)	-16:47:53.06 (0.16)	21.6	20.8 - 21.6	3.24×2.52 [7] (0.73×0.56 [88])	–	99 (8)	–	–	24	Maser
G14.33-0.64_b	18:18:54.519 (0.002)	-16:47:44.86 (0.04)	20.4	20.0 - 21.2	1.56×1.13 [47] (0.36×0.40 [45])	50 (10)	400 (10)	362 (7)	96 (5)	447	Maser
G14.33-0.64_c	18:18:54.678 (0.007)	-16:47:44.54 (0.14)	22.4	22.0 - 23.2	<2.87	8 (2)	41 (3)	31 (2)	–	7.1	Maser
G14.33-0.64_d	18:18:54.771 (0.007)	-16:47:49.84 (0.11)	22.8	22.4 - 23.2	3.18×<2.45 (0.32)	31 (6)	58 (3)	52 (5)	13 (2)	14.6	Maser
G14.63-0.58_a	18:19:15.46 (0.01)	-16:29:53.18 (0.32)	19.4	19.4 - 19.8	5.07×<2.50 (1.11) [14]	27 (5)	19 (3)	–	–	2.9	Thermal
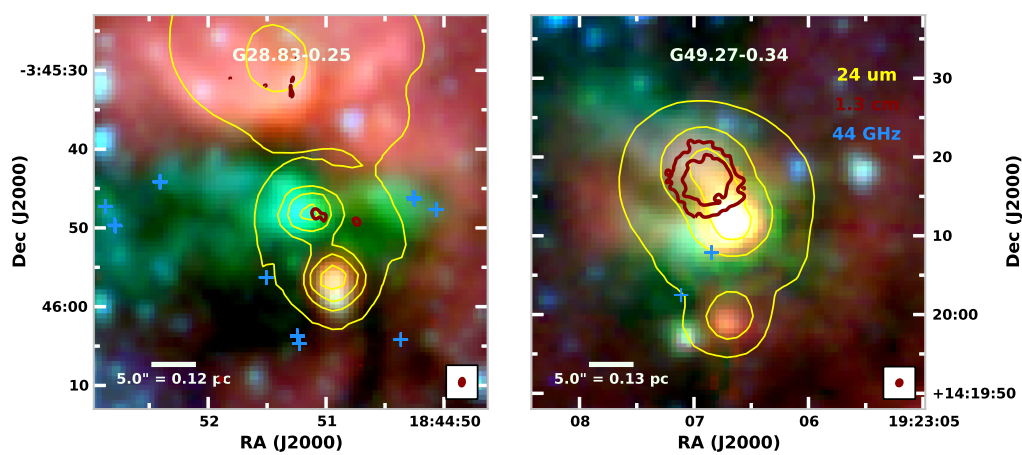
Fig. 3.4.— Same as Figs. 3.1 through 3.3, but for sources with 1.3 cm continuum detections but no detected 25 GHz CH$_3$OH emission. MIPSGAL 24 μm contour levels are: G28.83: 900, 1300, 1700 MJy sr^{-1}; G49.27: 800, 1600 MJy sr^{-1}.

Distinguishing maser and thermal emission

After fitting, we examined the properties of each distinct emission component and classified it as either maser or thermal emission. Ideally, we would use the line brightness temperature T_B to discriminate between maser and thermal emission (i.e. T_B exceeding a realistic thermal molecular gas temperature must be maser emission). For example, there are seven CH_3OH components with 5_2 T_B in excess of 1000 K, with a maximum of 10^5 K for G08.67-0.35_h (see Table 3.5) that are clearly due to non-thermal emission. However, due to the relatively poor angular resolution of some of the data, especially those observed only in the D-configuration (see Table 3.2), the current T_B lower limits are not always constraining. This is particularly problematic because EGOs are thought to harbor massive star formation, and relatively warm thermal gas (few 100 K) is a natural consequence. Indeed, some of the observed EGOs are known to harbor hot core line emission with gas temperatures as high as a few 100 K (see e.g. Cyganowski et al. 2011a; Brogan et al. 2011; Cyganowski et al. 2012; Cyganowski et al. 2014; Ilee et al. 2016). In a few cases the 25 GHz CH_3OH emission observed with the VLA is clearly thermal in origin, as evidenced by spectral breadth (several km s^{-1}) and/or large fitted emission size (i.e. significantly larger than the beam).

To distinguish the emission mechanism for modest T_B cases, we used two separate methods of analysis. The first uses the integer channel width (number of consecutive channels with emission $\geq 4\sigma$ at the location of interest) and fitted angular size as discriminators. Spectrally broad ($\geq 4\sigma$ in ≥ 5 channels, 2.0 km s^{-1}) emission with a large spatial extent (i.e. significantly spatially resolved fits) we classify as thermal emission. Emission that is spectrally narrow ($\geq 4\sigma$ in ≤ 4 channels, 1.6 km s^{-1}) and spatially consistent with an unresolved point source we consider a candidate for maser emission. Within the category "maser," there are two subcategories. Emission spots classified as "maser" are candidate

Table 3.5—Continued

Emission Region	Fitted Position (J2000) RA (h m s)	Dec (° ′ ″)	V_{peak}[c] (km s^{-1})	V_{range}[d] (km s^{-1})	Fitted Size[a] Major × Minor [PA] (″) × (″) [°]	Fitted Flux Densities[b] 3_2 Flux (mJy)	5_2 Flux (mJy)	8_2 Flux (mJy)	10_2 Flux (mJy)	$5_2 T_B$ (K)	Emission Type[e]
G16.59-0.05_a	18:21:09.104 (0.002)	-14:31:48.69 (0.07)	58.6	57.0 - 59.8	1.68×0.96 [167] (0.24×0.14 [12])	25 (4)	36 (3)	27 (3)	19 (3)	44	Thermal
G16.59-0.05_b	18:21:09.131 (0.0003)	-14:31:49.860 (0.01)	61.4	61.0 - 61.8	0.40×0.22 [178] (0.08×0.05 [19])	16 (3)	320 (6)	205 (4)	29 (4)	7200	Maser
G18.67+0.03_a	18:24:53.775 (0.005)	-12:39:21.01 (0.15)	78.2	78.2 - 79.4	1.68×0.91 [165] (0.51×0.34 [37])	–	12 (2)	6 (1)	–	15	Thermal
G19.36-0.03_a	18:26:25.604 (0.001)	-12:03:47.44 (0.03)	26.0	25.6 - 26.4	<1.75*	60 (10)	130 (3)	–	–	84	Maser
G19.36-0.03_b	18:26:25.765 (0.002)	-12:03:51.113 (0.05)	26.4	25.2 - 26.8	<3.51	29 (3)	91 (4)	117 (2)	38 (1)	14.4	Maser*
G19.36-0.03_c	18:26:25.803 (0.003)	-12:03:53.43 (0.16)	27.6	27.6 - 28.0	<3.51	–	46 (2)	–	–	7.4	Maser
G19.36-0.03_d	18:26:25.957 (0.0002)	-12:03:59.547 (0.01)	26.4	24.4 - 28.4	1.31×0.52 [30] (0.05×0.03 [2])	2870 (10)	6390 (20)	1370 (10)	135 (6)	18420	Maser
G22.04+0.22_a	18:30:34.603 (0.0002)	-09:34:48.087 (0.01)	51.8	51.0 - 55.0	<1.63*	1090 (10)	7650 (30)	3920 (10)	723 (6)	5660	Maser
G22.04+0.22_b	18:30:34.682 (0.005)	-09:34:46.91 (0.13)	50.2	47.8 - 50.6	2.71×1.70 [23] (0.58×0.39 [34])	70 (10)	200 (20)	160 (5)	70 (4)	86	Thermal
G22.04+0.22_c	18:30:34.729 (0.001)	-09:34:53.56 (0.02)	50.2	49.4 - 50.6	0.69×<1.63* (0.30)	48 (4)	342 (7)	47 (7)	–	598	Maser
G24.94+0.07_a	18:36:31.506 (0.010)	-07:04:17.12 (0.43)	42.2	39.0 - 45.0	<3.36	–	11 (3)	–	–	2.0	Thermal
G28.28-0.36_a	18:44:14.836 (0.003)	-04:17:45.29 (0.09)	48.2	47.4 - 49.0	1.87×<2.72 (0.48)	20 (5)	93 (7)	70 (7)	40 (10)	36	Maser
G35.03+0.35_a	18:54:00.554 (0.001)	+02:01:17.75 (0.07)	54.8	54.4 - 55.2	<3.25	–	19 (2)	48 (1)	18 (2)	3.6	Maser*
G35.03+0.35_b	18:54:01.058 (0.005)	+02:01:16.69 (0.01)	52.8	52.0 - 53.6	<1.63*	23 (4)	252 (3)	130 (4)	15 (5)	186	Maser
G45.47+0.05_a	19:14:25.671 (0.007)	+11:09:25.86 (0.10)	64.4	63.2 - 64.8	1.61×0.90 (0.37)	11 (2)	18 (4)	17 (2)	23 (5)	24	Thermal
G45.47+0.05_b	19:14:25.679 (0.001)	+11:09:25.71 (0.02)	66.4	65.2 - 67.2	<0.90	13 (2)	21 (1)	41 (1)	39 (2)	51	Maser*

[a]For sources for which the fitted size is poorly constrained (fitted size < 2× the statistical uncertainty from `imfit`) and the S/N<50, we report the geometric mean of the synthesized beam as an upper limit on the source size (indicated with "<"). For sources for which the fitted size is poorly constrained (fitted size < 2× the statistical uncertainty from `imfit`) and the S/N>50, we report half the geometric mean of the synthesized beam as an upper limit on the source size (indicated with "<" and a * after the value.)

[b]Dashes indicate non-detections (no emission above 4σ). The upper limits in these cases should be taken as 4 times the line rms from Table 3.2.

[c]Velocity of the peak emission in the 5_2 line.

[d]Velocity range over which emission was detected at the ≥4σ level and `imfit` was run.

[e]Classification of emission as "thermal" or "maser", as described in § 3.4.2. Sources denoted "maser" or "maser" are maser (non-thermal) emission, but their maximum fitted flux density occurs in a line higher than 5_2.

maser emission, and their highest flux density is in the 5_2 transition. Emission spots classi-
fied as "maser*" are likely to arise from non-thermal emission, but their highest flux density
is in a transition other than 5_2 (usually 8_2). Figure 3.5 shows examples of maser and thermal
spectra from our data.

The second method consisted of comparing our observed line ratios to line ratios pro-
duced by purely thermal, optically thin LTE emission. We numerically simulated line ratios
for the optically-thin LTE case, and plotted these ratios (3_2:5_2, 8_2:5_2, and 10_2:5_2) for T=0
K to T=300 K. We then compared the observed line ratios for each fitted emission site to
the simulated ratios. For lines with non-detections, we used an upper limit of 5σ in the
ratio, where σ is the line rms from Table 3.2. Emission sites with line ratios inconsistent
with LTE are candidates for maser emission. Ratios that match the simulated LTE emission
indicate candidate thermal emission.

Our findings with the second method largely matched our classifications from the first
method. We found only two exceptions to our original classifications: G12.91-0.03_b was
classified as a maser, but its line ratios are consistent with optically thin LTE emission at
lower temperatures (≤ 40 K). However, the T_B for the 5_2 emission is 82 K, far warmer than
the temperature required to produce optically thin thermal emission. We therefore consider
G12.91-0.03_b to be a maser. G22.04+0.22_b was classified as thermal emission based on
its large fitted size, but its line ratios are potentially more consistent with maser emission.
However, G22.04+0.22_b is in close proximity to G22.04+0.22_a ($\sim 1\rlap{.}''7$, and 2 channels),
the strongest maser detected in our sample (7650 mJy in 5_2). The very strong emission from
G22.04+0.22_a causes "ringing" in the surrounding channels, including those in which
G22.04+0.22_b lies, so it is possible that the fitted flux densities of the 5_2 and 8_2 lines are
skewed by this effect. It is also worth noting that G22.04+0.22_b would be the only 25 GHz
maser in the sample without a 44 GHz counterpart, and that the 25 GHz CH_3OH emission is

coincident with weak 1.3 cm emission (Table 3.4), increasing the chance of warm thermal gas at this location. Thus, we consider G22.04+0.22_b as most likely "thermal."

Detection Rates

Table 3.6 presents the number of 25 GHz CH_3OH detections in each transition by source, as well as the total number of maser and thermal emission spots for each EGO, and whether 1.3 cm continuum emission is detected associated with the EGO (within or touching the boundary of the extended 4.5 μm emission, § 3.4.1). Emission from different transitions is co-spatial so, e.g., co-spatial emission in the 3_2, 5_2, and 8_2 lines would be counted as a single maser spot in column 7. We detected 25 GHz CH_3OH emission above the 4σ level in 16 of our 20 targets, for an overall detection rate of 80%. For the 25 GHz Class I CH_3OH masers, we found that the emission was strongest in the 5_2 transition (see Table 3.7), but that the 8_2 transition was not significantly weaker than the 5_2 transition in general (median flux densities of 58.5 mJy and 52.0 mJy and median S/N ratios of 18.6 and 13.2 for 5_2 and 8_2, respectively). In total, we fit 44 sites of CH_3OH emission. Of these 44 sites, we classified ten as being purely thermal emission. Of the remaining 34 sites, we classified 30 as "maser" and 4 as "maser*" (as defined in § 3.4.2). Detection rates and flux density statistics by transition and emission type are summarized in Table 3.7.
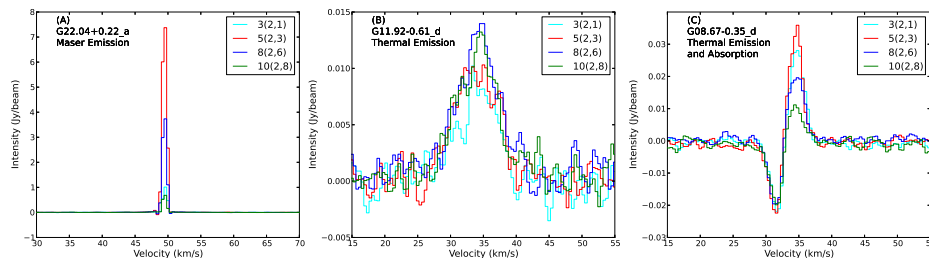
Fig. 3.5.— Example spectra for the two categories of emission (maser and thermal), as well as a spectrum showing both thermal absorption and emission. All three sets of spectra span 40 km s^{-1}.

Table 3.6. 25 GHz CH$_3$OH emission statistics by target

Source Name	25 GHz Emission	Total 25 GHz Detections				Maser Emission	Thermal Emission	1.3 cm EGO Continuum
		3_2	5_2	8_2	10_2			
G08.67-0.35	Y	4	9	6	2	8	1	Y
G10.29-0.13	Y	1	2	2	0	2	0	Y
G10.34-0.14	Y	3	3	2	0	2	1	N
G11.92-0.61	Y	4	5	2	1	4	1	Y
G12.68-0.18	Y	1	2	2	2	1	1	Y
G12.91-0.03	Y	1	2	1	0	2	0	Y
G14.33-0.64	Y	3	4	3	2	4	0	Y
G14.63-0.58	Y	1	1	0	0	0	1	Y
G16.59-0.05	Y	2	2	2	2	1	1	Y
G18.67+0.03	Y	0	1	1	0	0	1	Y
G18.89-0.47	N	0	0	0	0	0	0	N
G19.36-0.03	Y	3	4	2	2	4	0	Y
G22.04+0.22	Y	3	3	3	2	2	1	Y
G24.94+0.07	Y	0	1	0	0	0	1	Y
G25.27-0.43	N	0	0	0	0	0	0	N
G28.28-0.36	Y	1	1	1	1	1	0	N
G28.83-0.25	N	0	0	0	0	0	0	Y
G35.03+0.35	Y	1	2	2	2	2	0	Y
G45.47+0.05	Y	2	2	2	2	1	1	Y
G49.27-0.34	N	0	0	0	0	0	0	Y

Of the sites identified as thermal emission, one has emission only in the 5_2 line, one has emission only in the 3_2 and 5_2 lines, one has emission only in the 5_2 and 8_2 lines, and one has emission in the 3_2, 5_2, and 8_2 lines (Table 3.5). The remaining six sites have thermal emission in all four lines. For the source with thermal emission in 5_2 and 8_2 only (G18.67+0.03_a), we did identify weak thermal emission in the 3_2 line, but it is not above the 4σ level and so is not included in Table 3.5.

The 34 emission sites classified as "maser" or "maser*" have the following properties: 10 have emission above the 4σ level (where σ is the line rms from Table 3.2) in all four transitions (3_2, 5_2, 8_2, 10_2), including three of the four spots classified as "maser*"; eight have emission above the 4σ level in the 3_2, 5_2, and 8_2 lines only; two have emission above the 4σ level in the 5_2, 8_2, and 10_2 lines only; four have emission above the 4σ level in the 3_2 and 5_2 lines only; three have emission above the 4σ level in the 5_2 and 8_2 lines only; and seven have emission only in the 5_2 line. For this last group, the median and mean flux densities are 27.0 mJy and 35.9 mJy, respectively. These values are lower than the median and mean flux densities for the 5_2 population as a whole (see Table 3.7), but these masers are not the weakest masers in the overall population.

3.4.3   Notes on Individual Sources

The following subsections discuss each of the target EGOs for which we detect either 25 GHz CH_3OH or EGO-associated 1.3 cm continuum emission in greater detail, including notes on relevant high-resolution observations reported in the literature.

G08.67−0.35   We detect thermal 25 GHz CH_3OH in both emission and absorption (G08.67-0.35_d; see Fig. 3.5) and resolved 1.3 cm continuum emission coincident with the known UCH II region G8.67-0.36 (**?**). The northern edge of the UCH II region is coincident with

the southern end of the extended 4.5 μm emission of the G08.67−0.35 EGO (Fig. 3.1). It is currently unclear whether the extended 4.5 μm emission arises from an outflow associated with the UCH II region or from an outflow driven by a less-evolved source that is (as yet) undetected in 1.3 cm continuum. Four of the 25 GHz CH_3OH masers are coincident with the extended 4.5 μm emission, while three more lie in an arc 5-8″ west and north of it. The thermal 25 GHz CH_3OH emission is coincident with the UCH II region and with the Class II 6.7 GHz CH_3OH maser emission (G8.669−0.356) reported by Caswell (2009).

G10.29−0.13 Like Cyganowski et al. (2011b), we detect 1.3 cm continuum emission associated with the MIR-bright (MIPSGAL-saturated) source directly to the east of the EGO. Both the MIR-bright source and the EGO lie on the edge of the W31 H II region G10.32−00.15 (Westerhout 1958, see also discussion in Cyganowski et al. 2011b). In our image, the 1.3 cm continuum emission partially overlaps the extended 4.5 μm emission of the EGO and so is included in Tables 3.4 and 3.6 as an EGO-associated 1.3 cm source (§ 3.4.1). We note, however, that the morphology of the 1.3 cm continuum differs markedly from that of the extended 4.5 μm emission, and it is unclear if the two are really associated. Indeed, Cyganowski et al. (2011b) deem their 1.3 and 3.6 cm detections to be unrelated (at the higher resolution and poorer sensitivity of those data there is no overlap in the centimeter continuum and extended 4.5 μm emission). Higher angular resolution and sensitivity continuum observations are needed to verify that there is cm-λ emission directly associated with the EGO.

Unlike most EGOs, G10.29−0.13 lacks a discrete 24 μm counterpart, though it is associated with a 6.7 GHz Class II CH_3OH maser (Cyganowski et al. 2009). We do not detect any 25 GHz CH_3OH emission coincident with this EGO (Fig. 3.1). We do detect two 25 GHz CH_3OH masers in the field, located $\sim 25″$ NW and SE of the EGO, respectively, that appear to be distributed along the same line as the 44 GHz Class I CH_3OH masers

reported in Cyganowski et al. (2009). Neither 25 GHz maser is associated with 1.3 cm continuum or extended 4.5 μm emission.

G10.34–0.14   G10.34-0.14 is also located on the edge of the W31 H II region G10.32–00.15 (also see §*G10.29–0.13*). We do not detect 1.3 cm continuum emission associated with the EGO. Within the VLA FOV, we detect extended 1.3 cm continuum emission from the nearby MIR-bright H II region and a weak, unresolved 1.3 cm source $\sim 18''$ west of the EGO (Fig. 3.1; not included in Table 3.4).

We detect 25 GHz thermal CH$_3$OH emission coincident with the EGO and with Class II 6.7 GHz CH$_3$OH maser emission (Cyganowski et al. 2009). The thermal CH$_3$OH emission is fairly extended, with a T$_b$ of only 6 K (Table 3.5), and is coincident with the southern edge of a N-S elongated region of 24 μm emission. This MIR morphology may indicate the presence of two blended 24 μm sources. One 25 GHz CH$_3$OH maser is detected at the NW end of the extended 4.5 μm emission, coincident with a 44 GHz Class I CH$_3$OH maser reported by Cyganowski et al. (2009). The other 25 GHz maser is SE of the EGO, coincident with a separate patch of extended 4.5 μm emission and 44 GHz CH$_3$OH masers (Cyganowski et al. 2009).

G11.92–0.61   We detect three 1.3 cm continuum sources, two coincident with the EGO (CM1 and CM2, Table 3.4) and one at the SE edge of the extended 4.5 μm emission (Fig. 3.1). The strongest 1.3 cm source, CM1 (previously reported by Cyganowski et al. 2011b; Cyganowski et al. 2014; Moscadelli et al. 2016; Ilee et al. 2016), is coincident with the millimeter dust source and massive disk candidate MM1 (Cyganowski et al. 2011a; Ilee et al. 2016) and with 6.7 GHz CH$_3$OH maser emission (Cyganowski et al. 2009). Based on modelling the centimeter-submillimeter spectral energy distribution (SED) of MM1, Ilee et al. (2016) argue that its cm-λ emission is attributable to free-free emission

from a gravitationally trapped hypercompact (HC) H II region, with a possible contribution from a compact ionized jet (see also Moscadelli et al. 2016). We detect 25 GHz thermal CH_3OH emission coincident with CM1, consistent with the classification of MM1 as a hot core based on inteferometric (sub)millimeter line observations (Cyganowski et al. 2011a; Cyganowski et al. 2014; Ilee et al. 2016).

Located $\sim 3''$ north of CM1, CM2 is also coincident with 6.7 GHz Class II CH_3OH maser emission (Cyganowski et al. 2009). This weak, unresolved 1.3 cm source ($\sim$0.3 mJy beam^{-1}, Table 3.4) is the cm-λ counterpart of the millimeter source MM3−C1 (Cyganowski et al. 2011a, 2017), and was detected at 0.9 and 3 cm with the VLA by Cyganowski et al. (2017). The third 1.3 cm source is $\sim 13''$ SE of CM1, toward the edge of the extended 4.5 μm emission. This centimeter detection is weak and unresolved, and is not associated with compact 24 μm or (sub)millimeter emission. It is located within $1''$ of a 44 GHz Class I CH_3OH maser (Cyganowski et al. 2009), but the relationship between the maser and the centimeter emission is unclear.

We detect four 25 GHz CH_3OH masers in this target, all of which have 44 GHz CH_3OH maser counterparts. These masers are all located toward the edges of the extended 4.5 μm emission, and are distinctly separated ($> 5''$) from the centimeter emission and MIPSGAL 24 μm peak.

G12.68−0.18   We detect a compact 1.3 cm continuum source coincident with the EGO, as well as extended ($> 15''$) 1.3 cm emission coincident with similarly extended MIPSGAL 24 μm emission. The EGO-related centimeter source, which we denote CM1, was studied by Moscadelli et al. (2016) with the VLA. Based on their high-resolution multiwavelength observations (resolution $\lesssim 0.''3$ at 4.8, 2.3, and 1.4 cm), Moscadelli et al. (2016) suggest that the cm-λ continuum emission arises from an ionized jet.

CM1 is coincident with both thermal and masing 25 GHz CH_3OH emission (Fig. 3.1),

and with a 6.7 GHz Class II CH_3OH maser (Caswell 2009, see also discussion in Moscadelli et al. 2016). The 25 GHz thermal emission has a brightness temperature of 90 K, suggestive of warm gas on small size scales. This is consistent with the results from Submillimeter Array (SMA) observations of the W33 complex by Immer et al. (2014), who find that the millimeter continuum counterpart to CM1 (W33B; see their Fig. 6) is a hot core rich in nitrogen-bearing species, with gas temperatures of $\sim$220-350 K.

G12.91–0.03 We detect one weak, unresolved 1.3 cm continuum source and two 25 GHz CH_3OH masers in the VLA FOV. The 1.3 cm source, which we denote CM1, is located at the NE edge of the extended 4.5 μm emission (Fig. 3.1). One of the 25 GHz masers is coincident with the extended 4.5 μm emission, 24 μm emission, and the 6.7 GHz Class II CH_3OH maser G12.904–-0.031 (Green et al. 2010). The second 25 GHz maser is located just beyond the western edge of the extended 4.5 μm emission, toward the edge of a more evolved, 8 μm-bright region.

G14.33–0.64 This EGO is located $\sim 15''$ SE of the bright far-infrared source IRAS 18159-1648 (**?**), within a ridge of ammonia emission (VLA observations by Lu et al. 2014). We detect marginally-resolved 1.3 cm continuum emission coincident with the EGO (denoted CM1) and also the IRAS source (Fig. 3.2). The morphology of CM1 is consistent with two unresolved cm-λ continuum sources. Both components have emission above 6σ, but satisfactory two-component fits could not be achieved with the current data.

We detect four 25 GHz CH_3OH masers and no thermal CH_3OH emission in this source. The 25 GHz CH_3OH emission is, however, confused both spatially and spectrally. Consequently, there may be additional weak CH_3OH emission present that could not be separated in the current data. Two of the 25 GHz masers are located just within the 4σ contour of the 1.3 cm continuum emission; two are located north of the centimeter source.

G14.63−0.58 We detect two 1.3 cm continuum sources, both coincident with extended 4.5 μm emission (Fig. 3.2). The brighter centimeter source, CM1, is also coincident with compact 24 μm emission and with the 6.7 GHz CH$_3$OH maser G14.631−0.577, reported by Green et al. (2010). Thermal 25 GHz CH$_3$OH emission is detected towards CM2, the weaker centimeter continuum source. The brightness temperature of this thermal CH$_3$OH emission is only T$_b$ = 2.9 K, due to the extended nature of the emission and consequent large fitted size; our optically-thin calculation method gives a temperature range of T = 10 - 40 K. No 25 GHz CH$_3$OH masers are detected in the field.

G16.59−0.05 This EGO is adjacent to IRAS 18182−1433 (nominal separation $\sim$19$''$; Cyganowski et al. 2008); unusually among our sample, its cm-λ continuum emission has been well-studied, primarily by authors targeting the IRAS source (e.g. Zapata et al. 2006; Sanna et al. 2010; Hofner et al. 2011; Moscadelli et al. 2013, 2016; Rosero et al. 2016). We detect a single compact 1.3 cm continuum source (CM1), which is coincident with the EGO and with a local peak in the 24 μm emission (Fig. 3.2). CM1 corresponds to the brightest of the five components (18182-1433 C) detected at both 1.3 cm and 6 cm in deep VLA observations of this field by Rosero et al. (2016), who measure a spectral index of +0.8 $\pm$ 0.1 for this object. The compact 1.3 cm source is coincident with 6.7 GHz CH$_3$OH maser emission (e.g. Green et al. 2010; Sanna et al. 2010; Moscadelli et al. 2013). At longer wavelengths, the continuum emission is elongated E-W, with a sizescale of $\sim$4$''$ at 6 cm (Moscadelli et al. 2013, 2016). The orientation of this elongation, which is interpreted as an ionized jet (e.g. Moscadelli et al. 2013, 2016), is notably similar to that of the extended 4.5 μm emission of the EGO, which is elongated E-W on larger scales ($\sim$10-15$''$).

We detect thermal 25 GHz CH$_3$OH emission that is coincident with the EGO and CM1, and with the 6.7 GHz CH$_3$OH maser G16.585−0.051 reported by Green et al. (2010). The detection of thermal CH$_3$OH at 25 GHz is consistent with the identification of this source

as a hot core by Beuther et al. (2006) using SMA observations and by Lu et al. (2014) using VLA observations. We also detect one 25 GHz maser, located $< 1''$ S-SE of the thermal CH$_3$OH emission.

G18.67+0.03 We detect two sources of 1.3 cm continuum emission in the VLA FOV (Fig. 3.2). CM1 is weak, unresolved, and coincident with the EGO, a compact MIPS-GAL 24 μm source, and 6.7 GHz Class II CH$_3$OH maser emission (Cyganowski et al. 2009; Green et al. 2010, see also Cyganowski et al. 2012). The measured peak intensity of CM1 (0.18 mJy beam^{-1}, Table 3.4) is consistent with this source being undetected by Cyganowski et al. (2011b) (4σ upper limit of 0.94 mJy beam^{-1} at 1.3 cm). We also detect strong, resolved 1.3 cm continuum emission $\sim 13''$ W of the EGO, from the source designated "UCHII" by Cyganowski et al. (2012) (F G18.67+0.03-CM1 in Cyganowski et al. 2011b).

The only 25 GHz CH$_3$OH detection in the field is thermal, and is coincident with CM1 and 6.7 GHz CH$_3$OH maser emission. Unusually, CH$_3$OH emission is detected in the 5$_2$ and 8$_2$ lines, but not 3$_2$. The brightness temperature T$_b$ = 15 K, with the optically-thin LTE calculations suggesting a temperature range of 40 - 50 K. The detection of thermal CH$_3$OH at 25 GHz is consistent with the presence of strong hot core molecular line emission from the EGO in SMA observations by Cyganowski et al. (2012), who find a CH$_3$CN temperature of 175 K. Notably, though both the EGO and the UC HII region to the west are associated with 44 GHz Class I CH$_3$OH masers (Cyganowski et al. 2009, 2012), no 25 GHz CH$_3$OH maser emission is detected within the VLA field of view.

G18.89−0.47 No 1.3 cm continuum or 25 GHz CH$_3$OH line emission was detected toward this EGO.

G19.36−0.03   We detect three sources of 1.3 cm continuum emission in the field, two of which (CM1 and CM2) are associated with MIPSGAL 24 μm emission (Fig. 3.2). The 24 μm emission is elongated (NW-SE); its morphology suggests at least two components, separated by $\sim 6''$. The weak 1.3 cm source CM1 (1.3 mJy, Table 3.4) is associated with the NW 24 μm component and coincides with the previously detected 3.6 cm source denoted F-CM1 by Cyganowski et al. (2011b).

CM2 is a new cm-λ detection and is coincident with the EGO and with Class II 6.7 GHz CH$_3$OH maser emission (Cyganowski et al. 2009). CM2 is unresolved and weak (0.40 mJy, Table 3.4), consistent with the previous 4σ upper limit of 1 mJy at 1.3 cm (Cyganowski et al. 2011b). The third 1.3 cm continuum source lies partially off the southern edge of the field shown in Figure **??**, and was also detected by Cyganowski et al. (2011b) at 3.6 cm (their F-CM2).

We detect four 25 GHz Class I CH$_3$OH masers in this field, all of which have 44 GHz counterparts. The masers lie approximately along a line connecting the northern edge of CM1 and an arc of 44 GHz CH$_3$OH masers to the SW, including one that is near CM2.

G22.04+0.22   We detect two 1.3 cm continuum sources in the field. CM1 is a weak (0.6 mJy beam^{-1}, Table 3.4), unresolved source that is coincident with the EGO, compact 24 μm emission, and 6.7 GHz CH$_3$OH masers (Cyganowski et al. 2009). A second centimeter continuum source is detected $\sim 15''$ NW of the EGO, and does not appear to be associated. Neither centimeter continuum source was detected by Cyganowski et al. (2011b), consistent with their 4σ upper limit of 1 mJy at 1.3 cm.

We detect thermal 25 GHz CH$_3$OH emission coincident with CM1 and the 6.7 GHz masers (Fig. 3.2). We also detect two 25 GHz CH$_3$OH masers, one of which is $<2''$ SW of CM1 and its thermal 25 GHz CH$_3$OH emission. The second 25 GHz maser is coincident with a line of 44 GHz CH$_3$OH masers that extends to the south of the EGO (Cyganowski

et al. 2009).

G24.94+0.07 We detect weak 1.3 cm continuum emission coincident with this EGO (0.85 mJy beam^{-1}, Table 3.4). The 1.3 cm source, CM1, is coincident with compact MIPSGAL 24 μm emission and 6.7 GHz CH_3OH masers (Cyganowski et al. 2009). CM1 was detected by Cyganowski et al. (2011b) at 3.6 cm (peak intensity 0.53±0.04 mJy beam^{-1}); our 1.3 cm detection is consistent with their 4σ upper limit of 1.0 mJy at 1.3 cm. Unfortunately the mismatch in beam size between the 3.6 and 1.3 cm detections precludes analysis of the cm-wavelength SED. The only 25 GHz CH_3OH emission detected in this source is thermal emission associated with CM1 (Fig. 3.3).

G25.27−0.43 No 1.3 cm continuum emission is detected towards this EGO. An evolved H II region located $\sim 30''$ SE of the EGO is detected in 1.3 cm continuum; this source was detected by Cyganowski et al. (2011b) at 3.6 cm, who designated it F-CM2. No 25 GHz CH_3OH emission was detected within the VLA field of view.

G28.28−0.36 The only 1.3 cm continuum emission detected in this field is strong, re-solved emission associated with the well-known core-halo UC H II region G28.288-0.364 (e.g. Kurtz et al. 1994), $\sim 20''$ E-NE of the EGO (Fig. 3.3). This UC H II region was detected at 3.6 cm and 1.3 cm by Cyganowski et al. (2011b), who designated it F-CM1. Notably, we do not detect 1.3 cm continuum emission from the Cyganowski et al. (2011b) 3.6 cm source CM1, which is coincident with the EGO and $\sim 1\rlap{.}''2$ NE of a 6.7 GHz CH_3OH maser (Cyganowski et al. 2009, 2011b). The relatively high rms noise of the new 1.3 cm VLA image for this source (the third-highest of our sample, Table 3.2) means that our 1.3 cm limit is only a factor of ~ 1.4 improvement over that of Cyganowski et al. (2011b), and the mismatch in beam size precludes combining the two datasets to better constrain CM1's

cm-λ spectral index. Only one 25 GHz CH$_3$OH maser is detected within the VLA field of view; this maser is $\sim 7''$ north of F-CM1 and is coincident with a 44 GHz CH$_3$OH maser reported by Cyganowski et al. (2009).

G28.83−0.25 We detect two weak 1.3 cm continuum sources (<0.4 mJy beam^{-1}, Table 3.4) coincident with this EGO. The eastern centimeter source, CM2, is also coincident with compact MIPSGAL 24 μm emission and 6.7 GHz CH$_3$OH masers (Cyganowski et al. 2009). The 1.3 cm emission from this source is spatially extended E-W, with a morphology consistent with multiple unresolved or marginally-resolved sources (Fig. 3.4). The western centimeter source, CM1, is unresolved and located $\sim 4''$ west of CM2. Both CM1 and CM2 were detected by Cyganowski et al. (2011b) at 3.6 cm (but not at 1.3 cm; their 1.3 cm 4σ upper limit was 0.92 mJy beam^{-1}). Interestingly, at 3.6 cm the western source (CM1 in both papers) is the brighter of the two, while at 1.3 cm CM2 is the brighter source (Table 3.4 and Cyganowski et al. 2011b). This reversal suggests that CM2 either has a steeper free-free SED or more contribution from dust than CM1. We do not detect any 25 GHz CH$_3$OH emission above the 4σ level for this EGO. In at least three of the four CH$_3$OH lines there is, however, very weak emission ($\sim 3\sigma$, so not included in our analysis), likely thermal, coincident with CM2.

G35.03+0.35 The 1.3 cm VLA survey data for this source were presented in Brogan et al. (2011). As shown in Figure 3.3, there is strong, spatially extended 1.3 cm continuum emission coincident with the EGO. Cyganowski et al. (2011b) resolved five distinct sources at 3.6 cm (denoted CM1..CM5). The two strongest (CM1 and CM2) were also detected by these authors at 1.3 cm, and CM2 is associated with 6.7 GHz CH$_3$OH masers (Cyganowski et al. 2009, 2011b; Surcis et al. 2015). The morphology of the 1.3 cm continuum emission in our VLA image is consistent with multiple, unresolved centimeter sources, and is

spatially coincident with CM1, CM2, CM4, and CM5 from Cyganowski et al. (2011b). As we could not obtain satisfactory multi-component fits to the current data, we report the combined total 1.3 cm flux density (18.5 mJy) as a single 1.3 cm source, which we denote CM1 (Table 3.4).

We detect one 25 GHz CH$_3$OH maser coincident with the 1.3 cm continuum emission, and one at the eastern edge of the extended 4.5 μm emission, coincident with an arc of 44 GHz Class I CH$_3$OH masers reported by Cyganowski et al. (2009). Brogan et al. (2011) reported the 25 GHz CH$_3$OH maser results from these VLA data, along with the detection of an NH$_3$ (3,3) maser coincident with the 44 GHz Class I CH$_3$OH maser arc. Using H63α and H64α recombination lines, Brogan et al. (2011) find a velocity of 55.8 km s^{-1} for the free-free emission from CM1, in good agreement with the velocity of the coincident 25 GHz CH$_3$OH maser. Unfortunately, the Cyganowski et al. (2009) observations at 44 GHz only extend up to $\sim$54.4 km s^{-1}, and so the velocity at which the maser G35.03+0.35_a lies is not covered by the 44 GHz data. However, the spectrum presented in Kang et al. (2015) suggests an upper limit of $\sim$1 Jy.

G45.47+0.05 We detect strong, resolved 1.3 cm continuum emission coincident with the EGO and with the known UC H II region G45.47+0.05 (**?**Hofner et al. 1999), classified by **?**) as "irregular or multiply peaked." In the new 1.3 cm VLA image, CM1 appears elongated along a NW-SE axis, suggestive of a possible ionized jet (Fig. 3.3). The elongation direction of the cm-λ emission matches that of the extended 4.5 μm emission.

We detect both thermal and masing 25 GHz CH$_3$OH emission for this EGO, both coincident with a compact, southern component of CM1. The thermal emission is fairly compact compared to other thermal CH$_3$OH detections in the survey (1.61$\times$<0.90$''$), and has T$_b$ = 24 K. The optically-thin LTE calculations suggest a physical temperature of T $\sim$100 K.

G49.27−0.34 We detect strong, resolved 1.3 cm continuum emission coincident with this EGO (Fig. 3.4). This centimeter source, CM1, was detected by Cyganowski et al. (2011b) at 3.6 cm and 1.3 cm and by Mehringer (1994) at 20 cm; Cyganowski et al. (2011b) found that its cm-λ spectral index was consistent with optically-thin free-free emission. The 1.3 cm continuum emission from CM1 exhibits a roughly circular morphology and is coincident with both extended 4.5 μm and 24 μm emission (see also discussion in Cyganowski et al. 2011b). We do not detect a 1.3 cm counterpart to the weak, compact Cyganowski et al. (2011b) 3.6 cm source CM2 (0.61 mJy beam^{-1} at 3.6 cm) at the $>4\sigma$ level (4σ limit of 0.28 mJy beam^{-1} compared to 0.71 mJy beam^{-1} in Cyganowski et al. 2011b). Neither thermal nor masing 25 GHz CH$_3$OH emission is detected towards this EGO.

3.5 Discussion

3.5.1 Spatial Distribution of 25 GHz CH$_3$OH Emission Compared to 4.5 μm Emission

The overall correlation between 25 GHz CH$_3$OH emission and extended 4.5 μm emission is strong. In only two of our target regions is the 25 GHz emission entirely outside the boundaries of the extended 4.5 μm emission. In these cases (G10.29-0.13 and G28.28-0.36), the relationship between the 4.5 μm emission and the 25 GHz CH$_3$OH masers is unclear. In total, 25 of our 34 detected maser sites (74%) are coincident with extended 4.5 μm emission. The nine masers that are not coincident with extended 4.5 μm emission are predominantly located near dark clouds (Figs. 3.1 through 3.3).

Nine of the ten thermal CH$_3$OH detections (90%) are coincident with extended 4.5 μm emission (see Table 3.6); of these, all but one (G14.63−0.58) is also coincident with strong 24 μm emission (Figs. 3.1 through 3.3). The exception is the thermal CH$_3$OH emission

in G08.67-0.35, which is not coincident with the extended 4.5 μm emission but is instead coincident with 1.3 cm continuum emission and the known H II region G8.67-0.36 (**?**, see also Individual Sources section).

3.5.2 Spatial Distribution of 25 GHz CH₃OH Emission Compared to 1.3 cm Continuum Emission

We find a strong correlation between the presence of thermal CH$_3$OH emission at 25 GHz and the presence of 1.3 cm continuum emission. Nine of our ten thermal emission detections (90%) are coincident with a 1.3 cm detection (see Table 3.6). The exception is G10.34-0.14, which shows one thermal emission site but has no detected 1.3 cm continuum emission coincident with the EGO. However, there is strong 1.3 cm continuum emission to the south from the W31 star-forming complex, and this causes the G10.34-0.14 field to have one of the poorer continuum sensitivities due to dynamic range limitations. This may be limiting our ability to detect weak 1.3 cm emission towards the EGO in this case.

While sources that have thermal CH$_3$OH almost always have 1.3 cm continuum emission, we find that the reverse is not true: of our 19 sources of 1.3 cm emission, only nine (47%) have coincident thermal CH$_3$OH emission. In addition, we also find only a weak correlation between the presence of 25 GHz CH$_3$OH maser emission and the presence 1.3 cm continuum emission, with only only 8 masers (24%) coincident with continuum (where we define "coincident" as being within the boundary of the 4σ level of the 1.3 cm emission), while the other 26 masers lie outside the boundaries of any 1.3 cm continuum.

3.5.3 Correlation Between 6.7 GHz CH$_3$OH Masers, 1.3 cm Continuum, and Thermal 25 GHz CH$_3$OH Emission

Interestingly, 6.7 GHz Class II CH$_3$OH masers do appear to be correlated with both 1.3 cm continuum and 25 GHz thermal CH$_3$OH emission in our EGO sample. Nineteen of the 1.3 cm sources are in regions for which past 6.7 GHz data exist in the literature (the exception being G14.33−0.64_a, Table 3.1). Twelve of these nineteen 1.3 cm sources (63%) are coincident with 6.7 GHz masers (§3.4.3); of these, eight are new detections at 1.3 cm, and four (G14.63_CM1, G18.67_CM1, G19.36_CM2, and G22.04_CM1) are, to our knowledge, new detections at any cm-λ. Conversely, twelve of the eighteen Class II 6.7 GHz CH$_3$OH masers associated with our target EGOs (67%) are coincident with 1.3 cm emission in the VLA images. Of the six 6.7 GHz masers without cm-λ detections, three are in regions (G10.29−0.13, G10.34−0.14, and G28.28−0.36) that have 2-6 times poorer sensitivity than the majority of the sample due to dynamic range limitations (Table 3.2). The detection of weak cm-λ continuum emission associated with Class II CH$_3$OH masers is consistent with both phenomena tracing young, deeply embedded massive (proto)stars. Similarly, thermal 25 GHz CH$_3$OH emission in the VLA data may pinpoint hot core emission, which has been observed in association with 6.7 GHz masers in large-scale single-dish surveys (e.g. Purcell et al. 2006, 2009). Of the ten sources of thermal 25 GHz CH$_3$OH emission seen with the VLA, eight are coincident with 6.7 GHz masers. The exceptions are G14.63-0.58_a, in which the thermal CH$_3$OH emission is coincident with the weaker centimeter source CM2 but the 6.7 GHz masers are coincident with the stronger centimeter source CM1, and G45.47+0.05_a, which has thermal CH$_3$OH emission but no 6.7 GHz masers. High-resolution observations in other hot-core tracers (e.g. with (sub)millimeter interferometers) will illuminate the nature of these objects.

3.5.4 Detailed Comparison of 25 GHz and 44 GHz Class I CH$_3$OH Masers

Current models for the pumping of Class I CH$_3$OH masers suggest that 25 GHz masers are excited under an overlapping but narrower region of parameter space than 44 GHz masers (Sobolev et al. 2007). Thus, we do not expect 25 GHz masers to be present without a 44 GHz counterpart. In order to test this hypothesis observationally, we compare our 25 GHz CH$_3$OH maser properties with the 44 GHz CH$_3$OH maser results from the VLA survey of Cyganowski et al. (2009). Of the 13 EGO fields with 25 GHz CH$_3$OH maser detections, seven were also included in the Cyganowski et al. (2009) survey. A total of 17 individual 25 GHz CH$_3$OH masers were detected toward the EGOs in common between the two surveys. Of these 17 masers, two (G10.29-0.13_b and G35.03+0.35_a) do not have complementary 44 GHz data because the spectral breadth of the 44 GHz observations did not cover the 25 GHz maser velocity. This leaves 15 masers with interferometric observations at both 25 GHz and 44 GHz. In order to compare the 25 and 44 GHz CH$_3$OH masers, we first regridded the Cyganowski et al. (2009) 44 GHz image cubes (with a channel width of 0.17 km s^{-1}) to 0.4 km s^{-1} channels to match the 25 GHz data. After testing, we elected not to convolve the 44 GHz image cubes to the poorer angular resolution of the 25 GHz data. The 44 GHz data have significantly higher angular resolution (0.''5 to 1.''0) for most sources, and there are typically many more 44 GHz masers in a given region than 25 GHz masers (see Figs. 3.1 through 3.3). Preserving the higher angular resolution of the 44 GHz data allows us to pinpoint which 44 GHz maser provided the closest positional match for each 25 GHz detection.

For each of the fifteen 25 GHz masers with 44 GHz data, the properties of the 44 GHz maser in closest positional and kinematic proximity (typically matching to within one channel) were fit using the procedure described in § 3.4.2. We then compared the 25 GHz (5$_2$

Table 3.7.   25 GHz CH$_3$OH Emission Statistics by Transition

Transition	Detection Rate	Median Flux Density (mJy)	Mean Flux Density (mJy)	Median S$_{peak}$/N	Mean S$_{peak}$/N
Maser Emission					
3(2,1)-3(1,2)	60% (12/20)	30.0	261.7 (75.5)	7.8	47.4 (13.7)
5(2,3)-5(1,4)	65% (13/20)	58.5	613.2 (170.1)	18.6	120.7 (33.5)
8(2,6)-8(1,7)	65% (13/20)	52.0	327.1 (90.7)	13.2	58.3 (16.2)
10(2,8)-10(1,9)	45% (9/20)	33.5	98.3 (32.8)	9.7	19.0 (6.3)
Thermal Emission					
3(2,1)-3(1,2)	40% (8/20)	28.5	48.4 (17.1)	8.9	21.9 (7.7)
5(2,3)-5(1,4)	50% (10/20)	34.5	55.4 (17.5)	10.6	21.5 (6.8)
8(2,6)-8(1,7)	40% (8/20)	38.0	48.8 (17.3)	12.4	17.6 (6.2)
10(2,8)-10(1,9)	30% (6/20)	41.0	39.5 (16.1)	14.4	17.4 (7.1)

Note. — Columns 5 and 6 list the mean and median signal-to-noise (S$_{peak}$/N) for detections in each transition, where S$_{peak}$/N is calculated for each maser using the line rms from Table 3.2. Uncertainties in columns 4 and 6 are the Standard Error of the Mean.
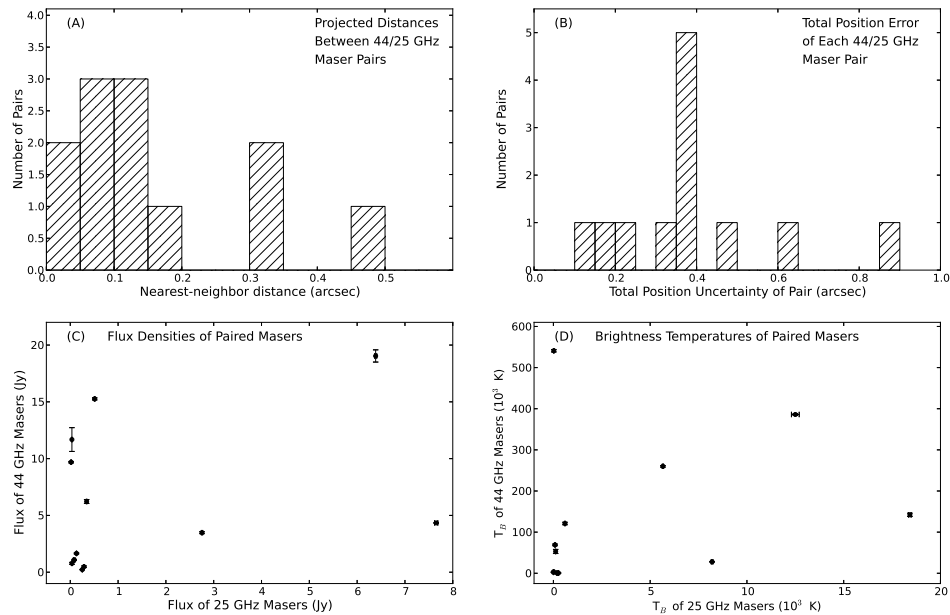
Fig. 3.6.— (a) Nearest-neighbor distances, (b) position uncertainties, (c) 44 GHz vs. 25 GHz fluxes, and (d) 44 GHz vs. 25 GHz brightness temperatures of paired masers.

transition) and 44 GHz fitted positions (Figure 3.6a), and considered them a pair if:

$$\Delta\theta_{\text{sep}} < \sqrt{\sigma_{RA_{25}}^2 + \sigma_{Dec_{25}}^2} + \sqrt{\sigma_{RA_{44}}^2 + \sigma_{Dec_{44}}^2} + 0.1\theta_{25_{\text{beam}}} \tag{3.1}$$

where $\Delta\theta_{\text{sep}}$ is the angular separation, in arcseconds, between the fitted positions of the 25 GHz and 44 GHz masers. The quantity on the right is the angular separation threshold (σ_{pos}), which consists of the sum of three terms: σ_{RA} and σ_{Dec} are the uncertainties on the fitted positions of the 25 and 44 GHz masers in arcseconds, and the final term is one-tenth the geometric mean of the synthesized beam of the 25 GHz data (in arcseconds). We add this additional factor to account for the extra uncertainty introduced because the two data sets were observed at different times and with different phase calibrators, so the absolute positions might differ by up to $0.1\theta_{\text{beam}}$ even when the fitted position uncertainties of the individual masers are quite small.

Of the 25 GHz CH_3OH masers with complementary 44 GHz data, 12 of 15 have 44 GHz counterparts with $\Delta\theta_{\text{sep}} < 1\sigma_{pos}$; we consider these to be "pairs", i.e. spatially coincident. Figures 3.6(a) and (b) show the distributions of maser separations and $1\sigma_{pos}$ values for the paired masers; as shown in Figure 3.6(a), maser pairs are co-located within $0.''5$. The three remaining 25 GHz masers have 44 GHz counterparts within $\Delta\theta_{\text{sep}}$ of 1.15 to $1.43\sigma_{pos}$. These masers - G19.36-0.03_b, G19.36-0.03_c, and G28.28-0.36_a - have fitted 25 GHz 5_2 flux densities of 91±4 mJy, 46±2 mJy, and 93±7 mJy, respectively. While on the lower end of our observed range, these flux densities are by no means exceptional. It is notable that in general, there does not appear to be a correlation between the flux density of the 5_2 transition and the nearest-neighbor distance. It is possible that for these two regions (G19.36−0.03 and G28.28−0.36) there is a greater absolute position mismatch than for the other targets. Thus, at the present angular resolution it is plausible that all 25 GHz masers have a detectable 44 GHz counterpart. Higher resolution observations in multiple maser

transitions would be useful to further constrain the exact position coincidence and also the physical size of the maser spots.

The 25 GHz CH_3OH masers are weaker than their 44 GHz counterparts by a median factor of 13. The two exceptions are G22.04+0.22_a and G35.03+0.35_b, which are stronger than their counterparts by factors of 1.8 and 1.1, respectively. Notably, we find no correlation between the 25 GHz and 44 GHz maser flux densities or brightness temperatures for paired masers (Fig. 3.6(c-d)), which is consistent with the results of Voronkov et al. (2007), who found no correlation between the flux densities of 25 GHz and other Class I CH_3OH masers. Both 44 GHz and 25 GHz CH_3OH masers have also been observed to exhibit variations in brightness on a range of timescales (Sobolev et al. 2007; Pratap et al. 2007), so the difference in observation dates between the 44 GHz and 25 GHz data may contribute to the lack of correlation in the flux densities. Furthermore, 44 GHz masers arise from A-type CH_3OH, while 25 GHz masers arise from E-type CH_3OH; thus it is possible that this difference in parity also contributes to the lack of correlation between maser flux densities. Finally, despite the high detection rate (85%) of 95 GHz Class I maser emission from our sample (Table 3.1), we cannot perform a similar comparison with the 25 GHz maser results due to the absence of interferometric observations in the higher frequency line.

3.5.5   Comparison with Millimeter Molecular Line Surveys of EGOs

Here we focus on comparison with other molecular line surveys of EGOs that target complex molecules ($\geq$6 atoms; Herbst & van Dishoeck 2009) and include a significant fraction of our sample. He et al. (2012) conducted a survey of 89 northern EGOs ($\delta > -38°$) with the Arizona Radio Observatory Submillimeter Telescope (ARO SMT; beam size $\sim$29$''$) in multiple transitions of $H^{13}CO^+$, SiO, SO, CH_3OH, CH_3OCH_3, CH_3CH_2CN, $HCOOCH_3$,

and HN^{13}C, c-HCCCH, and H$_2$CCO, as well as the unidentified line U260365. They detected 18 of the EGOs in our VLA sample in one or more transition (G08.67-0.35 was not targeted and G25.27-0.43 was targeted but not detected). We compared their detection rates in each line to our EGOs with and without 25 GHz thermal CH$_3$OH emission to search for a correlation between the presence of 25 GHz thermal CH$_3$OH and other species. We find that sources with thermal 25 GHz CH$_3$OH have higher overall detection rates (considering all observed transitions) in He et al. (2012) than sources without thermal CH$_3$OH. However, this difference is primarily due to the higher detection rates that our sample have in the He et al. (2012) sample, specifically in the CH$_3$OH lines. Sources with 25 GHz thermal CH$_3$OH have a typical detection rate of 67-78% in the CH$_3$OH lines of the He sample, while the sources without thermal CH$_3$OH have a typical detection rate of only 30-40%. Detection rates among non-CH$_3$OH species are about the same for sources with and without 25 GHz thermal CH$_3$OH. The only such species detected in the majority of our sources are H^{13}CO$^+$, SiO, and SO, and these detection rates are equally high for sources with and without 25 GHz thermal CH$_3$OH. Although we do not find a correlation between thermal CH$_3$OH in our sample and any particular non-CH$_3$OH species, we do find that sources with thermal CH$_3$OH are detected in a greater *number* of non-CH$_3$OH species than those without, indicating a possible correlation between the presence of 25 GHz thermal CH$_3$OH emission and a richer gas chemistry.

Ge et al. (2014) use the data of He et al. (2012) to determine rotational temperatures and abundances for four of the species observed (CH$_3$OH, CH$_3$OCH$_3$, HCOOCH$_3$, and CH$_3$CH$_2$CN). They list results for seven of the EGOs with 25 GHz thermal CH$_3$OH and for four of the EGOs without. The EGOs with thermal CH$_3$OH do not appear to be significantly hotter or cooler than those without, based on these rotational temperatures. The median CH$_3$OH abundance of the EGOs with thermal CH$_3$OH is 1.43×10^{-9} and 1.06×10^{-9} for

those without. While the abundance is slightly higher for sources with 25 GHz thermal CH$_3$OH, it is worth noting that the source with the highest abundance, G14.33-0.64, has an abundance a factor of ten higher than the median but does not have detectable 25 GHz thermal CH$_3$OH emission at the current sensitivity.

3.6 Conclusions

In a high-resolution VLA survey of 20 Extended Green Objects (EGOs) in the Milky Way, we identify 34 sites of 25 GHz Class I CH$_3$OH maser emission, 10 sites of thermal CH$_3$OH emission, and 20 sources of 1.3 cm continuum emission. Thirteen of the continuum sources are new detections at 1.3 cm, having a typical peak intensity of 0.5 mJy beam^{-1}. To our knowledge, seven of these objects are new detections at any cm-λ, while 12 are either coincident with or within 2$''$ of 6.7 GHz Class II CH$_3$OH maser emission. Regardless of the type of CH$_3$OH emission (maser or thermal), it is strongly correlated in position with 4.5 μm EGO emission. We also find a strong correlation between the presence of thermal CH$_3$OH emission and the presence of 1.3 cm continuum emission, with the two occurring coincidentally in nine out of ten cases (see §3.4.3 for a discussion of the lone exception to this trend, G10.34−0.14). Note that the inverse relation is not true: of the twenty sources of 1.3 cm emission, only nine have coincident thermal CH$_3$OH emission. While there is a correlation between the *presence* of 1.3 cm emission and 25 GHz Class I CH$_3$OH masers, there is an anti-correlation between their *positions*. Specifically, of our 16 targets with both 1.3 cm continuum and CH$_3$OH line emission, ten have 25 GHz CH$_3$OH maser emission. However, only 8 of 34 masers lie within the boundaries of the 4σ contours of the 1.3 cm continuum emission.

For the sites classified as maser emission, the fitted flux densities are strongest in the 5$_2$ transition (see Table 3.7), but the 8$_2$ transition is not significantly weaker than the 5$_2$

transition in general. The rarest transition is 10_2, which is detected in only 45% of targets compared to the 60% detection rate for 3_2 and the 80% detection rates for 5_2 and 8_2. For the 25 GHz masers for which we have complementary 44 GHz Class I CH_3OH maser data, we find likely or possible 44 GHz companions for every 25 GHz maser, which is consistent with the suggestion that Class I CH_3OH masers at 25 GHz and 44 GHz trace similar excitation conditions (Sobolev et al. 2007). In general, the 25 GHz masers are significantly weaker than their 44 GHz counterparts, however, we do not find any correlation between the flux densities or brightness temperatures of the paired masers. Higher matched resolution observations of masers at both wavelengths are needed in order to further constrain both the brightness temperatures and exact positions of each 25 GHz and 44 GHz maser.

3.7 Acknowledgments

Chapter 4

VLA Observations of 9 Extended Green Objects in the Milky Way: Ubiquitous Weak, Compact Continuum Emission, and Maser Emission from CH$_3$OH, H$_2$O, and NH$_3$

4.1   Chapter Summary

In massive star-forming regions (protoclusters) the question of when and how MYSOs begin producing significant ionizing radiation is key not only for understanding the formation of individual massive stars, but for understanding protocluster evolution as a whole. Nascent H II regions will emit in the centimeter wavelength regime, but there are several other process which do so as well (free-free emission from ionized jets or stellar winds,

thermal emission from warm dust, and non-thermal emission sources). We have observed a sample of 9 Extended Green Objects (EGOs) at 1.3 and 5 cm with sub-arcsecond, 7-12 μJy beam^{-1}-sensitivities with the VLA in order to characterize the centimeter continuum emission in these sources. We find ubiquitous continuum emission of typically a few tens to a few hundreds of μJy, most of which remains unresolved. The derived spectral indices of these detections are consistent with a wide array of physical processes, including some non-thermal. We also find ubiquitous 6.7 GHz CH_3OH and 22 GHz H_2O maser emission, and NH_3 (3,3) masers in about 45% of the sample. We conclude that EGOs likely host multiple different centimeter continuum-producing processes simultaneously. Therefore, in order to truly disentangle the multiple emission processes which may be present in each source, we suggest that high angular-resolution data are required at additional, millimeter wavelengths.

4.2 Introduction

Most stars form in groups called protoclusters (Lada & Lada 2003). Massive protoclusters (clusters of protostars in which at least one member is massive) differ from low-mass star-forming regions in their total mass and bolometric luminosity, but also in the internal distribution of protostars within the clump. Unlike their low-mass counterparts, which can be found forming in relative isolation within a star-forming clump, massive protostars are consistently found with close ($\lesssim$0.1 pc, 20,000 au) protostellar companions of varying masses (Cyganowski et al. 2017; Beuther et al. 2018; Hunter et al. 2017). Theoretical explanations for these differences include Hierarchical Collapse models of protocluster formation, in which nearby protostars compete for the same overall gas reservoir and form sub-clusters within an overall protocluster (Bonnell & Bate 2006; Vázquez-Semadeni et al. 2017), and Monolithic Collapse models, in which individual stars or binary systems form

from single cores which largely do not interact with each other as they evolve but whose initial distribution may still be environment-dependent (McKee & Tan 2002; Banerjee & Kroupa 2017).

Distinguishing between these theoretical possibilities requires observing massive star-forming regions in a state of evolution late enough that the presence of massive protostars can be confirmed but early enough that the natal clump remains intact. Crucially, these observations must have high enough sensitivity and angular resolutions that the small spatial scales in question ($\lesssim$5,000 au) can be directly observed. Interferometric centimeter continuum observations have become a common tool for observing massive protoclusters, both because of the high sensitivities and angular resolutions available and because multiple processes important to massive star formation emit in the centimeter regime.

The primary sources of emission are expected to be: radiatively-ionized emission from nascent H II regions, thermal free-free emission from ionized jets or stellar winds, the Rayleigh-Jeans tail of warm dust emission, and non-thermal synchrotron emission. Nascent H II regions have been predicted to exhibit a range of morphologies from bipolar to spherical, or even sizes and morphologies that are variable with time; additionally, some emission could also come not from an expanding radiatively-ionized region, but from ionized accretion flows onto the central protostar (Keto 2003, 2007; Klessen et al. 2011; Tanaka et al. 2016). Despite this broad range of potential formation mechanisms, centimeter continuum emission from very young H II regions is generally expected to be weak ($\lesssim$1 mJy) and compact ($\lesssim$2,000 au), as the ionized regions themselves are still quite small. It may exhibit a spectral index α (where $S_\nu \sim \nu^\alpha$) anywhere between $0 < \alpha < 2$, depending on size and electron density (n_e).

Thermal free-free emission from protostellar jets is generally assumed to be shock-ionized, and can exhibit a similar range of spectral indices as nascent H II regions. Reynolds

(1986) show in great detail how an unresolved, partially-ionized bipolar jet can produce a spectral index between $-0.1 \leq \alpha \leq 2$, depending on ionization fraction, acceleration or recombination within the flow, and density gradients. Measurements of jet properties such as mass-loss rate and total momentum can help to constrain important properties of both individual protostars (e.g. accretion rate) and energy feedback into the protocluster system as a whole. Additionally, some theories of H II region formation require the formation of jets before the formation of H II regions (Tanaka et al. 2016). Given the causal link between accretion and ejection (Frank et al. 2014), MYSO jets are also one potential avenue for probing massive accretion disks around MYSOs, of which there are currently very few direct observations (see, e.g., Ilee et al. 2018). Jets have largely been treated as distinguishable from HC H II regions by their comparatively elongated morphologies at sufficiently high angular resolutions, but their predicted aggregate properties (weak continuum emission, compact except at very high resolutions, and spectral indices) are quite similar to those predicted for nascent H II regions.

The Rayleigh-Jeans tail of thermal emission from warm dust is expected to be optically thick, and generally should be expected to be coincident with dust cores in millimeter and submillimeter data. Non-thermal emission will have $\alpha < 0$, and could potentially come from the magnetospheres of pre-main sequence (PMS) stars, or from synchrotron emission from relativistically-accelerated electrons in shocks driven by strong jets (Carrasco-González et al. 2010; Reid et al. 1995).

Recent interferometric observations of massive star-forming regions have shown ubiquitous weak, compact centimeter continuum emission that is consistent with thermal free-free emission. Purser et al. (2016) targeted 49 massive star-forming regions at 5.5, 9.0, 17.0, and 22.8 GHz using the Australia Telescope Compact Array (ATCA) with $0\overset{''}{.}5$ maximum resolution and typical noise levels of 17, 20, 40, and $\sim$85 μJy beam^{-1} in the four bands, re-

spectively. They report a high incidence of jets in their data: based on source spectral index and morphology, they identify 26 of their 45 detections as jets or jet candidates, 14 as H $_{II}$ regions, and the others as either disk winds or of ambiguous origin. Rosero et al. (2016) use the VLA to examine 58 high-mass star forming regions at 6 and 1.3 cm with $\sim$0.''3 resolution (300$\sim$3690 au depending on source distance) and 3$\sim$10μJy beam^{-1} sensitivity, and detect a total of 70 centimeter continuum sources in 34 of their targets. Rosero et al. (2019b) report that 80% of these detections have spectral indices consistent with thermal free-free emission from ionized gas ($-0.1 \leq \alpha \leq 2$). They state that at least 30% of their detections are likely to be ionized jets associated with massive protostars but note that, for the most compact sources, they cannot rule out the possibility of pressure-confined or gravitationally-trapped HC H $_{II}$ regions with the current data.

Sanna et al. (2018) are conducting the Protostellar Outflows and the EarliesT Stages (POETS) study, which specifically targets outflows and jets in massive star-forming regions. The 36 POETS sources were originally reported in Moscadelli et al. (2016), and have no or weak ($\leq$50 mJy) radio-continuum emission in previous observations, no UC H $_{II}$ regions, and rich 22 GHz H$_2$O maser emission; observations were performed with 0.''1 resolution and $\sim$10 μJy beam^{-1} sensitivity at 6, 15, and 22 GHz using the VLA. Sanna et al. (2018) report a total of 33 continuum sites in 25 regions with a spectral index range of $-0.1 \leq \alpha \leq 1.3$, and conclude that the continuum emission in their sample is predominantly produced by ionized gas in stellar winds and jets.

4.2.1 The EGO Sample

In this paper, we present VLA 1.3 and 5 cm continuum and maser-line observations of 9 Extended Green Objects (EGOs; **?**). EGOs are massive protoclusters thought to be in a specific stage of evolution just prior to the formation of HC H $_{II}$ regions. Their extended

emission at 4.5 μm is generally accepted to be due to shocked H_2 (Marston et al. 2004) in protostellar outflows, and their strong association with Class I (collisionally-pumped) CH_3OH masers at 44 and 25 GHz lends additional support to this conclusion (Cyganowski et al. 2009; Towner et al. 2017). EGOs are also strongly correlated with 6.7 GHz Class II CH_3OH maser emission, which is exclusively associated with massive protostars (Minier et al. 2003), and with IRDCs (Cyganowski et al. 2009). EGOs, then, are objects in which the presence of massive protostars can be confirmed but for which the host clump is still largely intact. In other words, they are in a unique and extremely useful stage of evolution for distinguishing between different models of protocluster formation.

The specific EGOs we present in this paper are part of a subsample of the >300 EGOs originally presented in Cyganowski et al. (2008). We have been conducting high-angular resolution, multi-wavelength observations of this subsample in order to accurately constrain their properties over a broad range of wavelengths (5 cm to 3.6 μm). In particular, previous observations at 1.3 cm with the VLA revealed weak (<1 mJy) or no continuum emission in these regions (Towner et al. 2017). Dedicated observations at 19.7 and 37.1 μm combined with archival data have allowed us to model the Spectral Energy Distributions (SEDs) of these sources from 3.6 to 870 μm, and constrain overall properties of the protoclusters such as mass, temperature, and luminosity (Towner et al. 2019). The general properties of these EGOs are presented in Table 4.1.

By observing these 9 EGOs with sub-arcsecond resolutions and at μJy continuum sensitivities, we seek to address the question of the origins of centimeter-continuum emission when it first appears in massive protoclusters. As multiple processes can produce centimeter continuum emission in massive protoclusters, we will use the continuum spectral indices and source morphologies to distinguish between the possibilities (nascent H II regions, ionized jets, warm dust, and non-thermal emission). The maser-line data will pro-

Table 4.1.   EGO Source Properties

EGO Name	V_{LSR}^a (km s^{-1})	Distance^b (kpc)	M_{clump}^c ($M_\odot$)	T_{dust}^d (K)	L_{bol}^e (10^3 $L_\odot$)
G10.29–0.13	14	1.9	84	24 (1)	2.53 (2.06)
G10.34–0.14	12	1.6	59	26 (1)	1.85 (0.65)
G12.91–0.03	36	4.5	638	23 (1)	5.61 (0.62)
G14.33–0.64	23	$1.13^{+0.14}_{-0.11}$ (2.3)	146	29 (2)	3.85 (0.67)
G14.63–0.58	19	$1.83^{+0.08}_{-0.07}$ (1.9)	244	22 (1)	1.29 (0.34)
G18.89–0.47	66	4.2	752	22 (1)	2.53 (0.33)
G19.36–0.03	27	2.2	151	26 (1)	3.09 (0.44)
G22.04+0.22	51	3.4	253	26 (1)	4.97 (0.26)
G28.83–0.25	87	4.8	806	26 (1)	28.1 (4.1)

[a]LSRK velocities are the single-dish NH_3 (1,1) values from Cyganowski et al. (2013).

[b]Distances without errors are estimated from the LSRK velocity and the Galactic rotation curve parameters from Reid et al. (2014). Parallax distances (with their uncertainties) are given where available from Reid et al. (2014) and references therein, with the kinematic distance in parentheses for comparison. All kinematic distances are the near distance. The uncertainty on each kinematic distance is assumed to be 15%, as in Towner et al. (2019).

[c]Masses are the average of the greybody-derived and NH_3-derived masses presented in Towner et al. (2019). See their Table 8. Greybody-derived masses determine M_{clump} using the 870 μm integrated flux densities and T_{dust} returned by single-component greybody fits to the far-infrared flux densities (70, 160, and 970 μm. NH_3-derived masses determine M_{clump} using the 870 μm integrated flux densities and $T_{kin}(NH_3)$ derived by Cyganowski et al. (2013), and assume that $T_{dust} = T_{kin}(NH_3)$.

[d]These are the dust temperatures derived from single-component graybody fits to far-IR (70, 160, & 870 μm) data for these sources; see Table 8 of Towner et al. (2019).

[e]Each L_{bol} listed here is the median of the four luminosities derived for each EGO by Towner et al. (2019), and the uncertainty is the median absolute deviation from the median. Towner et al. (2019) derive four luminosities for each EGO using single-component greybody fitting and three radiative-transfer modeling packages. The data for which they perform these fits span 3.6 to 870 μm. For this paper, we adopt their median L_{bol} for each EGO.

vide additional constraints on the possible emission mechanisms, such as by identifying definitively-massive continuum sources (6.7 GHz CH_3OH) and allowing us to explore the relationship between maser and continuum luminosities (primarily H_2O), for which relationships at lower masses are relatively well understood (see Anglada et al. 2018, for a recent review of jet emission in star-forming regions). We present our observations and data reduction methods in § 2, our results including high-resolution images in § 3, our analysis of spectral indices, maser emission, and luminosity correlations in § 4, and conclusions and future work in § 5.

4.3 Observations and Data Reduction

WWe used the Karl G. Jansky Very Large Array (VLA) to observe 9 EGOs at 1.3 cm (22 GHz, K-band) and 5 cm (6 GHz, C-band) under projects 17B-323 and 18A-249. Data for project 17B-323 were taken between 30 December 2017 and 13 February 2018, which will be referred to as "observing epoch 2018.1." 5 cm data for project 18A-249 were taken in May and June of 2018 (observing epoch 2018.4), and 1.3 cm data for 18A-249 were taken in July 2019 (observing epoch 2019.6). All 1.3 cm data were taken in either B- or BnA-configuration and all 5 cm data were taken in A-configuration. Tables 4.2 and 4.3 summarize the parameters of the 1.3 cm and 5 cm observations, respectively. Typical angular resolutions are $\sim0\rlap{.}''35\times0\rlap{.}''3$ in the continuum at both wavelengths. The line and continuum σ reported for each band are the scaled MAD values (1.482$\times$MAD), where MAD is the median absolute deviation from the median. The 1.3 cm data have typical continuum noise values of ~12 μJy beam^{-1} and line values of ~4-15 μJy beam^{-1}. Typical 5 cm noise values are ~7 μJy beam^{-1} in the continuum and ~3 μJy beam^{-1} for the 6.7 GHz CH_3OH line data. All sources were observed in two observing blocks at 5 cm, approximately two days apart; the data from each block were combined to create final images for

each source. Most sources were observed only once at 1.3 cm; those that were observed twice were observed in epochs 2018.1 and 2019.6.

The 1.3 cm spectral setup used 61 wide-band (128 MHz) spectral windows spanning the range 18 to 26 GHz. Three narrow-band (16 MHz) windows covered the H_2O $6_{1,6}-5_{2,3}$ transition at 22.235 GHz, and the NH_3 (3,3) and (6,6) metastable transitions at 23.870 and 25.056 GHz, respectively. The 5 cm spectral setup used 32 wide-band (128 MHz) spectral windows for 4 GHz total continuum coverage and one narrow-band (4.0 MHz) window covering the CH_3OH $5_{1,5}-6_{0,6}$ A^+ transition at 6.669 GHz. All observations were performed in dual-polarization mode. In addition to the standard calibrations applied by the VLA pipeline, we self-calibrated both the line and continuum data using H_2O maser emission at 1.3 cm and CH_3OH maser emission at 5 cm. This calibration is described in more detail in the imaging subsections, below.

The full width at half power (FWHP) of the 25 m VLA dishes at 1.3 cm is $\sim 1.9'$, and at 5 cm is $\sim 7'$. While the nominal largest angular scales (LAS) of our data are $7\rlap{.}''9$ at 1.3 cm and $8\rlap{.}''9$ at 5 cm, RFI flagging during the calibration and imaging process (see below) resulted in the actual LAS values for our sample being significantly smaller. At 1.3 cm, our LAS values − calculated from the 20% quantile of projected baselines for each source − range from $1\rlap{.}''7$ to $2\rlap{.}''6$, with a median value of $2\rlap{.}''4$. At 5 cm, our LAS values range from $2\rlap{.}''6$ to $3\rlap{.}''1$, with a median value of $3\rlap{.}''0$. The phase calibrators are J1832-1035, J1832-2039, and J1851+0035 (see Tables 4.2 and 4.3). The flux and bandpass calibrators for all sources were 3C286 (J1331+3030) and J1924-2914, respectively.

4.3.1   1.3 cm Line and Continuum Imaging

At 1.3 cm, persistent radio-frequency interference (RFI) in the G19.36−0.03 and G22.04+0.22 data required significant flagging in both the bandpass calibrators and the science targets,

which led to noise levels $\sim 2\times$ those of the rest of the sample. Sources G10.29–0.13 and G12.91–0.03 suffered from similarly high noise values at 1.3 cm due to shorter observation times ($\sim 0.6\times$) than the other sources. Therefore, these four targets were observed again at 1.3 cm in the 2019.6 observing epoch. These additional observations were sufficient to bring the noise of these sources in line with our target noise levels ($\sim 12\ \mu$Jy). G14.63–0.58 was observed entirely during the 2019.6 epoch; significant RFI and subsequent flagging resulted in a 1.3 cm continuum noise level for this source of $\sim 1.5\times$ the rest of the sample.

The 22 GHz H_2O maser emission was strong enough to obtain good self-cal solutions in all but one source. The exception was G19.36–0.03, which had neither any line nor any centimeter continuum emission strong enough for this purpose; therefore, all K-band data for G19.36–0.03 have the standard pipeline-reduction calibration applied, but no additional, self-calibration corrections.

The continuum data were imaged using line-free regions of the wide-band spectral windows, with the H_2O-derived self-calibration applied. For those sources which were observed twice at 1.3 cm, the two data sets were combined to create a single continuum image (i.e. we did not create separate continuum images for each semester), but the H_2O-derived self-calibration corrections from each semester were applied to that semester separately before the two data sets were combined. The H_2O and NH_3 cubes were both self-calibrated using the H_2O maser emission, and sampled with a velocity channel width of 0.25 km s^{-1}. For those sources which were observed twice at 1.3 cm, we did *not* combine the data from the two observation epochs to create the H_2O and NH_3 cubes, due to the possibility of a change in kinematic or spatial properties of the emission during the 18-month period between the two observations. For these sources, instead, we created one cube for each semester, and we report each semester's results separately. All imaging − both line and continuum − was performed with a cell size at least $5\times$ smaller than the beam minor axis,

and were primary beam-corrected.

4.3.2 5 cm Line and Continuum Imaging

All 5 cm data were self-calibrated using the 6.7 GHz CH_3OH maser emission for each source. Unlike the 1.3 cm data, all 5 cm science targets were observed in two scheduling blocks, taken on two different days (see Table 4.3 for details). Each dataset was therefore flagged and self-calibrated separately, and final images were created using the combined data for each source. Unlike the H_2O and NH_3 data, we *did* combine datasets for the 6.7 GHz CH_3OH observations, due to the relatively short time difference between observations and in order to improve the signal-to-noise (S/N) of our data. The 6.7 GHz CH_3OH maser emission was sufficient for self-calibration in all sources, and the final 6.7 GHz cubes were sampled with a velocity channel width of 0.25 km s^{-1}. Continuum imaging was performed by first applying the CH_3OH-derived self-calibration solutions for each day's observations separately, and then imaging the combined, corrected continuum data sets. All images were primary beam-corrected, and created with a cell size at least 5$\times$ smaller than the beam minor axis.

4.4 Results

For the remainder of this paper, we report and discuss all emission at both wavelengths that is found within the FWHM of the 1.3 cm continuum primary beam for each source. For our sample, this FWHM (1$'$.9) corresponds to a physical area of 0.62 to 2.65 pc. This is large enough in all cases to encompass sources we might reasonably expect to be associated with each EGO protocluster, given typical clump sizes of order $\sim$0.1 pc. Our source-identification and photometry procedures are described in § 4.4.1 and 4.4.2, below,

Table 4.2.   VLA K-band (22 GHz/1.3 cm) Observing Parameters

EGO	Pointing Center (J2000) RA (^{h} ^{m} ^{s})	Dec (° ′ ″)	Observation[a] Date	Phase Cal	Cont. Synth. Beam ″ × ″ (°)	σ Cont.[b] (μJy/beam)	σ H₂O[c] (mJy/beam)	σ NH₃[c] (mJy/beam)	TOS (min.)
G10.29−0.13	18:08:49.3	−20:05:57	2018 Feb 13 & 2019 Jun 27	J1832-2039	0.24×0.16 (83)	13.9	7.9 & 15	7.5 & 10	40.6
G10.34−0.14	18:09:00.0	−20:03:35	2017 Dec 30	J1832-2039	0.41×0.23 (8)	12.9	4.5	4.2	33
G12.91−0.03	18:13:48.2	−17:45:39	2018 Jan 08 & 2019 Jul 09	J1832-2039	0.23×0.17 (83)	11.4	8.4 & 13.1	6.8 & 7.6	42.6
G14.33−0.64	18:18:54.4	−16:47:46	2017 Dec 30	J1832-2039	0.38×0.23 (6)	11.4	4.3	4.03	33
G14.63−0.58	18:19:15.4	−16:30:07	2019 Jun 27	J1832-2039	0.23×0.15 (87)	18.4	12	11	36.8
G18.89−0.47	18:27:07.9	−12:41:36	2018 Jan 27	J1832-1035	0.32×0.204 (-4)	12.6	4.2	4.4	26.4
G19.36−0.03	18:26:25.8	−12:03:57	2018 Jan 06 & 2019 Jul 11	J1832-1035	0.24×0.18 (77)	12.2	11 & 13	5.4 & 8.8	62.8
G22.04+0.22	18:30:34.7	−09:34:47	2018 Jan 06 & 2019 Jul 11	J1832-1035	0.25×0.16 (79)	12.3	6.2 & 13	5.6 & 8.8	62.7
G28.83−0.25	18:44:51.3	−03:45:48	2018 Jan 27	J1832-1035	0.26×0.21 (-9)	11.8	3.8	3.7	33.5

[a]All sources except G14.63−0.58 were observed at 1.3 cm during observing epoch 2018.1 (VLA Semester 2017B) in B-configuration. G14.63−0.58 was observed at 1.3 cm during epoch 2019.6 (Semester 2018A) in BnA-configuration, along with four sources (G10.29−0.13, G12.91−0.03, G19.36−0.03, G22.04+0.22) which had previously been observed in epoch 2018.1. These four sources were observed again due to significant RFI in the 2018.1 observations leading to high rms values.

[b]These 1σ values are 1.482×medabs, the scaled median absolute deviation from the median (MAD). In most cases this is identical to the standard deviation, but in images with significant artifacts from resolved-out sources, we consider the scaled MAD (1.482×medabs) value to be less susceptible to non-Gaussian structures in the noise. We measure the MAD in a representative emission-free region in each image separately.

[c]These 1σ values are measured in a representative line-free channel in each data cube. The values reported for NH₃ are for the NH₃ (3,3) data cubes only; no maser emission was detected in the NH₃ (6,6) data. For sources observed during two different epochs, the 1σ values are listed separately in order of epoch. For the H₂O cubes, the min, max, and median 1σ values in Kelvin are 118 K, 966 K, and 454 K, respectively. The min, max, and median 1σ values for NH₃ (3,3) in Kelvin are 96 K, 684 K, and 301 K, respectively. The NH₃ (6,6) 1σ values over all data sets range from 3.5 to 8.7 mJy beam⁻¹ (79 to 491 K), with a median of 5.6 mJy beam⁻¹ (242 K).

Table 4.3.   VLA C-Band (6 GHz/5 cm) Observing Parameters

EGO	Pointing Center (J2000) RA ($^h\,^m\,^s$)	Dec (° ′ ″)	Observation[a] Date	Phase Cal	Cont. Synth. Beam ″ × ″ (°)	σ Cont.[b] (μJy/beam)	σ CH$_3$OH[c] (mJy/beam)	TOS (min.)
G10.29−0.13	18:08:49.3	−20:05:57	2018 May 01 & May 02	J1832−2039	0.53×0.27 (−12)	7.3	3.2	34.6
G10.34−0.14	18:09:00.0	−20:03:35	2018 May 01 & May 02	J1832−2039	0.53×0.27 (−11)	7.0	3.05	34.5
G12.91−0.03	18:13:48.2	−17:45:39	2018 Jun 04 & Jun 07	J1832−2039	0.40×0.23 (−3)	7.9	3.01	33.7
G14.33−0.64	18:18:54.4	−16:47:46	2018 May 01 & May 02	J1832−2039	0.47×0.24 (−14)	7.1	3.1	34.6
G14.63−0.58	18:19:15.4	−16:30:07	2018 May 01 & May 02	J1832−2039	0.503×0.29 (−14)	5.1	2.9	34.6
G18.89−0.47	18:27:07.9	−12:41:36	2018 Jun 04 & Jun 07	J1832−1035	0.35×0.24 (1)	8.8	3.5	41.1
G19.36−0.03	18:26:25.8	−12:03:57	2018 May 01 & May 02	J1832−2039	0.41×0.25 (−15)	7.8	3	33.7
G22.04+0.22	18:30:34.7	−09:34:47	2018 Jun 04 & Jun 07	J1832−1035	0.32×0.24 (−1)	7.5	3	38.4
G28.83−0.25	18:44:51.3	−03:45:48	2018 Jun 04 & Jun 07	J1851+0035	0.29×0.26 (−3)	7.1	2.9	33.8

[a]All sources were observed in C-band during VLA Semester 2018A in A-configuration.

[b]These 1σ values are 1.482×medabs, the scaled median absolute deviation from the median (MAD). In most cases this is identical to the standard deviation, but in images with significant artifacts from resolved-out sources, we consider the scaled MAD (1.482×medabs) value to be less susceptible to non-Gaussian structures in the noise. We measure the MAD in a representative emission-free region in each image separately.

[c]These 1σ values are the standard deviation of a representative line-free channel in each data cube. The min, max, and median 1σ values in Kelvin are 547 K, 1145 K, and 838 K, respectively.

and our continuum and maser results are summarized in Tables 4.4 & 4.5 and Table 4.6, respectively.

Figures 4.1 through 4.3 show three-color (RGB) images for each EGO. In all panels, the background image shows *Spitzer* IRAC data with 8.0, 4.5, and 3.6 μm mapped to R, G, and B, respectively. The positions of the CH_3OH, H_2O, and NH_3 (3,3) masers (if present) in each source are indicated with color-coded symbols. For the sources observed twice at 1.3 cm, we show only the H_2O and NH_3 emission from the first epoch of observations (2018.1) in this set of images; figures showing kinematic details of the maser emission for each source, including a comparison of multi-epoch observations, are presented in § 4.4.2. For each EGO, the left-hand panel shows a 90″ FOV of the target, with SOFIA 37 μm emission overlaid in black[1] and APEX LABOCA 870 μm contours overlaid in silver[2]. These panels show the full extent of the extended 4.5 μm emission by which each EGO was originally identified, the 870 μm dust clumps in which they reside, and the associated bright 37 μm emission which may be indicative of outflow cavities or internally-heated envelopes from massive protostars. The right-hand panels show a 14.″4 FOV for most sources (0.04 to 0.17 pc); G14.63−0.58 and G18.89−0.47 show a 18″ FOV (0.06 and 0.15 pc, respectively). These FOV were chosen to highlight the centimeter continuum and maser emission signposts of massive protostellar activity in the central region of each EGO. The 1.3 cm and 5 cm continuum emission contours are overlaid in dark red and orange, respectively, and 37 μm contours are again overlaid in black.

---

[1]The SOFIA 37 μm data were taken with the Faint Object infraRed CAmera for the SOFIA Telescope (FORCAST, Herter et al. 2012) under Plan ID 04_0159; see Towner et al. (2019) for observing details (§2.1) and photometry procedures (§3.1).

[2]The APEX data were part of the APEX Telescope Large Area Survey of the Galaxy (ATLASGAL, Schuller et al. 2009) and were retrieved from the ATLASGAL Database Server at http://atlasgal.mpifr-bonn.mpg.de/cgi-bin/ATLASGAL_DATABASE.cgi
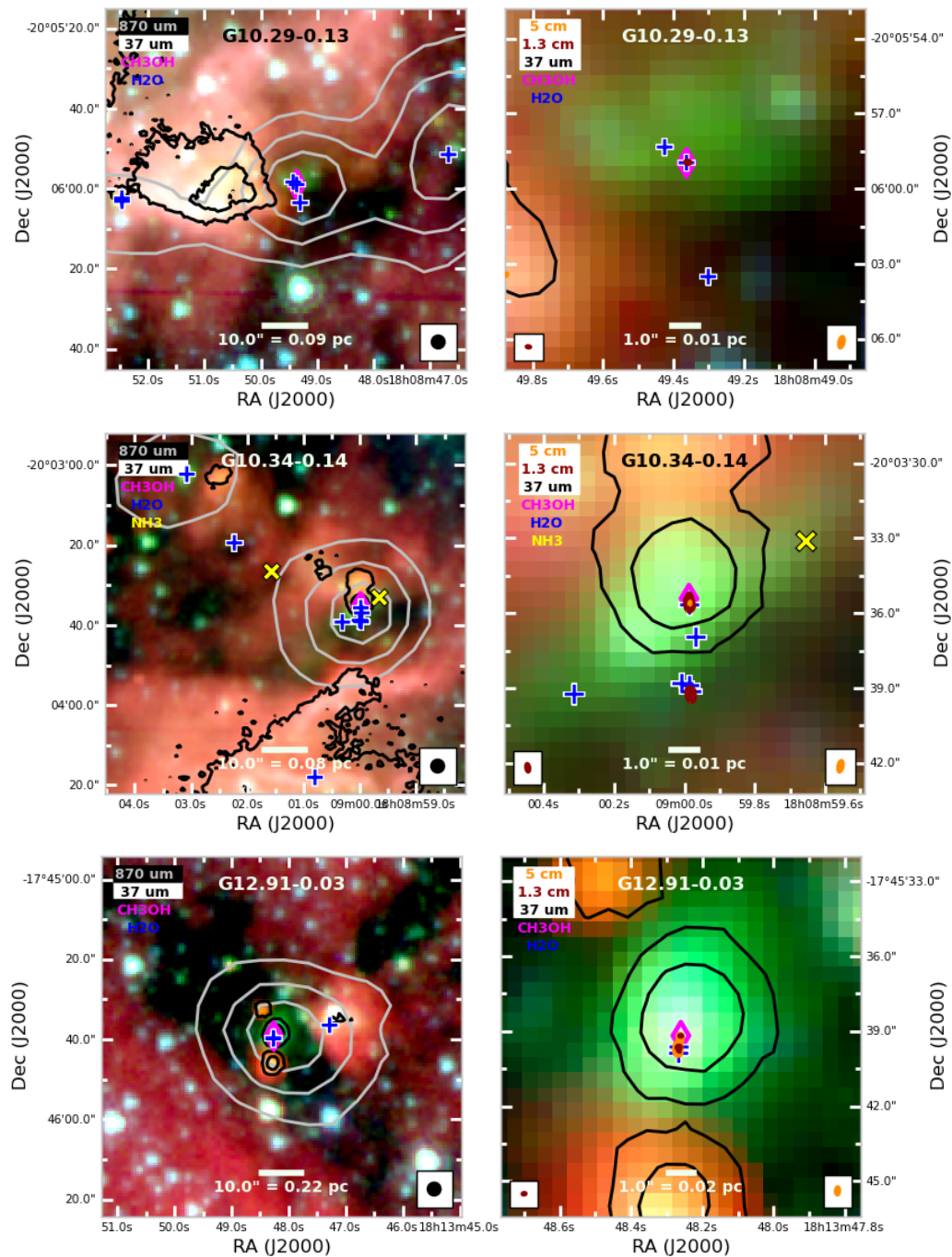
Fig. 4.1.— RGB mid-infrared images for the EGO sources are shown. CH$_3$OH 6.7 GHz masers are shown as magenta diamonds ($\diamond$). 22 GHz H$_2$O masers are shows as blue +. NH$_3$ (3,3) masers, if detected, are shown with yellow ○. *Left:* 90″ FOV of each EGO with ATLASGAL 870 μm contours overlaid in silver and SOFIA FORCAST 37.1 μm contours overlaid in black. Background image shows *Spitzer* IRAC 8.0, 4.5, and 3.6 μm data mapped to R, G, and B, respectively. ATLASGAL contour levels are [0.25,0.50,0.75]×I$_{peak}$; SOFIA contour levels are [5,15,45,125,250]×σ, where σ is the scaled MAD. SOFIA 37 μm scaled MAD values are 0.26, 0.30, 0.18 Jy beam^{-1} for G10.29–0.13, G10.34–0.14, G12.91–0.03, respectively. ATLASGAL 870 μm I$_{peak}$ values are 3.31, 4.4, 2.78 Jy beam^{-1}, respectively. 37.1 μm beam is shown in the lower right. *Right:* 7.″2 FOV of each EGO with 1.3 cm continuum emission overlaid in red contours (levels: [4.5,10]×σ) and 5 cm continuum overlaid in orange contours (levels: [4.5,10]×σ). SOFIA 37 μm contours are overlaid in black with the same contour levels as in the left-hand panels. 1.3 cm beam is shown in the lower left; 5 cm beam is shown in the lower right.
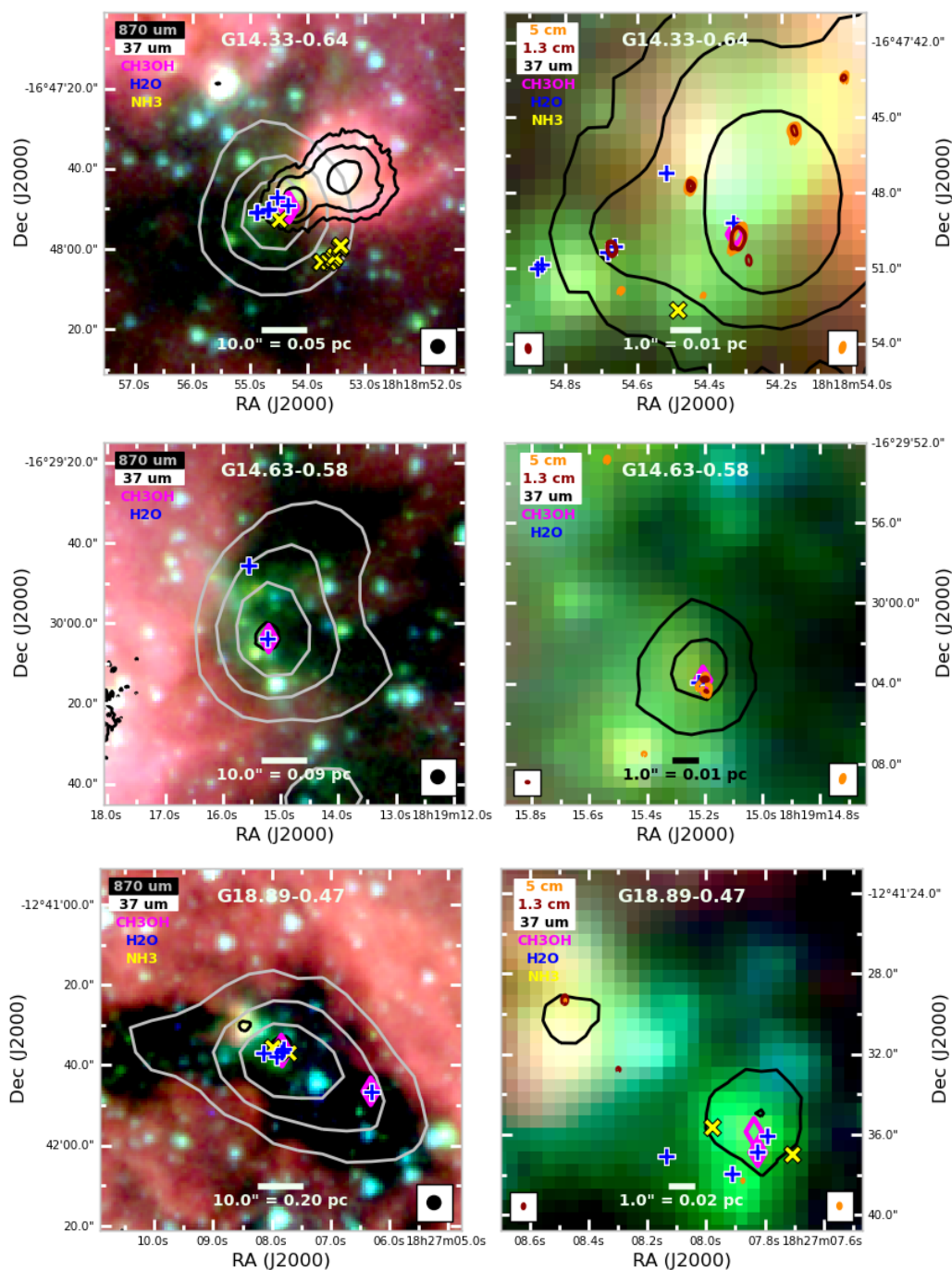
Fig. 4.2.— Same contour and marker system as in Figure 4.1. FOV for right-hand panels is unchanged; FOV for left-hand panels is 14″4 for G14.33−0.64 and 18″0 for the other two sources. ATLASGAL I_{peak} values are 12.98, 4.35, and 3.30 Jy beam^{-1} for G14.33−0.64, G14.63−0.58, and G18.89−0.47, respectively. SOFIA 37 μm scaled MAD values are 0.24, 0.22, 0.25 Jy beam^{-1}, respectively. 1.3 and 5 cm contour levels are [4.5,10]×σ for G14.33−0.64 and G18.89−0.47, and for 14.63−0.58 are [4.5,10,15]×σ at 1.3 cm and [4.5,15]×σ at 5 cm.
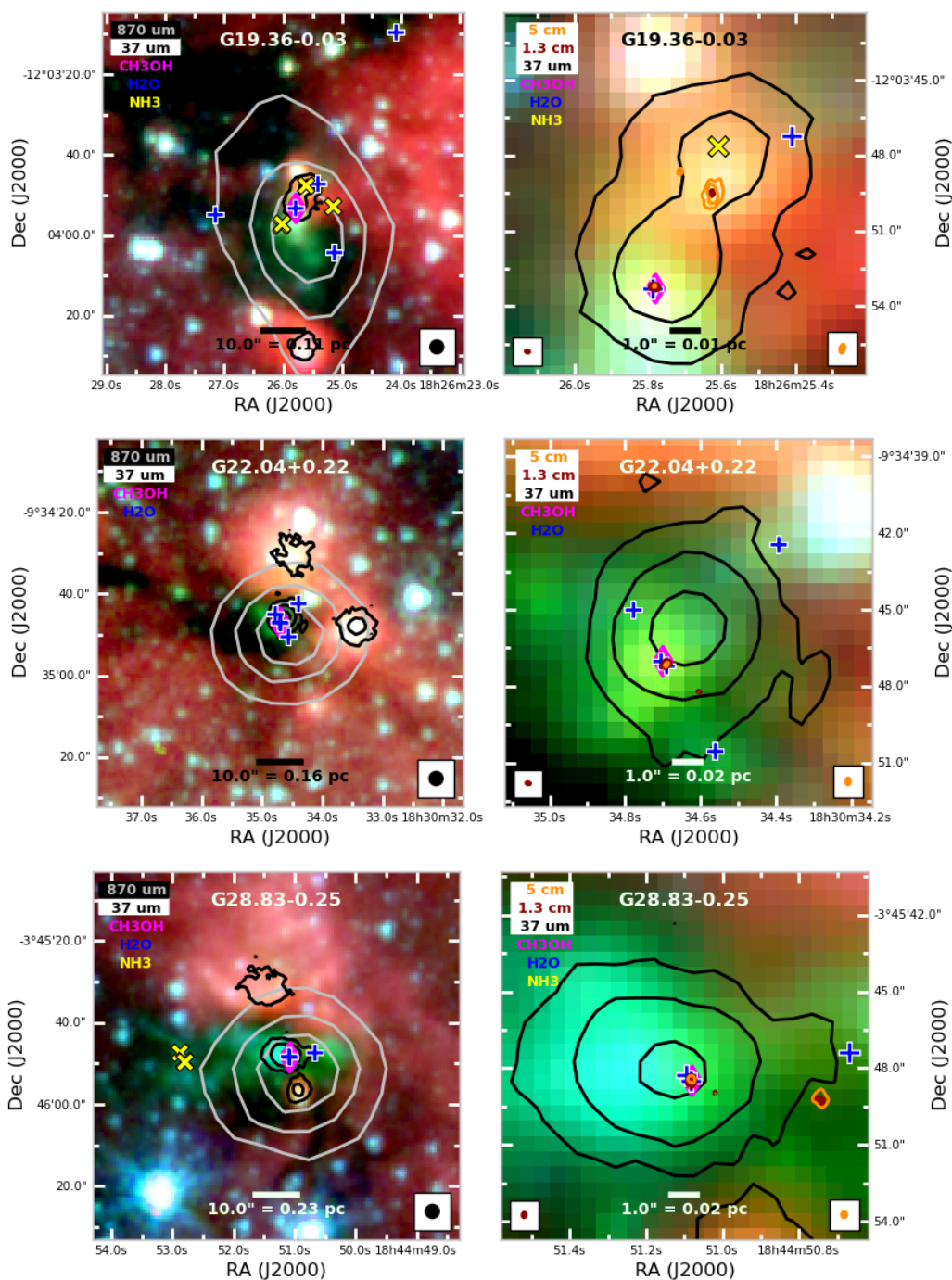
Fig. 4.3.— Same contour and marker system as in Figure 4.1. FOV for right-hand panels is unchanged; FOV for left-hand panels is 14.4″4 for all three sources. ATLASGAL I_{peak} values are 2.90, 3.33, and 4.08 Jy beam^{-1} for G19.36−0.03, G22.04+0.22, and G28.83−0.25, respectively. SOFIA 37 μm scaled MAD values are 0.46, 0.21, and 0.26 Jy beam^{-1}, respectively. Contour levels are [4.5,10]$\times\sigma$ for all three sources at both 1.3 and 5 cm, except for G28.83−0.25 at 5 cm, which shows only the 4.5 μm contour.

4.4.1 Centimeter Continuum Emission: Photometry and Properties

We find a total of 42 centimeter continuum detections within $1.'9$ of the pointing centers across our nine EGOs. Six of these detections have peak flux densities $>4.5\sigma$, but their flux densities cannot be fully recovered in our data because some of their emission is resolved out. We report the 36 centimeter continuum detections with constrained flux densities in Table 4.4, and the remaining six detections in Table 4.5. For the sources with resolved-out emission, Table 4.5 reports approximate center positions, measured peak intensities and approximate sizes at each band, and whether or not the source is coincident with any sources previously published in the literature; these sources are not discussed further in this paper.

For the remaining 36 sources, we determine their total flux density and size (if possible) using either aperture photometry or the `imfit` task in the Common Astronomy Software Applications (CASA) version 5.4.1-32 (McMullin et al. 2007). For sources with irregular or non-Gaussian morphology, we determined the total flux density inside the $2-3\sigma$ contour (exact contour levels were chosen based on source morphology and separability from other nearby sources), and then subtracted the product of the aperture size (in beams) and the background noise level (in Jy beam^{-1}). Compact Gaussian soruces were fit with 2-dimensional gaussians usint `imfit`. Fits were considered 'good' if the pixel values of the residual image were less than 3 times the rms of the residual, and if the fitted integrated flux density was greater than the fitted peak intensity; fits which did not meet these standards were iteratively improved until they did, usually by holding the major and minor axes of the gaussian fixed during the fit. For sources for which it was not clear whether aperture photometry or *imfit* would be more appropriate (e.g. any *potential* extended emission was at $<5\sigma$), we measured the integrated flux density using both aperture photometry and `imfit`, and compared results. If the `imfit` result did not meet the $3\times$rms criteria de-

spite iterative improvements, we used the aperture-photometry flux density results for that source. If the source could be successfully deconvolved from the beam with `imfit`, we report that deconvolved size in both milli-arcseconds (mas) and au in Table 4.4. Sizes in au are listed beneath the mas sizes in otherwise blank rows. If a source's angular size could not be successfully measured with `imfit`, its size is listed as 'unres' in the table. If we could only obtain a good fit for a source by fixing its major and minor axes to those of the synthesized beam, its size is listed as 'fixed.' We consider 'fixed' sources to be unresolved. If a source's flux density was measured using aperture photometry, we report an upper limit on its size; this upper limit is the size of the maximum extent of the polygonal aperture used to measure the flux density. For each EGO, the numbering order in Table 4.4 is determined by the 1.3 cm integrated flux density of each detection. The brightest 1.3 cm source in an EGO is CM1, the second-brightest is CM2, etc. Sources which are detected only at 5 cm and not at 1.3 cm are reported after all 1.3 cm sources, and are then reported in decreasing order of 5 cm flux density.

As reported in Table 4.4, we detect at least one source of centimeter continuum emission in every EGO at each wavelength, for a detection rate of 100% at both 1.3 cm and 5 cm. The number of continuum detections (1.3 and 5 cm combined) per EGO ranges from 1 to 11, with a median of 3. Across the entire EGO sample, we detect 18 continuum sources at both 1.3 cm and 5 cm, 5 continuum sources at 1.3 cm only, and 13 sources at 5 cm only. The general trend among our continuum detections is that sources detected at both wavelengths are stronger at both wavelengths, and sources detected in only one wavelength tend to be weak detections in that single wavelength. For the total sample of 36 centimeter continuum sources, 1.3 cm and 5 cm median flux densities are 120 μJy and 52 μJy, respectively. For the sources detected at both wavelengths, the median 1.3 cm and 5 cm flux densities are 181 μJy and 63 μJy, respectively. The median flux density of sources detected only at

1.3 cm is 69 μJy, and the median flux density of sources detected only at 5 cm is 29.3 μJy.

The centimeter continuum sources are generally compact – either a point source or less than $\sim$1″ in diameter. In 7 EGOs, the majority of the centimeter continuum emission is coincident with or within a few arcseconds of the brightest source at 37 μm. The exceptions are G10.29–0.13, which was a non-detection at 37 μm, and G18.89–0.47, in which there are centimeter continuum detections within the 5σ contour of the *second*-brightest 37 μm source, but none coincident with the brightest 37 μm source. Likewise, nearly all continuum detections are within the 5σ contour of the 870 μm emission (31/36, 86%); the sources that are not within the 870 μm emission are preferentially detected only at 5 cm.

Table 4.4 also reports the calculated 1.3–5 cm (6–22 GHz) spectral index (α, where $S_\nu \propto \nu^\alpha$) for each centimeter continuum detection. All spectral indices were calculated using a Monte-Carlo analysis to determine α and its uncertainty given two flux density values. For sources detected at both wavelengths, $\alpha \pm \Delta\alpha$ comes directly from the measured flux densities. For sources detected only at 1.3 cm, we calculate α using the 4σ upper limit at 5 cm as the 5 cm 'flux density,' and report the resulting spectral index as a lower limit. We use the same approach for sources detected only at 5 cm: we use the 1.3 cm 4σ upper limit as the 1.3 cm 'flux density,' and report the resulting spectral index as an upper limit. In total, for sources detected at both 1.3 cm and 5 cm, the spectral indices span -0.50 < α < 1.58, with a median value of α = 0.72 $\pm$ 0.53. The uncertainty in α_{median} is the median absolute deviation from the median. The nature of the centimeter continuum emission is discussed in § 4.4.1.

Table 4.4.   Properties of Compact Centimeter Continuum Sources

| EGO Source[a] Name | Position[b] (J2000) | | 1.3 cm Properties[c] | | 5 cm Properties[c] | | Spectral Index |
	RA (h m s)	Dec (° ' ")	Flux (μJy)	Size mas × mas (pa)	Flux (μJy)	Size mas × mas (pa)	(α)
G10.29CM1	18:08:49.359 (0.001)	−20:05:58.938 (0.009)	82 (13)	fixed	41 (7)	fixed	0.54 (0.18)
G10.34CM1	18:08:59.9859 (0.0006)	−20:03:35.61 (0.03)	209 (29)	357 × 146 (179) 571 × 234 au	35 (6)	fixed	1.38 (0.17)
CM2	18:08:59.983 (0.001)	−20:03:39.24 (0.03)	195 (35)	379 × 225 (34) 606 × 360 au	33 (6)	fixed	1.38 (0.20)
CM3	18:09:01.455 (0.001)	−20:03:38.71 (0.02)	88 (11)	fixed	< 28	⋯	> 0.89
G12.91CM1	18:13:48.265 (0.002)	−17:45:39.66 (0.03)	110 (18)	< 360 < 1620 au	130 (15)	unres	−0.13 (0.15)
CM2	18:13:48.260 (0.001)	−17:45:39.19 (0.01)	77 (13)	fixed	52 (8)	fixed	0.304 (0.169)
CM3	18:13:44.5899 (0.0008)	−17:45:21.17 (0.02)	< 52	⋯	82 (14)	unres	< −0.35
G14.33CM1	18:18:54.319 (0.003)	−16:47:49.80 (0.04)	1752 (26)	< 1100 < 1240 au	742 (17)	< 1600 < 1810 au	0.67 (0.02)
CM2	18:18:55.3712 (0.0002)	−16:47:31.322 (0.005)	429 (19)	unres	126 (11)	unres	0.95 (0.08)
CM3	18:18:54.6714 (0.0002)	−16:47:50.22 (0.01)	270 (21)	unres	< 28	⋯	> 1.75

Table 4.4—Continued

EGO Source[a] Name	Position[b] (J2000) RA (h m s)	Dec (° ′ ″)	1.3 cm Properties[c] Flux (μJy)	Size mas × mas (pa)	5 cm Properties[c] Flux (μJy)	Size mas × mas (pa)	Spectral Index (α)
CM4	18:18:54.4525 (0.0005)	−16:47:47.72 (0.02)	122 (11)	fixed	132 (13)	unres	−0.06 (0.10)
CM5	18:18:54.1650 (0.0007)	−16:47:45.54 (0.03)	85 (11)	fixed	158 (14)	< 1100 < 1240 au	−0.48 (0.12)
CM6	18:18:54.2905 (0.0007)	−16:47:50.69 (0.03)	83 (11)	fixed	< 28	...	> 0.84
CM7	18:18:54.0289 (0.0009)	−16:47:43.42 (0.03)	64 (11)	fixed	56 (7)	fixed	0.10 (0.16)
CM8	18:18:55.9115 (0.0007)	−16:48:32.03 (0.03)	< 46	...	64 (7)	fixed	< −0.26
CM9	18:18:54.418 (0.001)	−16:47:52.08 (0.04)	< 46	...	44 (7)	fixed	< 0.03
CM10	18:18:54.645 (0.001)	−16:47:51.87 (0.04)	< 46	...	40 (7)	fixed	< 0.101
CM11	18:18:53.579 (0.001)	−16:47:38.20 (0.05)	< 46	...	36 (7)	fixed	< 0.18
G14.63 CM1	18:19:15.2004 (0.0005)	−16:30:03.802 (0.003)	418 (38)	154 × 36 (100) 282 × 66 au	54 (7)	fixed	1.58 (0.12)
CM2	18:19:15.195 (0.002)	−16:30:04.375 (0.025)	72 (19)	< 280 < 512 au	53 (4)	< 850 < 1556 au	0.24 (0.21)
CM3	18:19:15.216 (0.001)	−16:30:04.13 (0.02)	< 73	...	44 (5)	fixed	< 0.39
CM4	18:19:14.2033 (0.0008)	−16:30:38.00 (0.03)	< 73	...	35 (5)	fixed	< 0.57
CM5	18:19:15.5382 (0.0006)	−16:29:52.87 (0.02)	< 73	...	27 (5)	fixed	< 0.77
CM6	18:19:15.411 (0.002)	−16:30:07.520 (0.025)	< 73	...	17 (3)	< 620 < 1135 au	< 1.13

Table 4.4—Continued

EGO Source[a] Name	Position[b] (J2000)		1.3 cm Properties[c]		5 cm Properties[c]		Spectral Index
	RA (h m s)	Dec (° ' ")	Flux (μJy)	Size mas × mas (pa)	Flux (μJy)	Size mas × mas (pa)	(α)
G18.89CM1	18:27:08.4814 (0.0004)	−12:41:29.30 (0.02)	137 (12)	fixed	39 (9)	fixed	0.97 (0.19)
CM2	18:27:08.7530 (0.0007)	−12:42:20.34 (0.03)	83 (12)	fixed	< 35	...	> 0.67
CM3	18:27:08.2986 (0.0009)	−12:41:32.76 (0.03)	63 (12)	fixed	< 35	...	> 0.46
CM4	18:27:07.8752 (0.0009)	−12:41:38.29 (0.03)	< 51	...	53 (9)	fixed	< −0.03
G19.36CM1	18:26:26.37742 (0.00004)	−12:04:19.9330 (0.0004)	2656 (23)	62 × 51 (128) 136 × 112 au	985 (14)	76 × 41 (157) 167 × 90 au	0.77 (0.01)
CM2	18:26:25.7827 (0.0006)	−12:03:53.235 (0.005)	213 (24)	115 × 57 (75) 253 × 125 au	39 (7)	fixed	1.31 (0.17)
CM3	18:26:25.711 (0.001)	−12:03:48.62 (0.03)	< 49	...	54 (7)	fixed	< −0.08
G22.04CM1	18:30:34.690 (0.002)	−09:34:47.12 (0.03)	179 (24)	< 600 < 2040 au	53 (11)	< 875 < 2975 au	0.94 (0.19)
CM2	18:30:37.268 (0.001)	−09:34:47.67 (0.03)	< 49	...	35 (7)	fixed	< 0.26
CM3	18:30:33.668 (0.001)	−09:34:56.58 (0.03)	< 49	...	34 (7)	fixed	< 0.28
G28.83CM1	18:44:51.084 (0.003)	−03:45:48.52 (0.04)	264 (13)	< 760 < 3650 au	75 (13)	unres	0.97 (0.14)

4.4.2   Maser Emission: Fitting Procedure and Properties

For each maser species, we perform 2D gaussian fitting to all maser emission in each channel which is within the FWHM of the 1.3 cm continuum primary beam. All masers were fit as point sources, i.e., they have their major and minor axes fixed to match the major and minor axes of the synthesized beam (see Tables 4.2 and 4.3 for synthesized beam parameters). This choice reflects our assumption that the maser emission is unresolved at the current angular resolution. We call each Gaussian fit a "maser spot," i.e., a single unresolved masing region in a single channel. As with the centimeter continuum emission, the peak of the residual image was required to be $<3\times$rms of the residual for the fit of each maser spot to be considered good. Some more complicated regions required iteratively fitting the maser spots while holding some maser-spot properties (namely position) fixed during the fit, but in most cases, iterative fitting was not necessary. We report all detections whose fitted peaks are $>5\sigma$, where σ is the rms of the specific channel in which each fit was performed.

Table 4.6 summarizes the overall maser properties for each EGO. Within each EGO, every maser spot that we report is assigned to a "Maser Group." Maser groups (column 4) are named for the centimeter continuum source with which they are associated, and for their maser species (e.g. the group of H_2O masers associated with the G14.63−0.58 centimeter continuum source CM1 is denoted "CM1-W1," while the CH_3OH emission associated with that same continuum source is denoted "CM1-M1"). A maser group is generally considered "associated" with a centimeter continuum source if any of its member spots are within $1''$ of the centimeter continuum. If a maser group is not associated with any centimeter continuum emission, it is denoted by "NC" (for "no centimeter continuum") and the maser species. For example, the group of H_2O masers in G14.63−0.58 to the northwest of CM1 is not associated with any centimeter continuum emission, and so is denoted "NC-

Table 4.4—Continued

| EGOSource[a] Name | Position[b] (J2000) | | 1.3 cm Properties[c] | | 5 cm Properties[c] | | Spectral Index |
	RA (h m s)	Dec (° ' ")	Flux (μJy)	Size mas × mas (pa)	Flux (μJy)	Size mas × mas (pa)	(α)
CM2	18:44:50.744 (0.003)	−03:45:49.32 (0.04)	178 (15)	< 890 < 4270 au	338 (22)	< 1414 < 6790 au	−0.50 (0.08)

[a]Source nomenclature is based on I_{peak} at 1.3 cm. Source 'a' is the brightest source at 1.3 cm, source 'b' is the second-brightest at 1.3 cm, etc. Sources which are not detected at 1.3 cm but are detected at 5 cm are listed after all 1.3 cm detections, in decreasing order of S_{5cm}.

[b]All positions are the peak 1.3 cm position, unless the source is not detected at 1.3 cm. In that case, the reported position is the position of the peak at 5 cm.

[c]Source properties are from either a) 2-dimensional Gaussian fitting using the CASA task imfit, or b) by-hand aperture photometry in CASAViewer. Sources with a listed angular size in mas, 'unres', or 'fixed' were fit with imfit; sources with an upper limit on angular size were measured using aperture photometry. A '<' in a 'Flux' column indicates a non-detection at that wavelength, in which case the reported value is the 4σ upper limit.

[d]All spectral indices were calculated using the au.spectralindex task in CASA. For sources detected at only one wavelength, we use the 4.5σ non-detection upper limit as an exact flux density "measurement," with 1σ errors, and then report the resulting spectral index as either an upper or a lower limit. For sources that are not detected at 5 cm, α is a lower limit; for sources not detected at 1.3 cm, α is an upper limit.

Table 4.5.   Sources Whose Flux Density Cannot be Recovered in One or Both Bands

EGO	Source[a] Name	1.3 cm Properties			5 cm Properties			Lit.?[b]
		RA (h m s)	Dec (° ′ ″)	Approx. Size[c] (″ × ″)	RA (h m s)	Dec (° ′ ″)	Approx. Size[c] (″ × ″)	
G10.29−0.13	NR-CM1	18:08:51	−20:06:01	22×15	18:08:51	−20:06:01	22×15	C11
G10.34−0.14	NR-CM1	18:09:01	−20:04:29	48×24	18:09:01	−20:04:36	58×31	G02
	NR-CM2	18:09:00	−20:04:03	26×12	...	...	...	G00
	NR-CM3	18:09:02	−20:03:03	7×4	18:09:02	−20:03:04	7×3	D15
G14.33−0.64	NR-CM1	...	...	...	18:18:53	−16:47:43	5×5	H94
G19.36−0.03[d]	NR-CM1	18:26:25.6	−12:03:49.5	2.1×1.4	18:26:25.5	−12:03:49	2×2	C11

[a]Sources are listed here as "NR-CM1, NR-CM2, ..." to indicate that their flux density is not recoverable from our data. While we cannot definitively say whether or not these sources are associated with our target EGOs, we also cannot recover their flux density or morphology, and so we do not analyze these sources further.

[b]If the position of the source is consistent with a previous literature publication (within our estimated size for each source), that publication is listed here. C11: Cyganowski et al. (2011b); D15: Deharveng et al. (2015); G00: Goedhart et al. (2000); G02: Goedhart et al. (2002); H94: Hughes & MacLeod (1994)

[c]These approximate sizes are not based on Gaussian fitting, which is not appropriate for these sources. Instead the sizes are based on the apparent morphology of the source in our data. This means that they may underestimate source sizes in one or more direction, and should only be treated as approximate.

[d]Though the dimensions of this source are lower than its LAS (1″7), we nonetheless were unable to recover its flux density. This is due in part to its decreased S/N at scales ≳1″. Although there does appear to be some emission at scales ≳1″ at 1.3 cm and ≳2″ at 5 cm, it is all at <3σ and can neither be fit nor adequately extracted from the noise using aperture photometry.

W1." The "NC" numbering scheme increases with increasing Right Ascension within a given EGO. If a given species and group lists " $\cdots$ " this means that the maser group in question was not detected during that observing epoch.

We detect at least two sites of 22 GHz H_2O maser emission and at least one site of 6.7 GHz CH_3OH maser emission in every EGO, for detection rates of 100% for both species. In most cases, 22 GHz H_2O maser emission had previously detected toward these EGOs in single-dish data (Cyganowski et al. 2013), but not in interferometric studies. The exceptions are G19.36−0.03, which was not detected by Cyganowski et al. (2013), and G14.63−0.58, for which NC-W1 was detected in the VLBI observations of Sanna et al. (2018). Likewise, 6.7 GHz CH_3OH masers have been previously detected toward most sources using either the VLA (Cyganowski et al. 2009) or Australia Telescope Compact Array (ATCA; Green et al. 2010). The exception is G14.33−0.64, for which the observations reported in this work are, to the best of our knowledge, the first reported interferometric observations of 6.7 GHz CH_3OH masers in this source. We detect NH_3 (3,3) maser emission in five of our nine EGOs (56% detection rate), but do not detect any NH_3 (6,6) maser emission in any EGOs at the current sensitivity and angular resolution. Our surface brightness sensitivities (see table notes in Tables 4.2 and 4.3) preclude the possibility of observing thermal line emission for these molecules.

The number of H_2O maser spots per EGO ranges from 2 to 7, with a median of 5; the number of NH_3 (3,3) maser spots per EGO is 2-3, with a median of 2. (Note: for the purposes of NH_3 maser statistics, G14.33−0.64 NC-A1 is treated as a single maser group, despite the fact that it exhibits arc-like morphology, because the individual components in this arc are almost all blended at this angular and velocity resolution.) In most EGOs, we detect only one site of 6.7 GHz CH_3OH maser emission; the lone exception is G18.89−0.47, which has three sites of 6.7 GHz maser emission. The majority of the H_2O masers are not

associated with detectable centimeter continuum emission, but strong centimeter continuum emission *is* strongly associated with H_2O masers: either CM1 or CM2 (the strongest and second-strongest centimeter continuum source) is associated with H_2O maser emission in 8 out of 9 EGOs. The 6.7 GHz CH_3OH masers are nearly always associated with either CM1 or CM2 (the brightest or second-brightest 1.3 cm continuum source) for a given EGO. The lone exception to both the H_2O and CH_3OH trends is G18.89–0.47, in which only CM4 has associated H_2O masers, and none of the three CH_3OH maser detections is associated with detectable centimeter continuum emission.

The spatial distribution of the masers in our sample varies by molecular species. H_2O masers are typically found $\sim 3''$-$8''$ (but as much as $\sim 50''$) away from the pointing center, and NH_3 (3,3) masers are more bimodally distributed, with about half the detections $\sim 4''$ from the pointing center and half $\sim 20''$ away. The 6.7 GHz CH_3OH masers are generally located at or near the center of the ATLASGAL clump hosting the EGO, and are usually also coincident with the brightest 37 μm source in the field. The exception to all of these trends is again G18.89–0.47, in which the CH_3OH maser NC-M1 is located $\sim 20''$ to the southwest of the nearest 37 μm source, and well away from the center of the ATLASGAL clump. G10.29–0.13 was not detected at 37 μm in Towner et al. (2019), so it is excluded from the trends related to 37 μm emission.

As noted above, for those sources which were observed twice in K-band, the two H_2O maser data sets are analyzed separately, due to the possibility of kinematic or spatial changes in the maser emission during the 18-month period between the first and second observing epochs. For these sources, the detection statistics described above includes both epochs. The variation of maser emission with time in these data sets – as well as between our maser data and observations from the literature – are discussed in § 4.5.9.

Table 4.6. Summary of Maser Emission for All Sources

EGO	Maser[a] Species	Obs[b] Epoch	Comp[c] Name	Centroid Position[d] RA (h m s)	Dec (° ′ ″)	V_{Min}, V_{Max}^e (km/s)	V_{Peak}^f (km/s)	S_{Peak}^g (Jy)
G10.29–0.13	CH$_3$OH	2018A	CM1-M1	18:08:49.363	-20:05:58.96	1.25, 20.75	8.00	3.88 (0.01)
	H$_2$O	2017B	CM1-W1	18:08:49.364	-20:05:58.98	5.50, 14.00	10.25	1.67 (0.02)
			NC-W1	18:08:46.669	-20:05:51.47	6.50, 21.25	12.50	23.1 (0.1)
			NC-W2	18:08:49.300	-20:06:03.53	-12.00, 15.75	15.00	0.43 (0.01)
			NC-W3	18:08:49.424	-20:05:58.34	14.25, 17.75	15.00	4.18 (0.01)
			NC-W4	18:08:52.464	-20:06:02.62	6.50, 22.00	8.00	9.64 (0.02)
		2018A	CM1-W1	18:08:49.366	-20:05:58.99	5.75, 12.00	6.50	2.88 (0.03)
			NC-W1	18:08:46.670	-20:05:51.47	2.75, 13.00	9.50	8.53 (0.04)
			NC-W2	18:08:49.301	-20:06:03.54	-2.25, 9.50	0.75	0.38 (0.03)
			NC-W3	18:08:49.421	-20:05:58.34	17.00, 17.50	17.25	0.28 (0.03)
			NC-W4	18:08:52.465	-20:06:02.77	8.00, 21.75	21.00	3.75 (0.03)
G10.34–0.14	CH$_3$OH	2018A	CM1-M1	18:08:59.986	-20:03:35.45	4.50, 20.50	11.50	10.2 (0.1)
	H$_2$O	2017B	CM1-W1	18:08:59.986	-20:03:35.67	-1.00, 23.75	17.75	13.0 (0.1)
			CM2-W1	18:08:59.990	-20:03:39.00	-34.25, 49.25	13.25	9.86 (0.01)
			NC-W1	18:08:59.967	-20:03:36.97	13.00, 15.50	13.75	6.25 (0.01)
			NC-W2	18:09:00.311	-20:03:39.24	14.50, 16.00	15.25	0.100 (0.01)
			NC-W3	18:09:00.792	-20:04:18.00	0.50, 23.25	10.25	0.497 (0.008)
			NC-W4	18:09:02.320	-20:03:19.41	5.50, 20.75	11.50	1.40 (0.01)
			NC-W5	18:09:03.074	-20:03:02.27	40.75, 41.75	41.25	0.093 (0.007)
	NH$_3$	2017B	NC-A1	18:08:59.653	-20:03:33.14	14.25, 15.00	14.50	0.168 (0.008)
			NC-A2	18:09:01.567	-20:03:26.60	12.00, 12.50	12.25	0.08 (0.01)
G12.91–0.03	CH$_3$OH	2018A	CM2-M1	18:13:48.260	-17:45:39.18	50.5, 61.75	59.5	23.1 (0.1)

Table 4.6—Continued

EGO	Maser[a] Species	Obs[b] Epoch	Comp[c] Name	Centroid Position[d] RA (h m s)	Dec (° ′ ″)	V_{Min}, V_{Max}^e (km/s)	V_{Peak}^f (km/s)	S_{Peak}^g (Jy)
	H_2O	2017B	CM1-W1	18:13:48.265	-17:45:39.79	61.00, 71.75	64.75	3.77 (0.02)
			NC-W1	⋯	⋯	⋯	⋯	⋯
			NC-W2	18:13:47.282	-17:45:36.47	-4.75, 96.50	30.75	3.59 (0.02)
			NC-W3	⋯	⋯	⋯	⋯	⋯
			NC-W4	⋯	⋯	⋯	⋯	⋯
		2018A	CM1-W1	18:13:48.265	-17:45:39.67	62.50, 73.75	70.75	3.94 (0.02)
			NC-W1	18:13:46.665	-17:45:25.81	49.00, 60.00	59.25	0.998 (0.015)
			NC-W2	18:13:47.282	-17:45:36.46	20.25, 40.75	20.75	0.24 (0.02)
			NC-W3	18:13:47.499	-17:45:42.11	44.50, 46.75	46.00	1.47 (0.02)
			NC-W4	18:13:48.323	-17:45:37.45	11.75, 14.50	13.50	1.04 (0.02)
G14.33–0.64	CH_3OH	2018A	CM1-M1	18:18:54.324	-16:47:49.66	20.25, 24.25	22.25	0.640 (0.005)
	H_2O	2017B	CM1-W1	18:18:54.334	-16:47:49.19	20.50, 22.25	21.25	0.298 (0.008)
			CM3-W1	18:18:54.667	-16:47:50.20	15.75, 33.75	32.75	2.84 (0.01)
			NC-W1	18:18:54.519	-16:47:48.23	6.25, 16.75	14.75	0.235 (0.008)
			NC-W2	18:18:54.871	-16:47:50.95	21.00, 23.50	21.50	0.073 (0.007)
	NH_3	2017B	NC-A1	18:18:53.524	-16:48:01.27	23.00, 24.50	23.25	0.169 (0.053)
			NC-A2	18:18:54.487	-16:47:52.66	20.25, 21.50	21.00	0.027 (0.006)
G14.63–0.58	CH_3OH	2018A	CM1-M1	18:19:15.205	-16:30:03.83	24.25, 26.00	25.00	4.31 (0.01)
	H_2O	2018A	CM1-W1	18:19:15.220	-16:30:03.97	21.50, 31.00	29.25	2.29 (0.02)
			NC-W1	18:19:15.542	-16:29:45.78	15.75, 21.00	16.50	1.20 (0.02)
G18.89–0.47	CH_3OH	2018A	NC-M1	18:27:06.313	-12:41:46.52	73.25, 74.75	73.50	0.169 (0.006)
			NC-M2	18:27:07.823	-12:41:36.90	72.00, 73.25	72.50	0.271 (0.006)

Table 4.6—Continued

EGO	Maser[a] Species	Obs[b] Epoch	Comp[c] Name	Centroid Position[d] RA (h m s)	Dec (° ′ ″)	V_{Min}, V_{Max}^e (km/s)	V_{Peak}^f (km/s)	S_{Peak}^g (Jy)
	H$_2$O	2017B	NC-M3	18:27:07.859	-12:41:36.56	52.50, 65.50	55.50	2.59 (0.01)
			CM4-W1	18:27:07.910	-12:41:37.98	54.75, 57.50	56.50	0.024 (0.007)
			NC-W1	18:27:06.292	-12:41:46.79	42.25, 66.50	47.50	1.29 (0.01)
			NC-W2	18:27:07.789	-12:41:36.12	64.75, 66.50	65.25	0.052 (0.006)
			NC-W3	18:27:07.824	-12:41:36.88	51.25, 57.75	52.25	0.711 (0.007)
			NC-W4	18:27:07.973	-12:41:37.73	55.50, 57.00	56.50	0.292 (0.008)
	NH$_3$	2017B	NC-A1	18:27:07.705	-12:41:37.01	65.50, 66.50	66.00	0.224 (0.008)
			NC-A2	18:27:07.978	-12:41:35.63	63.50, 66.25	65.00	0.113 (0.009)
G19.36–0.03	CH$_3$OH	2018A	CM2-M1	18:26:25.781	-12:03:53.27	24.00, 30.25	25.25	23.0 (0.1)
	H$_2$O	2017B	CM2-W1	18:26:25.788	-12:03:53.31	19.50, 21.25	20.25	0.71 (0.02)
			NC-W1	18:26:24.086	-12:03:09.58	12.25, 13.00	12.75	0.416 (0.018)
			NC-W2	18:26:25.131	-12:04:04.29	25.50, 26.00	25.75	0.077 (0.014)
			NC-W3	18:26:25.409	-12:03:47.25	24.50, 25.75	25.00	0.371 (0.017)
			NC-W4	18:26:27.150	-12:03:54.91	-9.25, 6.00	-5.75	0.580 (0.017)
	H$_2$O	2018A	CM2-W1	18:26:25.787	-12:03:53.32	19.75, 24.25	21.75	0.235 (0.023)
			NC-W1	⋯	⋯	⋯	⋯	⋯
			NC-W2	⋯	⋯	⋯	⋯	⋯
			NC-W3	18:26:25.421	-12:03:47.09	16.75, 26.00	25.25	0.27 (0.02)
			NC-W4	18:26:27.148	-12:03:54.92	-5.00, -4.00	-4.50	0.230 (0.018)
	NH$_3$	2017B	NC-A1	18:26:25.148	-12:03:52.88	25.50, 26.25	25.75	0.094 (0.011)
			NC-A2	18:26:25.609	-12:03:47.65	25.75, 26.50	26.00	0.198 (0.010)
			NC-A3	18:26:26.018	-12:03:57.27	26.50, 28.00	27.50	0.34 (0.01)

We report detailed, per-channel fit results for all EGOs, species, and epochs in our on-line tables. These results include the maser group with which each maser is associated, velocity of the channel in which each fit was performed, fitted position, and fitted flux density and uncertainty. Fitted sizes are not reported, since all masers were fit as point sources. Table 4.7 shows abbreviated versions of the per-channel fit results for G10.34−0.14 as an example of the information contained in the online tables.

Table 4.6—Continued

EGO	Maser[a] Species	Obs[b] Epoch	Comp[c] Name	Centroid Position[d] RA (h m s)	Dec (° ′ ″)	V_{Min}, V_{Max}[e] (km/s)	V^f_{Peak} (km/s)	S^g_{Peak} (Jy)
	NH_3	2018A	NC-A1	18:26:25.148	-12:03:52.89	25.50, 26.00	25.50	0.061 (0.007)
			NC-A2	18:26:25.607	-12:03:47.67	25.75, 26.50	26.00	0.178 (0.018)
			NC-A3	18:26:26.017	-12:03:57.23	26.75, 28.00	27.25	0.31 (0.01)
G22.04+0.22	CH_3OH	2018A	CM1-M1	18:30:34.698	-09:34:47.00	44.50, 55.50	54.50	9.31 (0.01)
	H_2O	2017B	CM1-W1	18:30:34.691	-09:34:47.20	43.75, 54.75	52.75	10.1 (0.1)
			NC-W1	18:30:34.394	-09:34:42.46	54.25, 58.25	55.00	0.840 (0.010)
			NC-W2	18:30:34.561	-09:34:50.53	50.00, 52.25	51.50	2.07 (0.01)
			NC-W3	18:30:34.776	-09:34:45.00	47.00, 48.25	47.25	0.08 (0.01)
	H_2O	2018A	CM1-W1	18:30:34.691	-09:34:47.21	44.25, 60.00	46.25	7.40 (0.02)
			NC-W1	...	...	...	...	...
			NC-W2	...	...	...	...	...
			NC-W3	...	...	...	...	...
G28.83−0.25	CH_3OH	2018A	CM1-M1	18:44:51.084	-03:45:48.44	79.50, 94.00	83.50	61.4 (0.1)
	H_2O	2017B	CM1-W1	18:44:51.086	-03:45:48.45	72.75, 101.75	85.00	2.47 (0.01)
			NC-W1	18:44:50.678	-03:45:47.41	87.75, 88.00	87.75	0.034 (0.007)
	NH_3	2017B	NC-A1	18:44:52.794	-03:45:49.67	86.00, 86.75	86.50	0.192 (0.007)
			NC-A2	18:44:52.876	-03:45:47.43	85.00, 88.00	86.75	0.177 (0.007)

[a]The molecular species of the maser emission. Emission denoted "NH_3" refers exclusively to the NH_3 (3,3) metastable state, as we did not detect any NH_3 (6,6) emission with these observations.

[b]The VLA scheduling semester in which the listed observations were taken. Exact dates for each observation can be found in Tables 4.2 & 4.3.

[c]Name of the maser group for which the data are reported. Maser components are named for the centimeter continuum source with which they are associated, and for their maser species. If a maser group is not associated with any centimeter continuum emission, it is named "NC" (for "no centimeter continuum") and the maser species. The "NC" numbering scheme increases with increasing Right Ascension within a given EGO.

[d]The emission-weighted position of each maser group.

[e]The minimum and maximum velocity at which maser emission of a given species is detected in each group.

[f]The velocity at which the brightest individual maser in each group appears, as determined by the integrated flux density of its 2D Gaussian fit.

[g]The integrated flux density of the brightest individual maser in each group, as determined by its 2D Gaussian fit.

Table 4.7.   G10.34−0.14 Maser Emission: 2D Gaussian Fit Results[a]

Num[b]	Comp[c] Name	Velocity[d] (km/s)	RA[e] (h m s)	Dec[e] (° ′ ″)	Flux[f] (Jy)
22 GHz H₂O					
1	CM2-W1	-34.25	18:08:59.9775	-20:03:39.094	0.027 (0.006)
2	CM2-W1	-34.00	18:08:59.9763	-20:03:39.167	0.079 (0.009)
3	CM2-W1	-33.75	18:08:59.9784	-20:03:39.148	0.184 (0.008)
4	CM2-W1	-33.50	18:08:59.9783	-20:03:39.143	0.446 (0.009)
5	CM2-W1	-33.25	18:08:59.9784	-20:03:39.139	0.923 (0.008)
6	CM2-W1	-33.00	18:08:59.9785	-20:03:39.139	1.39 (0.01)
7	CM2-W1	-32.75	18:08:59.9785	-20:03:39.142	1.33 (0.01)
8	CM2-W1	-32.50	18:08:59.9787	-20:03:39.140	1.08 (0.01)
9	CM2-W1	-32.25	18:08:59.9790	-20:03:39.141	0.998 (0.008)
10	CM2-W1	-32.00	18:08:59.9790	-20:03:39.141	1.01 (0.01)
6.7 GHz CH₃OH					
1	CM1-M1	+4.50	18:08:59.9878	-20:03:35.647	0.060 (0.005)
2	CM1-M1	+4.75	18:08:59.9874	-20:03:35.653	0.697 (0.006)
3	CM1-M1	+5.00	18:08:59.9874	-20:03:35.653	0.970 (0.006)
4	CM1-M1	+5.25	18:08:59.9872	-20:03:35.647	0.237 (0.006)
5	CM1-M1	+5.50	18:08:59.9872	-20:03:35.655	0.139 (0.006)
6	CM1-M1	+5.75	18:08:59.9893	-20:03:35.637	0.272 (0.006)
7	CM1-M1	+6.00	18:08:59.9903	-20:03:35.635	0.994 (0.006)
8	CM1-M1	+6.25	18:08:59.9896	-20:03:35.636	0.654 (0.007)
9	CM1-M1	+6.50	18:08:59.9886	-20:03:35.638	0.376 (0.006)
10	CM1-M1	+6.75	18:08:59.9878	-20:03:35.638	0.895 (0.006)
NH₃ (3,3)					
1	NC-A2	+12.00	18:09:01.5676	-20:03:26.635	0.035 (0.007)
2	NC-A2	+12.25	18:09:01.5680	-20:03:26.611	0.08 (0.01)
3	NC-A2	+12.50	18:09:01.5655	-20:03:26.518	0.03 (0.02)

Figures 4.4 through 4.20 show "spot maps" of the maser emission in each EGO. Each EGO has one overview panel, labeled with the EGO name only, which shows the 37 μm emission as a greyscale background with 37 μm contours overlaid in light yellow, and maser emission overlaid using the symbol scheme described above. Additional greyscale images are shown for individual maser groups, and are labeled with both the EGO name and the maser group name. The overview panels show the position and peak velocity for each maser group as reported in Table 4.6; the greyscale images show a separate symbol for each maser spot in a maser group (i.e. what is reported in Table 4.7), color-coded by velocity. The background greyscale is 1.3 cm if there is a 1.3 cm continuum detection associated with that maser group, and 5 cm if there is a 5 cm continuum detection. Maser groups with both 1.3 cm and 5 cm continuum associations have one panel for each wavelength. If present, 1.3 cm emission is also overlaid in black contours, and 5 cm emission is overlaid in light grey. If a maser group has no centimeter continuum emission at all, the greyscale background is 1.3 cm by default.

4.5 Analysis

In this section we discuss the nature of the continuum and maser emission in our sample as a whole. In § 4.5.1, we discuss the distribution of spectral indices among our sample, how this compares to similar samples, and what this implies about the general nature of weak, compact/unresolved continuum emission in our EGOs. In § 4.5.2, we examine how our continuum detections compare to established observational relations between various source properties.

Table 4.7—Continued

Num[b]	Comp[c] Name	Velocity[d] (km/s)	RA[e] (h m s)	Dec[e] (° ′ ″)	Flux[f] (Jy)
4	NC-A1	+14.25	18:08:59.6531	-20:03:33.136	0.088 (0.007)
5	NC-A1	+14.50	18:08:59.6533	-20:03:33.141	0.168 (0.008)
6	NC-A1	+14.75	18:08:59.6536	-20:03:33.131	0.124 (0.008)
7	NC-A1	+15.00	18:08:59.6543	-20:03:33.129	0.039 (0.008)

[a]This table shows the velocity, position, and flux density of each maser fit within a given data cube for G10.34–0.14. This specific table is truncated at no more than 10 lines per maser species; full tables for all sources can be found in the online materials. The NH_3 (3,3) results for this particular source only show 7 components because the NH_3 (3,3) emission in this source only spans 7 channels.

[b]This number refers to each individual 2D Gaussian fit within the data cube. Fits are performed separately for each spatial component of emission ("maser spot") within each channel.

[c]The name of the "maser group" with which each maser is associated. Maser components are named for the centimeter continuum source with which they are associated, and for their maser species. If a maser group is not associated with any centimeter continuum emission, it is named "NC" (for "no centimeter continuum") and the maser species. The "NC" numbering scheme increases with increasing Right Ascension within a given EGO

[d]The velocity of the channel(s) in which the fit(s) was performed. If multiple maser spots were fit within the same channel, the fit for each spot is listed separately, in alphabetical and numerical order according to group name.

[e]J2000 coordinates of each maser spot, as returned by `imfit`.

[f]The integrated flux density of the 2D Gaussian fit to the maser spot.
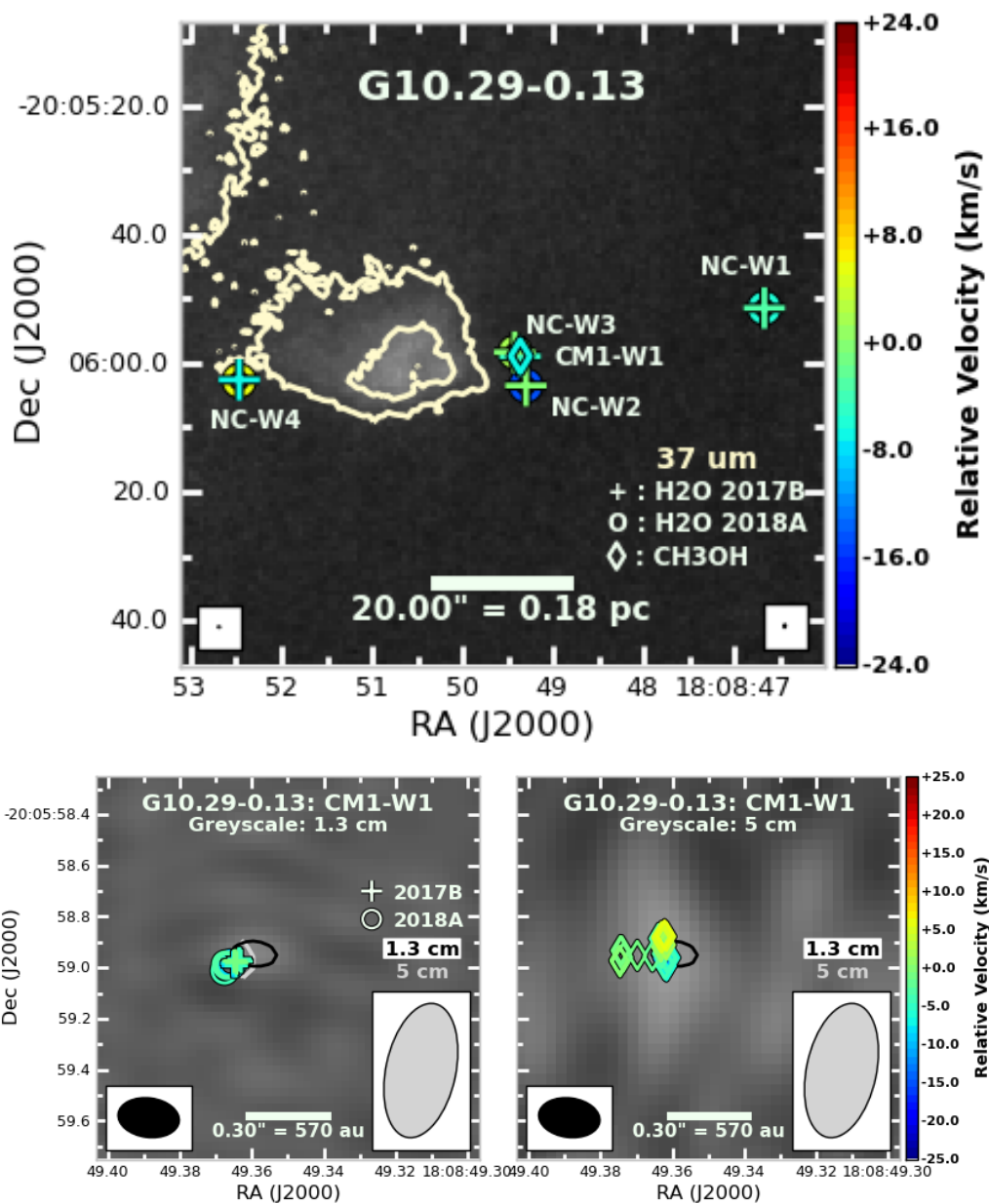
Fig. 4.4.— Maser spot maps for G10.29–0.13. Masers are color-coded by velocity in most panels. In the full FOV (100″), maser clumps are color-coded by peak velocity only, and 37 μm contour levels are [5,15,45]$\times\sigma$, where σ = 0.26 Jy beam^{-1} is the 37 μm scaled MAD. The background greyscale is 37 μm SOFIA data. In the CM1-W1 image, continuum contour levels are [4.5,10]$\times\sigma$ at both 1.3 cm (black) and 5 cm (silver), and the FOV is 1″.5. H_2O maser data from observing epoch 2018.1 (Semester 2017B) are shown with + symbols, and H_2O maser data from epoch 2019.6 (Semester 2018A) are shown with ○. The background greyscale is 1.3 cm in the left-hand panel, and 5 cm in the right-hand panel. Maser symbols are color-coded according to velocity relative to source V_{LSR} (14.0 km s^{-1}).

Fig. 4.5.— Maser spot maps for G10.29−0.13, continued. The FOV is 1″.5 for all four panels. Background greyscale is 1.3 cm in all cases; no contours are shown because there is no continuum emission above 4.5 σ in these FOV. H_2O maser data from observing epoch 2018.1 (Semester 2017B) is shown with + symbols, and H_2O maser data from epoch 2019.6 (Semester 2018A) is shown with ○. Maser symbols are color-coded according to velocity relative to source V_{LSR} (14.0 km s^{-1}).
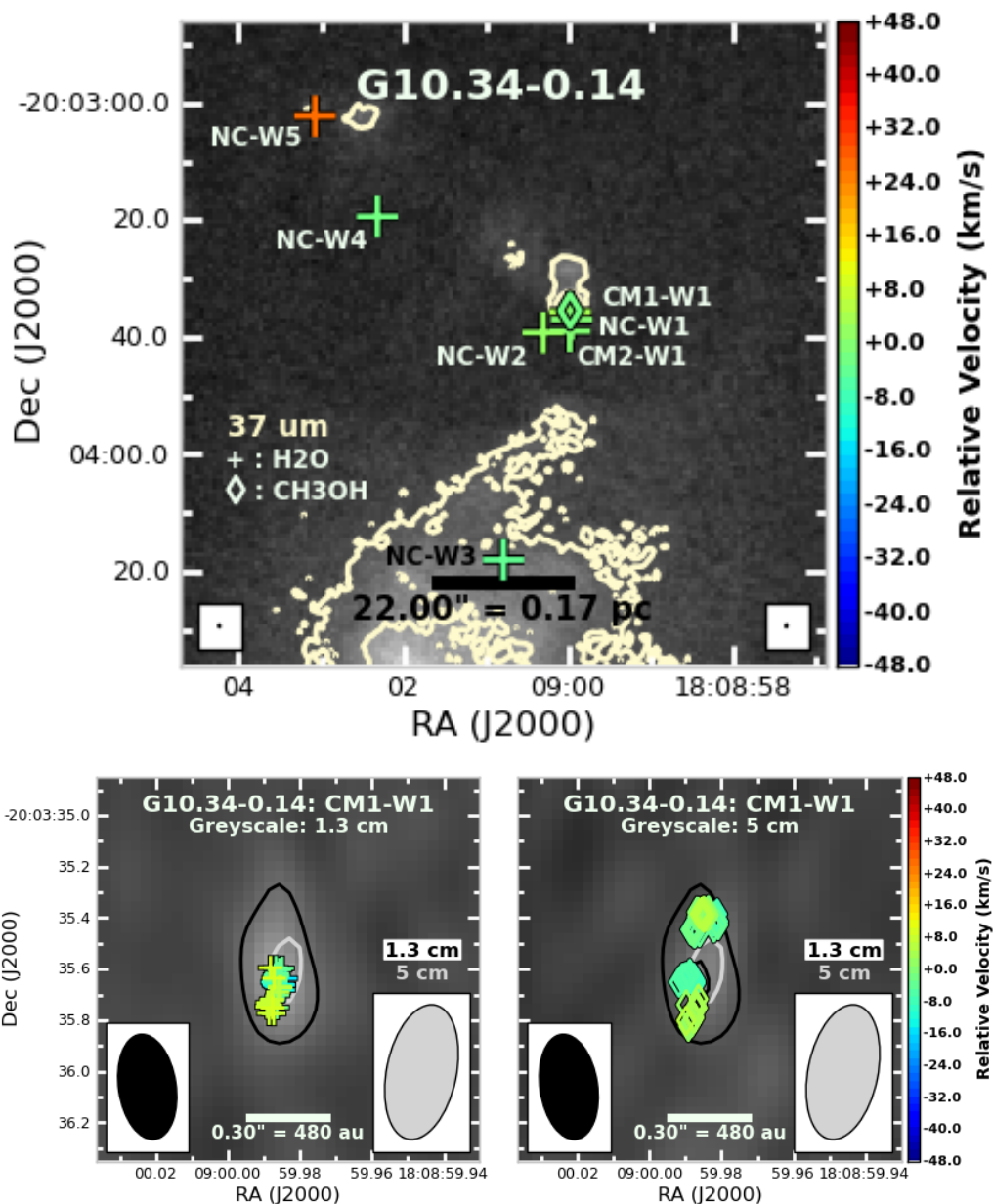
Fig. 4.6.— Maser spot maps for G10.34−0.14. Masers are color-coded by velocity in most panels. In the full FOV (110″), maser clumps are color-coded by peak velocity only, and 37 μm contour levels are [6,15,45]×σ, where σ = 0.30 Jy beam^{-1} is the 37 μm scaled MAD. The background greyscale is 37 μm SOFIA data. In the CM1-W1 image, contour levels are [4.5,10]×σ at both 1.3 cm (black) and 5 cm (silver), and the FOV is 1″.5. The background greyscale is 1.3 cm in the left-hand panel, and 5 cm in the right-hand panel. Maser symbols are color-coded according to velocity relative to source V$_{LSR}$ (12.0 km s^{-1}).
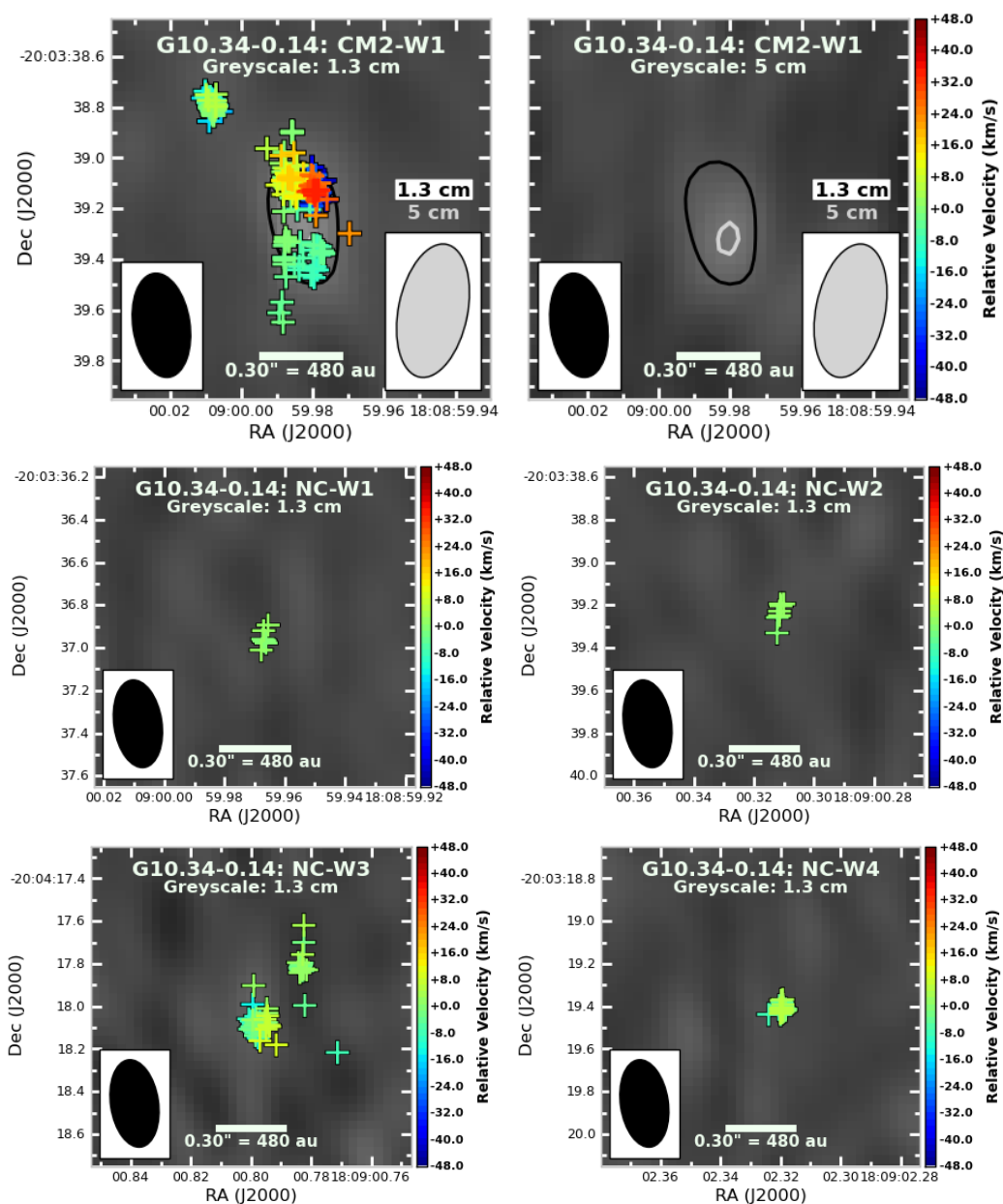
Fig. 4.7.— Maser spot maps for G10.34−0.14, continued. For CM2-W1, the background greyscale is 1.3 cm in the left-hand panel and 5 cm in the right-hand panel, and contour levels are [4.5,10]×σ for both wavelengths. FOV is 1.″5 in all cases. For all "NC" panels, the background greyscale is 1.3 cm continuum, and no contours are shown because there is no emission above 4.5 σ. Maser symbols are color-coded according to velocity relative to source V_{LSR} (12.0 km s^{-1}).
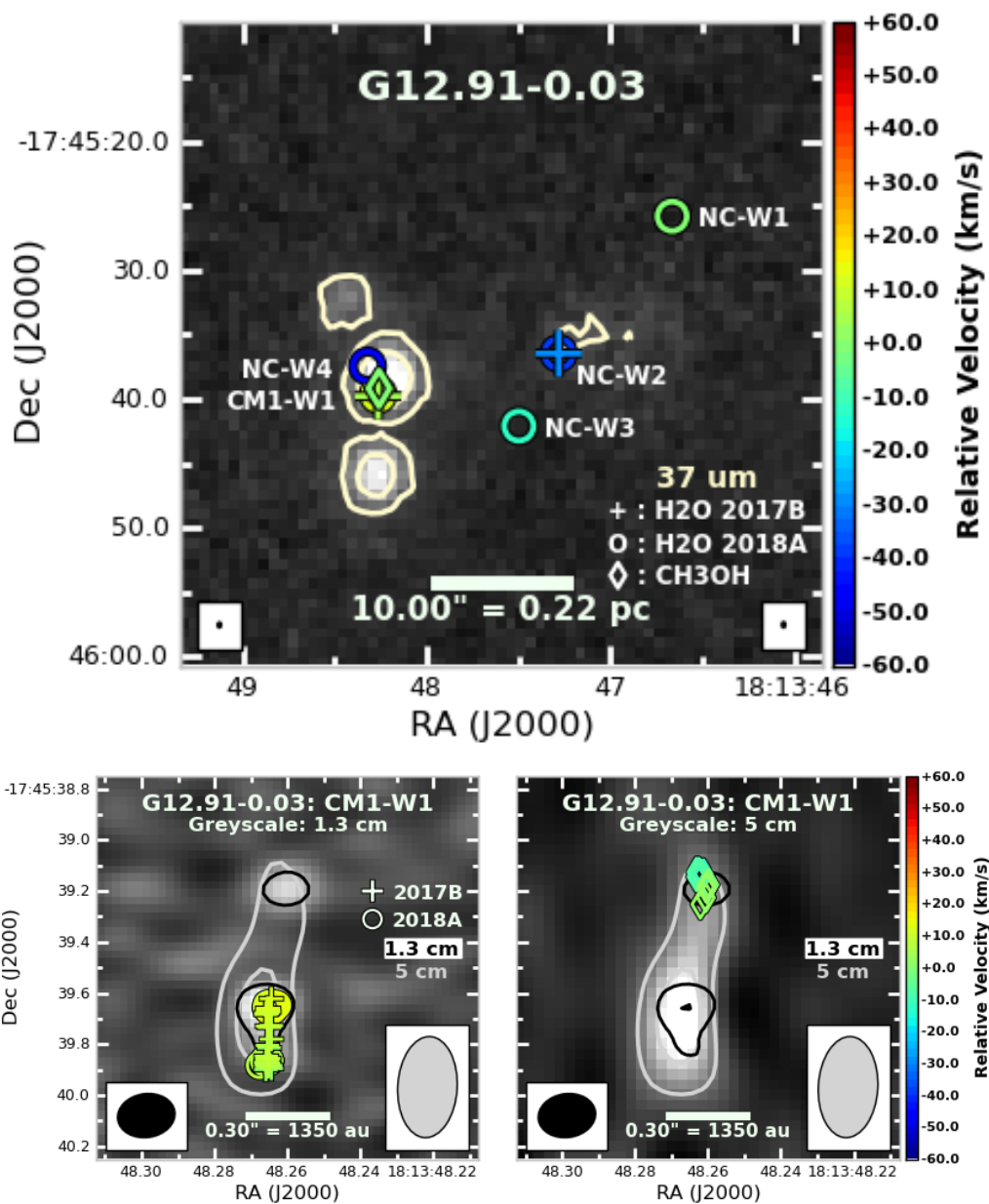
Fig. 4.8.— Maser spot maps for G12.91−0.03. Masers are color-coded by velocity in most panels. In the full FOV (50″), maser clumps are color-coded by peak velocity only, and 37 μm contour levels are [5,15,45]×σ, where $\sigma = 0.18$ Jy beam^{-1} is the 37 μm scaled MAD. The background greyscale is 37 μm SOFIA data. In the CM1-W1 image, continuum contour levels are [4.5,10]×σ at both 1.3 cm (black) and 5 cm (silver), and the FOV is 1.″5. H_2O maser data from observing epoch 2018.1 (Semester 2017B) are shown with + symbols, and H_2O maser data from epoch 2019.6 (Semester 2018A) are shown with ∘. The background greyscale is 1.3 cm in the left-hand panel, and 5 cm in the right-hand panel. Maser symbols are color-coded according to velocity relative to source V$_{LSR}$ (57.0 km s^{-1}).
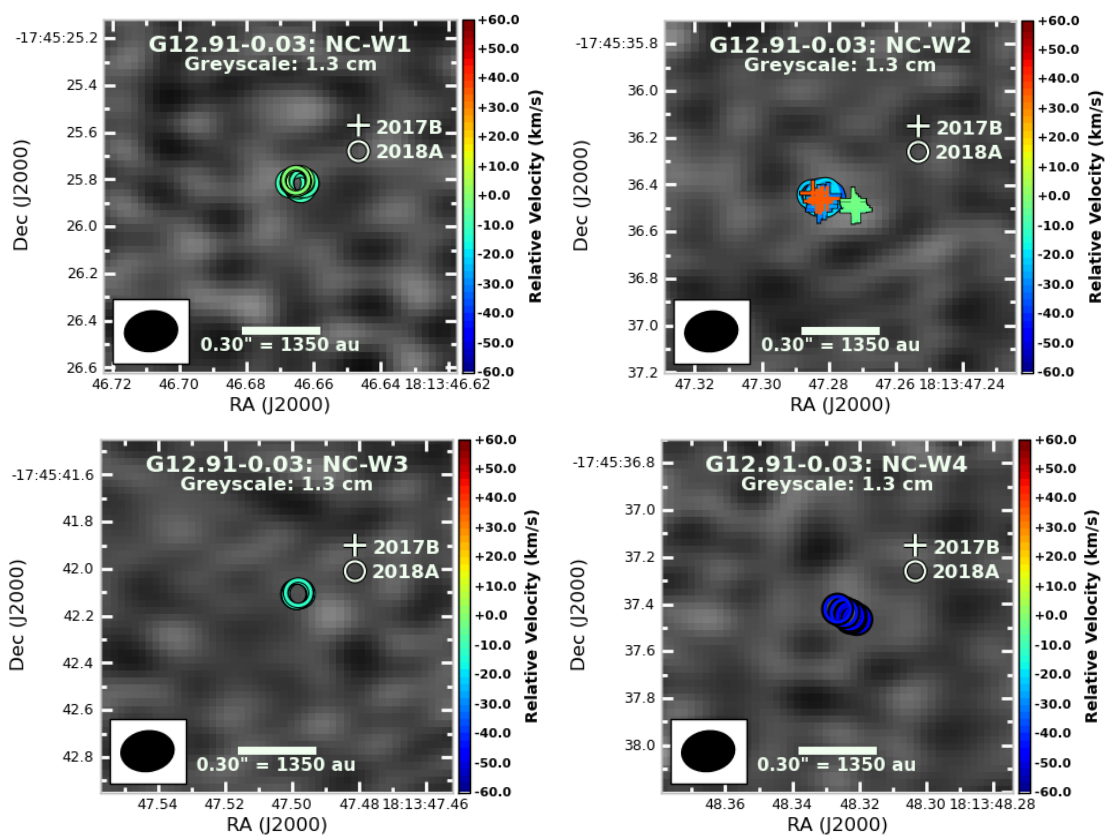
Fig. 4.9.— Maser spot maps for G12.91−0.03, continued. The FOV is 1″.5 for all four panels. Background greyscale is 1.3 cm in all cases; no contours are shown because there is no continuum emission above 4.5 σ in these FOV. H_2O maser data from observing epoch 2018.1 (Semester 2017B) is shown with + symbols, and H_2O maser data from epoch 2019.6 (Semester 2018A) is shown with ◦. Maser symbols are color-coded according to velocity relative to source V_{LSR} (57.0 km s^{-1}).
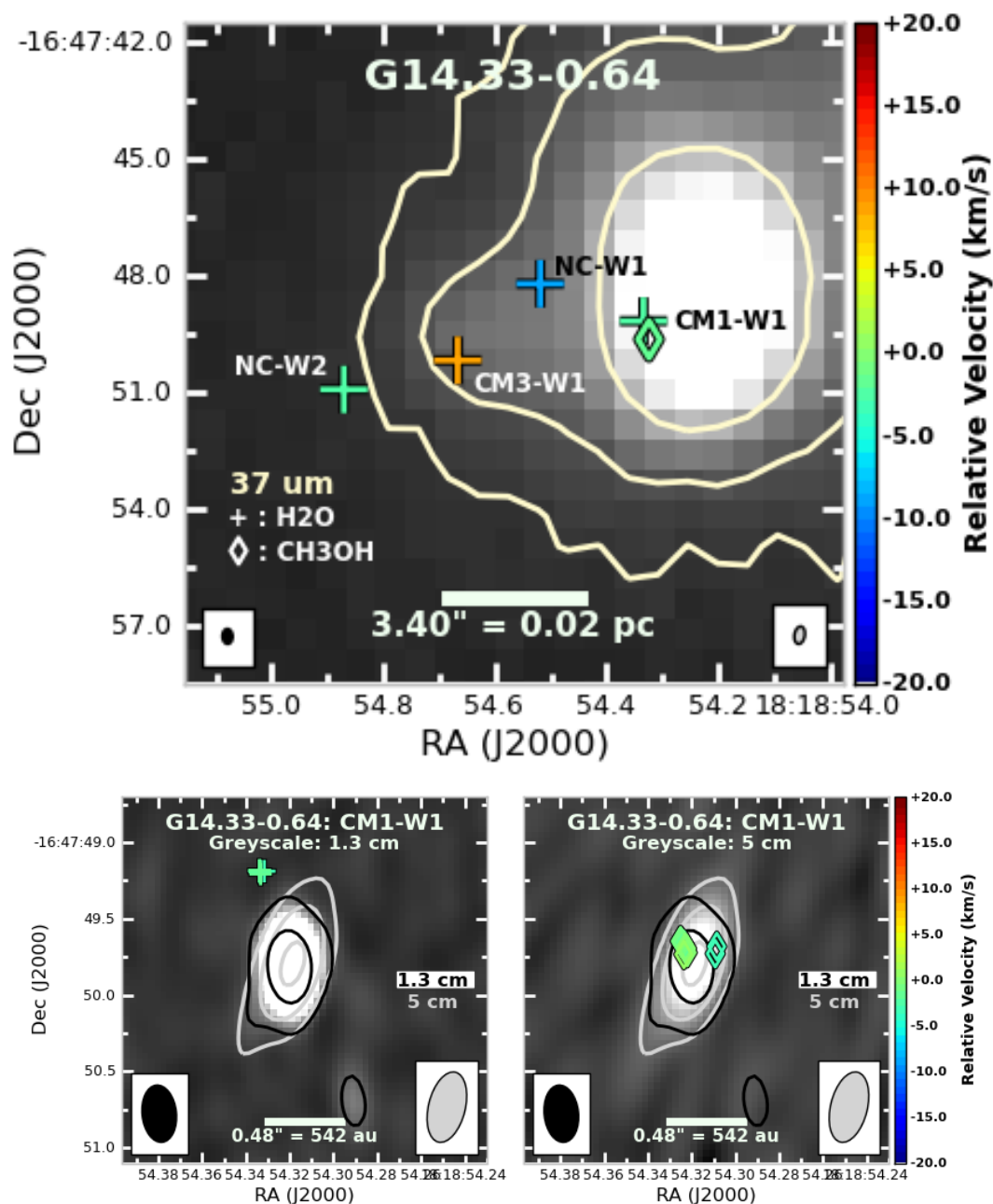
Fig. 4.10.— Maser spot maps for G14.33−0.64. Masers are color-coded by velocity in most panels. In the full FOV (17″), maser clumps are color-coded by peak velocity only, and 37 μm contour levels are [5,15,45]×σ, where σ = 0.24 Jy beam^{-1} is the 37 μm scaled MAD. The background greyscale is 37 μm SOFIA data. In the CM1-W1 image, contour levels are [5,50,150]×σ at 1.3 cm (black) and [5,20,70]×σ at 5 cm (silver), and the FOV is 2.″4. The background greyscale is 1.3 cm in the left-hand panel, and 5 cm in the right-hand panel. Maser symbols are color-coded according to velocity relative to source V$_{LSR}$ (23.0 km s^{-1}).
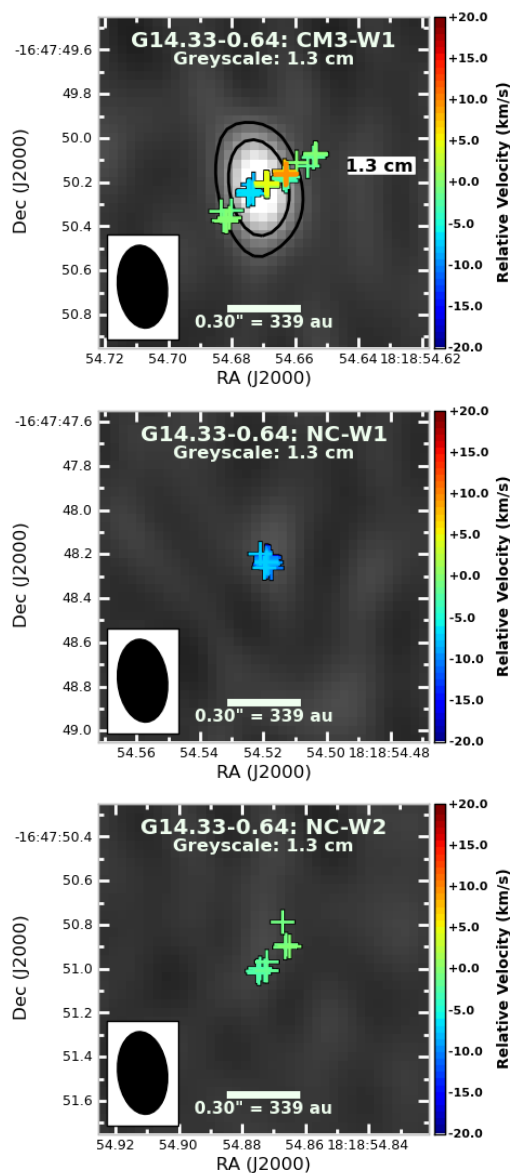
Fig. 4.11.— Maser spot maps for G10.34−0.14, continued. For CM3-W1, the background greyscale is 1.3 cm, and contour levels are [4.5,10]×σ for 1.3 cm (black). There is no emission above 4.5σ at 5 cm. For all "NC" panels, the background greyscale is 1.3 cm continuum, and no contours are shown because there is no emission above 4.5 σ. FOV is 1″5 in all cases. Maser symbols are color-coded according to velocity relative to source V$_{LSR}$ (23.0 km s^{-1}).
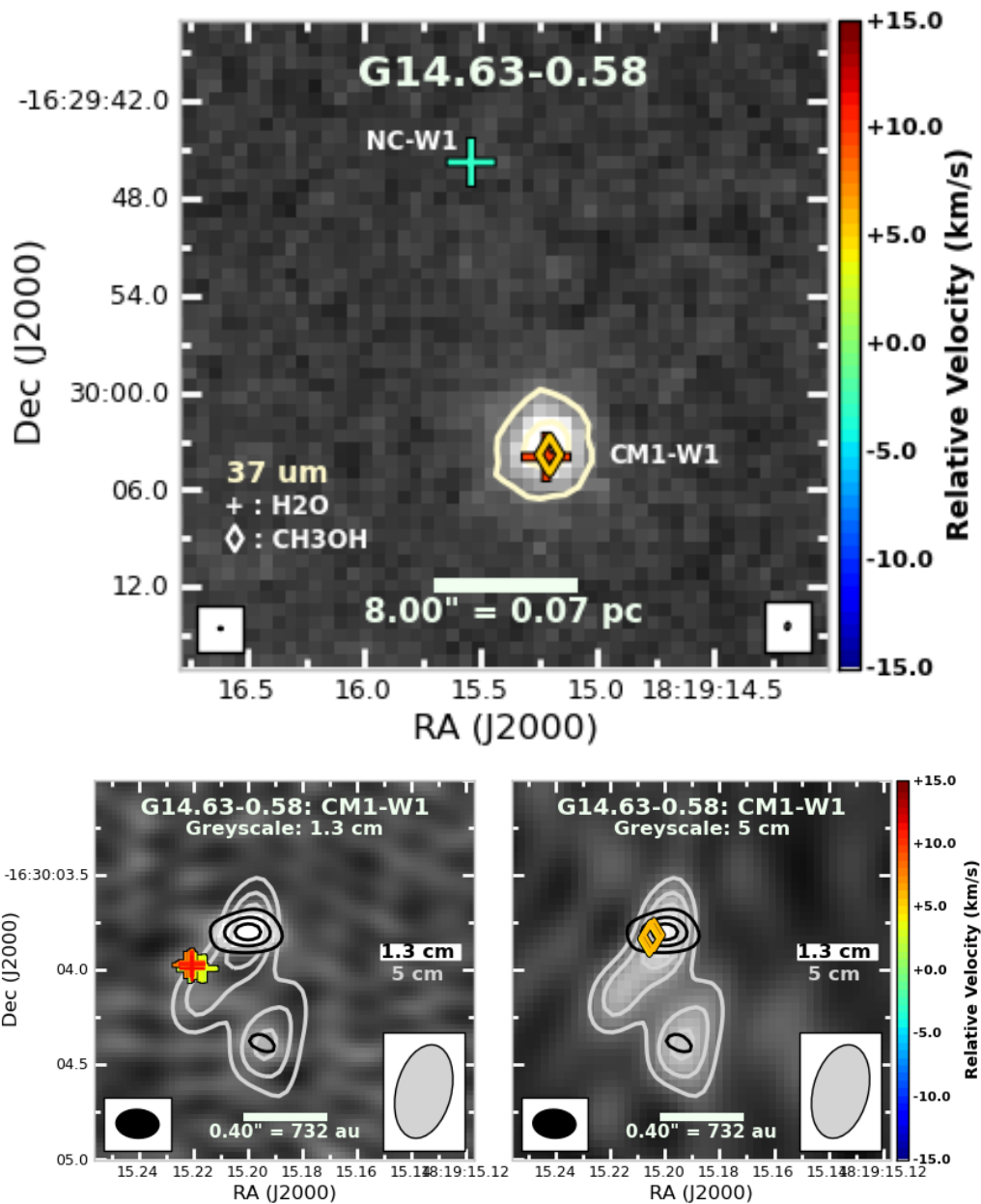
Fig. 4.12.— Maser spot maps for G14.63−0.58. Masers are color-coded by velocity in most panels. In the full FOV (40″), maser clumps are color-coded by peak velocity only, and 37 μm contour levels are [5,15,45]$\times\sigma$, where $\sigma = 0.22$ Jy beam^{-1} is the 37 μm scaled MAD. The background greyscale is 37 μm SOFIA data. In the CM1-W1 image, contour levels are [4.5,10,15]$\times\sigma$ at 1.3 cm (black) and [4.5,7.5,10]$\times\sigma$ at 5 cm (silver), and the FOV is 2″0. The background greyscale is 1.3 cm in the left-hand panel, and 5 cm in the right-hand panel. Maser symbols are color-coded according to velocity relative to source V$_{LSR}$ (19.0 km s^{-1}).

4.5.1 Spectral Indices of the Continuum Detections

Figure 4.21 shows the distribution of spectral indices (α) for the continuum detections in our sample in steps of $\Delta\alpha$ = 0.25. The bottom panel shows the distribution of α for sources detected at both 5 and 1.3 cm (i.e. fully-constrained measurements). The top panel shows the distribution of spectral indices which are upper or lower limits (i.e. for sources which were detected only one of the two wavelengths). For sources detected only at 1.3 cm (22 GHz), the derived α values are lower limits; these sources are shown in red. For sources detected only at 5 cm (6 GHz), the derived α values are upper limits, and these sources are shown in blue. Note that the upper- and lower-limit values are "stacked" on each other, so that the color of each bin represents how many spectral indices in that range are upper or lower limits. For instance, in this panel, there are three spectral indices in the range $0.75 < \alpha < 1.0$ - two are lower limits (red) and one is an upper limit (blue).

Of the sources detected at both 1.3 and 5 cm, the minimum and maximum α are -0.50 and 1.58, respectively, with a median of $\alpha = 0.72 \pm 0.53$ and a mean of $\alpha = 0.61 \pm 0.63$. (The uncertainty of the median is the median absolute deviation from the median ('medabsdevmed') and the uncertainty of the mean is the standard deviation of the distribution). These high medabsdevmed and standard deviation values are reflective of the relatively broad spread of α values that we derive for these sources. The median uncertainty for each individual measurement is $\Delta\alpha$ = 0.16, and the median fractional uncertainty ($\Delta\alpha$ / α) is 0.125. That is, while the total distribution of derived α is fairly broad, the derived α for individual sources are reasonably well-constrained. Our derived lower limits range from $0.46 < \alpha < 1.75$, with a median of 0.84, and our derived upper limits range from $-0.35 < \alpha < 1.13$, with a median of 0.18. It is important to note that, since we used a 4σ upper limit value for each nondetection, our upper and lower limits are not solely a reflection of source properties but are also dependent on the noise in our data. The highest upper limits

we derive for α (e.g. $\alpha < 1.13$) come from those sources with the highest noise levels at 1.3 cm.

These results are consistent with findings of other teams. For their sample, Rosero et al. (2016) find a total range of $-1.2 \leq \alpha \leq 1.8$, with the majority in the range $-0.1 < \alpha < 1.1$ and a median of $\alpha = 0.5$. Purser et al. (2016) do not report the range of α for their whole sample, but do find a median of $\alpha \sim 0.6$ for their jet sample specifically, as expected for those sources. Sanna et al. (2018) do not report a median α for their sample, but find a total range of $-0.1 \leq \alpha \leq 2.5$. Purser et al. (2016) and Rosero et al. (2019b) use source morphology (when possible) to distinguish between the various possible sources of free-free emission in their sample. In our sample, however, only five sources have spatially-resolved sizes (only 14% of the 36 detections in Table 4.4). Of these, four have $\alpha > 1.1$, and the last (G19.36−0.03 CM1) has $\alpha = 0.77$ (0.01). The aspect ratio of this source is ~ 1 at 1.3 cm and nearly 2 at 5 cm. Of the four remaining sources, three have aspect ratios >2. Our remaining sources are either entirely unresolved or only have upper limits on their sizes. At the distances of our sample, the high number of unresolved sources suggests that most of these emitting regions are quite small (<500 au).

In the absence of clear morphological markers for source type for the majority of our detections, even at these high angular resolutions, we examine our distribution of α within specific ranges to see if we can distinguish dominant emission mechanisms within the sample. The distribution of α in the bottom panel of Figure 4.21 has a clear peak in the bin $0.75 < \alpha < 1.0$, and a "tail" of detections between $-0.5 < \alpha < 0.25$. In general, free-free emission in star-forming regions can produce α anywhere between -0.1 (completely optically thin emission) and 2 (optically thick emission). The canonical value for a partially-ionized spherical, isothermal, constant-velocity stellar wind is $\alpha = 0.6$, but this value can also be produced by, e.g., a conical, partially-ionized jet. Reynolds (1986) showed that α for such

a jet can range from $-0.1 \leq \alpha \leq 1.1$ depending on the properties of the flow, such as gradients in temperature, ionization fraction, and velocity. Of the sources we detected at both wavelengths, the majority (11/18, 61%) fall in the range $-0.1 < \alpha < 1.1$. That is, they are consistent with the standard values for thermal free-free emission from an ionized or partially-ionized source which is mostly optically thin. The sources with $\alpha > 1.1$ are the sources with resolved sizes, discussed above.

On the other end of our distribution, we find that five out of our 36 detections (14%) have $\alpha < -0.1$, and four of these (11% of the total sample) have $\alpha < -0.25$. As $\alpha = -0.1$ is the minimum spectral index which can be produced by free-free emission in a jet (for the special case of completely optically-thin free-free emission), this suggests a small but non-trivial population of sources whose spectral indices are consistent with non-thermal emission. There is some suggestion within the literature that other samples display similar trends in the distribution of α. Rosero et al. (2019b) conclude that at least 10% of the continuum detections in their sample have spectral indices consistent with non-thermal emission (which they define as $\alpha < -0.25$). Purser et al. (2016) suggest that synchrotron emission may be commonplace within their jet sample; they state that they "derive non-thermal spectral indices for lobes associated with 10 of the 13 jets" in their sample and the average value of these non-thermal spectral indices is -0.55. They conclude that synchrotron radiation is relatively commonplace within the jets detected in their sample (75% occurrence rate). It must be noted, however, that Purser et al. (2016) 1) have the necessary range in angular scales to distinguish between the more compact 'jet' and the more extended 'lobe' emission, which we and Rosero et al. (2016) do not, and 2) present these results explicitly for their jets and jet candidates only, which is only a subset of the complete sample of continuum sources they detect; the authors do not comment on the expected detection rate of synchrotron emission in massive star-forming regions more generally. Sanna

et al. (2018) notably do not detect any sources with $\alpha < -0.1$ within their sample, though this is possibly due to their selection criteria as they are specifically targeting very young protostellar outflows.

When interpreting the spectral index data for our sample, two caveats must be kept in mind: resolution limitations and contamination by warm dust. Both Reynolds (1986) and Purser et al. (2016) note the strong effect that spatial resolution can have on derived spectral indices. Reynolds (1986) suggest a model for a bipolar conical jet powered by a spherical region of hot, dense ionized material (see their Figure 2). With this model, the optically-thick central spherical region will dominate at higher frequencies with a spectral index of $\alpha = 2$, the (confined) inner jet will become prominent at slightly lower frequencies with a shallower spectral index ($\alpha \sim 0.2$ depending on jet properties), and the (unconfined) outer jet will dominate at the lowest frequencies with a slightly steeper spectral index ($\alpha \sim 0.6$ in this model). Therefore, unresolved observations which blend emission from these different physical components can change the derived spectral index. In order to understand potential bias in their results, Purser et al. (2016) examine how the spectral indices of two of their reasonably resolved jet-lobe sources would change if those sources became unresolved. They found that combining emission from the jets and lobes for each source would, in both cases, flatten the measured spectral index, but that the emission would still be fit well with a simple power law. They suggest that significant numbers of unresolved sources could lead to a flattening of the spectral indices in a jet population overall.

Contamination by warm dust, which is also not accounted for in the power-law fits of Purser et al. (2016) or Rosero et al. (2016), would have the opposite effect of resolution limitations. Dust contamination will decrease with increasing wavelength (assuming grey-body emission), so shorter wavelengths will be affected more strongly, and the measured spectral indices will be more positive than they would be without the dust emission. Bro-

gan et al. (2016) found, in their examination of the massive star-forming region NGC6334I, that the spectral energy distributions for two of their sources (MM1B and MM1D) could only be accurately fit with a combination of thermal dust and free-free emission. For these objects, the $\tau \sim 1$ warm dust (438 and 309 K, respectively) emission components produced flux densities of ~ 200 μJy at 22 GHz (1.3 cm). At the noise levels (12 μJy beam^{-1}) and typical flux densities (tens to a few hundred μJy) of our sources, therefore, even moderate dust contamination could significantly alter the derived spectral indices.

The best solution to both the resolution and potential dust-contamination problems is data at additional, shorter wavelengths. Warm or hot dust in star-forming cores emits strongly in the millimeter and submillimeter regimes, and Reynolds (1986) suggest that the homogeneous core in their Figure 2 will produce a steep rising spectrum at millimeter wavelengths as well. Therefore, in order to account for both the potential for multiple emission mechanisms (free-free versus dust) and the effects of resolution on derived spectral indices, we conclude that additional data are required for these sources. We discuss these additional data in § 4.6.

In summary, the α we derive our centimeter continuum detections are broadly consistent with the range of spectral indices predicted for thermal free-free emission and with the results of other teams Purser et al. (2016); Rosero et al. (2016); Sanna et al. (2018). However, between the large proportion of our sample whose sizes are not precisely known and the possibility of dust contamination at 1.3 cm, we are unable to distinguished between jets, stellar winds, or other non-radiatively ionized processes (e.g. Reynolds 1986) and radiatively-ionized regions such as gravitationally-trapped or bipolar H II regions (Keto 2003; Tanaka et al. 2016). For those sources whose major and minor axes could be deconvolved from the beam, the fitted sizes range from a few tens of au to a few hundred au, but never more than 1000 au. These spatially-resolved sources have a tendency toward

elongated emission (aspect ratio >2) which is consistent with both shock-ionized jets and bipolar H II regions. However, this comparison could only be made for 14% of the sample (five sources), so we refrain from drawing any conclusions about the sample as a whole from these results. For the sources for which we could only place an upper limit on source size, these upper limits range from 280 - 4270 au at 1.3 cm to 620 - 6790 au at 5 cm. Additionally, we find a small population of detections with $\alpha < -0.1$, which is consistent with non-thermal emission and is consistent with results presented in the literature for other samples of high-mass star-forming regions (Rosero et al. 2016; Purser et al. 2016). In order to more fully constrain the spectral energy distributions of our unresolved sources and thus disentangle multiple potential sources of emission, observations at additional wavelengths are needed.

4.5.2 Radio versus Bolometric and H$_2$O-Maser Luminosities

Another means of testing the nature of our centimeter continuum sources is to examine the relationships between various source properties and compare these trends to observationally-derived correlations for particular emission mechanisms. In the following subsections, we discuss the relationship between radio distance-luminosity (L_{radio}) and the corresponding bolometric (L_{bol}) and water-maser (L_{H_2O}) luminosities for each source. We define radio distance luminosity as $L_\nu = S_\nu \times D^2$, where D is the heliocentric distance in kpc, S_ν is the flux density in mJy, and ν is the observation frequency. L_ν has units of mJy kpc^2. We determine the luminosity of each maser clump listed in Table 4.6 separately, using the standard formula for isotropic luminosity for 22 GHz H$_2$O masers:

$$\left[\frac{L_{H_2O}}{L_\odot}\right] = 2.30 \times 10^{-8} \left[\frac{\int S_\nu dV}{\text{Jy km s}^{-1}}\right] \left[\frac{D}{\text{kpc}}\right]^2 \tag{4.1}$$

where $\int S_\nu dV$ is the total maser flux density (integrated over all channels) in Jy km s^{-1},

and D is in kpc (see, e.g. Anglada et al. 1996; Cyganowski et al. 2013). L_{bol} for this analysis comes from Towner et al. (2019), who use multiwavelength photometry and Spectral Energy Distribution (SED) modeling to derive four L_{bol} values for each source using three radiative-transfer models and a one-component greybody fit; the L_{bol} we use here is the median of these four values for each source. (See Towner et al. (2019) for a discussion of the photometric and modeling techniques used for this process.)

In order to compare L_{radio}, L_{bol}, and L_{H_2O}, we must determine the physical area over which we should consider maser and continuum emission. There are multiple centimeter continuum detections in all sources except G10.29–0.13, and multiple sites of H_2O maser emission in all sources except G22.04+0.22, Semester 2018A. Furthermore, the bolometric luminosity for each source is ultimately dependent on the aperture photometry described in Towner et al. (2019). For this photometry, the authors used apertures of different sizes at different wavelengths in order to accommodate changes in source morphology and telescope resolution with increasing wavelength, as well as extended, variable background structures at 70 μm and greater. In most cases, the shape of the full SED (and thus the total L_{Bol}) was significantly constrained by the flux density at 37.1 μm. The relationship (if any) between L_{radio}, L_{bol}, and L_{H_2O} will therefore depend on which maser and continuum emission we define as being associated with the EGO, and which we do not.

In order to avoid systematic bias as much as possible, we determine three values each for L_{radio} and L_{H_2O}. Each value comes from a progressively smaller region within each EGO target, and we present results for all three apertures at each wavelength. Only measured radio flux densities are included in the total continuum S_ν for a given aperture; the upper limits listed in Table 4.4 are not considered. First, we determine L_{radio} and L_{H_2O} by summing the flux density of all continuum components and maser clumps, respectively, within the ATLASGAL 870 μm 5σ contour. This is the largest region. Second, we determine

L_{radio} and L_{H_2O} from by summing the flux density of all continuum and maser detections within the SOFIA 37 μm 5σ contour[3]. Third, we determine L_{radio} and L_{H_2O} on the scale of individual protostars (<2000 au). In the case of L_{radio} versus L_{H_2O}, we examine L_{radio} and L_{H_2O} for all continuum sources which have H_2O masers within 1000 au. For L_{radio} versus L_{bol}, we plot L_{radio}-L_{bol} for the single continuum source in each EGO which is associated with 6.7 GHz masers.

In order to better compare our results to the literature (e.g., Purser et al. 2016; Sanna et al. 2018), we interpolate 8 GHz flux densities from our data using the spectral index and 6 GHz flux density of each source. For sources detected only at one wavelength, we take the 5σ upper limit as a "true" measurement for the purposes of completing the interpolation, and the final result is then taken as an upper limit for the flux density at 8 GHz.

4.5.3 L_{radio} vs L_{bol}

Figure 4.22 shows L_{radio} versus L_{bol} for the ATLASGAL-selected, SOFIA-selected, and 6.7 GHz-selected L_{radio} in the left, middle, and right-hand columns, respectively. G10.29–0.13 is not included in the SOFIA plots because it is a non-detection at 37 μm. Additionally, G18.89–0.47 is not shown on the SOFIA- and 6.7 GHz-selected plots as it has no centimeter continuum detections coincident with its 37 μm emission, and no 6.7 GHz CH_3OH masers coincident with its continuum detections. There are three sources (G10.29–0.13, G14.33–0.64, G19.36–0.03) which have centimeter continuum emission within the ATLASGAL aperture whose flux density cannot be recovered (see Table 4.5); these points are shown as lower limits in L_{radio} in the ATLASGAL column of Figure 4.22.

In the discussion below, we specifically compare our 8 GHz results to those of the Protostellar Outflows at the EarliesT Stages (POETS) survey (Moscadelli et al. 2020; Sanna

---

[3]For this analysis, we only consider the 37 μm 'a' sources - the brightest 37 μm sources within each EGO - as those are the 37 μm flux densities on which the L_{bol} are based.

et al. 2018). The sample of 36 massive star-forming regions was drawn from data from the Bar and Spiral Structure Legacy (BeSSel) Survey as published in Reid et al. (2014). Sources were selected on the basis of having rich H_2O-maser emission (>10 sites of H_2O masers stronger than 1 Jy), L_{bol} corresponding to stellar type B3 to O7, weak or no prior radio-continuum detections (i.e. below 50 mJy in flux density and $1''$ in size), and a helio-centric distance within 9 kpc. Typical L_{bol} for the POETS sample is $10^3 - 10^4 \, L_\odot$, although some sources do have lower or higher luminosities. This sample is therefore an appropriate comparison sample for our own, and although our sample was not selected on the basis of H_2O-maser emission, every EGO in the sample does have at least two H_2O maser sites.

Overall, we find that there is a positive trend in L_{radio} with L_{bol} in all three wavelengths, and that this trend holds regardless of the method of flux density-selection used. The bottom panels in Figure 4.22 explicitly compare our 8 GHz results for each aperture with the best-fit line for the POETS sample. The dotted lines show the best-fit line to the data of Sanna et al. (2018): $\log(L_{radio}) = (0.62 \pm 0.04) \times \log(L_{bol}) + (-2.2 \pm 0.1)$. The shaded region in each plot corresponds to the 1σ dispersion around that best-fit line ($1\sigma = 0.36$; A. Sanna, private communication). See Figure 5, panel B of Sanna et al. (2018) for the figure from which this best fit is drawn. The median absolute value of the difference between our 8 GHz L_{radio} and the Sanna et al. (2018) best-fit line is 0.29 for the ATLASGAL-selected flux densities, 0.20 for the SOFIA-selected flux densities, and 0.24 for the CH_3OH maser-selected flux densities, i.e., our results agree with the Sanna et al. (2018) fit within the 1σ level. These results are also consistent with the statistically-identical L_{radio}-L_{bol} relations derived for other samples: Rosero et al. (2019b), who derive $L_{radio} \sim L_{bol}^{0.63}$ at 5 GHz, and with Purser et al. (2016), who derive $L_{radio} \sim L_{bol}^{0.64 \pm 0.04}$ at 9 GHz. In other words, the relationship between L_{radio} and L_{bol} for our sample is consistent with the well-established L_{radio}-L_{bol} relationship for star-forming regions derived in the literature over six orders of

magnitude in L_{bol}. This suggests that the dominant source of radio continuum emission in our sample is likely the same as that proposed by these other teams, i.e., ionized emission in jets driven by YSOs. We note that this does not preclude non-trivial emission from other emission mechanisms - it merely suggests a common mechanism for the most *dominant* sources of flux density.

However, there is an important caveat to these 8 GHz comparisons. The fact that we do not include upper limits in our L_{radio} values means that only sources which are detected at *both wavelengths* contribute to the L_{radio} included in the 8 GHz analysis. Recall also that sources which are detected at both wavelengths tend to be brighter at both wavelengths than sources detected in only one or the other. Essentially, our 8 GHz L_{radio} values are biased toward the stronger sources in our sample. While the overall scatter of the 8 GHz interpolated L_{radio} is typically quite similar to the scatter of L_{radio} at 22 and 6 GHz, this is still an important caveat to keep in mind when considering the broader implications of these results.

We find that median L_{radio} decreases at all three wavelengths as we move from the ATLASGAL- to 6.7 GHz-selected luminosities, which is expected considering that less flux density will contribute over smaller areas. Perhaps more surprising is the comparatively small effect this has on the distributions overall. However, an examination of the flux densities reported in Table 4.4 explains this trend. In most cases, the continuum source which is associated with 6.7 GHz masers is the brightest reported for a given EGO, usually by a wide margin, and these sources tend to be found toward the center of the 870 μm clump hosting each EGO. It therefore should not be surprising that examining the radio-continuum luminosity on progressively smaller scales will have only a limited effect on L_{radio}.

4.5.4 L_{radio} vs L_{H_2O}

While an examination of L_{radio} versus L_{bol} can provide clues as to the physical source of centimeter-continuum emission around YSOs, i.e., ionized jets, Sanna et al. (2018) also sought to determine the physical mechanism which produced this ionization by examining L_{radio} versus L_{H_2O}. Their suggestion was that, if the source of the radio-continuum emission is the same in low- and high-mass objects, then the mechanism through which those jets are ionized might be the same in low- and high-mass objects as well. To test this hypothesis, Sanna et al. (2018) also examined L_{radio} versus L_{H_2O} for their sample of high-mass sources, and compared their results to those for low- and intermediate-mass sources in the literature. Based on their analysis of L_{radio}-L_{H_2O} for the POETS sources, combined with their derived L_{radio}-L_{bol} relation, Sanna et al. (2018) conclude that the mechanism of ionization in jets from high-mass YSOs is the same as that in low-mass YSOs, i.e., shock-ionization rather that photoionization. However, they do note that it is also possible that H_2O masers are simply a preferred signpost of ionized jets.

Figure 4.23 shows L_{radio} versus L_{H_2O} for our sample. The ATLASGAL-, SOFIA-, and 1000 au-selected luminosities are again shown in the left, middle, and right-hand columns, respectively. For the four sources which have two epochs of H_2O-maser observations (G10.29−0.13, G12.91−0.03, G19.36−0.03, and G22.04+0.22) L_{H_2O} for each epoch is shown separately, and L_{H_2O} for the second epoch is denoted by blue symbols rather than black. For the ATLASGAL and SOFIA apertures, we do not require that the maser emission be associated with a particular continuum source in order to be included in the total L_{H_2O} (i.e. we include the "NC" maser associations in the total L_{H_2O}, if they are located inside the relevant aperture).

For the 1000 au-selected panels, we plot L_{radio} versus L_{H_2O} for all continuum detections which have H_2O-maser emission within 1000 au. We do not require that a continuum

source be detected at both 1.3 cm and 5 cm in order to show it on these plots. If a source is detected at only one wavelength, L_{radio} for the non-detected wavelength is plotted as an upper limit based on the 5σ flux density limit in that band. Note that the populations shown here expands on that shown in the right-hand column of Figure 4.22. Although all continuum sources with 6.7 GHz masers also have associated H_2O maser emission, there are several additional continuum sources which have H_2O maser emission but no CH_3OH masers.

The choice of 1000 au as the distance cutoff for this analysis comes from recent statistical analysis of H_2O maser emission by the POETS team. While Sanna et al. (2018) use VLBI and kinematic analysis to determine the association of H_2O masers with specific continuum sources, we cannot replicate this approach for our own data. Instead, we draw from Moscadelli et al. (2020), who find that $\sim$84% of H_2O masers in their sample which can be positively kinematically associated with a specific centimeter source lie within 1000 au of that source[4]. Given the overall similarities between the POETS sample and ours, we adopt a 1000-au cutoff for this specific analysis.

For the ATLASGAL-selected data, there is a general trend of L_{radio} increasing with L_{H_2O}. This should not be surprising on $\sim$1 pc scales, as there are many well-established correlations between outflow properties, including momentum and luminosity, and clump bolometric luminosity at these size scales (see, e.g. Urquhart et al. 2011) However, as aperture size decreases, we find that our L_{H_2O} typically decreases, but L_{radio} does not. This is consistent with the fact that the radio continuum sources in our EGOs are typically centrally-concentrated, but the H_2O maser emission are more widely dispersed. Consequently, these continuum sources typically become underluminous in L_{H_2O} compared to their L_{radio} values as aperture size decreases.

The dotted line in the 8 GHz (bottom) panels of Figure 4.23 is the best fit for L_{radio} ver-

---

[4]Moscadelli et al. (2020) examined H_2O maser sources out to a distance of $\sim$18,000 au from their targets.

sus L_{H_2O} derived by Sanna et al. (2018) for the POETS sample: $\log(L_{radio}) = (0.74 \pm 0.07) \times \log(L_{H_2O}) + (3.8 \pm 0.4)$. The shaded region indicates the 1σ dispersion about this best-fit line (0.47; A. Sanna, private communication). The median absolute value of the difference between our 8 GHz L_{radio} results and this best-fit line is 0.40 for the ATLASGAL-selected data, 0.28 for the SOFIA-selected data, and 0.32 for the 1000 au-selected data. We use median absolute value of the deviation rather than standard deviation because the different apertures have slightly different samples (as discussed) above, and median deviation is more robust against small-number effects than standard deviation. These deviations are all well within the 1σ dispersion of the POETS sample.

It is interesting to note that the dispersion increases when moving from the SOFIA-selected to 1000 au-selected sources. In examining these results, we must consider the limitations of our own angular resolution and the possibility that the $\sim$16% of H_2O masers that lie further from the source than 1000 au make a non-negligible contribution to the overall H_2O maser flux density. However, we note that the SOFIA-selected and 1000 au-selected luminosities are quite similar - in most cases there is no or very little change in L_{H_2O} between the two selection methods. This suggests that, in both cases, the increased dispersion is due to the exclusion of far-flung H_2O masers, rather than small-scale position uncertainties for masers very close to continuum sources.

There are several possible reasons for the statistical deviations between our results and the POETS results. The POETS sources were selected specifically for their particularly rich H_2O maser emission, while our sources - though they do all contain at least one H_2O maser - were not. It is possible that our L_{radio}-L_{H_2O} relation weakens at smaller scales because the samples are not sufficiently similar in their H_2O maser emission to be suitable for comparison - perhaps the POETS sources are in a more active state of accretion/outflow than our EGOs. It is also possible that, as Sanna et al. (2018) suggest, the H_2O masers in

both samples are merely a preferred signpost of ionized jets. This implies that, although L_{radio} and L_{H_2O} correlated in their data, the maser pumping mechanism (i.e. shocks) is not the source of ionization in the jets. This would require a non-trivial source of photoionization in these regions. While this might explain those continuum sources in our sample which are overluminous in L_{radio} compared to L_{H_2O} at small scales, it does not explain those which are underluminous.

4.5.5 L_{H_2O} vs L_{bol}

In Figure 4.24 we show L_{H_2O} versus L_{bol} for our own sample, where L_{H_2O} is the total H_2O-maser luminosity within the ATLASGAL aperture. We also compare our results to those of Urquhart et al. (2011), who examine a sample of $\sim$600 massive YSOs ($L_{bol} > 10^3 L_\odot$) drawn from the Red MSX Source catalog (Urquhart et al. 2011, see their Figure 16). In Figure 4.24, our data are shown in blue and black, and the Urquhart et al. (2011) points are shown in gray. As for Figure 4.23, the blue points represent the second epoch of observations for sources which were observed twice at 22 GHz. We find that our L_{H_2O} are well within the typical scatter of the Urquhart et al. (2011) sample, and follow a similar positive correlation with L_{bol}. This suggests that, as with the Urquhart et al. (2011) sample, there is a strong link between the driving source of the H_2O maser emission in the overall clump and the dominant source of L_{bol}. It is also consistent with our findings presented in Figure 4.22, which suggest that a significant fraction of the L_{radio} in each EGO is attributable to a single continuum source, and in the left-hand column of Figure 4.5.4, which suggest that L_{H_2O} is most strongly correlated with L_{radio} at $\gtrsim 0.5$ pc scales in our sources.

We must briefly note that the majority of our sources do lie above the best-fit line for L_{H_2O}-L_{bol} for the Urquhart et al. (2011) RMS sample. However, with only 15 data points (as compared to the $\sim$600 RMS-selected points), the probability that this trend is random

as opposed to physical in origin is too high to warrant even tentative conclusions.

4.5.6   Characteristics of the Maser Emission

In the following subsections we briefly analyze the characteristics of the maser emission in our sample. As the deep continuum images were the primary target of these observations, our maser data lack the sensitivity and velocity resolution necessary to perform detailed, small physical-scale kinematic analyses, such as would be possible with VLBI. Instead, we here limit ourselves to more general descriptions of the maser data, and make note of which sources may be good candidates for high-resolution follow up observations of the maser line emission.

4.5.7   Peak Velocity Offsets & Velocity Extents

Here we briefly present basic statistics about the maser emission in our sample as a whole. Statistics are calculated for individual maser clumps and presented for the population of clumps as a whole (i.e. the analysis is not per-channel). Here, "velocity extent" refers to the total velocity range over which maser emission is detected in a given clump (V_{max} - V_{min}). Note that this does not indicate there is *continuous* maser emission within that range - there may instead be multiple distinct velocity components within a given maser clump. "Peak velocity offset" refers to the difference between the peak velocity of each maser clump and the V_{LSR} of the source.

The H_2O maser clumps in our sample have a median and mean velocity extent of 7.38 and 12.51 km s^{-1}, respectively, with a minimum of 0.25 km s^{-1} (a 2-channel detection) and a maximum of 101.25 km s^{-1}. The median and mean peak velocity offsets are -1.75 and -4.51 km s^{-1}, respectively, with minimum and maximum values of -43.50 km s^{-1} and 29.25 km s^{-1}. In other words, the H_2O maser emission is typically centered on the

V_{LSR} for each source but spans a very broad range in velocity, with a slight preference for blueshifted emission. The NH$_3$ maser emission, in contrast, is also well-centered on the V_{LSR} of each source but spans a very narrow range in velocity compared to the H$_2$O emission. The NH$_3$ maser clumps have median and mean velocity extents of 0.88 and 1.21 km s^{-1}, respectively, with minimum and maximum values of 0.5 and 3.0 km s^{-1}. They have mean and median peak velocity offsets of only −0.38 and −0.34 km s^{-1}, respectively, with minimum and maximum values of only −2.00 and 2.50 km s^{-1}. The 6.7 GHz CH$_3$OH masers span a median and mean velocity range of 11.0 and 9.1 km s^{-1}, respectively - comparable to a typical H$_2$O maser clump - with minimum and maximum values of 1.25 and 19.5 km s^{-1}, respectively. However, the CH$_3$OH peak velocity offsets are more similar to the NH$_3$ emission, with median and mean offsets of −0.5 and 0.27 km s^{-1}, respectively (minimum and maximum values are −10.5 and 7.5 km s^{-1}). Overall, the NH$_3$ and CH$_3$OH masers are consistent with gas which has a relatively low peculiar velocity compared to the EGO V_{LSR}, while H$_2$O masers are consistent with both co-moving gas and gas which is moving quite rapidly compared to the systemic velocity. This latter point is consistent with H$_2$O maser emission which can arise from a wide range of sources, but definitely includes potential sources of emission which involve high relative velocities, such as outflows and jets.

4.5.8 6.7 GHz CH$_3$OH Masers as a Probe of Disks in MYSOs?

While 6.7 GHz CH$_3$OH masers are known to be exclusively associated with MYSOs (Minier et al. 2003), there has been some recent debate as to whether the masers themselves arise in the envelopes of these MYSOs or if, instead, they arise from gas within the (assumed) MYSO accretion disks. If the latter, then high angular resolution observations of 6.7 GHz CH$_3$OH masers may be a means of positively identifying massive disks around

MYSOs, of which there have been very few positive identifications to date (see Ilee et al. 2018, for one example), examining their kinematics, and perhaps obtaining an independent (dynamical) check on the mass of the central MYSO.

For each 6.7 GHz CH$_3$OH maser clump in our sample, we calculate the maximum projected linear size of each emitting region. For well-calibrated interferometric images, the relative position uncertainty of an unresolved (point) source relative to other unresolved sources is:

$$\Delta\theta \sim \frac{\theta_{synth.beam}}{2 \times (S/N)} \tag{4.2}$$

where S/N is the signal-to-noise of the source in question (see Cyganowski et al. 2009, and references therein). For a 10σ detection with a synthesized beam of $\sim 0\rlap{.}''30$, this gives a relative position uncertainty of 1.5 mas.

For each CH$_3$OH maser clump, we calculate $\Delta\theta$ for the fitted position in each channel. We then determine the angular distance between the fitted position of the maser in one channel and the fitted position in all other channels, and evaluate whether these positions are identical within $\Delta\theta$. If the maximum position-difference we measure for a given maser spot is greater than the sum of the position uncertainties for those individual channels, we calculate the (projected) linear separation of the two masers in au. We also calculate the difference in velocity between these channels. In total, we are able to calculate the projected linear separations for all 6.7 GHz masers except G18.89−0.47 NC-M1. The maximum projected linear sizes of the emitting regions range from 64 ± 58 to 2932 ± 23 au, with a median value of 370 au. The velocity range over which these distances were measured range from 0.5 to 9.25 km s^{-1}, with median $\Delta V = 4$ km s^{-1}. This is *not* the full range over which emission was detected, but rather is the velocity difference between the channels in which the two extreme positions were measured.

We explicitly note three things. First, the median *angular* position-difference measured is 0.″173, which is only slightly smaller than the typical minor axis of the beam for these data. Second, while there is no particular trend in uncertainty with size, four of our ten derived sizes have uncertainties in excess of 80%. Third, the velocity range over which these projected separations are measured are relatively small (no more than 10 km s^{-1}), and with the channel width of our data (0.25 km s^{-1}) are not especially well-sampled.

With these caveats in mind, we conclude that it is not possible to determine whether the 6.7 GHz CH$_3$OH maser emission in our data arises from disk emission or not. While our minimum measured size could potentially be consistent with a disk, our two most well-constrained sizes (2932 $\pm$ 32 au and 736 $\pm$ 5 au) are more consistent with the size scales of protostellar envelopes than disks. The median size (370 au) *is* consistent with the measured sizes of MYSO accretion disks; Ilee et al. (2018) examine an accretion disk around the massive protostar G11.92−0.61 MM1 and determine a size of $R \sim 800$ au. However, it is also possible that this could merely be a projection effect.

The best way to distinguish between these possibilities - other than direct imaging - is to perform a kinematic analysis of the maser emission and determine if it is consistent with a Keplerian disk. We lack the velocity resolution to do so for this sample, however. as discussed above. Therefore, given the generally good S/N of our 6.7 GHz detections, and the typical physical sizes derived in this analysis, we identify these masers as excellent candidates for future high angular- and velocity-resolution follow-up observations for those teams wishing to address the question of disk-originated 6.7 GHz CH$_3$OH maser emission in MYSOs.

4.5.9 Maser Variation with Time

In this subsection, we examine the variation in our maser emission with time. All nine of our EGO targets were previously observed by Cyganowski et al. (2013), who used the 45-m Nobeyama telescope to observe 22 GHz H_2O and NH_3 (1,1), (2,2), and (3,3) emission in all 94 EGOs visible to the northern hemisphere. Additionally, six of our nine targets were included in the CH_3OH maser survey of Cyganowski et al. (2009), who used the VLA to observe 6.7 GHz Class II and 44 GHz Class I CH_3OH masers toward 20 EGOs with $\sim 3''$ resolution. We also examine the variation in H_2O and NH_3 (3,3) maser emission for those sources which were observed twice in our own 1.3 cm data.

22 GHz H_2O Masers - 10.5-year epoch

All 9 EGOs examined in this paper were observed by Cyganowski et al. (2013) in 2008-2010 using the 45-m Nobeyama telescope near Minamimaki, Nagano, Japan. The observations have $\sim 73''$ angular resolution, 0.5 km s^{-1} velocity resolution, and ~ 500 km s^{-1} bandwidth. Cyganowski et al. (2013) define a water maser detection as $> 4\sigma$ emission in at least two adjacent channels. With these criteria, Cyganowski et al. (2013) detect H_2O maser emission in 7 of 9 sources. The two sources with nondetections were G19.36–0.03 and G28.83–0.25, with 4σ upper limits of 0.64 and 0.68 Jy, respectively. We detect 22 GHz H_2O masers in G19.36–0.03 with a peak integrated flux density of 0.71 ± 0.02 Jy in the January 2018 data and 0.27 ± 0.02 Jy in the July 2019 data, and in G28.83–0.25 with a peak integrated flux density of 2.47 ± 0.01 Jy. Although our S$_{Peak}$ values are greater than the Cyganowski et al. (2013) 4σ values in two of these three cases, our results may not be inconsistent with theirs given the well-documented variability of 22 GHz H_2O masers in general and the long time scale between observations.

6.7 GHz Class II CH$_3$OH Masers - 10.5-year Epoch

This work has six EGO targets in common with Cyganowski et al. (2009): G10.29–0.13, G10.34–0.14, G18.89–0.47, G19.36–0.03, G22.04+0.22, and G28.83–0.25. In order to explore the variability of the 6.7 GHz Class II CH$_3$OH masers in these sources, we compare our data to that of Cyganowski et al. (2009) for these six sources. However, our 2018 observations have much higher angular resolution than the Cyganowski et al. (2009) data ($\sim$0$\rlap{.}''$5 versus $\sim$3$''$), and the Cyganowski et al. (2009) data have finer velocity resolution that the results we report in this work (0.139 km s^{-1} versus 0.25 km s^{-1}). Consequently, a comparison between our data and the results reported in Cyganowski et al. (2009) Table 7 or Table 9 was not feasible. Instead, we obtained the relevant data cubes directly from Cyganowski et al. (private communication) to perform a more exact comparison. We regridded the Cyganowski et al. (2009) data in velocity space to match the velocity resolution of our current data (0.25 km s^{-1}), and smoothed our current data to match the beam parameters (major and minor axes, and position angle) of each Cyganowski et al. (2009) cube (see Table 1 in Cyganowski et al. (2009) for the relevant synthesized beam parameters, and § 2.1 in that same work for the observational details of their data overall). We then compared the spectra for each "maser clump" reported in Cyganowski et al. (2009) Table 9 directly. These results are shown in Figure 4.25. We find that there is, in general, good agreement between the overall velocity structure and intensities (e.g. how many components and at which velocities) between the two epochs at the $\sim$5 km s^{-1} level. However, at the $\sim$1 km s^{-1} level, there is non-trivial variation in 6.7 GHz maser emission in five out of the six sources. In at least three cases (G10.29–0.13, G19.36–0.03, G22.04+0.22) an existing velocity component has increased in intensity by at least a factor of two. In the case of G18.89–0.47, the Cyganowski et al. (2009) line profile is somewhat confused, and it is unclear whether a truly new velocity component has appeared in this source or an existing

velocity component merely increased in brightness. Also, in at least three sources, one or more velocity components present in the Cyganowski et al. (2009) data had *decreased* brightness in our 2018 observations. Finally, the maser emission in G10.34−0.14 exhibited both characteristics (dimming of some components and brightening of others).

In no case do we observe a global increase or decrease in intensity for all velocity components in a given maser clump. Also, in only one source (G22.04+0.22) did a newly-bright velocity component reach a peak intensity greater than the maximum peak intensity observed in the 2008 data for that source. This behavior, coupled with the tendency of individual velocity components to flare/dim and the lack of any global brightening/dimming behavior for each source, suggests that the physical mechanism governing the variation in these maser line profiles is not the maser pumping mechanism itself (i.e. infrared radiation from the massive protostar) but variations in either the masing gas (e.g. a decrease in the physical length of the masing column) or in its orientation relative to us (e.g. a decrease in the *projected* length of the masing column).

22 GHz H$_2$O Maser Emission - 1.5-year epoch

Each of the four sources observed twice at 1.3 cm exhibits at least some variation in its H$_2$O maser emission. In G10.29−0.13, no individual maser clumps appear or disappear between the two observations, but every maser clump exhibits a change in the structure or peak of at least one velocity component. In G12.91−0.13, three new H$_2$O maser clumps appear in the July 2019 data (epoch 2019.6), and the velocity structure of the two clumps common to both epochs again exhibit significant changes. In G19.36−0.03, two clumps visible in the January 2018 (epoch 2018.1) data are no longer visible (above our sensitivity limit) in the July 2019 data, and in G22.04+0.22, three clumps are no longer visible in July 2019 which were present in January 2018. Again, for both sources, the maser clumps which are visible

in both epochs show variation in their kinematic structure.

Figures 4.26 through 4.29 show the January 2018 and July 2019 spectra for the maser clumps common to both observation epochs in these four sources. January 2018 spectra are shown in black, and July 2019 spectra are shown in red. All plots for a given EGO are shown on the same velocity axis.

Unlike the CH_3OH maser emission, we find high levels of variability in the H_2O maser emission. In particular, we note that the variability is not limited to existing velocity components. While some components do dim or flare over the 18-month period between observations, there are also some maser clumps which have entire velocity components appear or disappear between the two epochs. This is consistent with the previously-observed high levels of variability in H_2O maser emission, and suggests that this variability arises on extremely small scales ($\lesssim$500 au) given the angular resolution of these data.

NH$_3$ (3,3) Maser Emission - 1.5-year poch

G19.36–0.03 is the only source which has detectable NH$_3$ (3,3) maser emission at both epochs in our data, and we find that this emission is largely unchanged between the two data sets. Each clump has decreased in flux density between the first and second epochs, but these decreases are slight: 33 mJy, 20 mJy, and 30 mJy (35%, 10%, and 9%) for clumps NC-A1, NC-A2, and NC-A3, respectively. At the same time, our image noise has increased 63% between the two observations, from 5.4 to 8.8 mJy beam^{-1}. A change of 30 mJy is consistent with only a $\sim$3.4σ change in the 2018A data. The velocity structure in each maser clump is also largely unchanged between the two epochs; peak velocities and total velocity extents shift no more than 0.25 km s^{-1} (1 channel) between the two semesters. We are therefore cautious in drawing any conclusions as to flux density variability in these sources, especially considering that G19.36–0.03 is the only source in the sample which

could not be self-calibrated. While these maser spots may be good candidates for future high-sensitivity studies of typical flux density variation in NH_3 (3,3) masers, we find little evidence that their flux densities have changed significantly during the 18 months between observations.

4.6   Conclusions

We have examined a sample of 9 Extended Green Objects (EGOs) at 1.3 and 5 cm with sub-arcsecond angular resolution and 7-12 μJy continuum sensitivities, and found ubiquitous weak ($<$500 μJy), compact ($\lesssim$2000 au) or unresolved continuum emission. We detect a total of 42 continuum sources in our 9 EGOs, of which six are resolved out. Most EGOs have $\geq$3 continuum sources, of which one (usually) is associated with 6.7 GHz CH_3OH maser emission.

We find that the spectral indices of these detections span a broad range: $-0.47 < \alpha < 1.58$ for the sources detected at both 1.3 and 5 cm. Such a broad range is consistent with multiple different sources of continuum emission being present *simultaneously* within a given EGO. We find a small ($\sim$10%) population of sources whose spectral indices are consistent with non-thermal emission, which is consistent with the findings of other teams (e.g. Rosero et al. 2019b). The majority of our sources (61%) have α consistent with thermal free-free emission such as might be produced in a jet (Reynolds 1986; Purser et al. 2016) or a nascent H II region (Rosero et al. 2019b; Purser et al. 2016; Sanna et al. 2018). As most of our sources remain unresolved even at these resolutions, we are unable to use morphological characteristics (elongation/spherical morphology) to distinguish between these multiple possibilities. We do find a small population of sources (14%) which are resolved in at least one frequency, and these sources preferentially have $\alpha > 1.1$. These spectral indices are consistent with ionized jets which are undergoing acceleration or recombination

within the flow (Reynolds 1986), but also with partially optically-thick HC H II regions or, potentially, contamination by thermal emission from warm dust. With the present data, it is not possible to distinguish between these multiple possible emission mechanisms for any given source.

In general, we find that the relationship between radio distance-luminosity (L_{radio}) and bolometric luminosity (L_{bol}) for our sample is consistent with the relationship derived for radio emission dominated by thermal emission from jets (Anglada et al. 1996; Sanna et al. 2018; Rosero et al. 2019b), regardless of our selection criteria for L_{radio}. However, there is some reason to believe that these L_{radio} values are dominated by the most massive sources in each EGO (i.e. the 6.7 GHz maser-associated sources), so this correlation should be viewed with caution; it may describe emission from the massive sources well but this should not be taken as an indication that all continuum emission in these EGOs is due to jets.

When L_{radio} and L_{H_2O} are compared over relatively large areas for our sample, the trend matches those reported by Sanna et al. (2018) for their MYSO jet sample, but on 1000-au scales, the agreement between our data and their trend is poor. It is unclear whether this is due to a difference in our sample selection criteria - Sanna et al. (2018) specifically selected their sources based on rich H_2O maser emission over multiple epochs of observation - or some other reason. Overall our L_{bol}-L_{H_2O} values agree within errors with the relationship derived by Urquhart et al. (2011), as expected for massive clumps.

We find that the projected spatial extent of our 6.7 GHz CH_3OH maser emission is, in some cases, small enough to be consistent with emission from the accretion disks of massive protostars (Ilee et al. 2018). However, it is also possible that these separations are merely due to projection effects, and we lack the necessary velocity resolution to produce detailed kinematic maps to explore this possibility in most cases. We therefore identify these sources as good candidates for very high angular-resolution follow-up observations,

such as VLBI, to test whether these 6.7 GHz masers arise in MYSO accretion disks or in their protostellar envelopes.

In comparing the maser emission in our sources from multiple epochs, we find that the 22 GHz H_2O maser emission variation is about as expected, i.e., can be quite significant and does not appear to be systematic. In some cases entire maser clumps appear or disappear over the 1.5-year gap between our two 1.3 cm observing epochs; in other cases individual velocity components within a maser appear, disappear, flare, or dim. This is in contrast to the variation over a 10.5-year epoch of the 6.7 GHz CH_3OH maser emission, for which we find that the variation in maser flux density is limited only to existing velocity components. We suggest that this variation is therefore due to actual or projected changes in the length of the masing column, and not due to any strong variation in the maser pumping mechanism itself (i.e. the luminosity of the central star).

4.6.1   Future Work

In order to distinguish between the multiple possible sources of centimeter continuum emission in this sample, we must be able to model the source's SED at long wavelengths. This requires additional observations in the millimeter regime. We have recently obtained sub-arcsecond resolution observations of these EGOs at 1.3 and 3 mm using the Atacama Large Millimeter/submillimeter Array (ALMA). We will combine these data with the centimeter continuum data presented in this work in order to sample the SED of each continuum source over two decades in frequency and thus accurately model the emission. We will use these models to distinguish between dust, H II region, ionzied jet, and non-thermal emission in the sample, and thus thoroughly describe the demographics of the protostellar population in each EGO. These results will be published in our next paper.

4.7   Acknowledgements
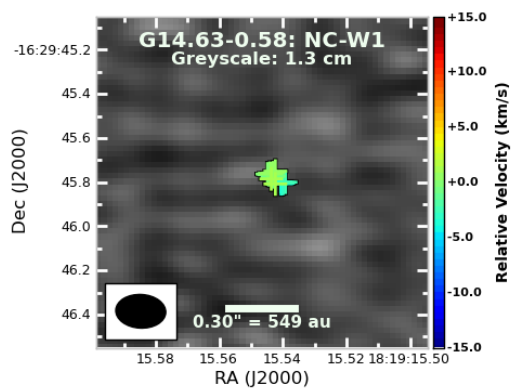
Fig. 4.13.— Maser spot maps for G14.63−0.58, continued. The FOV is 1."5. The background greyscale is 1.3 cm continuum, and no contours are shown because there is no emission above 4.5 σ at either 1.3 or 5 cm. Maser symbols are color-coded according to velocity relative to source V$_{LSR}$ (19.0 km s^{-1}).
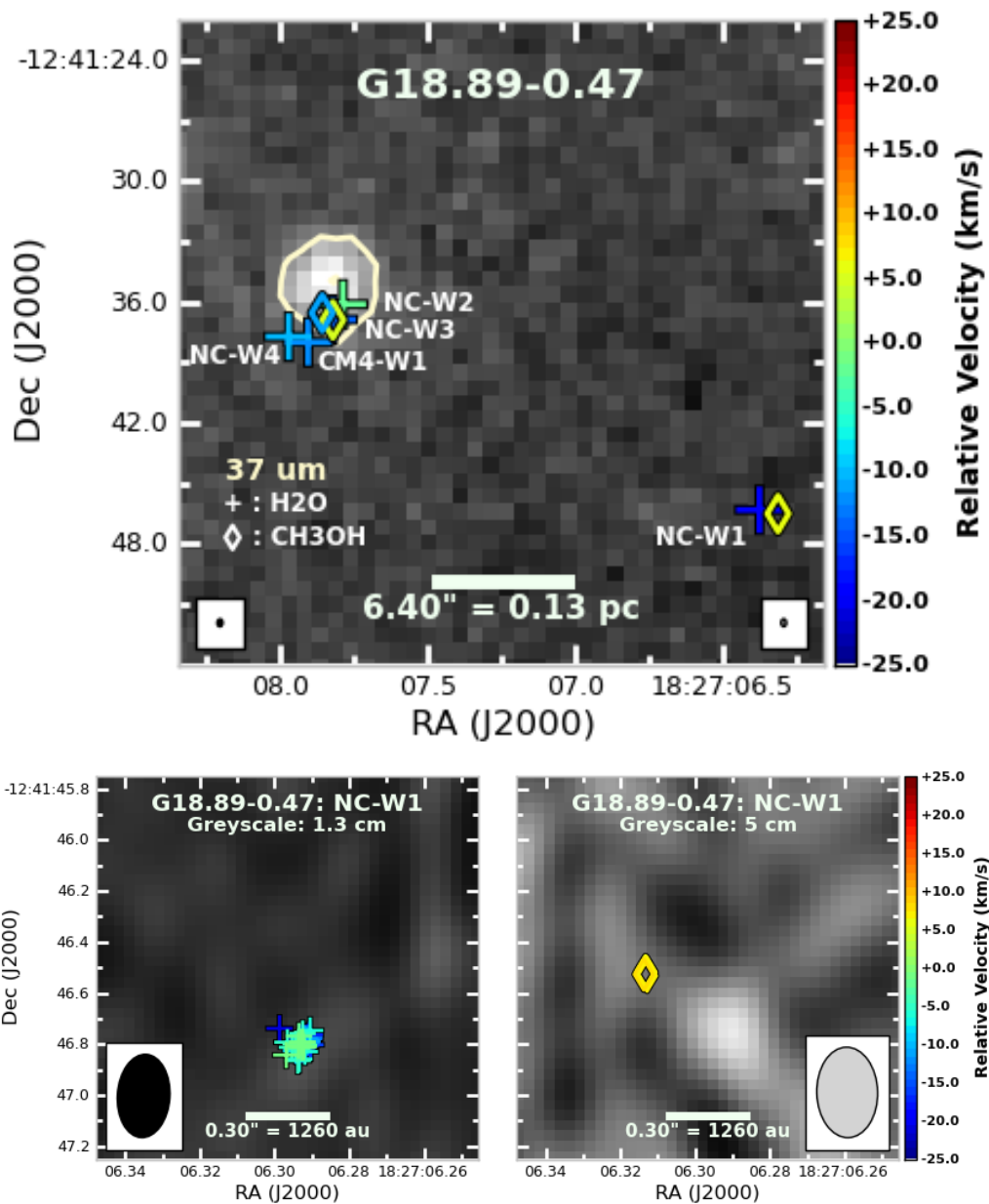
Fig. 4.14.— Maser spot maps for G18.89−0.47. Masers are color-coded by velocity in most panels. In the full FOV (32″), maser clumps are color-coded by peak velocity only, and 37 μm contour levels are [5,15,45]$\times\sigma$, where $\sigma = 0.25$ Jy beam^{-1} is the 37 μm scaled MAD. The background greyscale is 37 μm SOFIA data. In the NC-W1 image, the FOV is 1″.5, and the background greyscale is 1.3 cm in the left-hand panel, and 5 cm in the right-hand panel. No contours are shown because there is no emission above 4.5σ at either wavelength. Maser symbols are color-coded according to velocity relative to source V$_{LSR}$ (66.0 km s^{-1}).
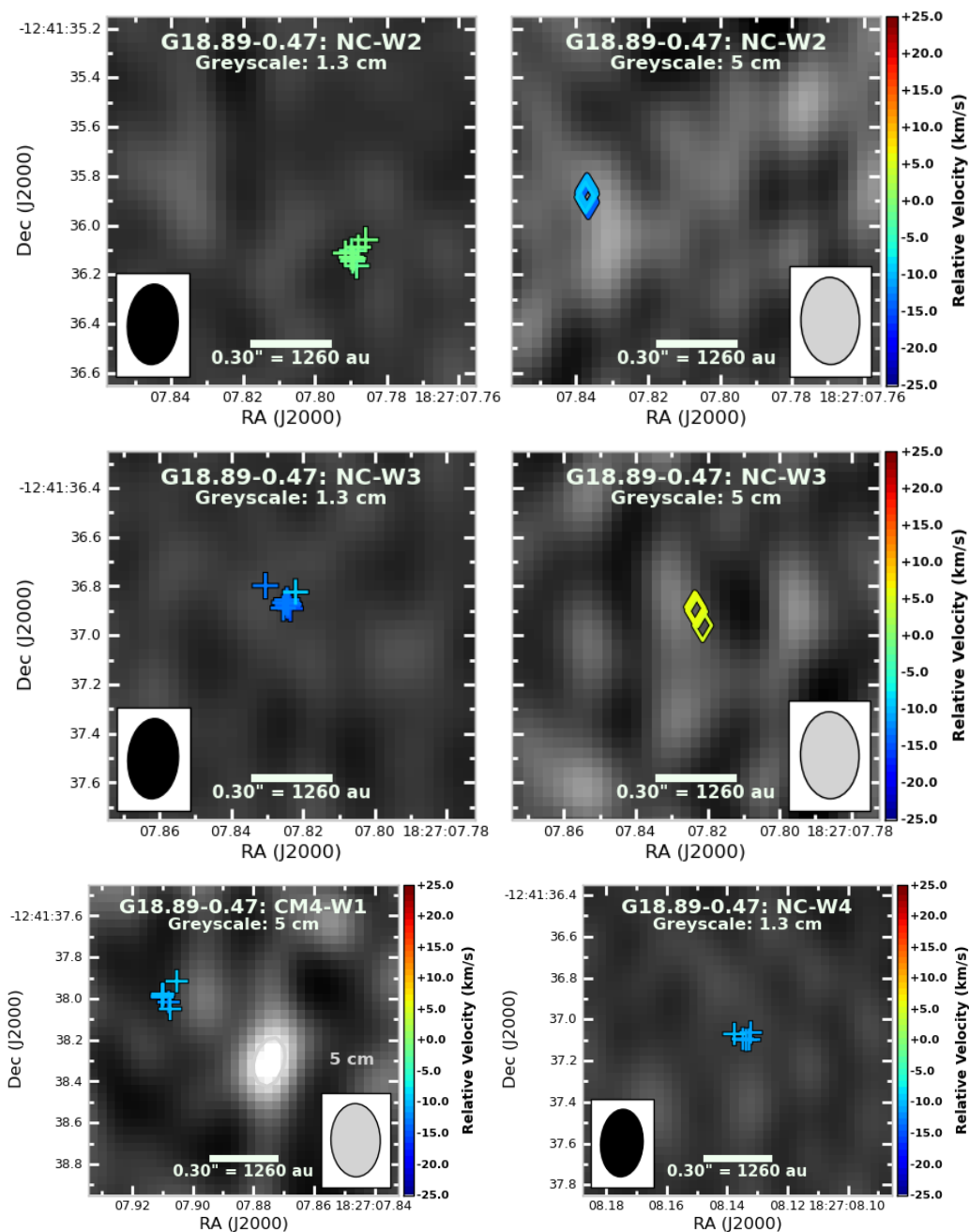
Fig. 4.15.— Maser spot maps for G18.89–0.47, continued. For NC-w2 and NC-W3, the background greyscale is 1.3 cm in the left-hand panels and 5 cm in the right-hand panels. For CM4-W1, background greyscale is 5 cm, and contour levels are [4.5]×σ at 5 cm (silver); no 1.3 cm (black) contours are shown as there is no emission above 4.5σ at 1.3 cm. For NC-W4, background greyscale is 1.3 cm. In the "NC" panels, no contours are shown as there is no emission above 4.5σ at either wavelength. FOV is 1$\farcs$5 in all panels. Maser symbols are color-coded according to velocity relative to source V$_{LSR}$ (66.0 km s^{-1}).
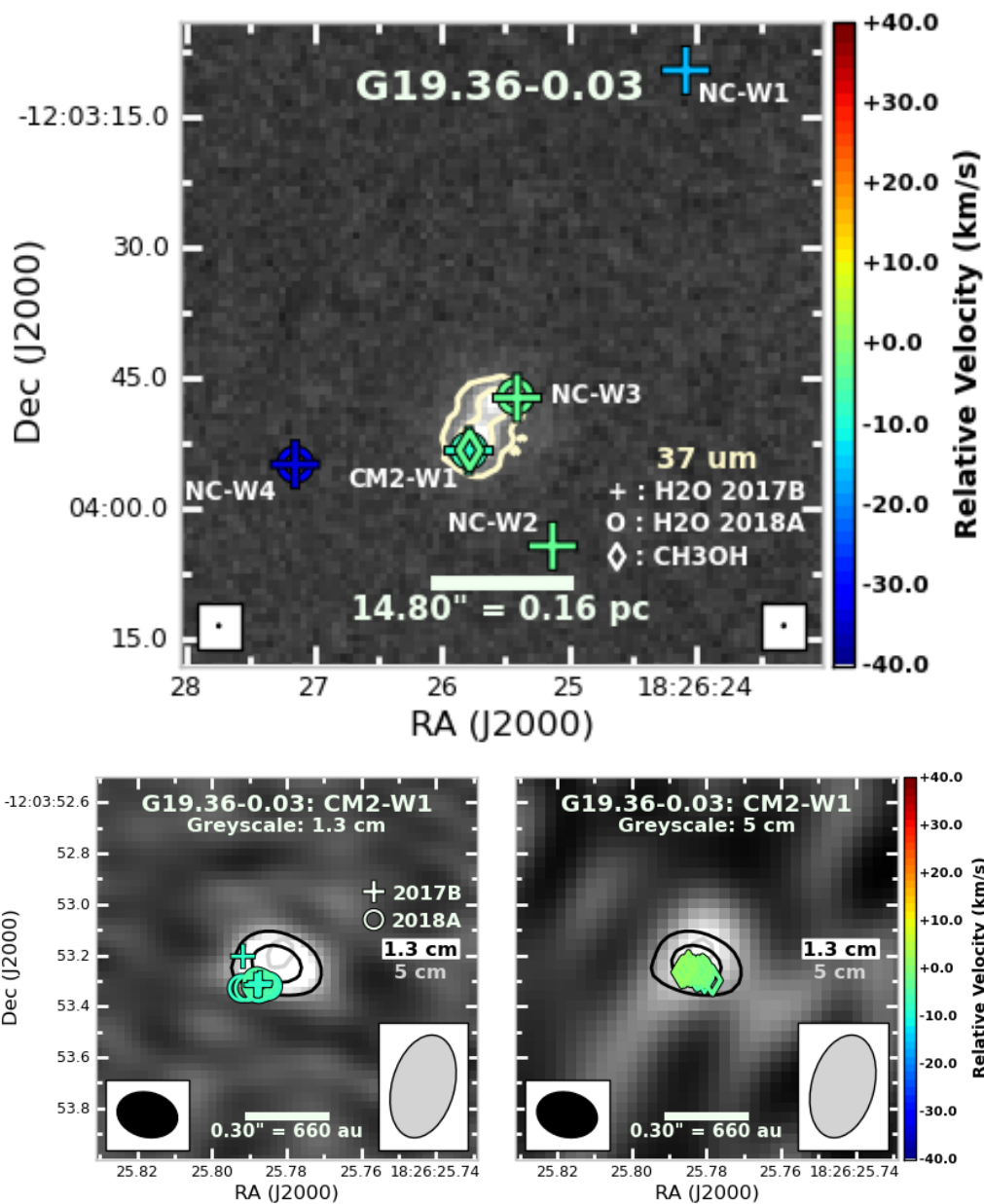
Fig. 4.16.— Maser spot maps for G19.36–0.03. Masers are color-coded by velocity in most panels. In the full FOV (74″), maser clumps are color-coded by peak velocity only, and 37 μm contour levels are [5,15,45]$\times\sigma$, where $\sigma = 0.46$ Jy beam^{-1} is the 37 μm scaled MAD. The background greyscale is 37 μm SOFIA data. In the CM2-W1 image, continuum contour levels are [4.5,10]$\times\sigma$ at both 1.3 cm (black) and 5 cm (silver), and the FOV is 1.″5. H$_2$O maser data from observing epoch 2018.1 (Semester 2017B) are shown with + symbols, and H$_2$O maser data from epoch 2019.6 (Semester 2018A) are shown with ∘. The background greyscale is 1.3 cm in the left-hand panel, and 5 cm in the right-hand panel. Maser symbols are color-coded according to velocity relative to source V$_{LSR}$ (27.0 km s^{-1}).
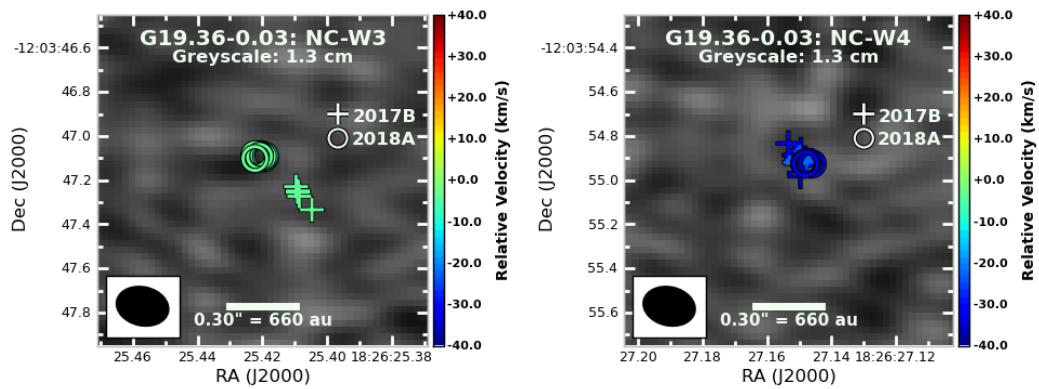
Fig. 4.17.— Maser spot maps for G19.36–0.03, continued. The FOV is 1″5 for both panels. Background greyscale is 1.3 cm in both cases; no contours are shown because there is no continuum emission above 4.5 σ in these FOV at either wavelength. H_2O maser data from observing epoch 2018.1 (Semester 2017B) is shown with + symbols, and H_2O maser data from epoch 2019.6 (Semester 2018A) is shown with ○. Maser symbols are color-coded according to velocity relative to source V_{LSR} (27.0 km s^{-1}).
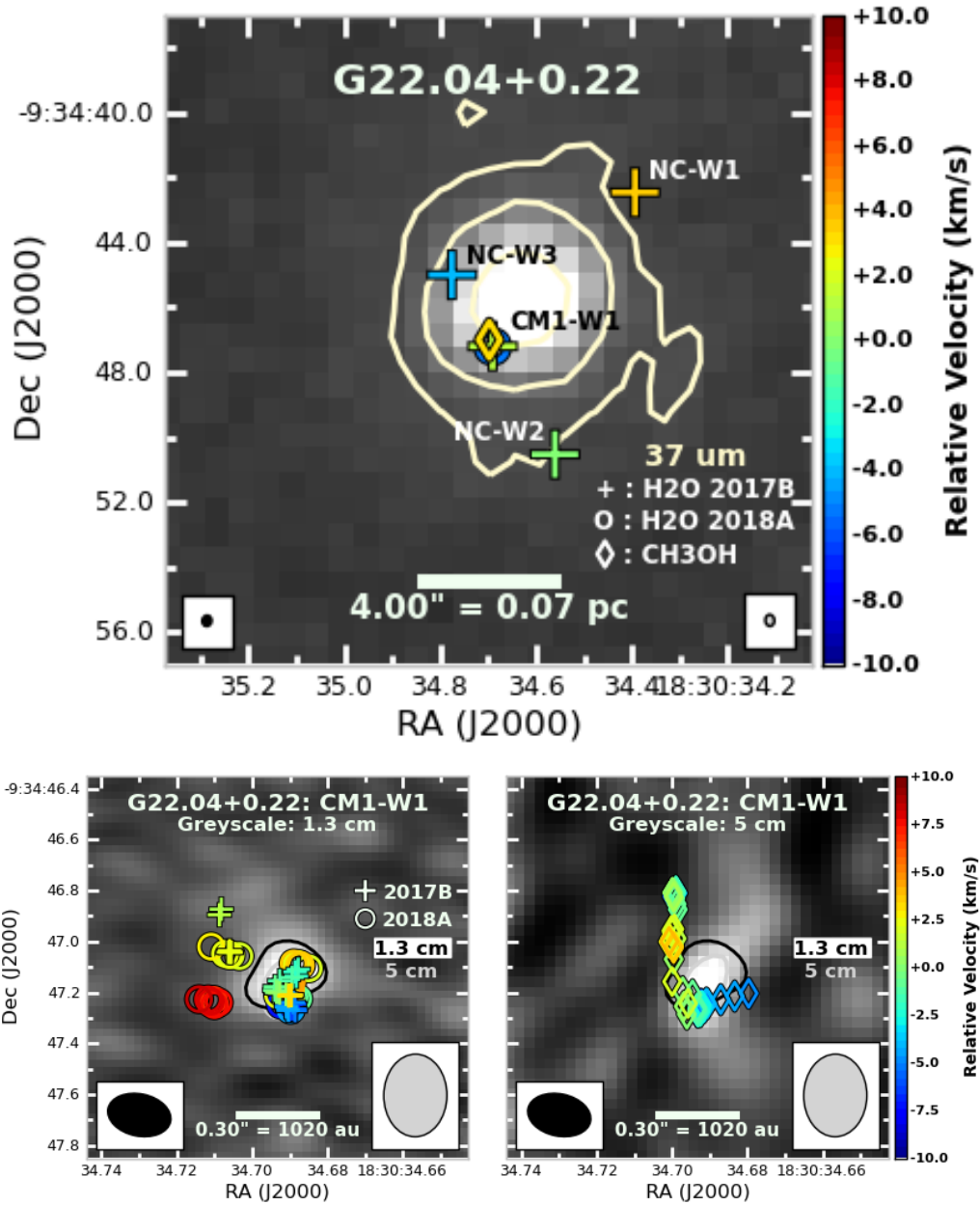
Fig. 4.18.— Maser spot maps for G22.04+0.22. Masers are color-coded by velocity in most panels. In the full FOV (20″), maser clumps are color-coded by peak velocity only, and 37 μm contour levels are [5,15,45]$\times\sigma$, where $\sigma = 0.21$ Jy beam^{-1} is the 37 μm scaled MAD. The background greyscale is 37 μm SOFIA data. In the CM1-W1 image, continuum contour levels are [4.5,10]$\times\sigma$ at both 1.3 cm (black) and 5 cm (silver), and the FOV is 1″5. H$_2$O maser data from observing epoch 2018.1 (Semester 2017B) are shown with + symbols, and H$_2$O maser data from epoch 2019.6 (Semester 2018A) are shown with ○. The background greyscale is 1.3 cm in the left-hand panel, and 5 cm in the right-hand panel. Maser symbols are color-coded according to velocity relative to source V$_{LSR}$ (51.0 km s^{-1}).
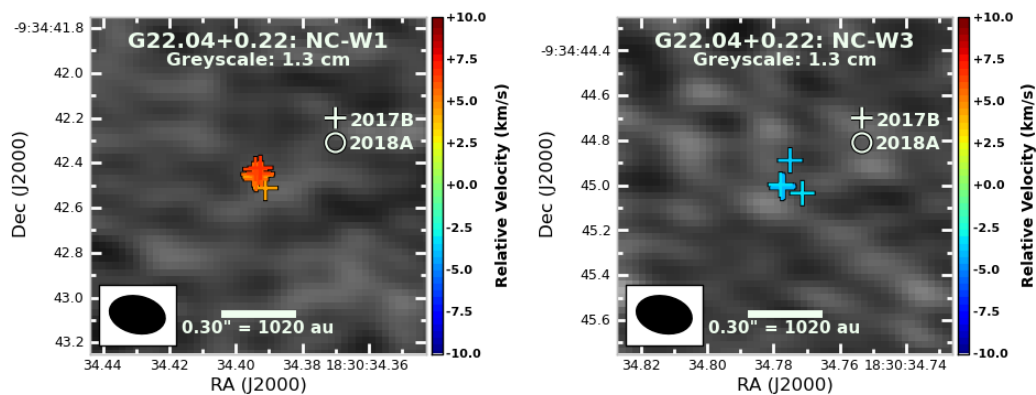
Fig. 4.19.— Maser spot maps for G22.04+0.22, continued. The FOV is 1″5 for all four panels. Background greyscale is 1.3 cm in both panels; no contours are shown because there is no continuum emission above 4.5 σ in these FOV at either wavelength. H_2O maser data from observing epoch 2018.1 (Semester 2017B) is shown with + symbols, and H_2O maser data from epoch 2019.6 (Semester 2018A) is shown with ∘. Maser symbols are color-coded according to velocity relative to source V_{LSR} (51.0 km s^{-1}).
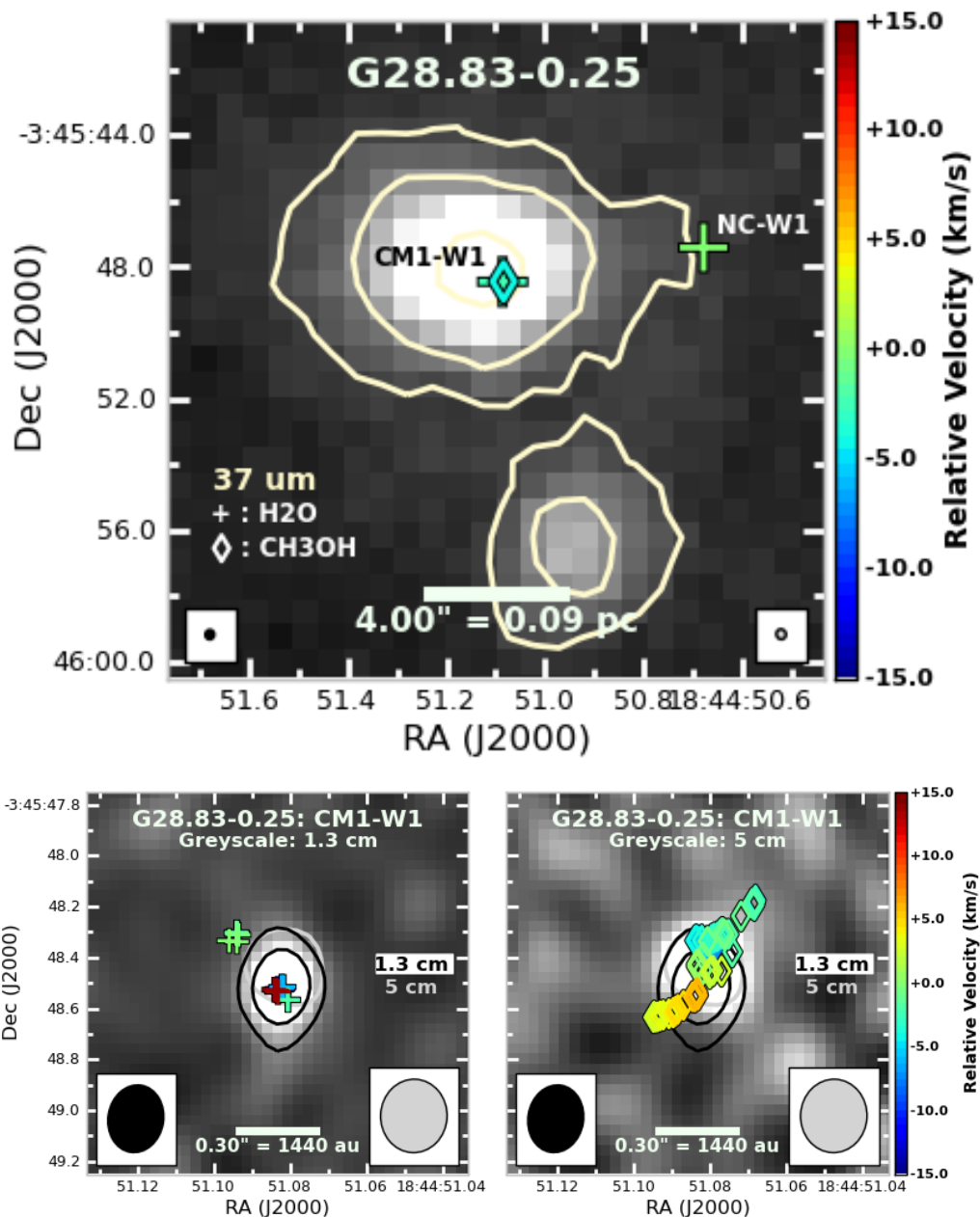
Fig. 4.20.— Maser spot maps for G28.83−0.25. Masers are color-coded by velocity in most panels. In the full FOV (20″), maser clumps are color-coded by peak velocity only, and 37 μm contour levels are [5,15,45]×σ, where σ = 0.26 Jy beam^{-1} is the 37 μm scaled MAD. The background greyscale is 37 μm SOFIA data. In the CM1-W1 image, contour levels are [4.5,10]×σ at both 1.3 cm (black) and 5 cm (silver), and the FOV is 1″.5. The background greyscale is 1.3 cm in the left-hand panel, and 5 cm in the right-hand panel. Maser symbols are color-coded according to velocity relative to source V$_{LSR}$ (87.0 km s^{-1}).
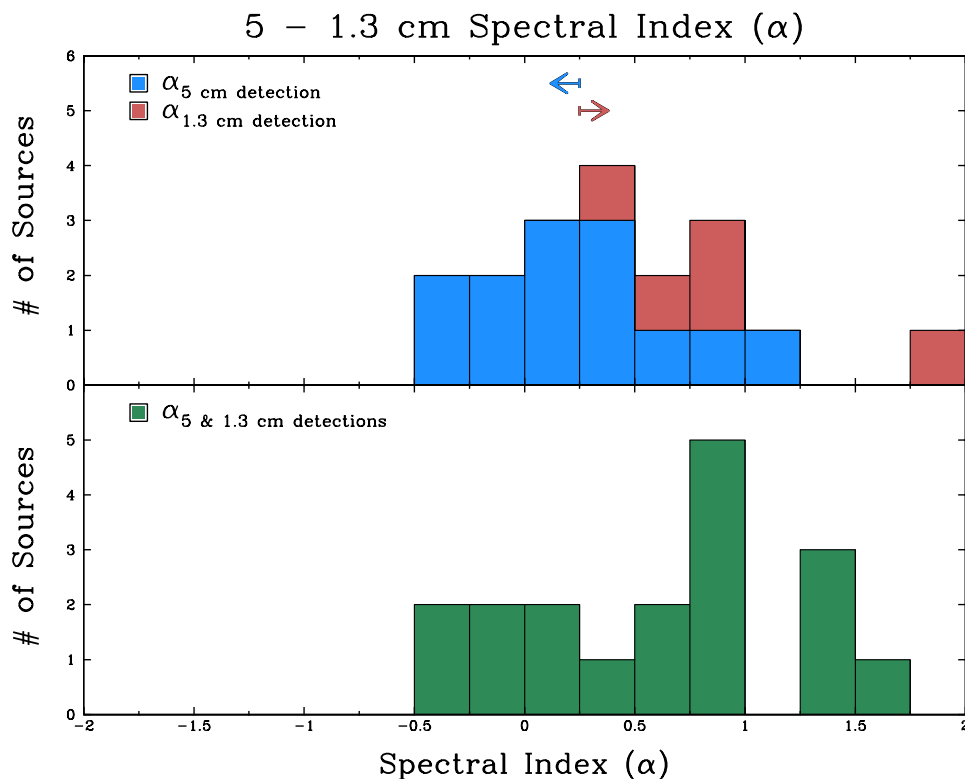
Fig. 4.21.— Histogram of spectral indices (α) for all centimeter continuum detections in the EGO-9 sample. The bottom panel shows the distribution of α for sources detected at both 1.3 and 5 cm (green). The top panel shows a color-coded distribution of spectral indices which are upper limits (blue) or lower limits (red). For instance: there are three spectral indices within $0.75 < \alpha < 1.0$ - two are lower limits (red) and one is an upper limit (blue). For sources detected at only one wavelength, we adopt the 4σ non-detection limit as the flux density "measurement" for the non-detected band in order to derive the upper/lower limit for α. The blue and red arrows at the top of this panel serve as a reminder that the α values in each bin are lower (upper) limits, and the true α for each source represented here could in fact be higher (lower).
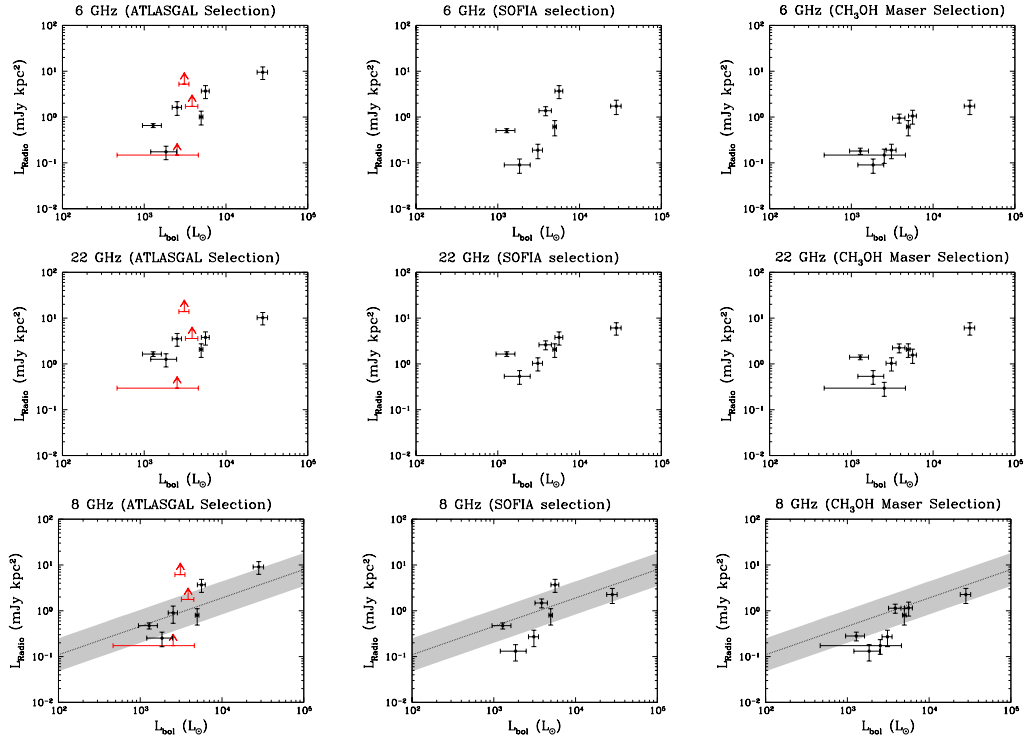
Fig. 4.22.— L_{radio} versus L_{bol} for the 9 EGO targets, where L_{radio} is the radio distance-luminosity ($S_\nu D^2$), and L_{bol} is the median of the four flux densities for each EGO derived by Towner et al. (2019). L_{radio} is derived three times in each band: ATLASGAL-, SOFIA-, and 6.7 GHz CH_3OH maser-selected regions. L_{radio} is derived from the sum of all continuum emission within each aperture at each band; a source need not be detected at 1.3 cm to be included in $L_{5\ cm}$, etc. Non-detections/upper limits are not included in the flux density totals. The left-hand column shows L_{radio}-L_{bol} where L_{radio} represents all radio continuum flux density within the ATLASGAL aperture, the middle column shows the same where L_{radio} is determined from all continuum flus within the SOFIA aperture, and in the right-hand column, L_{radio} is for those continuum sources which have associated 6.7 GHz masers. See the text for more information on each aperture. Upper limits are shown for sources which have resolved-out continuum emission within the ATLASGAL aperture. The 8 GHz distance-luminosity values were determined by interpolating each centimeter detection to 8 GHz using its unique spectral index and 22/6 GHz flux density values, and then summing the resulting 8 GHz flux densities within each appropriate aperture. The dotted lines and shaded regions on the 8 GHz plots show the best-fit line and 1σ dispersion of L_{radio} versus L_{bol} for the POETS sample of Sanna et al. (2018). The Sanna et al. (2018) best-fit line for L_{radio} versus L_{bol} is $\log(L_{radio}) = (0.62 \pm 0.04) \times \log(L_{bol}) + (-2.2 \pm 0.1)$.
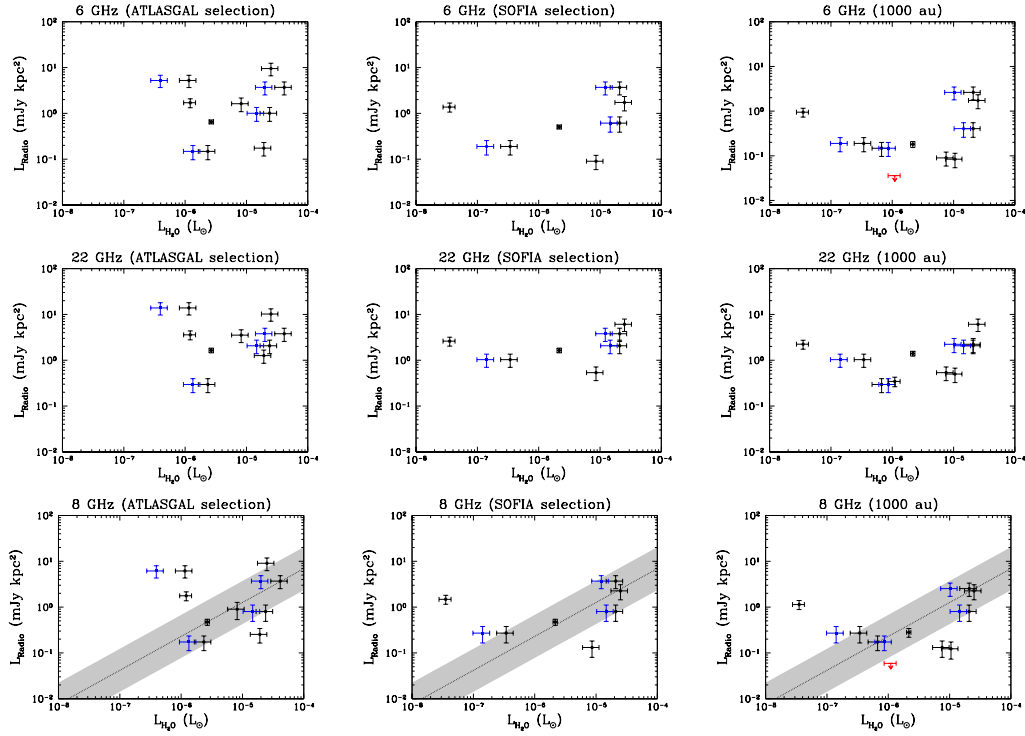
Fig. 4.23.— L_{radio} versus L_{H_2O} for the EGO-9 targets, where L_{radio} is the radio distance-luminosity ($S_\nu D^2$ and L_{H_2O} is the isotropic H_2O maser luminosity in $L_\odot$. L_{H_2O} is determined by summing the flux density in all maser spots over all channels within a given region. The left-hand column shows L_{radio} versus L_{H_2O} for the ATLASGAL-selected region, the middle column shows the same for the SOFIA-selected region, and the right-hand column shows $L_{radio}-L_{H_2O}$ for all continuum sources with H_2O-maser emission within 1000 au. See § 4.5.4 for a justification of the 1000-au limit. For those EGOs observed twice at K-band, the first epoch of observations is shown in black and the second in blue. The dotted and dashed lines in the top and middle panels of the 1000-au column show the maximum and minimum distance-rms values (rms$\times D^2$); these values indicate that the 6 GHz continuum non-detections are not significant. The dotted line and shaded region in the 8 GHz plots (bottom panels) show the best-fit line and 1σ dispersion of the L_{radio} versus L_{H_2O} for the POETS sample (Sanna et al. 2018, Figure 5, Panel a): $\log(L_{radio}) = (0.74 \pm 0.07) \times \log(L_{H_2O}) + (3.8 \pm 0.4)$.
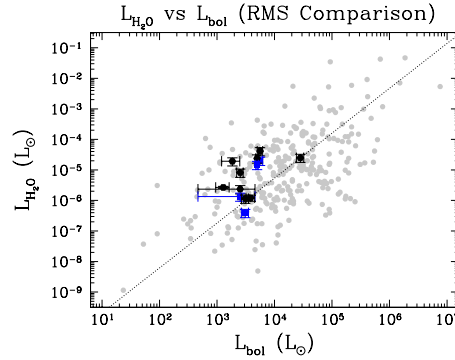
Fig. 4.24.— L_{H_2O} versus L_{bol} for our sample (black and blue points) compared to the sources in the Red MSX Source (RMS) survey (gray points; see Urquhart et al. 2011, Figure 16). The dotted line shows the best-fit relation for L_{H_2O} versus L_{bol} for the RMS-selected sources: $L_{H_2O} = 7.1 \times 10^{-12} \times L_{Bol}^{1.47}$. For our sources, L_{H_2O} is the luminosity of all H_2O maser emission within the ATLASGAL 870 μm contour used in Towner et al. (2019) (typically $5\sigma_{870\mu m}$).
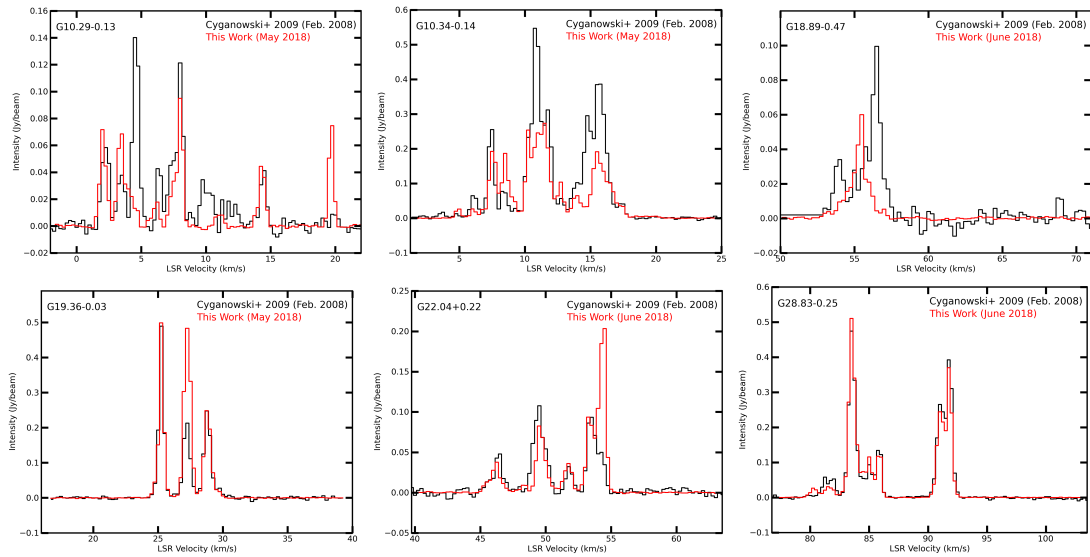
Fig. 4.25.— 6.7 GHz CH_3OH maser line profiles for 2008 (Cyganowski et al. 2009, black) and 2018 (this work, red). Line profiles were extracted over identical regions for the two epochs of each source. Images were regridded and convolved to have identical angular and velocity resolutions before the profiles were extracted. $\Delta V = 0.25$ km s^{-1} for all plots. The angular resolution of each image is $\sim 3''$; see Cyganowski et al. (2009) for exact values. These profiles suggest that some non-trivial variation in the 6.7 GHz CH_3OH maser kinematics over the 10-year period is not uncommon, but the lack of any extreme ($>10\times$) changes in flux density suggests that these variations are more likely due to variations in the masing gas (i.e. a change in the projected or actual length of the masing column) rather than any significant variations in the pumping mechanism itself (i.e. the luminosity of the central MYSO).
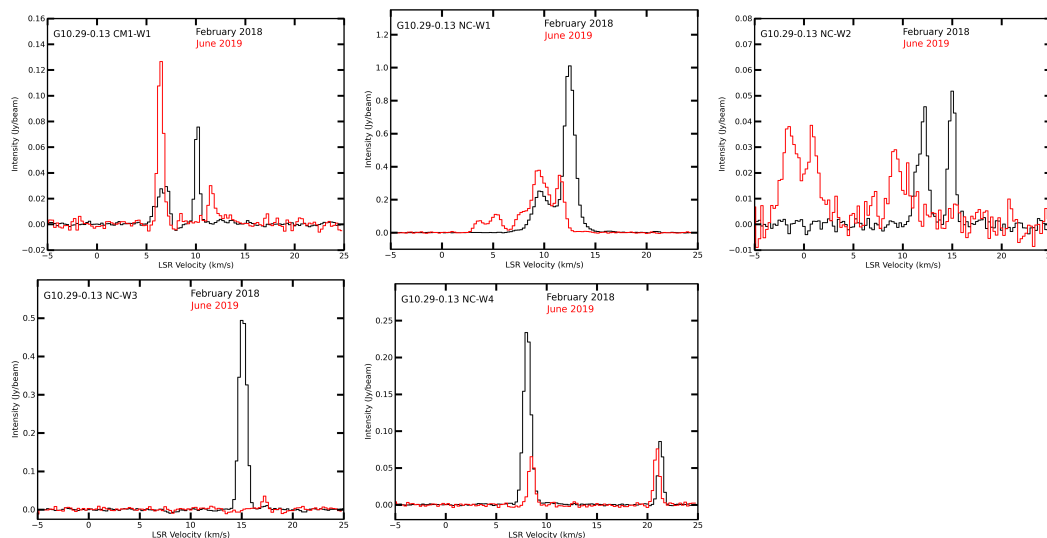
Fig. 4.26.— Epcoh 2018.1 (black) and 2019.6 (red) H_2O spectra for G10.29−0.13.
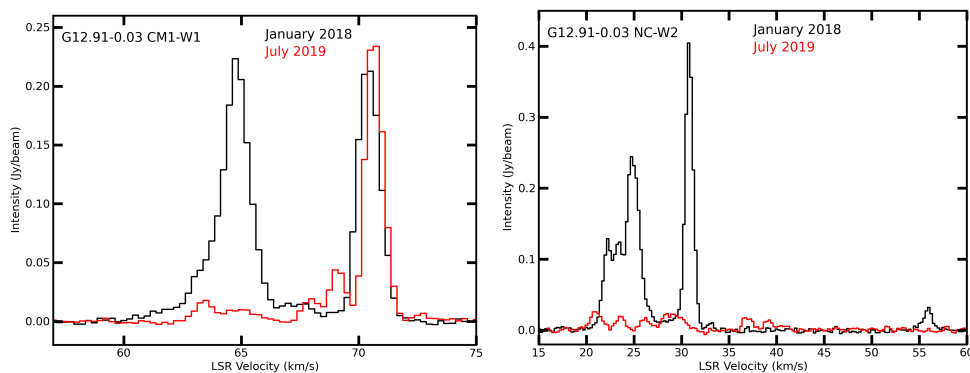
Fig. 4.27.— Epoch 2018.1 (black) and 2019.6 (red) H_2O spectra for G12.91−0.03.
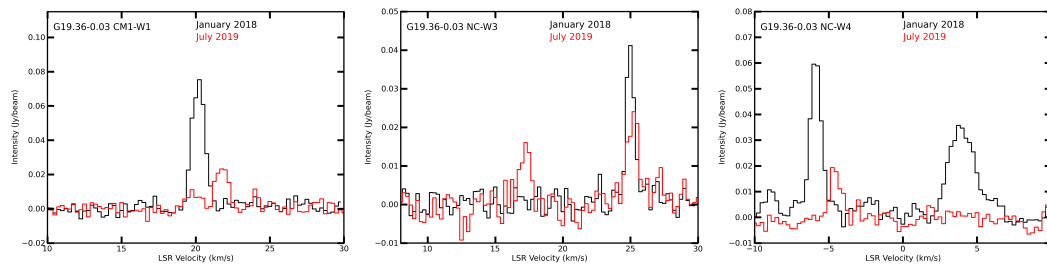
Fig. 4.28.— Epoch 2018.1 (black) and 2019.6 (red) H_2O spectra for G19.36−0.03.
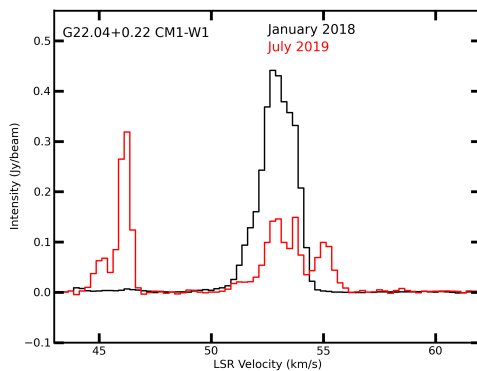
Fig. 4.29.— Epoch 2018.1 (black) and 2019.6 (black) H$_2$O spectra for G22.04+0.22.
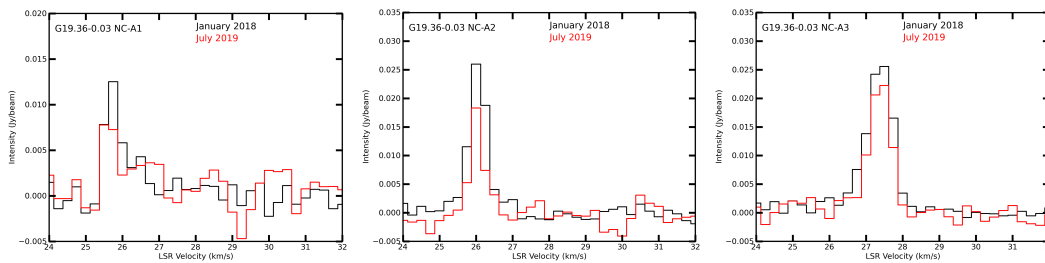
Fig. 4.30.— NH$_3$ (3,3) spectra for G19.36−0.03, for observation epochs January 2018 (black) and July 2019 (red). Our data show little variation at a statistically-significant level (>5σ) between the two epochs of observation. Typical rms values are 5.4 mJy beam^{-1} (2018.1) and 8.8 mJy beam^{-1} (2019.6), respectively.

Chapter 5

Summary and Conclusions

We have conducted a multi-wavelength analysis of a sample of 20 Extended Green Objects in the Milky Way in order to characterize the evolutionary state of each protocluster, the onset of strong feedback from the massive cluster members and their individual properties, and the demographics of the protostellar populations as a whole.

We find typical massive-source multiplicities of one to a few per EGO, regardless of whether infrared or 6.7 GHz maser-selection criteria are used. This is consistent with EGOs being typical massive protoclusters which will form one to a few massive stars, rather than extreme regions forming hundreds of OB stars (e.g. 30 Doradus). Using proprietary and archival infrared data (Chapter 2), we have constructed SEDs for each EGO from 3.6 to 870 μm, and fitted those SEDs using three publicly-available radiative-transfer modeling packages. We find that our different modeling methods generally converge to the same luminosity (L_{bol}) values, but give widely divergent results for other physical properties ($T_\star$, $R_\star$, disk mass if any, etc). We attribute this to the fact that all three modeling packages assume a single central star, and conclude that, at least at these spatial resolutions ($\sim$0.1 pc), this assumption for our sources is poor and there are multiple protostars present which contribute non-trivially to the total infrared flux density.

We further find that the L/M values for our sources show no trend with mass, but do seem to occupy a very specific range of values compared to other samples (24.7 ± 8.4 $L_\odot/M_\odot$). The L/M for our sources fall between the typical L/M values for the "IR-quiet" ($L/M \sim 3$ $L_\odot/M_\odot$) and "IR-bright" ($L/M \sim 70$ $L_\odot/M_\odot$) populations identified by other teams, which are suggested to be two evolutionary stages in a larger evolutionary sequence. The difference between the first and second state in the presence of a massive ($>8M_\odot$) protostar which is heating and ionizing the core in which it is embedded. This suggests that young EGOs such as we observe in this work (without known UC H II regions) may represent a transitional population between these two evolutionary states, i.e., a stage of evolution which is extremely useful for differentiating between competing theories of high-mass star formation.

Observations of these EGOs in the radio regime (Chapters 3 and 4) have shown ubiquitous weak (<1 mJy), compact 1.3 and 5 cm continuum emission, most of which remains unresolved even at $\sim$1000-2000 au resolutions. 100% of our EGOs have at least one 1.3 cm and one 5 cm detection, and most have 3 detections or more. All EGOs are associated with 22 GHz H_2O and 6.7 GHz CH_3OH masers, and $\sim$45% are associated with NH_3 (3,3) masers. The continuum sources which are associated with 6.7 GHz CH_3OH masers are also strongly associated with thermal CH_3OH emission. In all but one case, these sources are found within the 75% flux contour of the ATLASGAL host clump and the 5σ contour, i.e., at or very near the center of the clump.

The spectral indices we derive for these continuum detections span a broad range ($-0.5 \lesssim \alpha \lesssim 2$). There is a small but significant ($\sim$10%) population of sources whose spectral indices are consistent with non-thermal emission, and the majority of our sample (61%) is consistent with thermal free-free emission such as would be found in an ionized jet or nascent H II region. There are also a few sources with $\alpha > 1.1$, which is consistent with both

primarily optically-thick HC H II regions and with emission from thermal dust at 1.3 cm. This range suggests that, rather than the centimeter continuum emission in EGOs being attributable to a single emission mechanism, EGOs exhibit multiple centimeter continuum-producing processes simultaneously.

We therefore conclude that additional high-spatial resolution observations at millimeter wavelengths are needed. These observations will allow us to accurately model the radio-regime SEDs of each continuum detection to disentangle the multiple possible emission mechanisms at play.

5.1   Future Directions

We have recently obtained $\sim 0.''3$-resolution observations of these EGOs at 1.3 and 3 mm using the Atacama Large Millimeter/submillimeter Array (ALMA). We will use these data to perform the modeling discussed above for each centimeter and each millimeter contin-uum detection. This will allow us to sample the protostellar population in each EGO down to $\sim 0.1 M_\odot$. From these results, we will be able to more fully examine the mass distribution and segregation in these protoclusters, the evolutionary states of the individual protostars, and, for the most massive members, the presence or absence of nascent H II regions, and their properties.

Given the small sizes of the emitting regions implied by our data, we must also note that, in the centimeter regime, very high angular resolutions will be necessary in order to spatially resolve the scales of interest for the formation of HC H II regions. We are at the resolution limit of the VLA with these data at 5 cm already. Consequently, we suggest that observations such as this are excellent candidates for observation by the proposed Next Generation Very Large Array (ngVLA) facility, which would have the capacity to spatially resolve the scales of interest at ~ 5 cm wavelengths.

Appendix A

Robitaille (2017), Robitaille et al. (2006), & Zhang & Tan (2018) Model SED Plots for Individual Sources
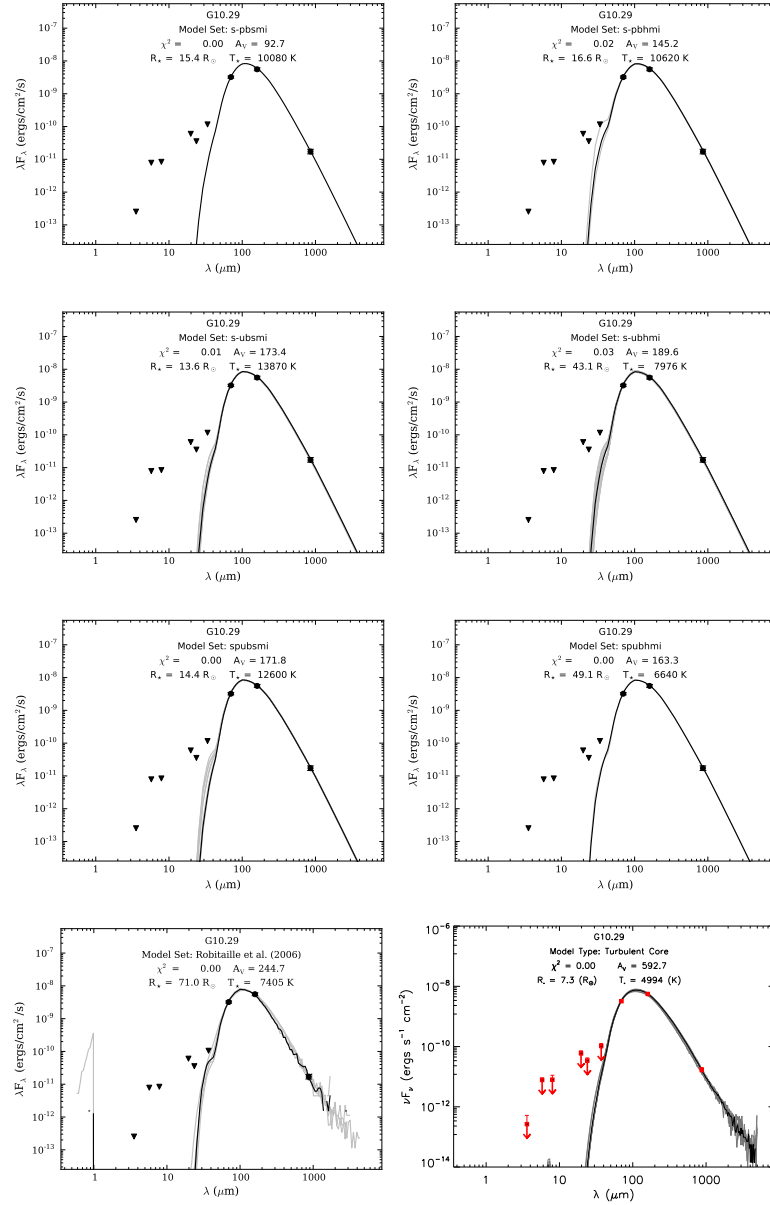
Fig. A.1.— SED modeling results for G10.29–0.13, showing: (top six panels) the six best model sets from the Robitaille (2017) models based on χ^2 values, (bottom left panel) the model results from Robitaille et al. (2006), and (bottom right panel) the model results from Zhang & Tan (2018).
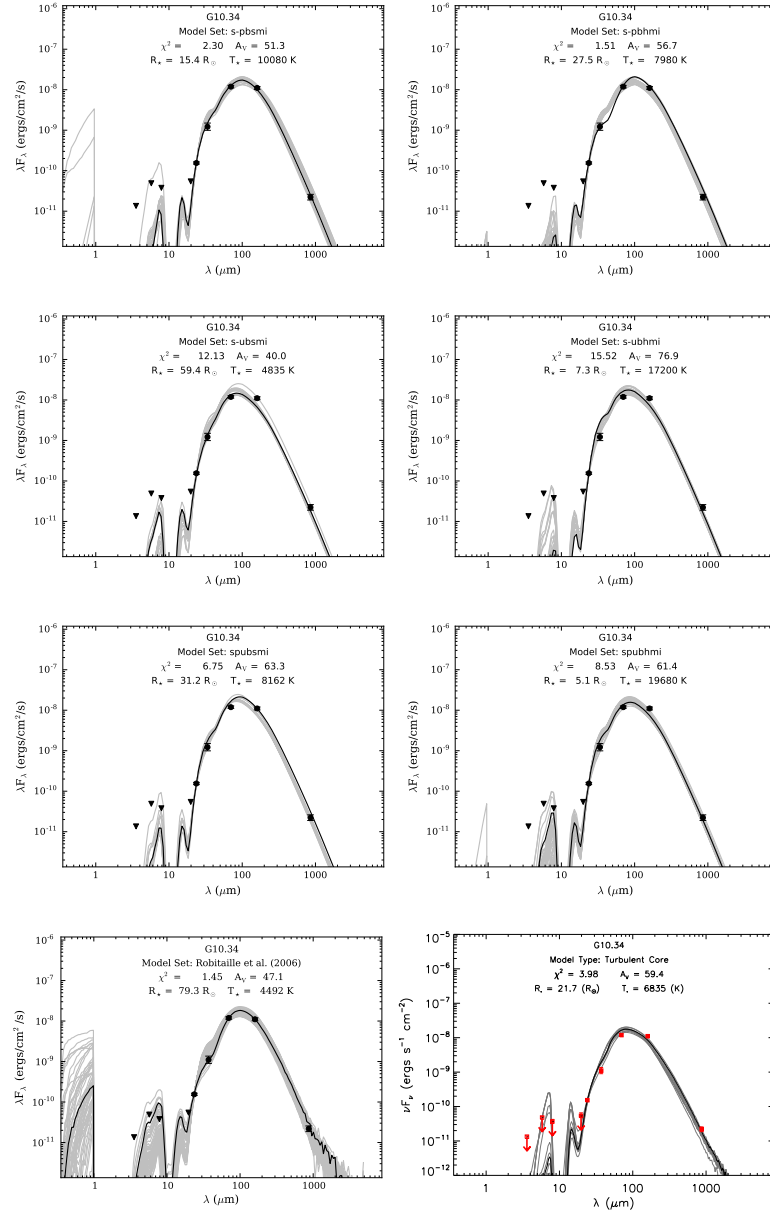
Fig. A.2.— SED modeling results for G10.34−0.14, showing: (top six panels) the six best model sets from the Robitaille (2017) models based on χ^2 values, (bottom left panel) the model results from Robitaille et al. (2006), and (bottom right panel) the model results from Zhang & Tan (2018).
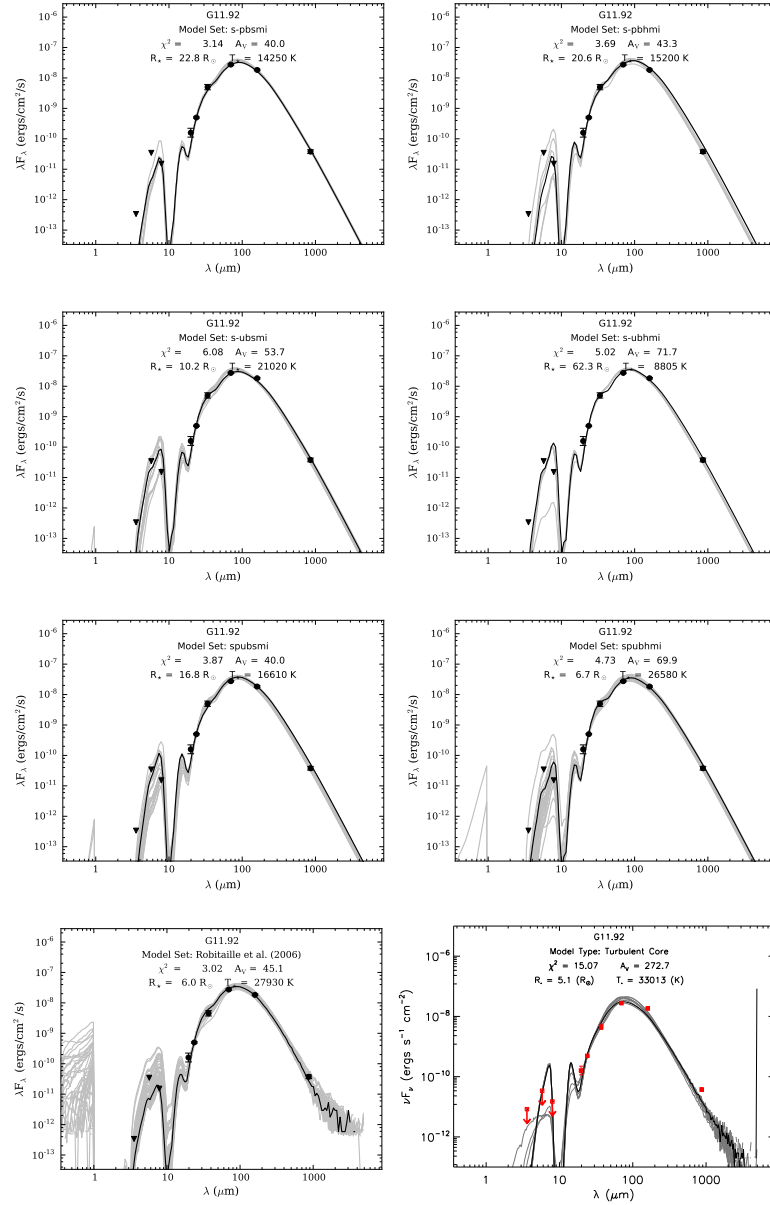
Fig. A.3.— SED modeling results for G11.92−0.61, showing: (top six panels) the six best model sets from the Robitaille (2017) models based on χ^2 values, (bottom left panel) the model results from Robitaille et al. (2006), and (bottom right panel) the model results from Zhang & Tan (2018).
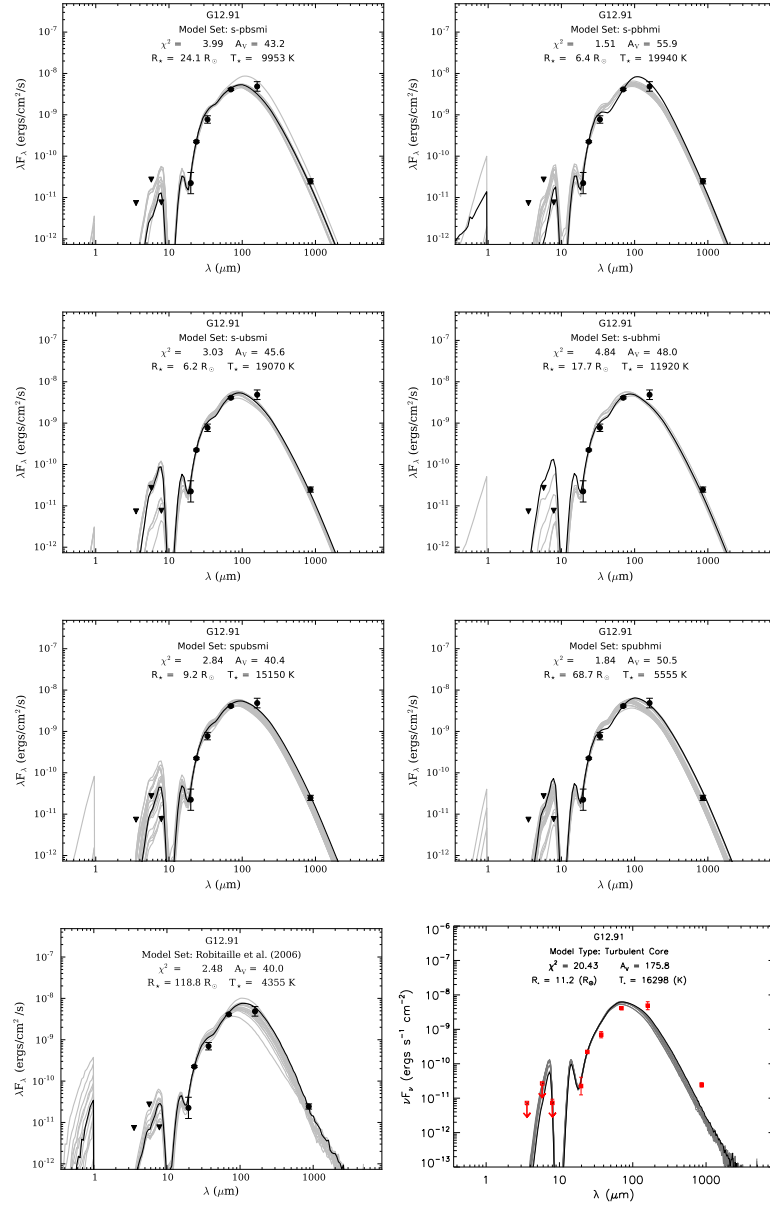
Fig. A.4.— SED modeling results for G12.91−0.03, showing: (top six panels) the six best model sets from the Robitaille (2017) models based on χ^2 values, (bottom left panel) the model results from Robitaille et al. (2006), and (bottom right panel) the model results from Zhang & Tan (2018).
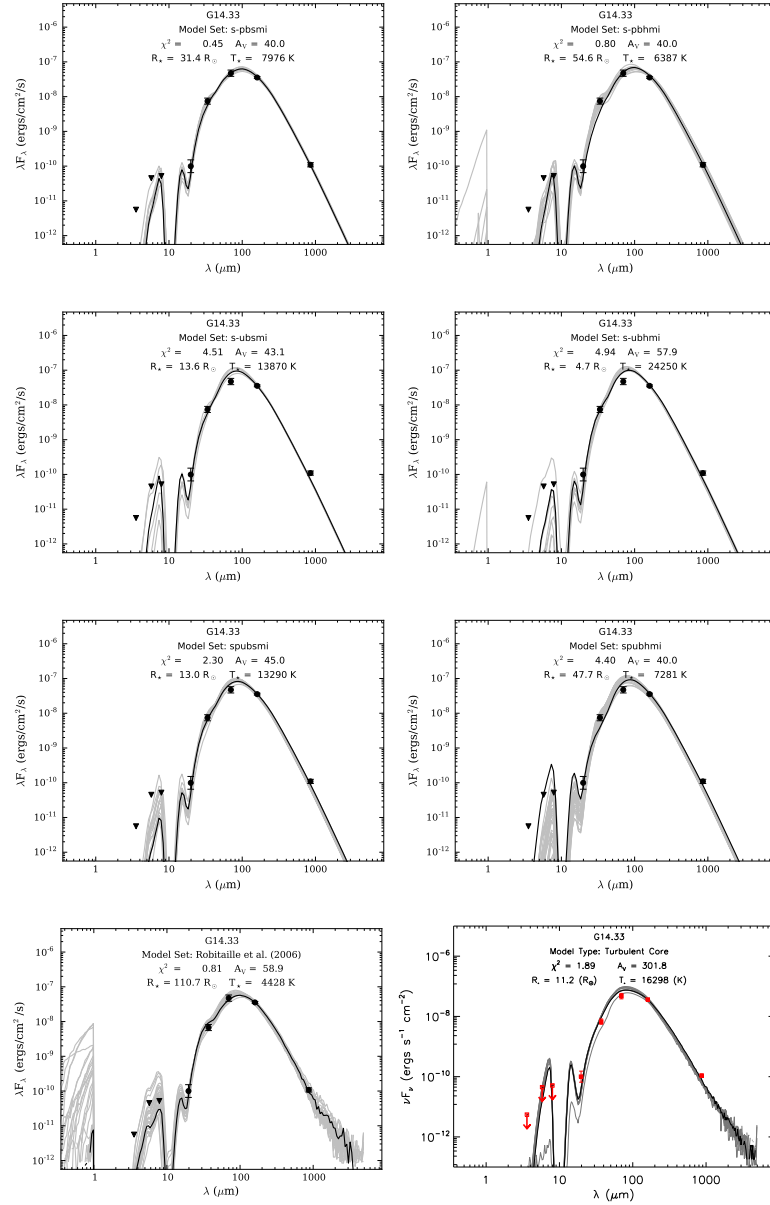
Fig. A.5.— SED modeling results for G14.33−0.64, showing: (top six panels) the six best model sets from the Robitaille (2017) models based on χ^2 values, (bottom left panel) the model results from Robitaille et al. (2006), and (bottom right panel) the model results from Zhang & Tan (2018).
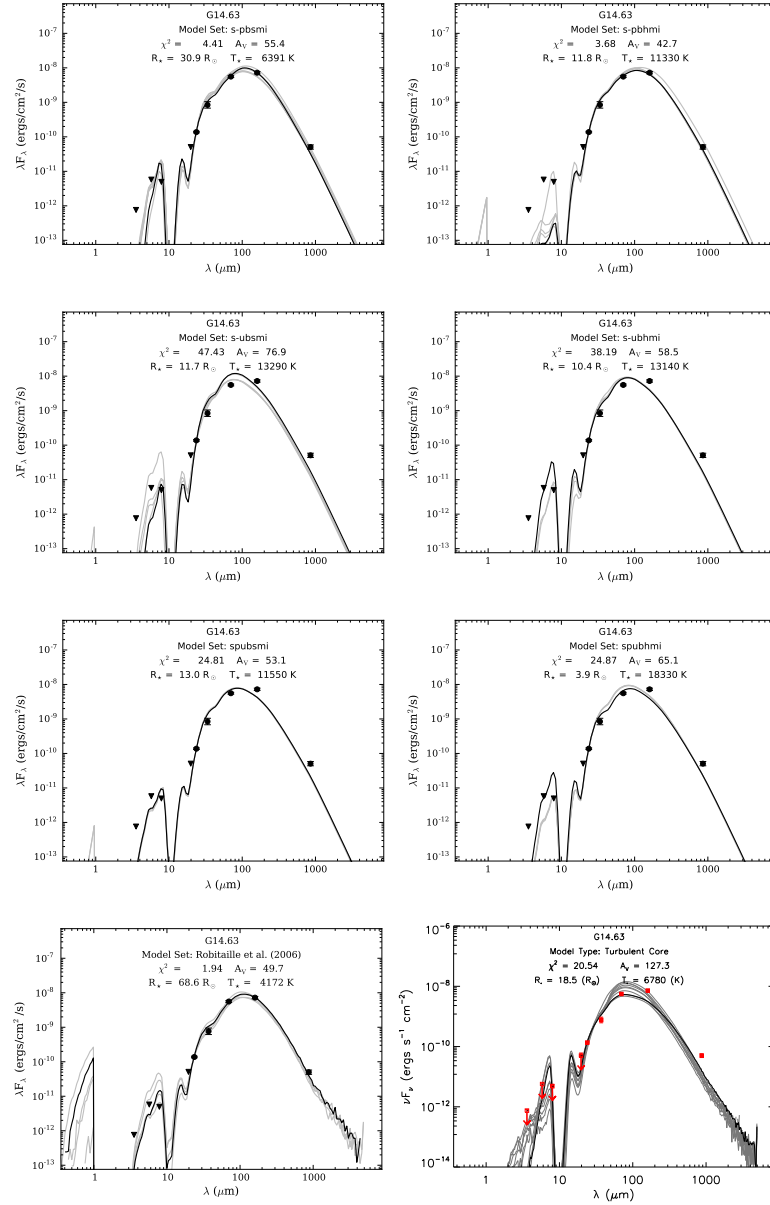
Fig. A.6.— SED modeling results for G14.63−0.58, showing: (top six panels) the six best model sets from the Robitaille (2017) models based on χ^2 values, (bottom left panel) the model results from Robitaille et al. (2006), and (bottom right panel) the model results from Zhang & Tan (2018).
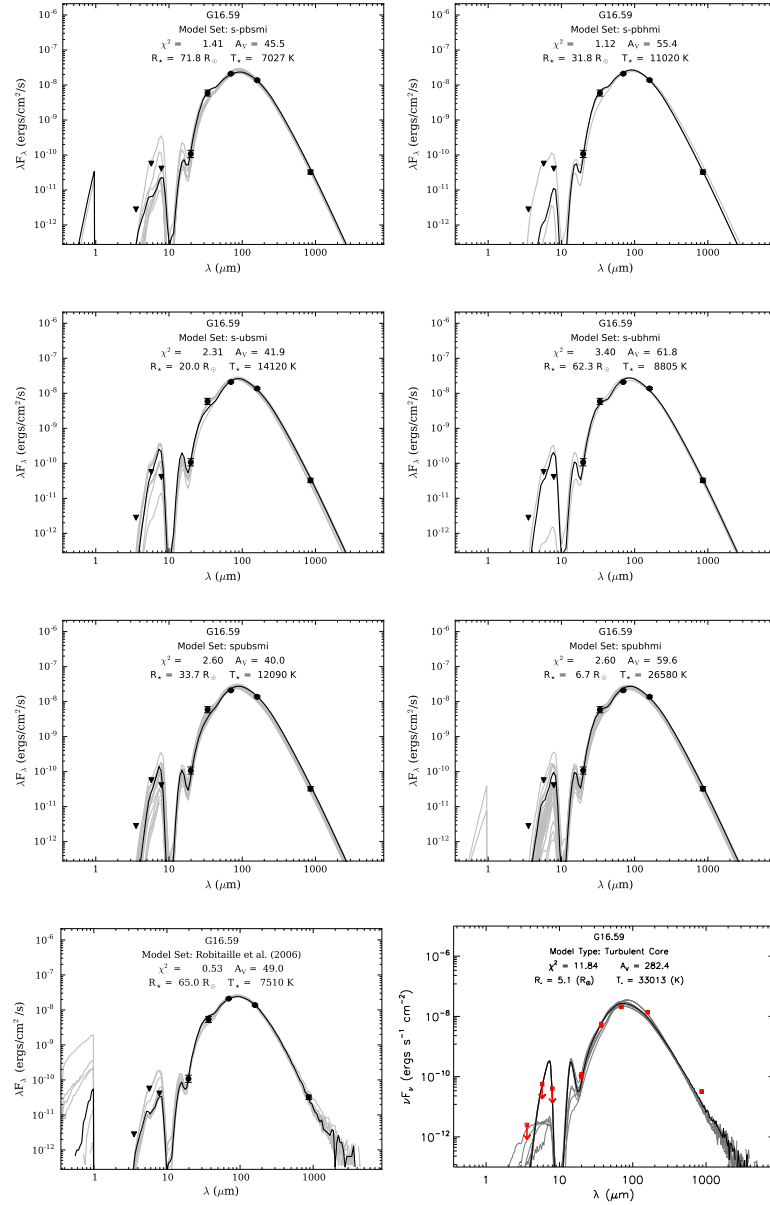
Fig. A.7.— SED modeling results for G16.59−0.05, showing: (top six panels) the six best model sets from the Robitaille (2017) models based on χ^2 values, (bottom left panel) the model results from Robitaille et al. (2006), and (bottom right panel) the model results from Zhang & Tan (2018).
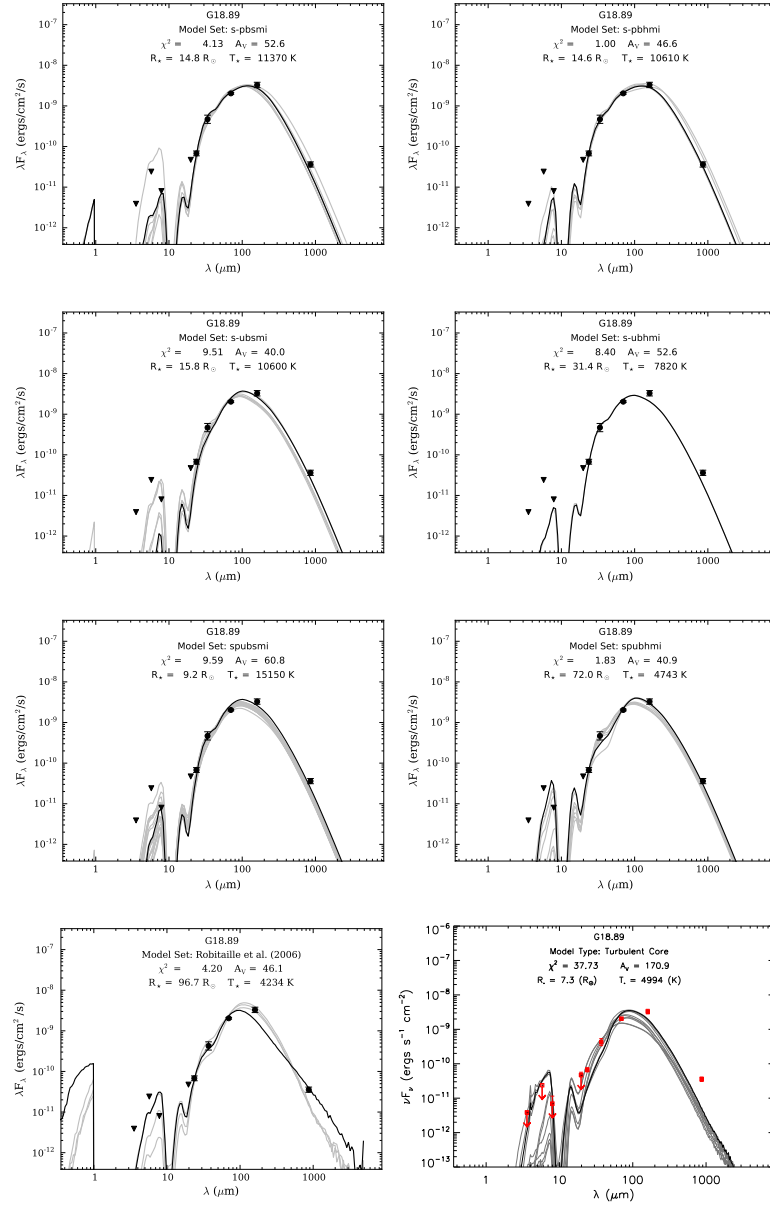
Fig. A.8.— SED modeling results for G18.89−0.47, showing: (top six panels) the six best model sets from the Robitaille (2017) models based on χ^2 values, (bottom left panel) the model results from Robitaille et al. (2006), and (bottom right panel) the model results from Zhang & Tan (2018).
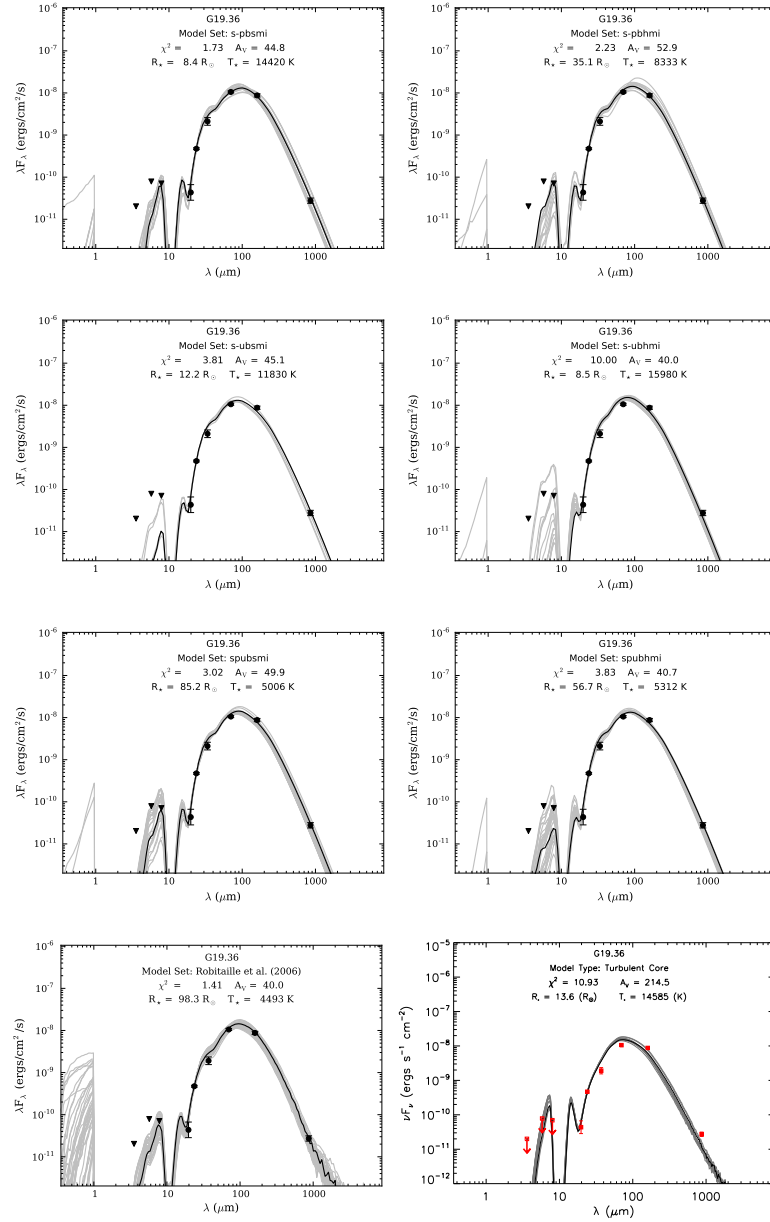
Fig. A.9.— SED modeling results for G19.36−0.03 showing: (top six panels) the six best model sets from the Robitaille (2017) models based on χ^2 values, (bottom left panel) the model results from Robitaille et al. (2006), and (bottom right panel) the model results from Zhang & Tan (2018).
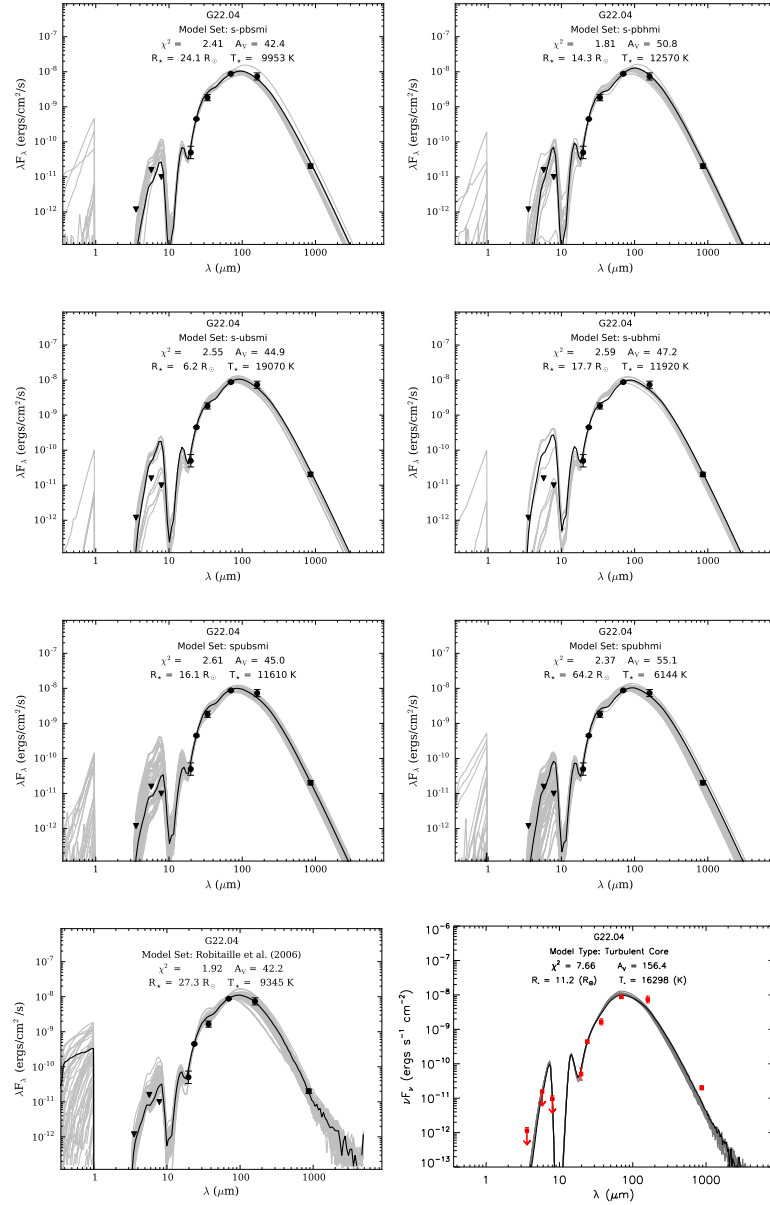
Fig. A.10.— SED modeling results for G22.04+0.22, showing: (top six panels) the six best model sets from the Robitaille (2017) models based on χ^2 values, (bottom left panel) the model results from Robitaille et al. (2006), and (bottom right panel) the model results from Zhang & Tan (2018).
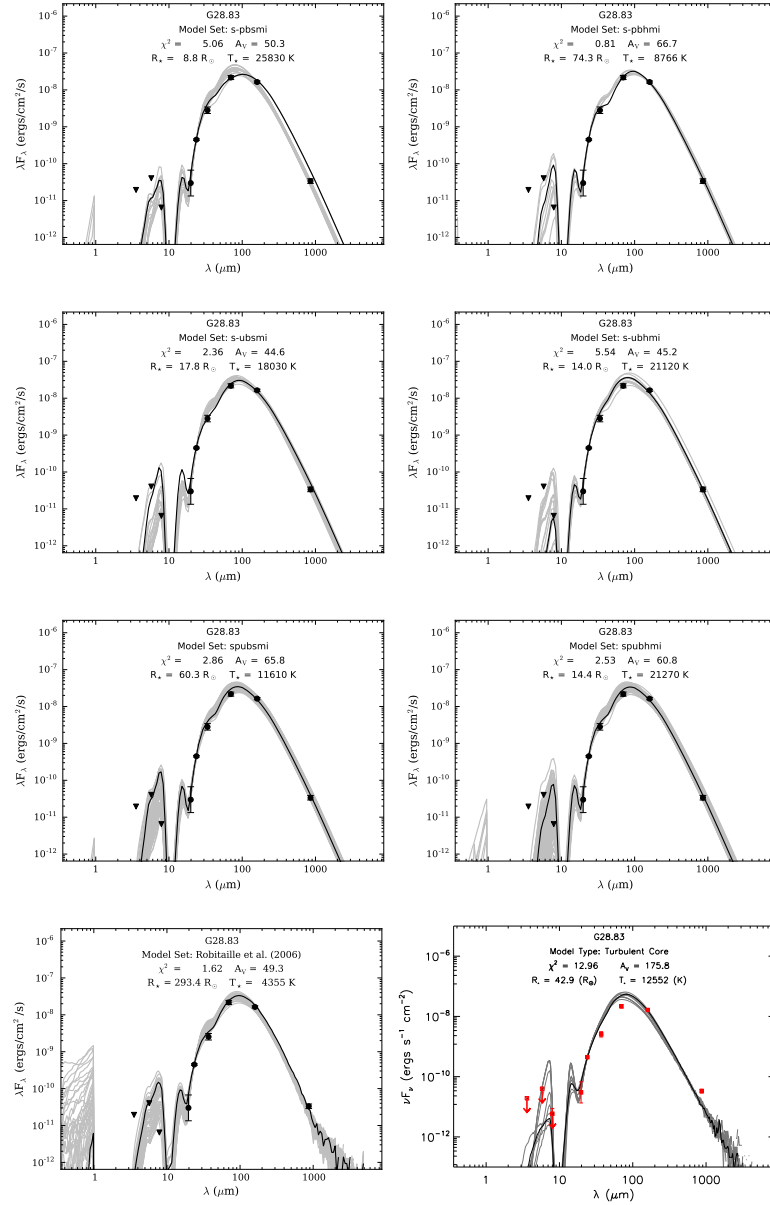
Fig. A.11.— SED modeling results for G28.83−0.25, showing: (top six panels) the six best model sets from the Robitaille (2017) models based on χ^2 values, (bottom left panel) the model results from Robitaille et al. (2006), and (bottom right panel) the model results from Zhang & Tan (2018).
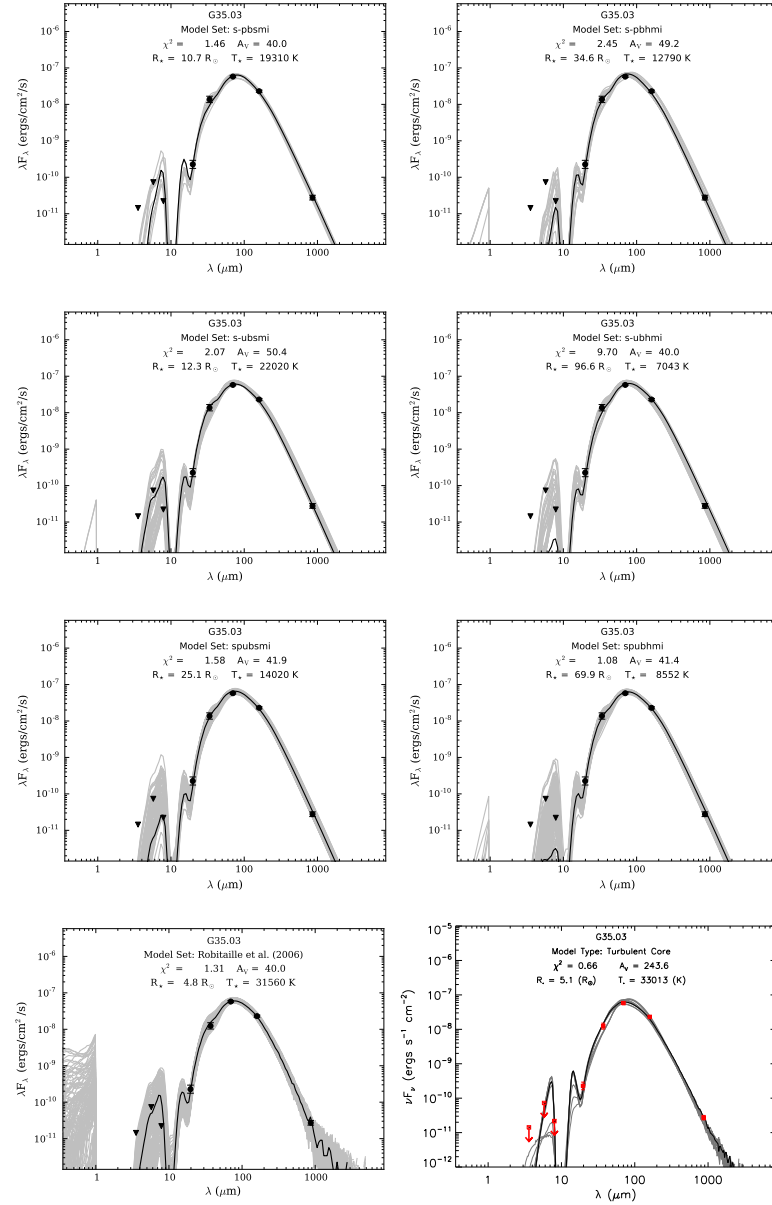
Fig. A.12.— SED modeling results for G35.03+0.35, showing: (top six panels) the six best model sets from the Robitaille (2017) models based on χ^2 values, (bottom left panel) the model results from Robitaille et al. (2006), and (bottom right panel) the model results from Zhang & Tan (2018).

Appendix B

Variations in the results of the Robitaille (2017) model packages with Bayesian versus χ^2 best-fit evaluations

Robitaille (2017) stress that χ^2 values alone may not be the optimal method of evaluating which source geometry best represents one's data. In order to assess the model sets in comparison to each other in a statistically robust way, Robitaille (2017) suggest calculating $P(D|M) \propto N_{good}/N$, where N_{good} is the total number of good models from a given model set, and N is the total number of models in that set. This method accounts for the possibility that one model set may have produced an unusually low χ^2 value that is not representative of the quality of that model set overall. In this approach, the model set with the highest number of good models is the best model set for a given source. The definition of "good" in this case is determined by the user; Robitaille (2017) use the convention $\chi^2 - \chi^2{}_{best} <$ Xn_{data}, where $\chi^2{}_{best}$ is the best χ^2 value across all model sets tested, n_{data} is the number of flux values that are not upper or lower limits, and X is a multiplicative factor chosen by the user. For the majority of our sources, $\chi^2 - \chi^2{}_{best} < 3n_{data}$ gives a reasonable split between

good and bad fits; the exception is G14.63−0.58, for which we used $X = 5$ for reasons discussed below. Table B.1 shows which model set best represents each source according to both the χ^2_{best} and $P(D|M)_{best}$ methods of determining "best representation."

Table B.1. χ^2 and P(D|M) Scores for Robitaille (2017) Model Sets[a,b]

G10.29–0.13

Model	χ^2	Model	P(D|M)
spubhmi	0.0003	s-u-smi	0.0519
spubsmi	0.002	spu-smi	0.0422
s-pbsmi	0.004	spubhmi	0.0408625
s-ubsmi	0.013	s-pbhmi	0.0384
s-u-smi	0.017	s-ubhmi	0.0359
s-pbhmi	0.022	spubsmi	0.02725
s-ubhmi	0.028	s-pbsmi	0.0261
spu-smi	0.044	s-ubsmi	0.0217

G10.34–0.14[c]

Model	χ^2	Model	P(D|M)
s-pbhmi	1.51	**s-pbhmi**	0.0029
s-pbsmi	2.30	s-pbsmi	0.0028
spubsmi	6.75	spubhmi	0.0008625
spubhmi	8.53	s-ubsmi	0.0008
s-ubsmi	12.13	spubsmi	0.0359
spubsmi	15.52	spubsmi	0.0325
spu-smi	21.70	spu-smi	0
s-u-smi	23.52	s-u-smi	0

G11.92–0.61

Model	χ^2	Model	P(D|M)
s-pbsmi	3.14	s-ubsmi	0.0015
s-pbhmi	3.69	s-pbsmi	0.0009
spubsmi	3.87	s-pbhmi	0.0007
spubhmi	4.73	spubsmi	0.000675
s-ubhmi	5.02	s-ubhmi	0.0006
s-ubsmi	6.08	spubhmi	0.0004125
s-u-smi	34.70	spu-smi	0
spu-smi	40.68	s-u-smi	0

G12.91–0.03

Model	χ^2	Model	P(D|M)
s-pbhmi	1.51	**s-pbhmi**	0.0013
spubhmi	1.84	s-ubsmi	0.0013
spubsmi	2.84	s-pbsmi	0.0011
s-ubsmi	3.03	s-ubhmi	0.0006
s-pbsmi	3.99	spubsmi	0.00055
s-ubhmi	4.84	spubhmi	0.00003375
s-u-smi	28.58	spu-smi	0
spu-smi	31.37	s-u-smi	0

G14.33–0.64

Model	χ^2	Model	P(D|M)
s-pbsmi	0.45	**s-pbsmi**	0.0034
s-pbhmi	0.80	s-pbhmi	0.003
spubsmi	2.30	s-ubhmi	0.0006
spubhmi	4.40	s-ubsmi	0.0006
s-ubsmi	4.51	spubhmi	0.000425
s-ubhmi	4.94	spubsmi	0.000425
spu-smi	12.78	spu-smi	0.0003
s-u-smi	12.84	s-u-smi	0.0002

G14.63–0.58

Model	χ^2	Model	P(D|M)
s-pbhmi	3.68	s-pbsmi	0.0007
s-pbsmi	4.41	s-pbhmi	0.0006
spubsmi	24.81	spubsmi	0.0001
spubhmi	24.87	spubhmi	0.00005
s-ubhmi	38.19	s-ubhmi	0
s-ubsmi	47.43	s-ubsmi	0
spu-smi	67.87	spu-smi	0
s-u-smi	70.85	s-u-smi	0

G16.59–0.05

Model	χ^2	Model	P(D|M)
s-pbhmi	1.12	s-pbsmi	0.0011
s-pbsmi	1.41	s-ubsmi	0.0008
s-ubsmi	2.32	spubsmi	0.00045
spubsmi	2.59	spubhmi	0.000425
s-pbhmi	2.60	s-pbhmi	0.0003
s-ubhmi	3.40	s-ubhmi	0.0003

G18.89–0.47

Model	χ^2	Model	P(D|M)
s-pbhmi	1.01	**s-pbhmi**	0.0008
spubhmi	1.83	s-pbsmi	0.0008
s-pbsmi	4.13	s-ubsmi	0.0007
s-ubsmi	8.40	spubsmi	0.000625
s-ubhmi	9.51	s-ubhmi	0.0002
spubsmi	9.59	spubhmi	0.0001

G19.36–0.03

Model	χ^2	Model	P(D|M)
s-pbsmi	1.73	**s-pbsmi**	0.0022
s-ubhmi	2.23	s-ubhmi	0.0019
s-pbhmi	3.02	s-pbhmi	0.0015
spubsmi	3.81	spubsmi	0.000625
s-ubsmi	3.83	s-ubsmi	0.0005
spubhmi	10.00	spubhmi	0.000425

The χ^2 and P(D|M) approaches yield the same best-fit model set in five cases (G10.34–0.14, G12.91–0.03, G14.33–0.64, G18.89–0.47, and G19.36–0.03), and different model sets in seven. Sources for which both approaches yield the same best-fit model set have their source name and best model set name marked in bold in Table B.1. Interestingly, both the χ^2 and Bayesian approaches tend to yield the same or very similar overall trends, such as, e.g., a strong preference for a power-law envelope or a slight preference for an inner hole. There are four sources for which the overall trends disagree on the presence or absence of at least one physical component (e.g. disk, inner hole); for one of these sources, the χ^2 and Bayesian methods return results that differ on every physical component. It is worth noting that the four sources for which the trends identified by the χ^2 and P(D|M) methods show disagreement either lack a 24 μm data point (the 24 μm flux densities have the lowest uncertainties in λF_λ-space, so a 24 μm non-detection has an outsize effect on the χ^2 values for all models for that source) or suffer from confusion problems at 160 μm as discussed in § 2.4.2. Interestingly, confusion problems at 70 μm do not seem to produce similar disagreements in the model results.

Below, we discuss best-fit geometries for each source in detail, using both the χ^2 and Bayesian methods of determining "best model."

G10.29–0.13 The χ^2 and Bayesian methods yield different best-fit model sets for this source (spubhmi for the former and s-u-smi for the latter), but both yield a general preference for a rotating-infalling (Ulrich-type) envelope and a slight preference for both a passive disk and no inner hole. All results for this particular source should be taken with the caveat that this source is quite poorly constrained (six of the nine flux densities used for SED modeling are upper limits).

Table B.1—Continued

spu-smi	32.60	spu-smi	0	spu-smi	44.43	spu-smi	0	s-u-smi	20.86	spu-smi	0
s-u-smi	35.47	s-u-smi	0	s-u-smi	44.73	s-u-smi	0	spu-smi	22.85	s-u-smi	0

G22.04+0.22				G28.83−0.25				G35.03+0.35			
Model	χ^2	Model	P(D|M)	Model	χ^2	Model	P(D|M)	Model	χ^2	Model	P(D|M)
s-pbhmi	1.81	spubsmi	0.001925	s-pbhmi	0.81	spubsmi	0.00255	spubhmi	1.08	s-ubsmi	0.0056
spubhmi	2.37	s-pbhmi	0.0019	s-ubsmi	2.36	s-ubsmi	0.0023	s-pbsmi	1.46	s-ubhmi	0.0034
s-pbsmi	2.41	s-pbsmi	0.0019	spubhmi	2.53	s-ubhmi	0.002	spubsmi	1.58	spubhmi	0.0033
s-ubsmi	2.55	s-ubsmi	0.0019	spubsmi	2.86	s-pbsmi	0.002	s-ubhmi	1.94	s-pbhmi	0.0033
s-ubhmi	2.59	s-u-smi	00017	s-pbsmi	5.06	spubhmi	0.00195	s-ubsmi	2.07	spubsmi	0.002775
spubsmi	2.61	spubhmi	0.001025	s-ubhmi	5.54	s-pbhmi	0.0011	s-pbhmi	2.45	s-u-smi	0.0019
s-u-smi	16.97	s-ubhmi	0.001	s-u-smi	18.12	s-u-smi	0.0006	spu-smi	9.47	spu-smi	0.0017
spu-smi	19.13	spu-smi	0.0005	spu-smi	20.02	spu-smi	0	s-u-smi	12.47	s-pbsmi	0.0014

[a]The χ^2 values shown are χ^2 per data point, as defined in § 2.5.2.

[b]Model sets are shown for each source in order of best (top row) to worst (bottom row). The first two columns for each source are the best model sets and χ^2 values according to the χ^2 method, and the second two columns for each source are the best model sets and χ^2 values according to the Bayesian method. We show all eight model sets used in order to more clearly illustrate source trends according to both the χ^2 and P(D|M) methods – that is, to illustrate trends not only in which model sets produce the best fits, but also in which model sets produce the worst fits.

[c]In cases where the χ^2 and P(D|M) methods produce the same best-fit model set, source names and best-fit model set names are highlighted in **bold**.

G10.34−0.14 Both methods yield the same trends for this source: a general preference for a power-law envelope and no passive disk for this source, with no real preference as to whether or not there is an inner hole. There is a significant increase (approximately a factor of 3) in χ^2 values between the two lowest-χ^2 model sets, which have no disk, and the third-best, which does. Likewise, there is a jump of approximately a factor of 3.5 in P(D|M) between the two best model sets (which do not have a passive disk) and the third-best, which does.

G11.92−0.61 All preferred Robitaille (2017) model sets for G11.92−0.61 favor a power-law envelope and no disk, with no strong preference as to the presence or absence of an inner hole. This is true for both the χ^2 and P(D|M) methods of determining the best model set. The fact that the results favor not having a disk is in direct contradiction with our knowledge of this source from high-resolution centimeter- and millimeter-wavelength observations (see Ilee et al. 2016, 2018). This disagreement is likely a result of the comparatively poor resolution of our SOFIA and archival infrared observations ($\sim 1''$ to $19''.2$) as compared with the millimeter observations ($\sim 0''.09$ to $\sim 0''.75$; Ilee et al. 2016, 2018); the infrared observations simply do not have sufficient resolution to distinguish the necessary small-scale structure in such a clustered source.

The discrepancy between the SED modeling results and the results of Ilee et al. (2016, 2018) warrant a closer look. Based on $\sim 0''.5$ (1550 au)-resolution Submillimeter Array (SMA) data, Ilee et al. (2016) estimated a disk gas mass of $\sim 2-3$ $M_\odot$ and an enclosed mass $M_{\mathrm{enc}} \sim 30-60$ $M_\odot$. Using $\sim 0''.09$ (310 au)-resolution ALMA observations, Ilee et al. (2018) find an enclosed mass M_{enc} of 40 ± 5 $M_\odot$ and a disk gas mass of $\sim 2-6$ $M_\odot$. The Robitaille et al. (2006) best-fit model returns a central source mass of 13.4 $M_\odot$ and a disk gas mass of 4.6×10^{-2} $M_\odot$, while the Zhang & Tan (2018) best-fit model gives a central source mass of 16 $M_\odot$ and a disk mass of 5.33 $M_\odot$ ($\frac{1}{3}$ the mass of the central source, as

discussed in § 2.5.2). In this case, while the Robitaille (2017) models do not favor the known physical geometry, the Robitaille et al. (2006) and Zhang & Tan (2018) models do not reproduce the observationally-derived stellar and disk masses. That is, none of the three models accurately describes the known physical parameters of this source.

G12.91−0.03 While the χ^2 and P(D|M) methods do produce the same best-fit model set for this source, the overall trends in the χ^2 and P(D|M) results disagree. Neither method particularly seems to favor one envelope type over another. However, the χ^2 results overall favor models which have an inner hole and a passive disk, whereas the P(D|M) evaluation shows a strong preference for having no disk, but no preference as to the presence or absence of an inner hole.

G14.33−0.64 Both the χ^2 values and P(D|M) show a strong preference for having no disk and a power-law envelope, and no real preference as to the presence or absence of an inner hole.

G14.63−0.58 Both methods show, for this source, a strong preference for no passive disk, and for a power-law envelope, with no real preference for or against an inner hole. The P(D|M) results for this source should be considered carefully, however. G14.63−0.58 has few good fits in any model set, and so for this source we used the cutoff $\chi^2 - \chi^2_{best} < 5n_{data}$ instead.

G16.59−0.05 The χ^2 and P(D|M) evaluations both favor models with no inner hole and no disk, but differ as to envelope type. The χ^2 values suggest that a power-law envelope produces the best fit to our data, while the Bayesian approach suggests an Ulrich-type envelope instead. G16.59−0.05 is saturated in the MIPSGAL data, so its SED lacks a flux density at that wavelength. MIR emission in YSOs tends to be dominated by emission

from the protostellar envelope and/or outflow cavities, and our fitted 24 μm flux densities were usually the best-constrained data points for a given source. It is possible that the discrepancy in preferred envelope type is due to this combination of factors.

As for the fact that both evaluations of the Robitaille (2017) results favor model sets with no disk, this is another source for which additional data in the literature show this implication to be incorrect. Moscadelli et al. (2016) identify G16.59−0.05 as a $\sim$20 $M_\odot$ YSO with a disk/jet system. The central source appears as compact Ku- and K-band continuum emission at 0$\farcs$2 and 0$\farcs$1 resolutions, respectively, and the rotating disk is traced by multi-epoch EVN observations of 6.7 GHz CH$_3$OH masers associated with the compact Ku- and K-band emission (for details of the EVN observations, see Moscadelli et al. 2016, and references therein). The jet is traced by extended C-band emission ($\sim$ 6 cm, 0$\farcs$4 resolution) in both Moscadelli et al. (2016) and Rosero et al. (2016).

Neither Moscadelli et al. (2016) nor Rosero et al. (2016) estimate disk mass or accretion rate, so we cannot asses the quality of the Robitaille et al. (2006) and Zhang & Tan (2018) results in that context. However, unlike as for G11.92−0.61, both the Robitaille et al. (2006) and Zhang & Tan (2018) models do give results for protostellar mass (15$M_\odot$ and 16$M_\odot$, respectively) that are fairly well in line with the mass reported by Moscadelli et al. (2016). While the specific parameters of the disk cannot be explored at this time, we can state that the Robitaille et al. (2006) and Zhang & Tan (2018) $M_\star$ results are consistent, for the moment, with the results available in the literature.

G18.89−0.47 Both methods of evaluation favor models with no disk and a power-law envelope for this source. However, the Bayesian approach suggests that models without an inner hole more accurately fit the data, whereas the χ^2 values favor models that do have an inner hole. G18.89−0.47 is one of our sources with a confusion problem at 160 μm.

G19.36−0.03   Both the χ^2 and P(D|M) values for this source strongly favor models with no disk, but neither shows any particular trend in envelope type or presence/absence of an inner hole.

G22.04+0.22   Both methods of model evaluation agree for this source: models which have no disk and no inner hole are favored, but there is no strong preference as to envelope type.

G28.83−0.25   The χ^2 and P(D|M) values for this source both favor models with an Ulrich-type envelope and no disk, with either no or a very slight preference for models with no inner hole.

G35.03+0.35   This is the one source for which the χ^2 and P(D|M) values produce entirely different trends. While the model sets with the best χ^2 values notably lack trends for any particular physical components, the P(D|M) values show a strong preference for models with an Ulrich envelope, no disk, and an inner hole. This is the one source which has a known UCH II region in the EGO itself (as opposed to an H II region nearby but not within the ATLASGAL clump which hosts the EGO, as is the case with G14.33−0.64).

References

Anglada, G., Rodríguez, L. F., & Carrasco-González, C. 2018, A&A Rev., 26, 3

Anglada, G., Estalella, R., Pastor, J., et al. 1996, ApJ, 463, 205

Banerjee, S., & Kroupa, P. 2017, A&A, 597, A28

Barrett, A. H., Ho, P., & Martin, R. N. 1975, ApJ, 198, L119

Barrett, A. H., Schwartz, P. R., & Waters, J. W. 1971, ApJ, 168, L101

Bayandina, O. S., Val'tts, I. E., & Kurtz, S. E. 2015, Astronomy Reports, 59, 998

Beltrán, M. T., Sánchez-Monge, Á., Cesaroni, R., et al. 2014, A&A, 571, A52

Benjamin, R. A., Churchwell, E., Babler, B. L., et al. 2003, PASP, 115, 953

Bernasconi, P. A., & Maeder, A. 1996, A&A, 307, 829

Beuther, H., Mottram, J. C., Ahmadi, A., et al. 2018, A&A, 617, A100

Beuther, H., Zhang, Q., Sridharan, T. K., Lee, C.-F., & Zapata, L. A. 2006, A&A, 454, 221

Bonnell, I. A., Bate, M. R., Clarke, C. J., & Pringle, J. E. 2001, MNRAS, 323, 785

Bonnell, I. A., Bate, M. R., & Vine, S. G. 2003, MNRAS, 343, 413

Bonnell, I. A., Vine, S. G., & Bate, M. R. 2004, MNRAS, 349, 735

Bonnell, I. A., & Bate, M. R. 2006, MNRAS, 370, 488

Breen, S. L., & Ellingsen, S. P. 2011, MNRAS, 416, 178

Britton, T. R., & Voronkov, M. A. 2012, Cosmic Masers - from OH to H0, IAU Symposium, 287, 282

Brogan, C. L., Hunter, T. R., Towner, A. P. M., et al. 2019, ApJ, 881, L39

Brogan, C. L., Hunter, T. R., Cyganowski, C. J., et al. 2016, ApJ, 832, 187

Brogan, C. L., Hunter, T. R., Cyganowski, C. J., et al. 2011, ApJ, 739, L16

Brogan, C. L., Hunter, T. R., Cyganowski, C. J., et al. 2009, ApJ, 707, 1

Bronfman, L., Nyman, L.-A., & May, J. 1996, A&AS, 115, 81

Carey, S. J., Noriega-Crespo, A., Mizuno, D. R., et al. 2009, PASP, 121, 76

Carpenter, J. M., Snell, R. L., & Schloerb, F. P. 1990, ApJ, 362, 147

Carrasco-González, C., Rodríguez, L. F., Anglada, G., et al. 2010, Science, 330, 1209

Carrasco-González, C., Torrelles, J. M., Cantó, J., et al. 2015, Science, 348, 114

Caswell, J. L. 2009, PASA, 26, 454

Chandler, C. J., & Butler, B. J. 2014, Proc. SPIE, 9149, 914917

Chen, X., Ellingsen, S. P., Shen, Z.-Q., Titmarsh, A., & Gan, C.-G. 2011, ApJS, 196, 9

Chen, X., Ellingsen, S. P., He, J.-H., et al. 2012, ApJS, 200, 5

Chen, X., Gan, C.-G., Ellingsen, S. P., et al. 2013, ApJS, 206, 9

Chini, R., Barr, A., Buda, L. S., et al. 2013, Central European Astrophysical Bulletin, 37, 295

Churchwell, E., Babler, B. L., Meade, M. R., et al. 2009, PASP, 121, 213

Cragg, D. M., Johns, K. P., Godfrey, P. D., & Brown, R. D. 1992, MNRAS, 259, 203

Csengeri, T., Leurini, S., Wyrowski, F., et al. 2016, A&A, 586, A149

Cyganowski, C. J., Brogan, C. L., & Hunter, T. R. 2007, AJ, 134, 346

Cyganowski, C. J., Whitney, B. A., Holden, E., et al. 2008, AJ, 136, 2391-2412

Cyganowski, C. J., Brogan, C. L., Hunter, T. R., & Churchwell, E. 2009, ApJ, 702, 1615

Cyganowski, C. J., Brogan, C. L., Hunter, T. R., & Churchwell, E. 2011, ApJ, 743, 56

Cyganowski, C. J., Brogan, C. L., Hunter, T. R., Churchwell, E., & Zhang, Q. 2011, ApJ, 729, 124

Cyganowski, C. J., Brogan, C. L., Hunter, T. R., et al. 2012, ApJ, 760, L20

Cyganowski, C. J., Koda, J., Rosolowski, E., et al. 2013, ApJ, 764, 61

Cyganowski, C. J., Brogan, C. L., Hunter, T. R., et al. 2014, ApJ, 796, L2

Cyganowski, C. J., Brogan, C. L., Hunter, T. R., et al. 2017, MNRAS, 468, 3694

De Buizer, J. M., Liu, M., Tan., J. C., et al. 2017, ApJ, 843, 33

Deharveng, L., Zavagno, A., Samal, M. R., et al. 2015, A&A, 582, A1

Deharveng, L., Schuller, F., Anderson, L. D., et al. 2010, A&A, 523, A6

de Villiers, H. M., Chrysostomou, A., Thompson, M. A., et al. 2014, MNRAS, 444, 566

Di Francesco, J., Johnstone, D., Kirk, H., MacKenzie, T., & Ledwosinska, E. 2008, ApJS, 175, 277

Di Francesco, J., Evans, N. J., Caselli, P., et al. 2007, Protostars and Planets V, 17

Di Francesco, J., Johnstone, D., Kirk, H., MacKenzie, T., & Ledwosinska, E. 2008, ApJS, 175, 277-295

Draine, B. T. 2003a, ApJ, 598, 1017

Draine, B. T. 2003b, ARA&A, 41, 241

Drew, J. E., Herrero, A., Mohr-Smith, M., et al. 2018, MNRAS, 480, 2109

Duarte-Cabral, A., Bontemps, S., Motte, F., et al. 2013, A&A, 558, A125

Egan, M. P., Price, S. D., & Kraemer, K. E. 2003, Bulletin of the American Astronomical Society, 35, 57.08

Elia, D., Molinari, S., Schisano, E., et al. 2017, MNRAS, 471, 100

Ellingsen, S. P. 2006, ApJ, 638, 241

Enoch, M. L., Evans, N. J., II, Sargent, A. I., & Glenn, J. 2009, ApJ, 692, 973

Fazio, G. G., Hora, J. L., Allen, L. E., et al. 2004, ApJS, 154, 10

Fontani, F., Beltrán, M. T., Brand, J., et al. 2005, A&A, 432, 921

Fontani, F., Cesaroni, R., & Furuya, R. S. 2010, A&A, 517, A56

Forster, J. R., and J. L. Caswell 2000, ApJ, 530, 371

Frank, A., Ray, T. P., Cabrit, S., et al. 2014, Protostars and Planets VI, 451

Gaczkowski, B., Preibisch, T., Ratzka, T., et al. 2013, A&A, 549, A67

Ge, J. X., He, J. H., Chen, X., & Takahashi, S. 2014, MNRAS, 445, 1170

Giannetti, A., Wyrowski, F., Brand, J., et al. 2014, A&A, 570, 65

Giannetti, A., Leurini, S., Wyrowski, F., et al. 2017, A&A, 603, 33

Goedhart, S., van der Walt, D. J., & Gaylard, M. J. 2002, MNRAS, 335, 125

Goedhart, S., van der Walt, D. J., & Schutte, A. J. 2000, MNRAS, 315, 316

Gómez, L., Luis, L., Hernández-Curiel, I., et al. 2010, ApJS, 191, 207

Green, J. A., Caswell, J. L., Fuller, G. A., et al. 2010, MNRAS, 409, 913

Green, C.-E., Green, J. A., Burton, M. G., et al. 2014, MNRAS, 443, 2252

Greene, T. 2001, American Scientist, 89, 316

Gutermuth, R. A., & Heyer, M. 2015, AJ, 149, 64

He, J. H., Takahashi, S., & Chen, X. 2012, ApJS, 202, 1

Herbst, E., & van Dishoeck, E. F. 2009, ARA&A, 47, 427

Herter, T. L., Adams, J. D., De Buizer, J. M., et al. 2012, ApJ, 749, L18

Hills, R., Pankonin, V., & Landecker, T. L. 1975, A&A, 39, 149

Hofner, P., & Churchwell, E. 1996, A&AS, 120, 283

Hofner, P., Peterson, S., & Cesaroni, R. 1999, ApJ, 514, 899

Hofner, P., Kurtz, S., Ellingsen, S. P., et al. 2011, ApJ, 739, L17

Hosokawa, T., & Omukai, K. 2009, ApJ, 691, 823

Hughes, V. A., & MacLeod, G. C. 1994, ApJ, 427, 857

Hunter, T. R., Brogan, C. L., MacLeod, G., et al. 2017, ApJ, 837, L29

Hunter, T. R., Brogan, C. L., Megeath, S. T., et al. 2006, ApJ, 649, 888

Ilee, J. D., Cyganowski, C. J., Brogan, C. L., et al. 2018, ApJ, 869, L24

Ilee, J. D., Cyganowski, C. J., Nazari, P., et al. 2016, MNRAS, 462, 4386

Immer, K., Galván-Madrid, R., König, C., Liu, H. B., & Menten, K. M. 2014, A&A, 572, A63

Jaffe, D. T., Stier, M. T., & Fazio, G. G. 1982, ApJ, 252, 601

Jaffe, D. T., Guesten, R., & Downes, D. 1981, ApJ, 250, 621

Johnston, K. J., Gaume, R., Stolovy, S., et al. 1992, ApJ, 385, 232

Kang, H., Kim, K.-T., Byun, D.-Y., Lee, S., & Park, Y.-S. 2015, ApJS, 221, 6

Kennicutt, R. C., & Evans, N. J. 2012, ARA&A, 50, 531

Keto, E. 2007, ApJ, 666, 976

Keto, E. 2003, ApJ, 599, 1196

Klein, R., Posselt, B., Schreyer, K., et al. 2005, ApJS, 161, 361

Klessen, R. S., Peters, T., Banerjee, R., et al. 2011, Computational Star Formation, 107

König, C., Urquhart, J. S., Csengeri, T., et al. 2017, A&A, 599, 139

Konigl, A. 1982, ApJ, 261, 115

Kraemer, K. E., Deutsch, L. K., Jackson, J. M., et al. 1999, ApJ, 516, 817

Kurtz, S., Hofner, P., & Álvarez, C. V. 2004, ApJS, 155, 149

Kurtz, S., Churchwell, E., & Wood, D. O. S. 1994, ApJS, 91, 659

Lada, C. J., & Lada, E. A. 2003, ARA&A, 41, 57

Laor, A., & Draine, B. T. 1993, ApJ, 402, 441

Lee, H.-T., Takami, M., Duan, H.-Y., et al. 2012, ApJS, 200, 2

Lee, H.-T., Liao, W.-T., Froebrich, D., et al. 2013, ApJS, 208, 23

Leurini, S., Menten, K. M., & Walmsley, C. M. 2016, A&A, 592, A31

Li, F. C., Xu, Y., Wu, Y. W., et al. 2016, AJ, 152, 92

Liechti, S., & Wilson, T. L. 1996, A&A, 314, 615

Lin, Y., Csengeri, T., Wyrowski, F., et al. 2019, A&A, 631, A72

Lu, X., Zhang, Q., Liu, H. B., Wang, J., & Gu, Q. 2014, ApJ, 790, 84

Lucas, W. E., Rybak, M., Bonnell, I. A., et al. 2018, MNRAS, 474, 3582

Markwardt, C. B. 2009, Astronomical Data Analysis Software and Systems XVIII, 411, 251

Marston, A. P., Reach, W. T., Noriega-Crespo, A., et al. 2004, ApJS, 154, 333

Massi, F., Weiss, A., Elia, D., et al. 2019, A&A, 628, A110

Matsakis, D. N., Wright, M. C. H., Townes, C. H., et al. 1980, ApJ, 236, 481

McKee, C. F., & Ostriker, E. C. 2007, ARA&A, 45, 565

McKee, C. F., & Tan, J. C. 2003, ApJ, 585, 850

McKee, C. F., & Tan, J. C. 2002, Nature, 416, 59

McMullin, J. P., Waters, B., Schiebel, D., Young, W., & Golap, K. 2007, Astronomical
    Data Analysis Software and Systems XVI (ASP Conf. Ser. 376), ed. R. A. Shaw, F. Hill,
    & D. J. Bell (San Francisco, CA: ASP), 127

Mehringer, D. M. 1994, ApJS, 91, 713

Menten, K. M., Walmsley, C. M., Henkel, C., & Wilson, T. L. 1986, A&A, 157, 318

Menten, K. M., Walmsley, C. M., Henkel, C., & Wilson, T. L. 1988, A&A, 198, 267

Minier, V., Ellingsen, S. P., Norris, R. P., et al. 2003, A&A, 403, 1095

Molinari, S., Brand, J., Cesaroni, R., & Palla, F. 1996, A&A, 308, 573

Molinari, S., Pezzuto, S., Cesaroni, R., et al. 2008, A&A, 481, 345

Molinari, S., Swinyard, B., Bally, J., et al. 2010, PASP, 122, 314

Molinari, S., Schisano, E., Elia, D., et al. 2016, A&A, 591, A149

Mooney, T. J., and Solomon, P. M., 1988, ApJ, 334, L51

Moscadelli, L., Sanna, A., Goddi, C., et al. 2020, A&A, 635, A118

Moscadelli, L., Sánchez-Monge, Á., Goddi, C., et al. 2016, A&A, 585, A71

Moscadelli, L., Cesaroni, R., Sánchez-Monge, Á., et al. 2013, A&A, 558, A145

Motte, F., Nony, T., Louvet, F., et al. 2018, Nature Astronomy, 2, 478

Motte, F., Bontemps, S., & Louvet, F. 2018b, ARA&A, 56, 41

Müller, H. S. P., Menten, K. M., & Mäder, H. 2004, A&A, 428, 1019

Neugebauer, G., Habing, H. J., van Duinen, R., et al. 1984, ApJ, 278, L1

Ossenkopf, V., & Henning, T. 1994, A&A, 291, 943

Perley, R. A., Chandler, C. J., Butler, B. J., & Wrobel, J. M. 2011, ApJ, 739, L1

Pestalozzi, M. R., Minier, V., & Booth, R. S. 2005, A&A, 432, 737

Plambeck, R. L., & Menten, K. M. 1990, ApJ, 364, 555

Poglitsch, A., Waelkens, C., Geis, N., et al. 2010, A&A, 518, L2

Plume, R., Jaffe, D. T., Evans, N. J., et al. 1997, ApJ, 476, 730

Pratap, P., Strelnitski, V., Hoffman, S., & Lemonias, J. 2007, Astrophysical Masers and their Environments, 242, 34

Purcell, C. R., Longmore, S. N., Burton, M. G., et al. 2009, MNRAS, 394, 323

Purcell, C. R., Balasubramanyam, R., Burton, M. G., et al. 2006, MNRAS, 367, 553

Purser, S. J. D., Lumsden, S. L., Hoare, M. G., et al. 2016, MNRAS, 460, 1039

Rathborne, J. M., Jackson, J. M., & Simon, R. 2006, ApJ, 641, 389

Rathborne, J. M., Simon, R., & Jackson, J. M. 2007, ApJ, 662, 1082

Reid, M. J., Menten, K. M., Brunthaler, A., et al. 2014, ApJ, 783, 130

Reid, M. J., Argon, A. L., Masson, C. R., et al. 1995, ApJ, 443, 238

Reynolds, S. P. 1986, ApJ, 304, 713

Rieke, G. H., Young, E. T., Engelbracht, C. W., et al. 2004, ApJS, 154, 25

Robitaille, T. P., Whitney, B. A., Indebetouw, R., Wood, K., & Denzmore, P. 2006, ApJS, 167, 256

Robitaille, T. P., Whitney, B. A., Indebetouw, R., & Wood, K. 2007, ApJS, 169, 328

Robitaille, T., & Bressert, E. 2012, APLpy: Astronomical Plotting Library in Python, Astrophysics Source Code Library. http://ascl.net/1208.017

Robitaille, T. P. 2017, A&A, 600, A11

Rosen, A. L., Krumholz, M. R., McKee, C. F., et al. 2016, MNRAS, 463, 2553

Rosero, V., Hofner, P., Claussen, M., et al. 2016, ApJS, 227, 25

Rosero, V., Tanaka, K. E. I., Tan, J. C., et al. 2019, ApJ, 873, 20

Rosero, V., Hofner, P., Kurtz, S., et al. 2019, ApJ, 880, 99

Rudnitskii, G. M., Lekht, E. E., Bayandina, O. S., Val'tts, I. E., & Khan, E. R. 2016, Astronomy Reports, 60, 129

Russeil, D., Zavagno, A., Motte, F., et al. 2010, A&A, 515, A55

Rygl, K. L. J., Wyrowski, F., Schuller, F., & Menten, K. M. 2010, A&A, 515, A42

Rygl, K. L. J., Wyrowski, F., Schuller, F., & Menten, K. M. 2013, A&A, 549, A5

Sadavoy, S. I., Stutz, A. M., Schnee, S., et al. 2016, A&A, 588, A30

Sadavoy, S. I., Di Francesco, J., Bontemps, S., et al. 2010, ApJ, 710, 1247

Salii, S. V. and A. M. Sobolev. 2006, Astronomy Reports, 50, 12: 965

Sanna, A., Moscadelli, L., Goddi, C., et al. 2019, A&A, 623, L3

Sanna, A., Moscadelli, L., Goddi, C., et al. 2018, A&A, 619, A107

Sanna, A., Moscadelli, L., Cesaroni, R., et al. 2010, A&A, 517, A71

Schuller, F., Menten, K. M., Contreras, Y., et al. 2009, A&A, 504, 415

Scoville, N. Z., and Good, J. C., 1989, ApJ, 339, 149

Shirley, Y. L., Nordhaus, M. K., Grcevich, J. M., et al. 2005, ApJ, 632, 982

Siess, L., Dufour, E., & Forestini, M. 2000, A&A, 358, 593

Slysh, V. I., Val'tts, I. E., Kalenskii, S. V., & Golubev, V. V. 1999, Astronomy Reports, 43, 785

Sobolev, A. M., Cragg, D. M., Ellingsen, S. P. et al. 2007, IAU Symposium, 242, 81

Spezzi, L., Cox, N. L. J., Prusti, T., et al. 2013, A&A, 555, A71

Sridharan, T. K., Beuther, H., Schilke, P., Menten, K. M., & Wyrowski, F. 2002, ApJ, 566, 931

Stahler, S. W., Palla, F., & Ho, P. T. P. 2000, Protostars and Planets IV, 327

Stephens, I. W., Gouliermis, D., Looney, L. W., et al. 2017, ApJ, 834, 94

Surcis, G., Vlemmings, W. H. T., van Langevelde, H. J., et al. 2015, A&A, 578, A102

Svoboda, B. E., Shirley, Y. L., Traficante, A., et al. 2019, ApJ, 886, 36

Szymczak, M., Pillai, T., & Menten, K. M. 2005, A&A, 434, 613

Tan, J. C., Beltrán, M. T., Caselli, P., et al. 2014, Protostars and Planets VI, 149

Tan, J. C., Kong, S., Butler, M. J., et al. 2013, ApJ, 779, 96

Tanaka, K. E. I., Tan, J. C., & Zhang, Y. 2016, ApJ, 818, 52

Temi, P., Marcum, P. M., Young, E., et al. 2014, ApJS, 212, 24

Thompson, M. A., Hatchell, J., Walsh, A. J. et al. 2006, A&A, 453, 1003

Tigé, J., Motte, F., Russeil, D., et al. 2017, A&A, 602, A77

Towner, A. P. M., Brogan, C. L., Hunter, T. R., et al. 2019, ApJ, 875, 135

Towner, A. P. M., Brogan, C. L., Hunter, T. R., et al. 2017, ApJS, 230, 22

Urquhart, J. S., König, C., Giannetti, A., et al. 2018, MNRAS, 473, 1059

Urquhart, J. S., Morgan, L. K., Figura, C. C., et al. 2011, MNRAS, 418, 1689

Val'tts, I. E., Ellingsen, S. P., Slysh, V. I., et al. 2000, MNRAS, 317, 315

Vázquez-Semadeni, E., González-Samaniego, A., & Colín, P. 2017, MNRAS, 467, 1313

Vig, S., Testi, L., Walmsley, M., et al. 2007, A&A, 470, 977

Voronkov, M. A., Brooks, K. J., Sobolev, A. M. et al. 2006, MNRAS, 373, 411

Voronkov, M. A., Sobolev, A. M., Ellingsen, S. P., et al. 2007, IAU Symposium, 242, 182

Voronkov, M. A., Caswell, J. L., Ellingsen, S. P., et al. 2012, Cosmic Masers - from OH to H0, 287, 433

Walsh, A. J., Hyland, A. R., Robinson, G., & Burton, M. G. 1997, MNRAS, 291, 261

Walsh, A. J., Macdonald, G. H., Alvey, N. D. S., Burton, M. G., & Lee, J.-K. 2003, A&A, 410, 597

Watson, C., Povich, M. S., Churchwell, E. B., et al. 2008, ApJ, 681, 1341-1355

Weingartner, J. C., & Draine, B. T. 2001, ApJ, 548, 296

Wenger, M., Ochsenbein, F., Egret, D., et al. 2000, A&AS, 143, 9

Westerhout, G. 1958, Bull. Astron. Inst. Netherlands, 14, 215

Wink, J. E., Altenhoff, W. J., & Mezger, P. G., 1982, A&A, 108, 227

Wolf-Chase, G., Moriarty-Schieven, G., Fich, M., et al. 2003, MNRAS, 344, 809

Wood, D. O. S., & Churchwell, E. 1989, ApJS, 69, 831

Wood, D. O. S., & Churchwell, E. 1989, ApJ, 340, 265

Wright, E. L., Eisenhardt, P. R. M., Mainzer, A. K., et al. 2010, AJ, 140, 1868

Yorke, H. W., Bodenheimer, P., & Laughlin, G. 1993, ApJ, 411, 274

Zapata, L. A., Rodríguez, L. F., Ho, P. T. P., Beuther, H., & Zhang, Q. 2006, AJ, 131, 939

Zavagno, A., Anderson, L. D., Russeil, D., et al. 2010, A&A, 518, L101

Zhang, Q., Sridharan, T. K., Hunter, T. R., et al. 2007, A&A, 470, 269

Zhang, Y., & Tan, J. C. 2018, ApJ, 853, 18

Zinnecker, H., & Yorke, H. W. 2007, ARA&A, 45, 481